

The influence of energetic bombardment on the structure formation of sputtered zinc oxide films

—

Development of an atomistic growth model and its application to tailor thin film properties

Von der Fakultät für Mathematik, Informatik und Naturwissenschaften der
RWTH Aachen University zur Erlangung des akademischen Grades eines
Doktors der Naturwissenschaften genehmigte Dissertation

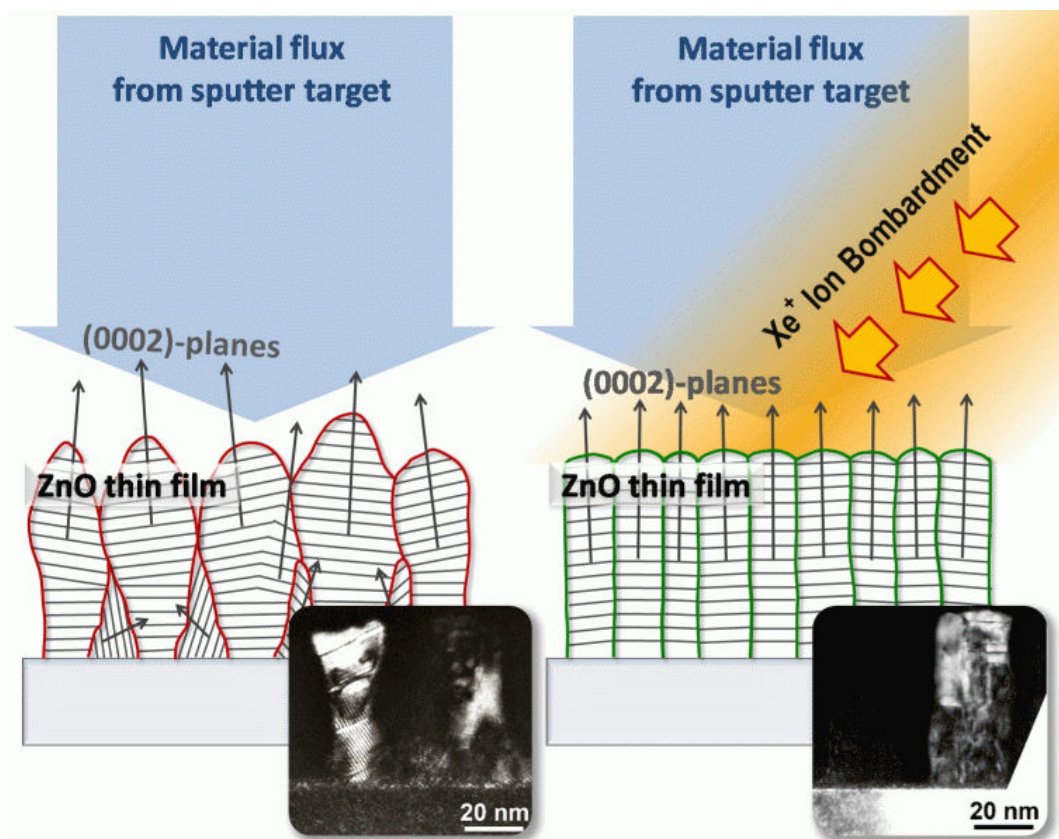
vorgelegt von

Diplom-Physiker
Dominik Köhl
aus Gießen

Berichter: Universitätsprofessor Matthias Wuttig
Universitätsprofessor Dieter Mergel

Tag der mündlichen Prüfung: 17.02.2011

Diese Dissertation ist auf den Internetseiten der Hochschulbibliothek online
verfügbar.



Contents

1	Introduction	5
2	Zinc oxide - properties, applications and growth	9
2.1	Material properties	9
2.1.1	Miller index notation in hexagonal systems	11
2.2	Properties of thin films	13
2.3	Crystal growth	16
2.4	Principles of textured thin film growth	20
2.4.1	Minimization of surface free energy as a driving force for preferred nucleation?	23
2.4.2	Minimization of strain energy as a driving force for preferred nucleation?	26
2.5	Thin film growth by chemical processes	30
2.5.1	Growth from chemical solution	30
2.5.2	Growth from chemical vapour	32
2.6	Thin film growth by physical vapour deposition (PVD) processes	38
2.6.1	Growth by pulsed laser deposition	38
2.6.2	Growth by magnetron sputtering	41
2.7	Summary: Texture formation in sputtered zinc oxide thin films	48
3	The magnetron sputtering processes	51
3.1	Coater 1: The IBAS setup	51
3.2	Coater 2: A conventional sputtering setup	56
4	Thin film analytics	59
4.1	X-ray techniques	59
4.1.1	X-ray diffraction (XRD)	59
4.1.2	Interpretation of grazing incidence XRD patterns	62
4.1.3	X-ray reflectometry (XRR)	64
4.2	Atomic force microscopy (AFM)	67
4.3	Transmission electron microscopy (TEM)	67
4.4	In-situ stress measurements - wafer curvature method	67
4.5	Optical techniques	71
4.5.1	Reflectance and transmittance	71
4.5.2	Ellipsometry	72
4.5.3	Modeling of the dielectric function	72
4.6	Electrical measurements	73

CONTENTS

5	I: Growth of zinc oxide films by IBAS	75
5.1	Growth conditions	79
5.2	Optimization of film structure	80
5.2.1	X-ray diffraction	80
5.2.2	Mechanical growth stresses	81
5.2.3	Surface topography	84
5.2.4	Microstructure	92
5.3	Discussion and evaluation	96
5.4	Development of a first growth model	101
6	II: Applications of modified zinc oxide structures	105
6.1	Homo-epitaxial growth of ZnO and ZnO:Al thin films	105
6.1.1	Tailoring buffer layers	106
6.1.2	Influence of modified buffer layers	119
6.2	Generalization of the growth model	126
6.3	Hetero-epitaxial growth of Ag thin films	132
6.3.1	Introduction	132
6.3.2	Silver structure improvement by modified ZnO seed layers	135
6.3.3	Microscopical growth study of Ag films on ZnO seed layers	147
7	III: Finally unravelling the origin of preferred orientation in zinc oxide thin films	157
7.1	Blocking (002) preferred orientation by IBAS: a-axis textured ZnO	158
7.2	Discussion: Preferred nucleation vs evolutionary selection and the influence of energetic oxygen ions	166
7.3	The final growth model	175
8	Summary and outlook	181
	References	185
	List of figures	195

Introduction

The focus of this work is the investigation of the growth of zinc oxide (ZnO) thin films. This material has attained increasing scientific interest during the last decade. Particularly, doped zinc oxide films have become the material of choice in the fabrication of transparent electrodes for silicon thin film solar cells, which offer a low-cost alternative to wafer-based highly efficient but expensive modules. Most commonly, zinc oxide is doped with aluminium to obtain a transparent conducting oxide (TCO). Such films exhibit high optical transparency and good (but not perfect) electrical conductivity. Nevertheless, this disadvantage is overcompensated by the low production costs due to large deposits of both zinc and aluminium in the terrestrial crust.

Another market segment where zinc oxide films are utilized is the fabrication of low-emissivity architectural glazing. The functionality of these energy saving windows arises from a combination of high optical reflectivity in the infrared spectral region with optimum transparency in the visible regime. This prerequisite could be easily achieved with an arbitrarily complex multi-layer stack. Competition however requires minimization of production costs. Therefore, typically one or two very thin silver films in combination with a minimum number of anti-reflective oxide layers are utilized. Maximization of production efficiency requires tweaking each single layer for optimum performance, which is particularly true for the silver films. Since the typical thickness of these silver films is almost at the percolation limit, the electrical and optical properties critically depend on the morphology of the films and hence on nucleation and grain growth. For this reason, zinc oxide films are utilized as seed layers for silver film growth since their close epitaxial relationship significantly promotes the formation of a well-ordered silver crystal structure with a preferred orientation. Thus, optimizing silver layer performance requires mastering zinc oxide film growth.

A common feature of these applications of zinc oxide thin films is that if material properties can be significantly improved, either the device efficiency can be maximized and/or the production costs can be minimized. It is therefore highly desirable to establish a thorough understanding of zinc oxide film growth. Particularly, this understanding must include the influence of energetic ion bombardment, a feature which is inherent in the coating process.

For the applications mentioned above zinc oxide is most commonly deposited in large scale onto amorphous float glass substrates by a deposition process far away from thermodynamic equilibrium: sputter deposition. Consequently, films often exhibit kinetically controlled structures. However, a self-texturing mechanism of zinc oxide that might originate from thermodynamics typically leads to high structural order with increasing film thickness. In spite of that mechanism there is unused potential since films are often weakly textured in the initial growth stage, a fact which also limits the achievable maximum in the structural order of thick films. Particularly in the fabrication of low-emissivity coatings, where very thin zinc oxide films are utilized, device performance critically depends on the structural quality obtained in the early growth stage of zinc oxide. It is therefore vital to understand how different process parameters affect structure formation. It is widely known that additional heating of the substrate (200-300 °C) during film growth improves the structural quality. On the other hand, it is also known that the bombardment of the growing film with highly energetic oxygen ions, which is an inevitable feature of the sputtering process, markedly deteriorates structural order. While substrate heating can compensate for this damage, such energetic ion bombardment has a detrimental effect on the zinc oxide film structure at room temperature. The necessity to heat the glass substrate adds process costs and reduces the energy balance of the final product.

In the literature on zinc oxide thin films it is comprehensively portrayed that films often exhibit structural inhomogeneities along the growth direction if grown on amorphous (non-epitaxial) substrates (see e.g. [1]). Also, the detrimental influence of highly energetic oxygen ion bombardment on film growth in general is extensively discussed. However, literature on possible positive influences of tailored ion bombardment is rare; just as literature on possible correlations between different growth stages of the zinc oxide films and the extent of structural modification/damage caused by ion bombardment. Closing this gap is the scope of this work.

It will be demonstrated that with a modified, ion beam assisted sputtering (IBAS) process, zinc oxide films can be deposited which exhibit a markedly improved crystalline order. Furthermore, it will be demonstrated that intense energetic oxygen ion bombardment can be utilized to change film texture from the typical (002)-self-texture to an a-axis texture where the (002)-planes are perpendicular to the substrate surface. An understanding of the underlying mechanisms will be developed which also facilitates a more detailed understanding of the action of ion bombardment during zinc oxide film growth. It will be shown that zinc oxide films are susceptible to the influence of ion bombardment particularly in the nucleation regime of growth and that this finding is generally true for all observed structural changes induced by ion bombardment with various species, energies and flux densities. These findings will therefore allow answering fundamental questions regarding the mechanisms governing structural evolution of zinc oxide thin films, which is also the scope of this work. It will be demonstrated not only

that the initial growth stage plays an important role in the formation of a preferred growth orientation but also that the action of texture forming mechanisms in subsequent growth stages is comparatively weak.

Detailed models of zinc oxide film growth with special respect to the influence of ion bombardment during different growth stages will be developed and discussed. First, the influence of low energy bombardment will be described. Subsequently it will be shown how this knowledge can be used to specifically improve the structural order of ZnO and ZnO:Al films with minimum additional technical efforts by utilizing seed layers. The investigation of the role of ZnO seed layers will allow for a substantive enhancement of the first growth model. Distinct structural improvements in thin silver films grown on modified ZnO seed layers will be demonstrated. This work will conclude with the fabrication of a-axis textured ZnO films by highly energetic ion bombardment and the development of a comprehensive growth model discussing the influence of ion bombardment, the role of different growth stages and the action of different mechanisms contributing to texture formation.

In the following chapter this work will start with a short discussion of basic properties of zinc oxide and zinc oxide thin films. Different mechanisms promoting the formation of preferred orientation in the films will also be introduced and discussed. Thereafter, the growth of zinc oxide by different techniques is discussed where special emphasis is put on sputtering. The modified sputtering system developed for performing ion beam assisted sputtering will also be introduced. A chapter on the analytical instruments and software utilized in the course of this work will concisely discuss the underlying principles and instrumental variations allowing for the comprehensive discussion of the presented experimental data. The main focus of this work will be on the discussion and evaluation of the experimental data. First, the growth of ZnO under additional xenon ion bombardment in the IBAS process will be comprehensively discussed and concluded in a growth model. Second, applications of structurally modified zinc oxide seed layers to the growth of ZnO:Al and Ag films will be demonstrated and discussed. The utilization of seed layers for the growth of ZnO:Al films will provide additional valuable insight to the growth of zinc oxide films in general. Third, the investigation of ion bombardment is extended to highly energetic oxygen ion bombardment utilized to grow a-axis textured films and to conclude on the growth mechanisms. A final comprehensive growth model will be developed.

Zinc oxide - properties, applications and growth

2.1 Material properties

Zinc oxide is a wide bandgap II-VI semiconductor with a direct gap of 3.37 eV and a refractive index of $n \approx 2$ in the visible spectral range. The mass density of ZnO is 5.61 g/cm³. Zinc oxide is known to crystallize in three different structures: the hexagonal wurtzite, the cubic zincblende and the rarely observed cubic rocksalt structure. However, only the hcp phase is stable under ambient conditions. The wurtzite structure has space group $P6_3mc$ (C_{6v}^4) and point group $6mm$ (C_{6v}) in Hermann-Mauguin (Schönflies) notation. This structure is similar to zincblende, except that the stacking sequence of the ZnO dimers is $ABABAB$ instead of $ABCABC$. The lattice constants are $a = 3.25 \text{ \AA}$ and $c = 5.21 \text{ \AA}$. The cations are in hcp stacking order and the anions are in alternate tetrahedral holes, thereby also forming a hcp stack (figure 2.1). Hence, each Zn^{2+} atom is tetrahedrally coordinated to four O^{2-} atoms by sp^3 -hybridization. However, wurtzite ZnO is at the borderline between covalent and ionic bonding. According to Pauling [2] the fraction of ionic character, f_i , correlates with the difference in electronegativity $\Delta\chi$ for diatomic compounds. This correlation is given by the following expression:

$$f_i = 1 - \left[\exp \left\{ -\frac{(\Delta\chi)^2}{4} \right\} \right]. \quad (2.1.1)$$

Inserting the electronegativity values for zinc and oxygen ($\chi_{\text{Zn}} = 1.65$ and $\chi_{\text{O}} = 3.44$) [3] yields an ionic fraction of approximately 55%. A consequence of the ionic character is that the zinc and oxygen planes bear electrical charge, a fact which is responsible for the strong piezoelectricity of the ZnO wurtzite structure. These polar planes are the (0001) and (000 $\bar{1}$) basal planes, which correspond to Zn- and O-terminated surfaces, respectively. The nonpolar prism faces (e.g. (10 $\bar{1}$ 0) and (11 $\bar{2}$ 0)) do not bear electrical charge since they contain the same number of zinc and oxygen atoms. The electromechanical coupling in ZnO is among the highest values of all semiconductors ($e_{33} = 1.22 \text{ C/m}^2$ for rf-sputtered

CHAPTER 2. ZINC OXIDE - PROPERTIES, APPLICATIONS AND GROWTH

films), where strain-induced polarization along the wurtzite c-axis is given by

$$P_z^{piezo} = e_{33}\varepsilon_z + e_{31}\varepsilon_{\perp} \quad (2.1.2)$$

where e_{33} and e_{31} are the components of the piezoelectric tensor and ε_z and ε_{\perp} are the strain along the c-axis and in the basal plane, respectively [4]. It is these piezoelectric properties that facilitate the application of zinc oxide in piezoelectric sensors and surface acoustic wave devices [5], the latter of which are widely used as GHz frequency filters in the tele-communications industry. Another feature of ZnO is the relatively large exciton binding energy of 60 meV (largest among all typical II-VI and III-V semiconductors). Consequently, ZnO has bound excitons at RT ($300\text{ K} \approx 26\text{ meV}$), which makes the material very suitable for UV laser diodes since it promotes a significant population inversion.

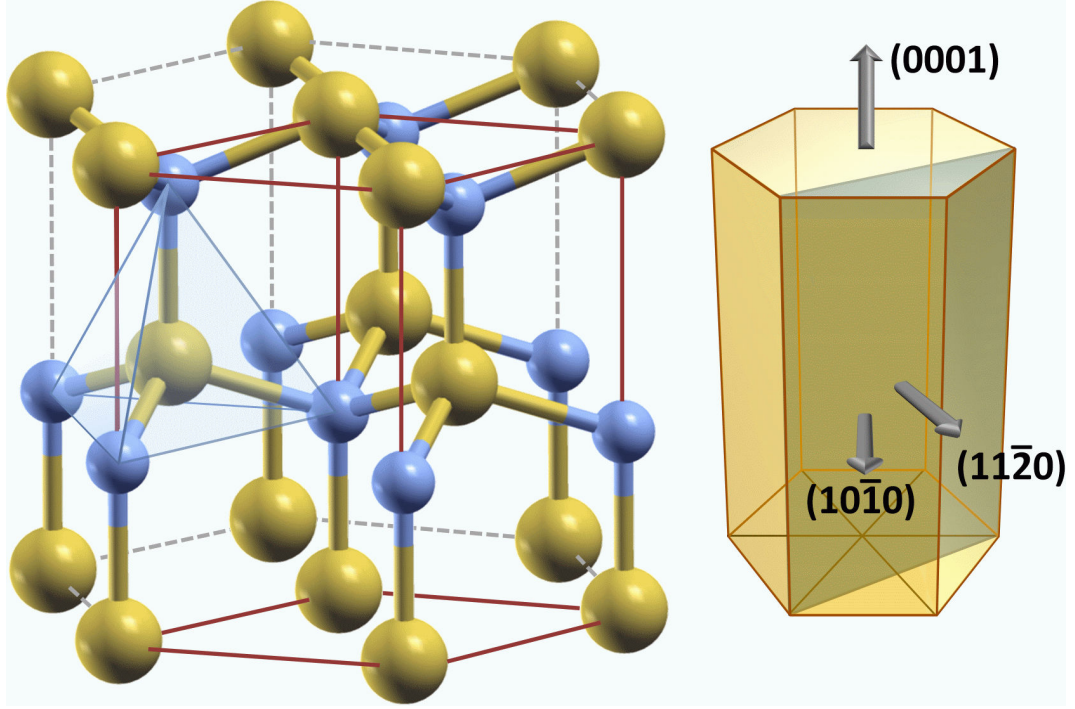


Figure 2.1: The hexagonal wurtzite structure. Red wireframe: unit cell. The zinc and oxygen atoms are tetrahedrally coordinated by sp^3 -hybridization. The schematic sketch of a single crystal demonstrates the orientation of the most important low-index crystal planes: the (0001) basal planes and the (10 $\bar{1}$ 0) and (11 $\bar{2}$ 0) prism planes. The {0001} direction is the c-axis.

Zinc oxide can be doped to become an n-type transparent conductive oxide (TCO). Typically there are two principal ways for extrinsic doping of a binary metal oxide like ZnO, which is cation or anion substitution. In the first case, the Zn^{2+} cations are substituted by group III ions like B^{3+} , Al^{3+} , Ga^{3+} or In^{3+} , the most commonly utilized element of which is Al. In the second case, the O^{2-}

2.1. MATERIAL PROPERTIES

ions are substituted by a halogenide like F^- . In both cases, the excess electron promotes electrical conductivity by excitation of these donors into the conduction band. ZnO:Al TCO films prepared by sputtering can have electrical resistivities as low as $300 \mu\Omega\text{cm}$ at room temperature [6], which is only a factor of 200 larger than the resistivity of bulk copper. ZnO:Al is a promising candidate for replacing $\text{In}_2\text{O}_3\text{:Sb}$ (ITO) as a TCO. ITO thin films exhibit a threefold lower resistivity, $110 \mu\Omega\text{cm}$, but the low abundance of indium combined with an increasing demand by the booming flat panel industry have triggered a significant increase in the costs of the raw material. Due to the abundant deposits of both zinc and aluminium, ZnO:Al has become an attractive low-cost alternative to ITO. An elementary summary of thin film TCO properties has been given by Szyszka [6]. Aluminium-doped zinc oxide films are presently utilized e.g. in the fabrication of silicon-based thin film solar cells, where the ZnO:Al films are applied as a transparent front electrode [5].

There have also been attempts to fabricate p-type doped ZnO films [7]. However, a fundamental difficulty arises from the fact that native defects in zinc oxide act as electron donors and therefore typically compensate for the low hole concentrations achieved in ZnO films so far [8]. This is also why the p-type conductivity of ZnO films reported in literature is often persistent only for several hours to several weeks [5].

For a comprehensive review of ZnO material properties and devices the reader is referred to [5] and the review articles of Özgür [4] and Norton et al. [9]. Some basic properties are also summarized in table 2.1.

2.1.1 Miller index notation in hexagonal systems

To take account of the crystal symmetry, planes in hexagonal systems are often labeled by 4 instead of 3 Miller indices. In this work notations with 3 and 4 Miller indices, respectively, are alternately used. Therefore, a short description of the respective basic vectors and the translation between both notations is given here. Figure 2.2 shows the basic vectors a_1, a_2, a_3 of the hexagonal unit cell. For a 4-index notation, an additional, linearly dependent vector a_i is introduced. It is obvious that the translation from a 3-index notation (HKL) to a 4-index notation (hkil) is as follows:

$$\begin{aligned} h &= H \\ k &= K \\ i &= -(H + K) \\ l &= L \end{aligned}$$

This notation satisfies the hexagonal symmetry of the lattice, as shown in the following example: Whereas in (HKL) notation it is not immediately evident that e.g. the $\{110\}$ and $\{\bar{1}20\}$ planes are crystallographically identical, in the (hkil)

CHAPTER 2. ZINC OXIDE - PROPERTIES, APPLICATIONS AND GROWTH

crystal structure	wurtzite (hcp) space group: $P6_3mc$ (C_{6v}^4) ^a point group: $6mm$ (C_{6v}) ^a
lattice parameters ^b	$a_0 = 3.2475..3.2501$ Å $c_0 = 5.2042..5.2075$ Å $c_0/a_0 = 1.593..1.6035$ ($c_0/a_0 = 1.6033$ for ideal hcp structure) $u = 0.383..0.3856$
mass density	5.61 g/cm ³ (bulk) $5.25 - 5.35$ g/cm ³ (sputtered films)
melting point	ZnO: $T_m = 1975$ °C ^f Zn: $T_m = 420$ °C
heat of formation ^d	$\Delta H_f = -3.61$ eV/atom (273.15 K)
binding	covalent/ionic fraction ^c : 45%/55%
electronegativities ^d	Zn: 1.65, O: 3.44
exciton binding energy	60 meV
piezoelectric tensor components ^e	$e_{33} = +1.22$ C/m ² $e_{31} = -0.51$ C/m ² $e_{15} = -0.45$ C/m ²
stiffness tensor components ^b	$c_{11} = 206$ GPa $c_{12} = 117$ GPa $c_{13} = 118$ GPa $c_{33} = 211$ GPa $c_{44} = 44.3$ GPa $c_{66} = 44.6$ GPa = $(c_{11} - c_{12})/2$
thermal expansion coefficients ^b	$\alpha_a = 2.9 \times 10^{-6}$ /K $\alpha_c = 4.75 \times 10^{-6}$ /K
optical band gap	3.37 eV
refractive index	$n \approx 2$ (at $\lambda = 550$ nm)
static dielectric constant ^f	$\epsilon_0 = 8.656$
intrinsic carrier concentration ^b	typically $10^{16} - 10^{17}$ /cm ³ for thin films
electron/hole effective mass ^f	0.24/0.59
electron Hall mobility ^f	$\mu_H \approx 200$ cm ² /Vs

^a Hermann-Mauguin (Schönflies) notation

^b range of values reported in [4] and references therein

^c according to formula 2.1.1 and electronegativities from [3]

^d from [3]

^e ref. 663 in [4]: investigation of rf-sputtered films on sapphire substrates

^f from [9]

Table 2.1: Basic physical properties of ZnO crystals and ZnO thin films.

2.2. PROPERTIES OF THIN FILMS

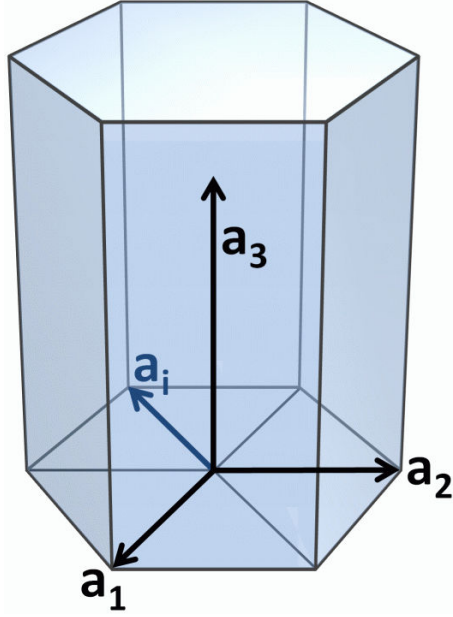


Figure 2.2: Basic vectors of the hexagonal unit cell. For symmetry reasons, planes in a hexagonal system are often labeled by a 4-index notation. The additional, linearly dependent vector in the basal plane is labeled a_i in the figure. See text for the translation from 3 (HKL) to 4 (hkil) Miller indices.

notation this is directly evident since $\{\bar{1}2\bar{1}0\}$ simply follows from $\{11\bar{2}0\}$ by a permutation of the type $\pm P \cdot (hki)$.

The interplanar distance d_{hkl} between adjacent planes is given by

$$\frac{1}{d_{hkl}^2} = \frac{4}{3a^2} (h^2 + k^2 + hk) + \frac{l^2}{c^2} \quad (2.1.3)$$

with a and c the unit cell parameters.

2.2 Properties of thin films

Applications of zinc oxide in various devices typically require the fabrication of thin films. The thickness of such films ranges from only a few nanometers to several microns, depending on the specific application. These films in general exhibit a polycrystalline structure. The orientational distribution of the crystallites as a whole is called the *texture* of a film¹. Further, a distinction is typically made between a so-called *out-of-plane texture* and an *in-plane texture*, which is illustrated in figure 2.3 (a)-(d). For instance, a zinc oxide film that is grown on a substrate where the c-axis of each crystallite aligns perpendicular to the substrate surface exhibits an out-of-plane (0002) texture where the texture axis is the c-axis (b). In a case where also the rotation along the c-axis is identical for all crystallites, which means that e.g. the $\{10\bar{1}0\}$ directions are all identical,

¹A strict definition of texture and an explanation of the corresponding x-ray measurement technique has been given e.g. by Birkholz [10].

CHAPTER 2. ZINC OXIDE - PROPERTIES, APPLICATIONS AND GROWTH

the film is also asserted to exhibit an in-plane texture (d). Note, however, that in-plane texture can also be present without an out-of-plane texture. Typically there is a smooth transition from a powder sample (entirely random orientation) to a perfectly textured sample. Hence, the quality of a texture is expressed by the characteristic widths of corresponding orientation distributions most commonly derived from either electron (TEM) or x-ray (XRD) diffraction patterns.

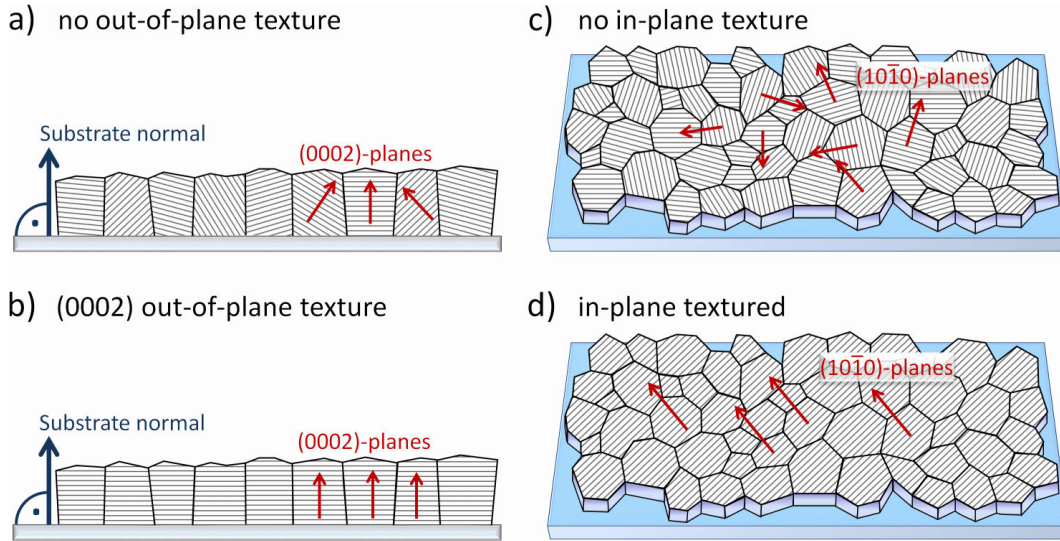


Figure 2.3: Schematic sketch of different types of film texture: **(a)** Random orientation with respect to the substrate plane: no out-of-plane texture. **(b)** Film with perfect (0002)-out-of-plane texture. **(c)** Film with all $\{10\bar{1}0\}$ crystal planes perpendicular to the substrate plane but with random rotation of the crystallites along the substrate normal: no in-plane texture. **(d)** Film with all $\{10\bar{1}0\}$ crystal planes perpendicular to the substrate plane and preferred rotation along the substrate normal: in-plane textured.

It is comprehensible that the physical properties of thin films could significantly differ from those of a single crystal. However, for several thin film applications growth of thin films with structural quality as close to a single crystal as possible is essential. For example, the performance of surface acoustic wave devices is strongly tied to a maximum possible c-axis texture [11–13] since the piezoelectricity of a ZnO crystallite is effective along this direction only. Another example is the electrical performance of n-type conducting doped zinc oxide films. Charge carrier mobility is not only limited by intra-grain scattering at impurities but also by scattering at grain boundaries (see [5] for a comprehensive summary). The electrical resistivity is therefore expected to increase with increasing density of grain boundaries, i.e. with decreasing grain size. Furthermore, it has been demonstrated [10] that even the relative orientation of neighbouring crystallites affects conductivity. In other words, electrical device performance is directly correlated with the texture of the ZnO film. Another important factor is surface

2.2. PROPERTIES OF THIN FILMS

topography. Depending on the application, the surface of zinc oxide films should be either ideally flat or exhibit a well-defined crater-like roughness. Flat surfaces are indispensable for example if ZnO is utilized as a seed layer for epitaxial growth of ultrathin (≈ 10 nm) silver layers for application in low-emissivity architectural glazing. Surfaces with a well-defined rough topography on the other hand are required for increasing the efficiency of thin film solar cells, where a doped zinc oxide film is utilized as a front electrode. A crater-like structure serves to effectively scatter the incoming light and therefore increases the distance covered in the absorber, which in turn increases the absorption probability and therefore the proportion of the incoming light converted into electricity [14–16]. As will be shown in the following sections, the evolution of surface roughness during thin film growth also strongly depends on the orientational order (texture) of the film. It will also be explained that the texture of a film is not simply a fixed number depending only on the growth conditions. Texture is often a function of film thickness, which means that the orientational order of the crystallites changes during growth of a film. However, changes in texture with film thickness do not seem to proceed arbitrarily but are rather influenced by the initial texture which forms in the early stage of film growth and by the conditions governing the subsequent evolution of the film.

At this stage it should be obvious that the crystal structure of zinc oxide thin films strongly influences their application potential. It is therefore one of the topmost goals to understand texture formation and to find ways for controlling the structure, which is the motivation of this work. To set the framework for the understanding and discussion of the results that will be presented in this work, the growth of zinc oxide will be discussed for a variety of different growth processes. The processes discussed cover crystal growth (mainly by the hydrothermal method), chemical routes comprising both chemical vapour processes and growth from liquid solutions and finally physical vapour deposition processes including e.g. pulsed laser ablation and the sputtering method.

A unique property of zinc oxide is the very strong tendency to predominantly grow along the $\{0002\}$ direction and to form a (0002) out-of-plane texture even on amorphous substrates. More interestingly, this property is not restricted to a specific deposition process but instead preferred growth directions are observed for all deposition methods with a few exceptions only². The strong tendency to form a pronounced texture without any influence of an epitaxial substrate is typically referred to as *self texture*. The origin, however, of the formation of the (0002) texture is different for various processes. For crystal growth and chemical thin film deposition processes convincing explanations for texture formation have been given and are widely accepted in literature (see section 2.3). In physical vapour deposition (PVD) processes in contrast manifold possible mechanisms

²Note, however, that in some rare cases films are also observed which exhibit preferred orientations other than (0002). These cases will also be discussed in the following sections.

governing texture formation are often controversially discussed and as a consequence there is no final consensus yet. Therefore the growth of zinc oxide will be subject of detailed discussion in the following sections including a discussion of the mechanisms that govern preferential nucleation and growth. Special emphasis will be put on the sputtering process that this chapter will close with.

2.3 Crystal growth

Zinc oxide single crystals can be grown by different processes, involving growth by a vapour-phase reaction [17], growth from a melt [18] and hydrothermal growth [19]. In the vapour-phase reaction Zn powder is evaporated in a furnace at temperatures around 600 °C. A gas flow ($\text{N}_2 + \text{H}_2$) transports the Zn vapour into an adjacent furnace where a reaction with oxygen takes place and, promoted by a temperature of 1150 °C in this oven, crystals grow at the walls of a porcelain funnel introduced into the oven. Large crystals can grow from condensation of the vapour. In the growth from a melt, ZnO is dissolved e.g. in PbF_2 by annealing in a Pt crucible to temperatures around 1150 °C for several hours. The solution is then slowly cooled (*quenched*) towards the eutectic point, where the solubility of ZnO in PbF_2 strongly decreases such that ZnO separates and can form a crystal plate. Hydrothermal growth is the most commonly used technique to grow large single crystals or powders [19–25]. A schematic sketch of a hydrothermal growth apparatus is given in [22]. The basic principle underlying hydrothermal synthesis can be summarized as follows: A nutrient is supplied in one end of a closed vessel together with an aqueous solution. Typical nutrients and solutions are ZnO with KOH and LiOH [22] or $\text{Zn}(\text{OH})_2$ with mixtures of pure water and KOH [20]. Separated by a baffle, at the other end of the vessel crystalline ZnO seed crystals are suspended. This vessel is placed in a vertical furnace which is capable of establishing and maintaining a small temperature gradient along the vessel. The nutrient end of the vessel is heated to temperatures typically in the range of 200 – 400 °C, whereas the seed crystal end is at a temperature several tens of degrees lower. Upon heating, the pressure in the vessel increases towards several 100 atm which results in dissolution of the nutrient. The saturated solution is transported by thermal convection to the seed crystal end of the vessel. In consequence of the reduced temperature the solution becomes supersaturated, resulting in precipitation of the nutrient and crystal growth at the seed.

The growth of ZnO crystallites in hydrothermal synthesis is often reported to be highly anisotropic in terms of the growth speed of different crystal facets. The preferred growth direction depends on the specific growth conditions, like temperature, supersaturation and basicity of the solution [21]. Some examples of typical shapes of hydrothermally grown zinc oxide crystals are shown in figure 2.4.

Most commonly, the fastest growth is observed along the [0001]-direction,

2.3. CRYSTAL GROWTH

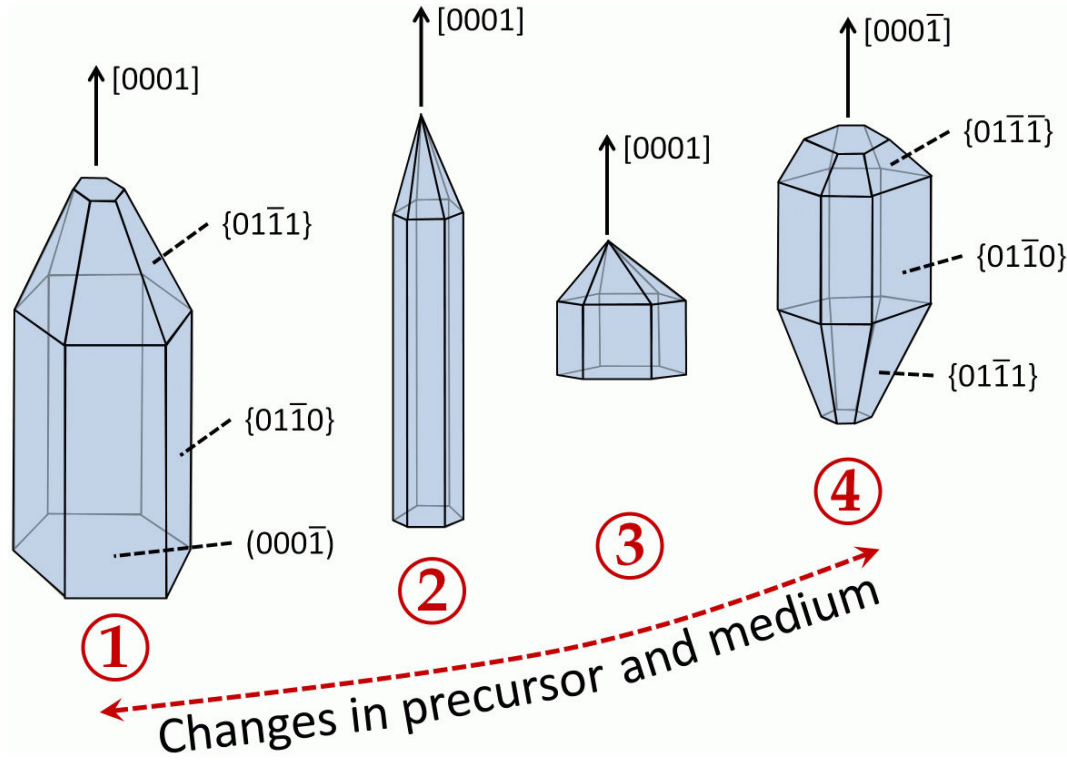


Figure 2.4: Typical crystal shapes of hydrothermally grown ZnO: Depending on the type of precursor, solution chemistry (especially the basicity of the solution) and temperature crystallites with various shapes can be grown (cf [20,21]). See text for discussion.

resulting in an elongated prismatic shape of single crystallites (cf e.g. [19–21]) corresponding to shape 1 or 2 in figure 2.4. Two slightly different growth models which both explain the observed shapes of grown zinc oxide crystals have been proposed by Wang [20] and Li [21], respectively. In the following, the model proposed by Li [21] will be discussed first:

- It is proposed that crystal growth is mediated by the formation of growth units which are suggested to be $\text{Zn}(\text{OH})_4^{2-}$ (cf fig. 2.5). The units are called “coordination polyhedra”. These coordination polyhedra can form clusters which precipitate upon reaching a critical size. In the interior of these clusters the Zn atoms are coordinated by O^{2-} ions while only the surface is terminated by OH^- ligands.
- The crystal structure of ZnO can be interpreted as a stacking order of coordination polyhedra, each polyhedron represented by a tetrahedron consisting of one Zn^{2+} and four O^{2-} (cf figures 2.1 and 2.5). These polyhedra are connected by sharing O^{2-} ions in the interior of the crystal while at the surface the terminal vertices of the polyhedra are occupied by OH^- ligands as exemplarily sketched for the Zn-terminated face in figure 2.5.

CHAPTER 2. ZINC OXIDE - PROPERTIES, APPLICATIONS AND GROWTH

- The coordination polyhedra have *corners* (positions of the OH^-), *edges* (connecting line between two OH^-) and *faces* (plane spanned by three OH^-). For each crystal facet, the surface is formed either by a corner, an edge or a face of these coordination polyhedra. As an example, the terminal vertex of the Zn-terminated facet is a corner, whereas the terminal vertex for the O-terminated facet is a face, which is also seen in figure 2.5. The authors state, that facets comprised of corners have the strongest bonding force³ since each corner can bond with three growth units due to the fourfold coordination [21]. The terminal vertex of a face in contrast can only bond with one growth unit.
- It is proposed that the facets with the strongest bonding force grow fastest. It directly follows that growth along the $[0001]$ -direction is fastest whereas the smallest growth speed is in $[000\bar{1}]$ -direction. By characterizing the remaining crystal facets by determining whether corners, edges or faces of the coordination polyhedra form the surface, it has been concluded that the growth speed v decreases in the order $v_{(0001)} > v_{(01\bar{1}\bar{1})} > v_{(01\bar{1}0)} > v_{(01\bar{1}1)} > v_{(000\bar{1})}$.

Changes in the relative growth speeds of different facets observed for different solutions (cf [20]) are explained by the presence of ions in the solution (e.g. in an alkali solution) that react with the crystal surfaces and thereby cause a *shielding* effect [21] which inhibits the incorporation of growth units or clusters into the crystal facets. The strength of this effect depends on the crystal facet and can therefore change the preferred growth direction. Differences in the basicity of such alkali solutions have been shown to promote the growth of crystals with various shapes such as sketched in figure 2.4, where the change in shape from index 2 to 4 correlates with an increase of the basicity of the solution.

The model proposed by Wang [20] is similar as that the same type of growth units ($\text{Zn}(\text{OH})_4^{2-}$) is proposed to form the crystal, but differs in the mechanism of incorporation of these units into the crystal surface. Wang argues that in media with low basicity only a fraction of the precursor molecules ($\text{Zn}(\text{OH})_2$) is complexed with OH^- . The attachment of growth units to the ZnO crystal is explained by dipole interaction. In an alkali medium, all precursor molecules are assumed to be complexed to $\text{Zn}(\text{OH})_4^{2-}$. Due to the negative charge of these units, it is argued that incorporation into the positively charged Zn-terminated crystal facet (see figure 2.5) is favoured to incorporation into the negatively charged O-terminated facet, which would explain the large difference between the growth speeds along these polar facets. For solutions with high basicity it is proposed that OH^- ions attach to the positive Zn face and inhibit the incorporation of

³The authors did not give a strict proof for this assumption. It is unclear whether this assumption will be consistent with considerations of the surface free energy of the various facets, which will be discussed in section 2.4.

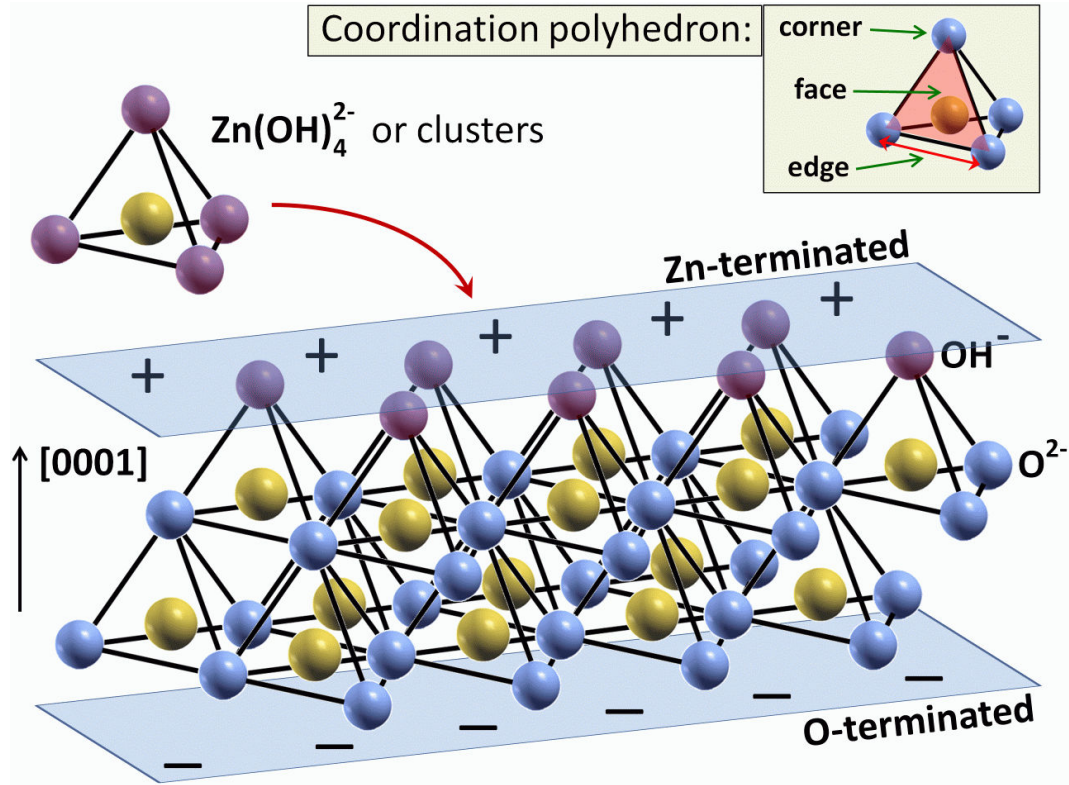


Figure 2.5: Hydrothermal growth of ZnO crystals: Upon dissolution of the precursor (e.g. Zn(OH)_2) in aqueous solution Zn(OH)_4^{2-} growth units form. The crystal can be interpreted as a stacking of these “coordination polyhedra”. The crystal surfaces are terminated by OH^- ligands, which is exemplarily indicated for the Zn-terminated surface in the image. Growth units or more likely precipitated clusters of growth units, the surface of which is also terminated by OH^- , can connect to the crystal by a dehydration process ($\text{OH}^- + \text{OH}^- = \text{H}_2\text{O} + \text{O}^{2-}$). See text for a discussion of growth speed anisotropy and the role of the medium.

growth units. Therefore, growth both along the $[0001]$ - and $[000\bar{1}]$ -direction is then inhibited.

Both elementary growth models explain the large growth speed of ZnO in direction of the +c-axis by taking account of chemical reactions linked with a specific growth process. The result, i.e. the large growth speed along the $[0001]$ -direction for a weakly basic medium is also often cited to explain preferred growth or orientations in thin film nano-structures (e.g. preferred orientation of nanorods with c-axis perpendicular to the substrate plane) grown by different chemical processes (e.g. [26–28]). It should be noted here, however, that these models do not apply to explain anisotropic growth speeds in PVD growth processes.

2.4 Principles of textured thin film growth

As already mentioned, zinc oxide thin films generally show a strong tendency to grow with a preferred orientation even on amorphous substrates. Most often, the crystallite c -axis is oriented perpendicular to the substrate surface but in some rare cases also films are observed where the orientation of the c -axis is parallel to the substrate surface (i.e. the a -axis is parallel to the substrate normal⁴). In the following, these two types of texture will be abbreviated with c_{\perp} and c_{\parallel} , respectively. The physical origin of this explicitly strong self-texturing mechanism in zinc oxide films has not been finally determined yet since there are many possible driving forces. A short summary about this issue has recently been given by Kajikawa [29].

First comprehensive reviews on the growth of vapour-deposited thin films and the preferred orientations during growth far from thermodynamic equilibrium have been given by Bauer [30, 31] in 1956. In these reviews a distinction is made between three stages of film growth: (1) initial stage, (2) transition stage and (3) final stage of growth. During the initial stage, film growth may be strongly governed by the interaction with the substrate, the influence of which becomes negligible in the transition stage and finally vanishes. Correlated with this classification into growth stages are also the definitions of nucleation-conditioned (ger: “*keimbildungsbedingt*”) and grain-growth-conditioned (ger: “*keimwachstumsbedingt*”) growth processes. During the initial stage, film growth is clearly governed by nucleation. On amorphous substrates with weak interaction a preferred orientation of crystallites in that stage is very likely shaped by surface energy considerations, i.e. orientations with a surface of low free energy parallel to the substrate are preferred. Very often these surfaces are parallel to the most densely packed crystal planes. Upon completion of the initial growth stage, grain growth processes dominate the structure formation. Texture evolution then depends on a variety of parameters like e.g. the orientation of the deposition flux, condensation probability, surface diffusion etc.

First attempts to model and calculate preferred orientations in thin film growth have been presented by van der Drift [32] in 1967, where several possible origins of a preferred orientation are discussed. Similar to the considerations of Bauer, two main reasons for preferred orientation are identified:

- (a) Films grow with an initial preferred orientation where nuclei form with the densest planes (i.e. lowest surface free energy) parallel to the surface of an amorphous substrate. The initial orientation distribution does not change upon subsequent film growth.

⁴Strictly, this definition would require that the “ a -axis” is defined as the linear combination of the a_1 and a_2 basic vectors (figure 2.2) that is exactly parallel to the substrate normal. This definition is implied in the use of the term “ a -axis-texture” throughout this work.

2.4. PRINCIPLES OF TEXTURED THIN FILM GROWTH

- (b) Films grow from an initially random orientation of nuclei. The vertical growth speeds of these nuclei depend on their orientation such that consequently grains with low vertical growth speeds become overgrown by those with large vertical growth speeds. This mode of texture formation was coined the “**principle of evolutionary selection**” by the author [32].

It was demonstrated that the principle of evolutionary selection results in films where crystals are oriented with their fastest growth direction perpendicular to the substrate surface.

More recently, Knuyt et al [33–35] suggested a mechanism of texture formation that is very similar to the principle of evolutionary selection. While van der Drift concluded on the direction of fastest growth speed from typical shapes in crystal growth experiments, Knuyt suggested that there is a net preferred surface diffusion towards facets with lower surface free energies. Therefore, the principle of the minimization of the total surface free energy of the film was suggested as the driving force for evolutionary selection. As a simplification of the calculations, it was assumed that the surface free energy is a simple monotonous function of the crystallite tilt with respect to the substrate surface, which makes this *ansatz* quite similar to that of van der Drift who assumed orientation-dependent vertical growth speeds. However, Knuyt’s model allows to investigate the influence of parameters like temperature and attempt frequency, which govern surface diffusion. Very similar to the work of Knuyt is a model proposed by Smith [36], where the driving force for a net surface diffusion towards grains with specific orientations has been replaced by the surface binding energy.

Both, the models from Knuyt and Smith, demonstrate the formation of a preferred orientation from an initially random distribution of crystallite orientations with increasing film thickness, while in addition Knuyt comprehensively discusses e.g. the evolution of the mean surface free energy and the angular orientation distribution as a function of time (i.e. film thickness).

In summary, the following statements can be made which will be of great importance for the discussion and understanding of texture formation in zinc oxide thin films in this work:

- Film growth has to be subclassified into different stages comprising at least an initial stage, mainly describing nucleation and coalescence at the substrate interface, and a final stage describing the evolution of a thick layer on the initial layer. Depending on the growth mode, a transition region between the final and initial stage can also be defined.
- The formation of a preferred orientation (texture) can either be induced by an interaction with the substrate surface, i.e. by **nucleation into a preferred orientation**, during the initial growth stage or be initiated

CHAPTER 2. ZINC OXIDE - PROPERTIES, APPLICATIONS AND GROWTH

by the principle of **evolutionary selection during the transition and final growth stages**. The simultaneous action of both mechanisms is also possible.

These different growth modes and the respective growth stages are displayed schematically in figure 2.6. Figure (a) shows a film which, from randomly oriented nuclei in the initial stage, develops a preferred orientation by evolutionary selection. Nuclei are assumed to grow fastest in the direction of their (0002)-plane normal. Film growth has not yet reached the final stage since there is still competitive growth. Figure (b) displays a film that already nucleates into a preferred nucleation. If this already is an energetically favourable orientation, no structural differences will occur between the initial and the final growth stage.

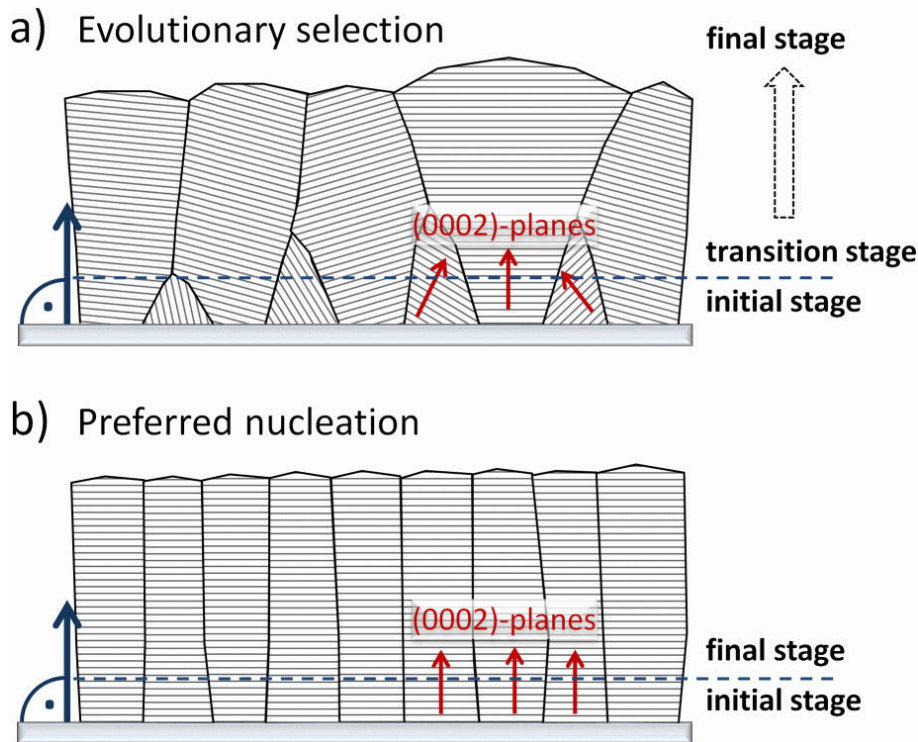


Figure 2.6: Schematic sketch of different film growth modes: (a) **Evolutionary selection:** In the initial stage, nuclei have random orientation. In the transition stage, some grains are overgrown by their neighbours by a principle of evolutionary selection. In the final stage, only a narrow range of crystallite orientations will survive. (b) **Preferred nucleation:** The film exhibits a preferred orientation already in the initial stage (nucleation regime). Assuming that this is an energetically favourable orientation, no competitive growth is induced in the later stages and therefore initial and final stages structurally do not differ.

Interestingly, in the presently available literature evidence for the action of both mechanisms is reported for the growth of zinc oxide films. Both, films with

2.4. PRINCIPLES OF TEXTURED THIN FILM GROWTH

initial preferred orientation and films with initially poor but gradually increasing preferred orientation in the transition growth stage, are reported. Respectively, arguments to explain the observed film structure most often include preferred nucleation or evolutionary selection mechanisms, respectively (see discussion in the following sections). Consequently, it is unclear which of the above-mentioned mechanisms dominates texture formation in zinc oxide films. This also includes a lack of knowledge about the contribution of the different growth stages to texture formation. These facts of course limit highly accurate tailoring of film properties. Mechanisms that could govern evolutionary selection have already been named in this section (anisotropic growth speeds, surface diffusion). Also, in this work it will be shown that initial preferred orientation is the dominant contribution to texture formation in sputtered zinc oxide films. Therefore, in the following two mechanisms promoting preferred nucleation will be discussed in detail. These mechanisms are often argued to govern preferred nucleation as will be discussed in sections 2.5 and 2.6. One of the mechanisms (strain energy minimization) is also sometimes discussed in context with evolutionary selection (e.g. [37]).

2.4.1 Minimization of surface free energy as a driving force for preferred nucleation?

Preferred nucleation will be found to strongly contribute to the formation of texture in zinc oxide thin films. A mechanism which is often put forward to explain the formation of (002)-oriented grains already in the nucleation stage of film growth is the minimization of the surface free energy. During nucleation the total energy of the forming clusters is at a minimum if the boundary surface has the lowest possible surface free energy. This statement always holds if there are no constraints imposed e.g. by an epitaxial substrate or by an external influence like ion bombardment. Consequently, the surface with the lowest free energy typically aligns parallel to the substrate surface. Unfortunately, since zinc oxide is a polar crystal the definition of the surface free energy is not straightforward for the polar $\{0001\}$ - and $\{000\bar{1}\}$ -surfaces. However, calculations of the surface free energy have also been performed where the polar feature has been neglected. Especially calculations performed by Fujimura [38] et al are often cited to explain the self-texture of zinc oxide films. The simple calculations are based on counting dangling bonds in the direction perpendicular to the respective crystal face. This method can be easily explained in an example for the calculation of the surface free energy of the $\{0001\}$ -face. In figure 2.1 it is sketched that the Zn^{2+} is fourfold coordinated to O^{2-} in the polyhedral growth unit. The strength of each bond can be derived from the latent heat of vaporization, which is 3.61 eV/atom for zinc oxide (see table 2.1). Each of the four bonds therefore has a strength of approximately 0.9 eV. Only one of these bonds is in the $[0001]$ -direction. It can also be seen in figure 2.1 that the density of these bonds along the $\{0001\}$ -plane is approx-

CHAPTER 2. ZINC OXIDE - PROPERTIES, APPLICATIONS AND GROWTH

imately 1 bond per 9.14 \AA^2 , which is twice the area of the footprint of the unit cell. Hence, the surface free energy of the $\{0001\}$ -face is $0.9/9.14 \text{ eV/\AA}^2 \approx 0.099 \text{ eV/\AA}^2$ (1.59 J/m^2). Similarly, the free energies of the $\{11\bar{2}0\}$ - and $\{10\bar{1}0\}$ -faces have been calculated to 0.123 eV/\AA^2 (1.97 J/m^2) and 0.209 eV/\AA^2 (3.35 J/m^2), respectively in [38]. It has therefore been concluded that growth along the $[0001]$ -direction is promoted by the minimization of surface free energy.

Claeysens et al [39] considered the polar character of the $\{0001\}$ - and $\{000\bar{1}\}$ -faces in their calculations of the cleavage energies along different planes. The cleavage energy is the energy needed to cleave a crystal along a specific direction. For the non-polar surfaces the surface free energy is simply half of the cleavage energy. For the polar faces, the surface free energy of the $\{0001\}$ - and the $\{000\bar{1}\}$ -faces differ and therefore cannot be derived from the cleavage energy. Upon calculating the cleavage energies for the $\{10\bar{1}0\}$ -, $\{11\bar{2}0\}$ - and $\{0001\}/\{000\bar{1}\}$ -faces as a function of film thickness Claeysens et al found that the growth of (0001)-oriented grains is energetically unfavourable, which is in contrast to the simple calculations performed by Fujimura [38]. However, it has also been found that zinc oxide might grow in an energetically favoured graphitic structure in the initial growth stage. This structure is very similar to (0001)-oriented wurtzite. Upon increasing film thickness, the cleavage energy of the graphitic structure first intersects with the cleavage energies of the $\{10\bar{1}0\}$ - and $\{11\bar{2}0\}$ -faces, which become energetically favourable above a film thickness of approximately 10 monolayers. A change towards growth with one of these preferred orientations however is inhibited by the additional energy that would be needed for the according structural rearrangement. At a thickness of approximately 18 monolayers the $\{0001\}/\{000\bar{1}\}$ -orientations become more favourable than the graphitic structure. Due to the small structural differences the energy barrier is small for a structural conversion towards growth in the wurtzite structure with one of these orientations. The film thickness at which a zinc oxide film would turn from a graphitic into the typical (002)-oriented wurtzite structure is approximately 4.7 nm [39].

Interestingly, even though the work of Claeysens demonstrates that the $\{0001\}$ - and $\{000\bar{1}\}$ -faces probably do not exhibit the lowest surface free energy, the conclusion that zinc oxide forms a (002)-texture due to a principle of energy minimization is still valid. It seems therefore reasonable to assume that energy minimization may govern preferred nucleation consistent with the typically observed (002)-self-texture.

In a thermodynamic approach the correlation between the surface free energy of zinc oxide and a preferred orientation of nuclei at the substrate interface can be explained as follows:

As already stated in [40], the formation of crystalline nuclei on a substrate (figure 2.7) is accompanied by a free energy change ΔG given by

$$\Delta G = a_3 r^3 \Delta G_V + a_1 r^2 \gamma_n + a_2 r^2 (\gamma_{ns} - \gamma_n) \quad (2.4.4)$$

2.4. PRINCIPLES OF TEXTURED THIN FILM GROWTH

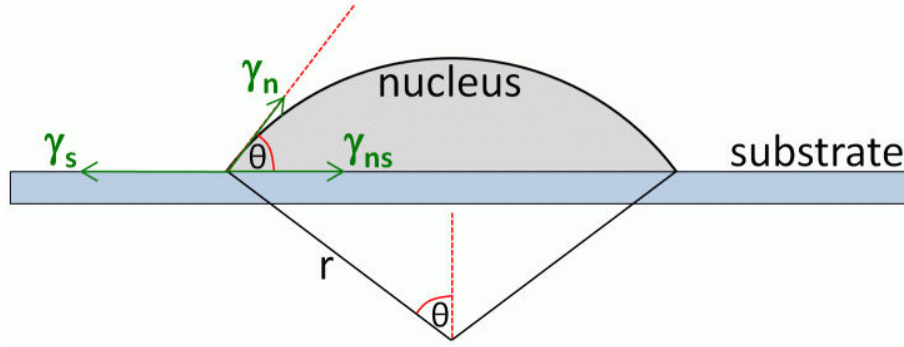


Figure 2.7: Formation of a spherical nucleus with radius r on an amorphous substrate. The correlation between the contact angle and the interfacial energies γ from which Young's equation can be deduced is shown.

where γ_n , γ_s and γ_{ns} are the interfacial energies of the nucleus, the substrate and the interface between the nucleus and the substrate, respectively. The energy ΔG_V is correlated with the volumetric change. To form a nucleus, a critical size has to be overcome which is determined by

$$\frac{\partial \Delta G}{\partial r} \Big|_{r=r_c} \stackrel{!}{=} 0 \quad \Rightarrow \quad r_c = \frac{-2(a_1\gamma_n - a_2(\gamma_s - \gamma_{ns}))}{3a_3\Delta G_V}. \quad (2.4.5)$$

The energy barrier that has to be overcome is then given by the value $\Delta G_c = \Delta G(r_c)$. From geometrical considerations it is directly evident that

$$a_1 = 2\pi(1 - \cos \theta) \quad (2.4.6)$$

$$a_2 = \pi \sin^2 \theta \quad (2.4.7)$$

$$a_3 = \frac{\pi}{3} (2(1 - \cos \theta) - \sin^2 \theta \cos \theta) \quad (2.4.8)$$

Furthermore, Young's equation states that

$$\cos \theta = \frac{\gamma_s - \gamma_{ns}}{\gamma_n}. \quad (2.4.9)$$

From equations 2.4.5 to 2.4.9 it directly follows that

$$\Delta G_c = \frac{16\pi(\gamma_n)^3}{3(\Delta G_V)^2} \cdot f(\theta) \quad (2.4.10)$$

$$f(\theta) = \frac{1}{4}(2 + \cos \theta)(1 - \cos \theta)^2 \quad (2.4.11)$$

The function $f(\theta)$ is monotonically increasing for $0^\circ \leq \theta \leq 180^\circ$. For $\theta = 0^\circ$ growth is homoepitaxial and hence the energy barrier is zero. For $\theta = 180^\circ$ a

CHAPTER 2. ZINC OXIDE - PROPERTIES, APPLICATIONS AND GROWTH

spherical nucleus forms without a substrate. In [41] it is argued that approximately $\gamma_{ns} = \alpha\gamma_n$ with $0 < \alpha < 1$. Then from equation 2.4.9 it follows that

$$\cos \theta = \left(\frac{\gamma_s}{\gamma_n} \right) - \alpha. \quad (2.4.12)$$

For $\alpha = \text{const.}$ and $\gamma_s = \text{const.}$ it follows from equations 2.4.10 to 2.4.12 that the energy barrier is smallest and therefore nucleation is preferred when the crystal face with the lowest surface free energy γ_n is oriented parallel to the substrate surface. In [41] it is also argued that amorphous ZnO has a higher interfacial energy than crystalline ZnO at the substrate surface. Therefore, even during later crystallization of amorphous films nucleation is proposed to take place preferentially at the substrate interface since this would be correlated with a decrease of the overall interfacial energy and therefore with a decrease of the energy barrier for forming stable nuclei.

2.4.2 Minimization of strain energy as a driving force for preferred nucleation?

In some reports it is argued that aside surface energy minimization also the minimization of internal stresses might play a role in the preferred orientation in zinc oxide films. To investigate that influence, a respective strain energy term has to be added to the Gibb's free energy. McKenzie et al [42] have shown that in a hexagonal polycrystalline material

$$G = G_0 + \sigma^2 \cdot f(\sigma_3) \quad (2.4.13)$$

$$f(\sigma_3) = -\frac{1}{2} [2(s_{11} + s_{12} - s_{33} - s_{13})\sigma_3 \quad (2.4.14)$$

$$+ (1 - \sigma_3)^2 s_{11} + \sigma_3^2 s_{33} + \sigma_3 (1 - \sigma_3) (2s_{13} + s_{44})] \quad (2.4.15)$$

where s_{ij} are elements of the compliance tensor and σ_3 correlates with the orientation of the crystallites in an external biaxial stress field. For $\sigma_3 = 1$ the crystal c-axis is oriented parallel to the normal of the stress field. Defining θ as the angle between the normal of the external biaxial stress field and the crystallographic c-axis, σ_3 varies as $\cos^2 \theta$. G_0 represents the sum of all other contributions to the Gibb's free energy. The parameter σ is the modulus of the biaxial film stress, which is typically of the order of up to several GPa for sputtered zinc oxide films [43]. The independent elements of the symmetric compliance tensor s_{ij} have been calculated from the stiffness tensor elements c_{ij} taken from [4] (see also table 2.1) according to $S \cdot C = I$ where I is the identity matrix. The values s_{ij} are listed in table 2.2.

2.4. PRINCIPLES OF TEXTURED THIN FILM GROWTH

Compliance	ZnO value $(GPa)^{-1}$
s_{11}	7.83×10^{-3}
s_{12}	-3.41×10^{-3}
s_{13}	-2.20×10^{-3}
s_{33}	6.93×10^{-3}
s_{44}	23.80×10^{-3}
s_{66}	22.70×10^{-3}

Table 2.2: Values of the components of the elastic compliance tensor for ZnO.

The angular dependence of $f(\sigma_3)$ has been calculated and is shown in figure 2.8. It has been assumed that the biaxial stress field acts in the direction of the substrate plane. Therefore $\theta = 0^\circ$ corresponds to a crystallite orientation with the c-axis parallel to the normal of the stress field and hence perpendicular to the substrate surface. It is evident that this is not the orientation with the lowest strain energy. From the figure it is obvious that orientations with the c-axis parallel to the substrate surface are energetically more favoured while the minimum in strain energy corresponds to an inclination of the c-axis by about 55° with respect to the substrate normal. This would approximately correspond to a (112)- or (101)-texture (cf fig. 4.3 in section 4.1.2). In consequence, minimization of strain energy during growth does not promote (002) preferred orientation.

However, it is argued e.g. in [44] that strain energy minimization might be responsible for changes in preferred texture as a function of film thickness, a feature which is sometimes observed for the growth of zinc oxide films. This is because the total strain energy of a film depends on film thickness. The unit of the strain energy term in the Gibb's free energy is $[J/m^3]$ (energy per unit volume). Upon multiplication with the film thickness this converts into a strain energy per unit area the normal of which is parallel to the normal of the biaxial film stress field. Assuming a large film stress of 4 GPa and a (002)-textured film the strain energy term in equation 2.4.13 is approximately $50.4 \times 10^6 J/m^3$ ($\theta = 0^\circ$ and the compliance tensor elements from table 2.2 were used for the calculation). In consequence, already for very thin films the strain energy term becomes larger than typical surface free energies. E.g. for a film thickness of 40 nm the strain energy per unit area becomes approximately $2 J/m^2$, which is comparable to the values of the surface free energies of the various crystal faces of zinc oxide (cf section 2.4.1). However, concerning an influence on growth orientation, not the total strain energy but the difference in strain energy for different orientations has to be considered as suggested in [44]. Regarding only the orientations where the c-axis is oriented perpendicular and parallel to the substrate surface, respectively, this yields a strain energy difference per unit volume of approximately $12 \times 10^6 J/m^3$. Consequently, strain energy minimization might affect preferred

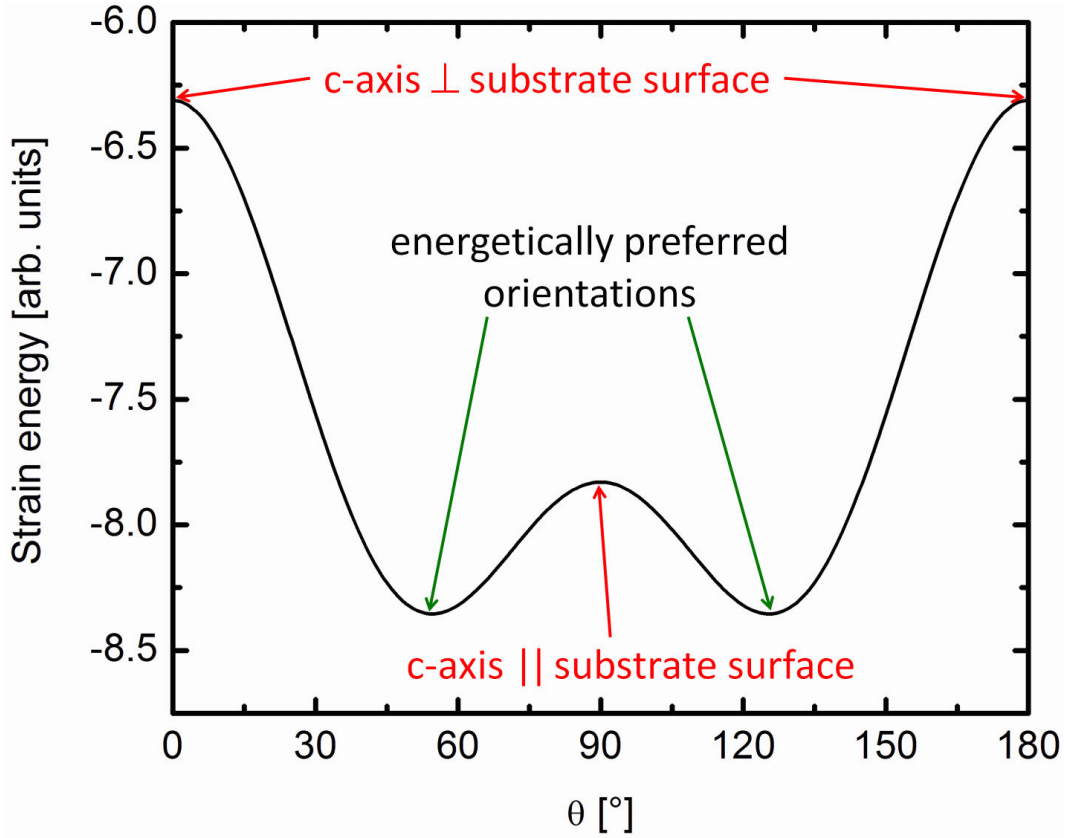


Figure 2.8: Strain energy of ZnO as a function of crystallite orientation in an external biaxial stress field. For $\theta = 0^\circ$ the c-axis is parallel to the normal of the stress field, i.e. strain is perpendicular to the direction of the c-axis. Assuming that biaxial stress acts in the substrate plane it is evident that (a) strain energy is smaller for an orientation of the c-axis along the stress field, i.e. parallel to the substrate surface, than for crystallites growing with the c-axis perpendicular to the substrate surface. (b) The minimum strain energy occurs for an inclination of approximately 60° of the crystallographic c-axis with respect to the substrate normal.

orientation above a critical film thickness t_{crit} larger than approximately 170 nm. Furthermore, the critical film thickness is inversely proportional to the square of the modulus of the biaxial stress as can be deduced from equation 2.4.13 and the discussion above:

$$t_{crit} \propto \frac{1}{\sigma^2}. \quad (2.4.16)$$

Hence, if the modulus of the film stress is only 2 GPa instead of 4 GPa this results in $t_{crit} = 680$ nm. It therefore strongly depends on deposition conditions (that govern growth stress) and film thickness whether a change in preferred orientation might be observed. Even though this theory seems to explain possible changes in preferred orientation during film growth and is therefore discussed in

2.4. PRINCIPLES OF TEXTURED THIN FILM GROWTH

this context in the literature (e.g. [44]), some critical comments have to be made:

1. It is questionable whether the strain energy integrated over film thickness is the correct number to discuss textural changes due to evolutionary selection. This is because the strain energy per unit area is distributed over the entire depth of the film and therefore still is a volumetric quantity. It should therefore not be mistaken or compared with a surface energy. Also, the strain energy per unit area diverges with increasing film thickness, while film strain certainly does not. Since it is the film strain at the surface which affects the growth of new layers, contrary to the statement made in [44] the growth habit of newly forming layers is proposed to be affected rather by the strain energy per unit area of the top layer or at most of a small fraction of the film near the surface only. Therefore, it seems to be reasonable to consider the strain energy per unit area for a monolayer for comparison with typical surface free energies. Since the thickness of one monolayer along the c-axis of zinc oxide is approximately 2.6 Å, this would correspond to a strain energy per unit area of only 13 mJ/m² for a (002)-oriented film for a constant film stress of 4 GPa as used in the example above. Analogously, the difference in strain energies for the two perpendicular orientations of the c-axis would be only 3 mJ/m², which is by far less than a typical surface free energy.
2. Film stress is not a constant value. As shown in [43] the film stress is a non-linear function of film thickness. An instantaneous stress can be attributed to each layer of the film as will be discussed in the section 4.4. For calculating the strain energy per unit area of a monolayer the instantaneous stress attributed to the formation of this layer should therefore be inserted into equation 2.4.13 instead of the average film stress.
3. The biaxial stress field discussed is mediated by the growth of new layers onto a strained film. That means that arriving particles must chemisorb at the film surface first, before strain can be induced by the deformation of the film underneath. This implies that very likely upon homoepitaxial growth a new monolayer is already chemically bonded to the film before the stress field may act on the structure. It is therefore expected that changes in growth orientation due to internal stresses are to a large extent inhibited by the energy barrier that has to be overcome for the structural rearrangement. This means that epitaxial growth is expected to inhibit changes of the preferred orientation.

In the following sections reports on the growth of zinc oxide films in various deposition processes are summarized. Special emphasis is put on the mechanisms governing structure formation that are proposed in these reports.

2.5 Thin film growth by chemical processes

Since there are many routes to chemically fabricate zinc oxide thin films and nanostructures, the discussion of corresponding techniques and film properties should be separated. In the following a differentiation will therefore be made between *wet solution* processes and *vapour deposition* processes. Growth of zinc oxide from wet solutions is typically performed either by *Spin-* or *Dip-Coating* of a substrate, followed by subsequent annealing steps to evaporate organic compounds to form a pure ZnO film, or by immersing a substrate in solution for direct formation of a ZnO film e.g. by precipitation of ZnO near the substrate surface in a chemical reaction. The first technique is often referred to as a *Sol-Gel* process while the latter technique is called *Chemical Bath Deposition* (CBD). Growth from vapours is typically referred to as *Chemical Vapour Deposition* (CVD), the basic principle of which is a reaction between gaseous precursors near or at the substrate surface to form zinc oxide. A special form of CVD is *Atomic Layer Deposition* (ALD) where the precursors containing zinc and oxygen, respectively, are alternately introduced into the reaction chamber by a gas pulsing sequence. To name only the most common variations of CVD involved in the deposition of ZnO films, often applied methods are *MO-CVD*, *LP-CVD* and *PE-CVD* which refer to the utilization of a **Metal-Organic** precursor, a **Low-Pressure** environment and a **Plasma-Enhanced** reaction between the different precursor gases, respectively. Very often combinations of these methods are utilized for ZnO deposition. In the following, film growth for the various chemical processes will be discussed.

2.5.1 Growth from chemical solution

As already mentioned, in the context of growth from chemical solutions a further distinction can be made between sol-gel coating (e.g. [41, 45–47]) and coating by CBD (e.g. [28, 48–51]). The principle procedure of a sol-gel spin coating process is depicted in detail e.g. in [47]. For a basic explanation of the CBD process see [48] or [51] for instance.

It is often reported that sol-gel-derived ZnO films exhibit c-axis texture [41, 45, 47] or that *texture can be controlled by the nature of the sol* [46]. Bao and coworkers [45] have observed that the texture of ZnO films (≈ 300 nm) depends on the annealing temperature, which typically ranges from 400 °C to 600 °C for sol-gel processes. *At the lower temperature a rather random orientation was evident from (10 $\bar{1}$ 0), (10 $\bar{1}$ 1) and (11 $\bar{2}$ 0) peaks appearing in a Bragg-Brentano XRD scan, whereas with increasing the temperature up to 550 °C a pure (0002) texture was observed.* At 600 °C other peaks appeared again in the diffraction pattern, which means that the c-axis texture deteriorates at high temperatures. No interpretation has been given by the authors on the origin of texture formation, however. Fujihara and coworkers [41] prepared 200 nm thick un-doped and Li-doped ZnO films. Their films exhibited comparatively weak crystallinity as shown by XRD

Chemistry seems to play a role in texture formation

Texture formation thermally activated

2.5. THIN FILM GROWTH BY CHEMICAL PROCESSES

patterns. Nonetheless, Li-doped films exhibited pure (0002) texture that increased with increasing the temperature ($T_{\max} = 500^\circ\text{C}$) while un-doped films showed some other peaks beside the dominant (0002) peak. A thermodynamic approach has been made to explain texture formation during the post-deposition annealing process. Crystallization has been treated in terms of nucleation driven by minimization of Gibb's free energy and interfacial energy considerations (cf section 2.4.1). From these, Fujihara and coworkers have argued that nucleation starting at the substrate interface is energetically more favourable than in the interior of the film and the formation of a (0002)-texture has been explained by the fact that the (0001) surface has the lowest surface free energy [38]. Aslan and coworkers [47] have fabricated films with considerably larger thicknesses of $1 - 1.5\ \mu\text{m}$ and crystallization was achieved by annealing at different temperatures varying between 450°C and 550°C . Strongest c-axis orientation was also observed for the high temperature. It has been proposed that minimization of surface free energy and of internal stresses might be responsible for the formation of the (0002) texture. However, in sections 2.4.1 and 2.4.2 it has been shown that only the minimization of surface free energy could promote (0002)-texture.

Different precursor chemistry affects texture

Texture governed by preferred nucleation

Texture governed by preferred nucleation; thermally promoted

A very different viewpoint on texture formation in sol-gel-derived ZnO films is given by Znaidi and coworkers [46] who have grown films from differently aged sols. During aging of the utilized sol, the formation of Zn-oxo-acetate colloids in the solution is possible. It has been found that for concentrated colloidal sols films with (0002)-texture form upon post-deposition annealing, whereas from diluted colloidal sols a pure (10 $\bar{1}$ 0) texture was formed. It has been suggested that the effective coverage of the substrate surface during growth is the dominant factor in determining the structure. In diluted sols, a particle-substrate interaction is dominant whereas in the concentrated sol a particle-particle interaction is governing structure formation. The authors have argued that the contact between particles is a critical parameter in texture formation. Further, the authors have proposed that a particle-particle interaction might also govern texture formation in PVD processes like sputtering. This statement however should be regarded with great caution since this statement was based on investigating growth from a colloidal precursor.

Preferred nucleation texture governs

In CBD processes, structure formation to some extent is similar to crystal growth processes. This similarity arises from the fact that structure formation is solely governed by chemical reactions and interactions of growth complexes with the emerging film structure. Furthermore, *films* deposited by CBD rather consist of dense nano-structures (e.g. a dense array of columnar nanorods [28]) instead of a homogeneous closed film. Consequently, principal structure forming mechanisms proposed are sometimes similar to those discussed in crystal growth. Control of the shape of the crystals formed in CBD processes is often achieved by mixing additional precursors to the bath to yield competition between different growth complexes at the various crystal facets [48]. A summary of the growth features observed in the references discussed in this section is given in table 2.3.

Chemistry controls texture

CHAPTER 2. ZINC OXIDE - PROPERTIES, APPLICATIONS AND GROWTH

Reference	Structure	Controlling parameter
[46]	variable	sol
[45]	variable	temperature
[41]	strong and weak c_{\perp}	sol & preferred nucleation (SE)
[47]	c_{\perp}	preferred nucleation (SE), temperature & internal stresses
[46]	c_{\perp} & c_{\parallel}	colloid concentration in the sol governs preferred nucleation
[48]	CBD: various crystal shapes	precursor: competition of growth complexes

Table 2.3: Summary of the crystal structures observed in the different references for growth from chemical solutions. The right column gives information about the main mechanism controlling the structure found/proposed in the reference. It is apparent that, aside chemical means like the composition of the sol, temperature and preferred nucleation govern structure formation. If preferred nucleation is attributed to the minimization of surface energy, this is indicated by (SE).

2.5.2 Growth from chemical vapour

In chemical vapour deposition of zinc oxide thin films, most commonly zinc and oxygen is introduced into the system by different precursors. Starting with the most frequently used precursors, zinc is introduced in form of either diethylzinc ($\text{Zn}(\text{C}_2\text{H}_5)_2$, DEZn) [13, 52–54], dimethylzinc ($\text{Zn}(\text{CH}_3)_2$, DMZn) [55, 56] or very rarely zinc acetate dihydrate ($\text{Zn}(\text{O}_2\text{CCH}_3)_2(\text{H}_2\text{O})_2$) [57]. The liquid DEZn or DMZn precursors are typically introduced into the deposition chamber by a carrier gas (Ar , H_2 or N_2) which saturates with the precursor in a *bubbler*. As an oxygen source, most often water vapour (H_2O) is utilized, followed by oxygen (O_2), carbon dioxide (CO_2) and very rarely tertiary butanol (tBuOH) as possible alternatives. Especially DEZn is very reactive with oxygen at room temperature. Typical difficulties of such CVD processes therefore arise from premature chemical reactions that result in the precipitation of large clusters which degrade film quality. This effect is minimized by specifically adapted gas inlet geometries that translocate mixing of the precursors as close to the substrate as possible.

N-type transparent conducting ZnO films can also be fabricated by CVD. Aluminium- and Boron-doped ZnO films have been prepared from DEZn and water upon addition of trimethylaluminium ($\text{Al}(\text{CH}_3)_3$, TMA) [58, 59] or diborane (B_2H_6) [60–63], respectively. Typical reactors for MO-CVD and PE-MO-CVD are sketched and explained in [53] and [52], respectively.

There are also processes utilizing only a single precursor containing both zinc and oxygen. A large variety of different possible precursors is typically utilized

2.5. THIN FILM GROWTH BY CHEMICAL PROCESSES

in such processes [64–68] which are referred to as single-source CVD (SS-CVD).

Research on CVD grown ZnO films is motivated by optimizing structural properties for specific applications like the fabrication of SAW devices or UV-light emitting laser diodes for instance. The functionality of these devices requires preparation of dense ZnO films with epitaxial quality. A perfect texture with the c-axis perpendicular (c_{\perp} -texture) to a Si or GaAs substrate is required e.g. for the integration in SAW devices [13]. In contrast, for UV-LEDs it was found that a texture with the c-axis parallel (c_{\parallel} -texture) to the substrate surface would probably be advantageous [68]. Consequently, many works report on the texture formation of CVD grown ZnO films and its dependence on deposition parameters.

Increasing attention has also been devoted to the investigation of doped ZnO films for application as TCO front electrodes in silicon-based thin film solar cells. Advantages with respect e.g. to sputter-deposited films arise from the possibility to grow films with large surface roughness without a post-deposition surface treatment. Rough surfaces promote efficient light-trapping and therefore increase cell efficiency. The formation of a rough surface has been found to be an inherent feature in films grown with the c-axis parallel to the substrate [62]. To induce crystallization in the growing ZnO films, additional energy is most commonly delivered by substrate heating. Typical substrate temperatures are approximately in the range of 300 – 500 °C but crystalline films have also been reported for lower temperatures [53]. Another method to decrease substrate temperature is the utilization of a PE-CVD process [52] where additional energy is delivered by energetic particles from the plasma.

Most of the works on structure formation by CVD report the observation of mixed textures in the sense that either the quality (i.e. weakly crystalline or any kind of texture) or the nature of the texture (i.e. c_{\perp} , c_{\parallel} or mixed) can be adjusted by the growth parameters. Most often a change of texture is observed as a function of substrate temperature during growth [52, 53, 56, 60, 63]. However, clear correlations have also been found with the film thickness [63] or the relative amount of zinc and oxygen precursors [55]. In the latter case it was found that the structure of films grown at a substrate temperature of 360 °C can be controlled by the amount of the oxygen precursor. With a low supply of oxygen, the films become weakly crystalline and exhibit almost random orientation and a very rough surface whereas films grown with large oxygen supply show clear c_{\perp} -texture and a smooth surface [55]. This is in line with an investigation of Koch and coworkers [65] who found that **the supply of the oxygen precursor strongly affects *self-texturing* in the initial growth stage**. Self-texturing was observed already for films with a thickness of only 50 Å at large oxygen supply, whereas a low supply did not result in a similar texturing. The effect of temperature at high growth rate and low oxygen precursor flows was investigated by Chen and

Oxygen supply affects preferred nucleation

CHAPTER 2. ZINC OXIDE - PROPERTIES, APPLICATIONS AND GROWTH

probably preferred nucleation by heating

Initial growth stage governs texture

Thermally activated surface diffusion promotes c_{\perp} -texture

Nucleation further away from thermodynamic equilibrium

Initial stage governs whole film in terms of c_{\perp} - or non- c_{\perp} -texture

A mechanism for evolutionary selection is proposed

coworkers [56]. It has been concluded that growth along the c-axis is suppressed at low temperatures (300 °C) leading to a weak mixed texture whereas at slightly higher temperatures (350 °C) the c-axis becomes aligned as c_{\perp} to some extent. High temperatures (400 °C) are assumed to cause coalescence of neighbouring grains, thereby limiting the formation of a perfect c_{\perp} -texture again. A two-step process where the temperature was increased from 350 °C to 400 °C during deposition yielded a c_{\perp} -texture with improved quality [56]. Kim and coworkers [53] as well as Li and coworkers [52] have proposed that the observed changes from random orientation to a c_{\perp} -texture with increasing substrate temperature may be attributed to an enhanced surface diffusion length that enables growth along the direction of lowest surface free energy. A very interesting correlation between texture and substrate temperature has been reported by Chen and coworkers [60], who found that films grow with dominant (0002)-texture at low temperatures (393 – 418 K) that changes to a rather random and finally to a prominent (10 $\bar{1}$ 1) texture with further increase of the temperature to 443 K. It has been proposed that this may be attributed to an activation of growth along surfaces with higher surface free energies promoted by the increased temperature. This means that surfaces other than {0002} could be oriented parallel to the substrate surface. This result and its interpretation however should be regarded with some caution since the deposition rate has been found to increase by a factor of approximately 2.5 upon increasing the temperature due to an increased reaction rate of the precursors in the vicinity of the heated substrate. Since deposition time has also not been corrected for the change in deposition rate, both the increase in the rate and the differences in film thickness could be responsible for the structural changes that have been observed. This assumption proves to be reasonable since Nicolay and coworkers [63] have reported a distinct correlation of the texture with both the substrate temperature and the film thickness. It has been demonstrated that at low (110 °C) and high (380 °C) temperatures films have c_{\perp} -texture for all thicknesses ranging from 40 nm to 3.5 μ m, whereas for intermediate temperatures other textures are observed that also change with film thickness. At (150 °C) films have very weak c_{\perp} -texture if they are thin and (11 $\bar{2}$ 0) c_{\parallel} -texture at larger thicknesses. At 220 °C different c_{\parallel} -textures form depending on the oxygen precursor flow. These findings have been summarized in a growth model [63]. This model is mainly based on the assumption that in the initial growth stage grains with both c_{\perp} and c_{\parallel} orientations form at the substrate interface. The role of temperature upon further growth is explained by considerations of surface diffusivity as a function of temperature and the corresponding preferred sites at which ad-atoms finally stick. Apparently there is some principal similarity with the theoretical models proposed by Knuyt [33–35] and Smith [36], as discussed in section 2.4.

Particularly noteworthy are also reports on the formation of c_{\perp} -texture by Deng and coworkers [67] and by Kobayashi and coworkers [57]. In [67] the growth of ZnO films is reported for various tilt angles of the non-epitaxial substrate with

2.5. THIN FILM GROWTH BY CHEMICAL PROCESSES

respect to the deposition source, which resulted in different oblique angles of incidence of the particle flux. The growth of tilted columns was observed to obey the tangential rule, which states that $\tan \alpha = 2 \tan \beta$ where α and β are the tilt angles of the incoming particle flux and the columnar growth direction with respect to the substrate normal, respectively. Quite interestingly, it has also been found that even in the tilted columnar growth the orientation of the {0002} planes is always parallel to the substrate surface. This result is interpreted by the growth with the facets of lowest surface free energy (i.e. (0002)) parallel to the substrate. An even stronger evidence for the tendency of the ZnO films to grow with c_{\perp} orientation has been observed in [57] where ZnO films have been grown on sapphire (1 $\bar{1}$ 02) substrates. The epitaxial relationship between ZnO and the substrate is such that the (11 $\bar{2}$ 0) planes of ZnO grow parallel to the substrate surface (c_{\parallel} -texture). However, it has been observed that at high growth rates this epitaxial relationship is disturbed and films grow with c_{\perp} -texture instead. However, no explanation for the formation of this c_{\perp} self texture is given.

Evidence for preferred nucleation

An innovative approach where the growth of a ZnO film is divided into a buffer layer growth and the subsequent stage of film *thickening* under different growth conditions, respectively, has been shown by Muthukumar and coworkers [13]. This approach has allowed for the preparation of tailored films with reduced surface roughness by adjusting growth parameters for optimum conditions for these separate growth stages. The result shows the possibilities that can arise from carefully tailoring the conditions governing the early growth stage.

Initial stage dictates structural evolution

The deposition of ZnO films by CVD with extremely distinct c_{\parallel} -textures has been reported by Dai and coworkers [68] and Fay and coworkers [62]. In the latter case, films have been Boron-doped for application in thin film solar cells. In both cases there is evidence that the c_{\parallel} -texture is present even at comparatively low film thicknesses. In [62] the substrate temperature is 155 °C while in [68] the temperature varies in the range of 300 – 450 °C. No statements are given on the origin of the pronounced c_{\parallel} -texture by the authors.

Thin films already c_{\parallel} -textured; no evolutionary selection

Films grown via Atomic Layer Deposition (ALD) should also be mentioned here since ALD is simply a specific CVD process. In ALD the zinc and oxygen precursor flows are alternately pulsed. Depending on the specific process there typically exists a parameter window (*self-limiting* regime) within which exactly a single atomic layer is grown in each growth cycle. The precursor types are often identical to that of standard CVD, i.e. DEZn and H₂O for instance. The deposition chamber is typically purged with an inert purge gas between each precursor pulse to avoid reactions of the precursors in the chamber volume. Guziewicz and coworkers [69] have found that at substrate temperatures above 140 °C the texture strongly depends on this purge time. At short purge times, i.e. at fast average growth rates⁵, a c_{\parallel} -texture forms whereas for long purge times a c_{\perp} -texture is formed.

Extent from thermodynamic equilibrium might affect preferred nucleation

⁵The growth rate of each monolayer is of course independent of the purge time. But the period between the depositions of subsequent monolayers changes.

CHAPTER 2. ZINC OXIDE - PROPERTIES, APPLICATIONS AND GROWTH

This is probably linked with the different times available for the formation of an equilibrium structure before deposition of the subsequent monolayer. In contrast, Sang and coworkers [70] have observed the formation only of c_{\parallel} films in the temperature range investigated (105 – 165 °C). However, these films were tailored to exhibit noticeable intrinsic electrical conductivity. Therefore, the films probably were slightly sub-stoichiometric although no explicit statement was made on that topic. The observed structures would then be in line with many reports on CVD grown films. A different result was obtained by Pung and coworkers [71]. They found that as a function of temperature texture changed from a mixed (10 $\bar{1}$ 0) & (0002) structure to completely c_{\parallel} and finally to c_{\perp} upon increasing the temperature from 130 °C to 300 °C. This is very similar to the observations of Nicolay and coworkers [63] for CVD for the same zinc and oxygen precursors. For the ALD process, however, this finding has been attributed to the possible dissociation of the ethyl group of the DEZn precursor, the anion fraction of which would attach to the positively charged (0001) surface of ZnO and thereby hinder growth along that direction⁶. At high temperatures further decomposition or desorption from the surface is proposed resulting in growth along the c-axis again.

Chemical reactions
govern texture

To summarize reports on texture formation in CVD grown zinc oxide films it can be stated that this technique principally allows for tailoring the texture in the whole range from explicit c_{\perp} to pronounced c_{\parallel} films (see also table 2.4). Some results seem to be contradictory at first sight which probably in some cases may be explained by differences in such growth parameters that are not typically reported or in the utilized precursors. Consequently, also the growth models, i.e. the mechanisms governing texture formation, are manifold and there does not yet seem to be an all-embracing general growth model that could apply to a majority of the various results reported. However, an important conclusion that can be drawn from the literature survey is that very often preferred nucleation appears to play a dominant role in texture formation. Furthermore, thermal energy seems to promote preferred nucleation in some cases. Films are mostly governed by their initial growth stage, especially if a c_{\perp} -texture is present. In case of thick films that exhibit c_{\parallel} -texture, the initial stage is often characterized either by a mixed texture with weak c_{\perp} -fraction or a clear c_{\parallel} -texture already. Hence, even in cases where mechanisms for evolutionary selection are proposed, film growth might probably also be understood as a consequence of preferred nucleation solely.

⁶Note the principal similarity to the growth models discussed for crystal growth in section 2.3.

2.5. THIN FILM GROWTH BY CHEMICAL PROCESSES

Ref.	Structure	Controlling parameter
[55]	strong and weak c_{\perp}	oxygen supply
[65]	weak c_{\perp}	oxygen supply affects preferred nucleation
[56]	mixed and c_{\perp}	temperature affects preferred nucleation; initial growth stage governs texture
[52, 53]	random to c_{\perp}	thermally activated surface diffusion promotes growth with c_{\perp} -texture by surface energy minimization
[60]	c_{\perp} to c_{\parallel} with increasing temperature	growth along surfaces with higher surface energies (thermally activated)
[63]	c_{\perp} and c_{\parallel} as a function of temperature and film thickness	evolutionary selection by thermally controlled diffusion
[57, 67]	c_{\perp}	preferred nucleation
[13]	c_{\perp} with tailored morphology by utilizing a seed layer	initial stage dictates structural evolution
[62, 68]	c_{\parallel}	preferred c_{\parallel} -nucleation; no evolutionary selection
[69]	c_{\perp} or c_{\parallel}	governed by ALD purge time; extent from thermodynamical equilibrium possibly controls texture
[71]	c_{\perp} and c_{\parallel} as a function of temperature	attributed to chemical reactions in the precursor

Table 2.4: Summary of the CVD-grown crystal structures observed in the different references. The right column gives information about the main mechanism controlling the structure found/proposed in the reference. Evidently preferred nucleation plays a dominant role in film growth. Furthermore, the initial stage is often observed to govern the structure of the final film. Thermally activated diffusion is also proposed to affect the texture of the films as proposed by some authors.

2.6 Thin film growth by physical vapour deposition (PVD) processes

There exists a large variety of physical vapour deposition techniques such as for instance thermal or e-beam evaporation, cathodic arc deposition, ion-plating, ion beam sputtering, pulsed laser deposition and various types of sputtering processes. Amongst these, **Pulsed Laser Deposition (PLD)** and Magnetron Sputtering techniques are chiefly utilized for the fabrication of zinc oxide thin films. In the following, this section therefore focuses on PLD and Sputtering techniques in the discussion of process parameters governing structure formation of ZnO films.

2.6.1 Growth by pulsed laser deposition

In a pulsed laser deposition process, a target is eroded in vacuum or low-pressure atmosphere by a focused laser beam of high intensity which is coupled into a vacuum system by appropriate UV-transparent windows. Commonly ArF ($\lambda = 193\text{ nm}$) or KrF ($\lambda = 248\text{ nm}$) excimer⁷ pulsed lasers are used. During a laser pulse, the target surface region is strongly heated locally which results in the evaporation of the target material and the ejection of electrons. A typical plasma plume is formed above the erosion area due to collision of particles, which also leads to the formation of ions which may strike the growing film. For homogeneous erosion, the target is typically rotated. Some oxygen is usually added to the atmosphere to grow fully stoichiometric films for both, ablation from a metallic Zn target and from a ceramic ZnO target. Since some energetic particles are generated in a PLD process that may hit the growing film with kinetic energies in the range of 10-100 eV [72], growth of textured crystalline films is possible already at room temperature in contrast to chemical deposition processes. However, substrates are usually heated to achieve optimum structural quality.

Zinc oxide films with excellent structural order are typically grown on epitaxial substrates such as sapphire [73, 74]. However, also on non-epitaxial or amorphous substrates PLD grown films generally exhibit preferred orientation, which typically is c_{\perp} [72, 75–78]. The growth of films with c_{\parallel} -texture is also reported for epitaxial growth on MgO (001) surfaces [79] in an RF-plasma-assisted PLD process, but no reports are known to exist on c_{\parallel} -texture by PLD on amorphous substrates. Regarding the mechanism of texture formation in ZnO films grown on amorphous substrates, Hayamizu and coworkers [72] have observed the formation of a thin amorphous ZnO layer (5 nm) at the substrate interface, followed by the formation of a thin poly-crystalline layer (5 – 10 nm) and subsequently by an oriented (c_{\perp}) thick layer. This has been explained in terms of the formation energy of the crystalline phase that has been stated to be high at the substrate inter-

⁷The correct term is *exciplex* lasers for these noble gas halogenides but the related term excimer is widely used.

2.6. THIN FILM GROWTH BY PHYSICAL VAPOUR DEPOSITION (PVD) PROCESSES

face (resulting in the amorphous phase) but to be lower on the initial amorphous ZnO film⁸, the presence of which therefore promotes the formation of crystallites. It has further been proposed that after crystallization the film grows with the most densely packed planes parallel to the substrate which explains the formation of the c_{\perp} -texture. Another observation that is particularly noteworthy is that structure formation is strongly governed by a ZnO seed layer grown under optimized conditions [72]. Such a buffer layer was shown to promote the formation of high quality film structures even at non-optimized growth conditions. The formation of c_{\perp} -oriented films on amorphous substrates was also observed by Choi and coworkers [76] except that there was no amorphous ZnO layer at the substrate interface. Surface energy minimization was also put forward to explain the self-texturing.

Evolutionary selection governed by density of (002)-planes

Initial stage governs film texture

Self-texturing by preferred nucleation

Another work that should be mentioned in the context of surface free energy minimization was published by Claeysens and coworkers [39]. As already discussed in section 2.4.1 a number of important statements regarding the surface free energies of the different zinc oxide crystal facets have been made [39]. Since the polar surfaces of zinc oxide are charged it has been argued that the *cleavage* energy would be more appropriate than surface energy in discussing preferred growth orientations. Cleavage energy is the amount of energy needed to separate two slabs of ZnO such that a zinc- and an oxygen-terminated surface forms, respectively. For the non-polar surfaces the cleavage energy is simply twice the surface energy but for the polar faces there is no such equivalent. It has been shown [39] that in terms of cleavage energies a c_{\parallel} -orientation would be energetically favoured since the cleavage energy for the (0002) surface is higher than that of the non-polar faces. However, it was proposed that in the initial growth stage zinc oxide may grow in a graphitic structure which is energetically favourable for the first 10 monolayers. A transformation of the film structure to wurtzite with c_{\perp} - instead of c_{\parallel} -orientation is explained by the transformation energy which is lowest for a change from graphitic to c_{\perp} -oriented texture. Further, the authors found that heating of the films only during the initial growth stage can significantly improve structural qualities and that further heat treatment is comparatively ineffective. Hence, the dominant effect of a structurally enhanced buffer layer on film growth was proven.

Preferred nucleation

Preferred nucleation promoted by heat; initial stage governs film structure

The possible role of energetic bombardment during texture formation has been discussed by Shao and coworkers [78] who utilized a plasma-assisted PLD process. While the c_{\perp} -self-texture has been suggested to originate from surface free energy minimization, it has been proposed that the additional energetic bombardment induced by the plasma strongly supports structure formation even at lower temperatures. However, thermal energy delivered to the growing film might

Preferred nucleation proposed

⁸This statement has been made without proof by the authors. It would also contradict with the statement given in [41], where nucleation at the substrate interface was argued to be energetically favourable (see also the discussion in section 2.4.1).

CHAPTER 2. ZINC OXIDE - PROPERTIES, APPLICATIONS AND GROWTH

Ref.	Structure	Controlling parameter
[72]	c_{\perp}	evolutionary selection by delayed crystallization; seed layer governs texture
[76]	c_{\perp}	preferred nucleation by surface energy minimization
[39]	c_{\perp}	preferred nucleation into graphitic structure finally yields c_{\perp} ; initial stage governs texture
[78]	c_{\perp}	preferred nucleation by surface energy minimization

Table 2.5: Summary of the PLD-grown crystal structures observed in the different references. The right column gives information about the main mechanism controlling the structure found/proposed in the reference. Evidently preferred nucleation plays a dominant role in film growth. Furthermore, the initial stage is often observed to govern the structure of the final film.

also increase due to the plasma.

The role of the oxygen partial pressure during structure formation is discussed in [77] and [74] for amorphous and epitaxial substrates respectively. The oxygen partial pressure does not change c_{\perp} -texture in both cases but otherwise morphology is noticeably affected. In [77] a change of the structure of individual grains is observed from columnar to conical shape with increasing oxygen pressure which is explained by the formation of dislocations. A possible origin of this structural change has not been discussed.

In summary, the formation of a c_{\perp} -self-texture on amorphous substrates in PLD growth is commonly explained in terms of minimization of surface free energy which would promote growth with the $\{0002\}$ planes parallel to the substrate by preferred nucleation (see also table 2.5). It is also widely accepted that energetic particle bombardment e.g. in plasma-assisted PLD supports the formation of high quality c_{\perp} -structures. In contrast to chemical deposition processes, formation of c_{\parallel} -oriented films is not observed on non-epitaxial substrates. Possible explanations for this striking difference between texture formation in CVD and PLD (PVD) processes might be (i) that the formation of c_{\parallel} -textures in CVD processes for the most part has a chemical origin e.g. like the mechanism proposed by Pung and coworkers [71] or (ii) that the impact of energetic species in PLD or plasma-assisted PLD processes (see for example [72] or [78]) strongly supports a self-texturing mechanism thereby promoting growth with c_{\perp} -orientation. It should be noted here that even though preferred nucleation was most often put forward as the mechanism determining film structure, some reports also presented evidence for a mechanism of evolutionary selection.

2.6. THIN FILM GROWTH BY PHYSICAL VAPOUR DEPOSITION (PVD) PROCESSES

2.6.2 Growth by magnetron sputtering

In sputter deposition the target material is vaporised by kinetic particle impact in a glow discharge⁹. In common magnetron sputtering systems the glow discharge is maintained at pressures typically in the range of 0.2-10 Pa and at negative target voltages in the range of 200-600 V¹⁰. Inert sputtering or reactive gas ions are accelerated towards the target surface and hence gain kinetic energies equivalent to the cathode voltage, thereby eroding (*sputtering*) the target. Depending on the type of the discharge (e.g. DC, RF, HiPIMS) some fraction of the sputtered material is also ionized. Additionally, a feature inherent in sputtering of metal oxides such as ZnO is the generation of negatively charged oxygen ions at the target surface due to the collisional impact of the sputtering ions. These ions are accelerated by the full cathode potential and therefore gain kinetic energies up to several hundred eV. In conclusion, films grown in a sputtering process are typically subject to bombardment by various ionic species the energy of which may vary between several ten and several hundred eV. Furthermore, secondary electrons can reach the growing film depending on the plasma confinement. While these electrons rather add to the thermal energy input to the substrate due to the low electron mass, the ionic species may significantly affect structure formation by momentum transfer or implantation of ions into the film structure upon collision. Additional energy is also delivered to the growing films as a consequence of substrate heating by the discharge.

Consequently, sputter-deposited zinc oxide films are typically crystalline already at room temperature (i.e. without intentional heating of the substrate). Furthermore, films are commonly textured in c_{\perp} -direction. Therefore, it is typically no challenge to deposit c_{\perp} -textured ZnO films by sputtering. However, at the same time massive structural damage is observed to be caused by the energetic particle bombardment. Specifically the bombardment by the highly energetic oxygen ions generated at the target surface plays a crucial role in structure formation. This was first shown by Tominaga and coworkers [81] who found that under conditions of strong oxygen ion bombardment the film structure can get degraded from c_{\perp} to almost powder structure¹¹. In a later publication [82] it was also shown that the oxygen ion bombardment strongly deteriorates the electrical conductivity of ZnO:Al films. There it was also demonstrated that ion damage is reduced in a magnetron sputtering system compared with diode sputtering due to the lower discharge voltages. These works [81, 82] further demonstrated that e.g. high pres-

⁹For a detailed discussion of glow discharges and the sputtering process the reader is referred to [80].

¹⁰This range is typical for common DC, RF, MF, pulsed DC or respective superimposed sputtering discharges. However, the target voltage may reach up to 3 kV in novel HiPIMS processes.

¹¹Tominaga et al investigated a cylindrical RF diode sputtering process where typical cathode voltages were in the range of 2-2.5 kV, thus yielding oxygen ions with extremely large kinetic energies as compared with today's magnetron sputtering processes.

CHAPTER 2. ZINC OXIDE - PROPERTIES, APPLICATIONS AND GROWTH

tures (which increases the probability of the energetic ions being scattered before they strike the growing film) or substrate positions away from the vicinity of the target surface (and therefore away from typical ion trajectories) could decrease ion damage. However, other problems like porous films and lower deposition rates can arise from such conditions which is why they are not typically applied. By Severin and coworkers [1] it was shown that the trajectories of the fast oxygen ions depend on target age. During sputtering of the target surface, a pronounced erosion trace is formed. Consequently, the surface normal is locally tilted in the erosion area. The electrical equipotential planes closely follow the wrinkled shape of the erosion trace. Since the oxygen ions are accelerated perpendicular to these planes their trajectories are altered with the target age. This is schematically sketched in figure 2.9.

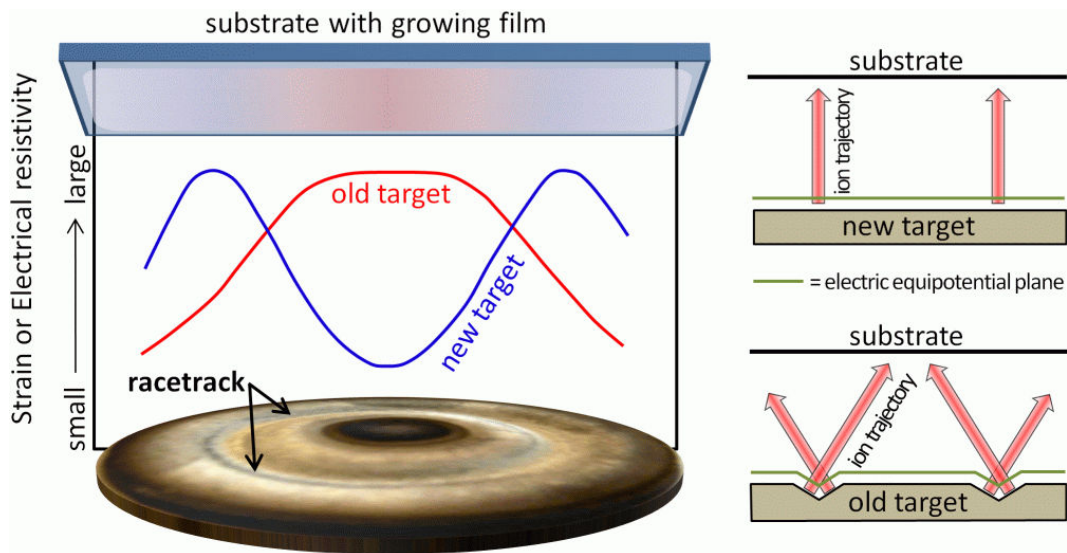


Figure 2.9: Energetic oxygen ion trajectories as a function of target age. As schematically sketched, the electric equipotential planes closely follow the shape of the target surface. Since negative oxygen ions are created directly at the target surface, their trajectories are parallel to the local electric field. The shape of the target racetrack which depends on target utilization therefore strongly affects these ion trajectories. Typical film properties that are significantly influenced by the ion bombardment are schematically sketched as a function of target age and position at the substrate.

Optimization of the structural quality for these reasons turned out to be a difficult task and the quest for fabricating films with excellent texture is two-fold. Therein, one task is to find parameters promoting the formation of a good texture, whereas the second task is to avoid massive structural damage by the energetic particle bombardment at the same time. Furthermore, there are works e.g. by Ngaruiya and coworkers [83] which propose that in the structure formation of transition metal oxides the oxygen ion bombardment is beneficial and

2.6. THIN FILM GROWTH BY PHYSICAL VAPOUR DEPOSITION (PVD) PROCESSES

promotes crystallization during growth of such films at room temperature. This might also apply to ZnO which would mean that the energetic oxygen ion bombardment could be *boon and bane* at the same time. Indeed, in the present work it will be demonstrated that ion bombardment under specific conditions is highly beneficial for the formation of high quality c_{\perp} -textures in sputtered ZnO films. Although it is often reported in literature that negative oxygen ion bombardment strongly influences film growth¹², there is no comprehensive discussion yet about how exactly the structure formation of zinc oxide is affected by the energetic bombardment. Preliminary investigations corresponding to this topic have been shown in [40]. A more detailed discussion will be given in chapters 5 to 7 of this work.

In the following a literature survey focusing on the structure formation of zinc oxide films in various sputtering processes will be given. Growth conditions and the film textures observed will be discussed as well as explanations given by several authors about the origin of the textures observed.

First results showing the influence of oxygen ions (but without knowledge of their existence yet) were already reported by Hada and coworkers [84] in 1970¹³. By changing the total pressure, either c_{\parallel} - or c_{\perp} -orientations were observed at low or high pressures, respectively. This is a direct fingerprint of the influence of the energetic ions which are effectively scattered at high pressures such that ion damage is reduced. First detailed investigations of texture formation as a function of oxygen ion bombardment have already been mentioned ([81, 82]). Motivated by this knowledge of the significant role of energetic oxygen ion bombardment in structure formation, many reports nowadays exist on film growth where conditions were varied such that particularly the ion bombardment was affected. Petrov and coworkers [85] investigated the influence of the oxygen flow and total pressure for various substrate positions and both diode and magnetron sputtering processes. For diode sputtering, substrates were placed opposite to the cathode (standard) and in vertical position aside the target. Whereas for the films deposited on the standard substrate the c_{\perp} -texture strongly deteriorated with increasing oxygen flow, c_{\perp} -texture on the vertical substrate was formed independent of oxygen flow. In the magnetron process, where discharge voltages are significantly smaller, c_{\perp} -oriented films were grown opposite to the cathode at all oxygen flows but with severe mechanical stresses especially at high oxygen flows. These stresses however reduced with increasing total pressure¹⁴. The authors attributed these observa-

Intense ion bombardment promotes c_{\parallel} -textured films

energetic ions damage c_{\perp} -texture

¹²The effect of such bombardment is also evident from experimental results even in works where oxygen ions are not considered as a possible origin for the structural features observed.

¹³The sputtering process utilized could be regarded as *magnet-assisted* diode sputtering since discharge voltages (1-1.5 kV) were still much higher than for today's magnetron processes.

¹⁴This typically indicates the action of energetic particles/ions since their kinetic energy and therefore their impact on film growth reduces by collisions in the gas phase especially at elevated pressures.

CHAPTER 2. ZINC OXIDE - PROPERTIES, APPLICATIONS AND GROWTH

tions to the action of energetic oxygen ions since the changes upon parameter variations were unambiguous fingerprints. Since an initial random orientation of crystallites was found in the early growth stage (10 nm), the formation of a pronounced c_{\perp} -texture was proposed to originate from a faster growth speed of the (0002)-oriented grains and subsequent evolutionary selection. Similar observations were reported by Lee and coworkers [86] on RF magnetron sputtered ZnO films. They also found typical fingerprints of oxygen ion bombardment upon changing the substrate position with respect to the target or increasing the oxygen flow. In all cases structure changed from c_{\perp} to a mixed texture under conditions where stronger bombardment was expected. Furthermore, it was also found that thick films (several μm) tend to exhibit c_{\parallel} -orientation while thin films exhibit c_{\perp} -structure. This interesting finding was proposed to originate from a selective deterioration of the most densely packed planes (i.e. {0002}) by the oxygen ion bombardment [86]. However, this explanation would to some extent conflict with the formation of the pronounced c_{\perp} -texture for thin films in the first place. An explicitly strong damage of film structure opposite to the target racetrack was observed by Sundaram and coworkers [11] for very small distances between the target and the substrate. The damaged regions were slightly opaque and showed a dominant c_{\parallel} -orientation in contrast to the non-damaged regions. Different attempts to influence particle bombardment of growing ZnO films were reported e.g. by Doh, Ma, Sharma, Nagata and respective coworkers [87–90]. Structural improvements were achieved by introducing biased grids between the target and the substrate to influence the flux of negative oxygen [87] and positive argon [88] ions. It was argued by Ma [88] that a certain flux of low energy positive argon ions would promote structure formation. Nagata [90] showed that structural damage caused by oxygen ions was reduced by utilizing xenon as a sputtering gas. It was argued that this would produce a lower oxygen ion flux density to the substrate. Sharma [89] demonstrated that films with structures different from c_{\perp} could be deposited from an unbalanced magnetron¹⁵. They assumed that the increased particle bombardment resulting from the expanded plasma was responsible for the structural changes. These films exhibited a pronounced Zn excess, i.e. the stoichiometry was $\text{Zn}_{1-x}\text{O}_{1-x}$. Interestingly, the effect of stoichiometry is often observed/proposed to have an influence on film texture [38, 91, 92] where usually oxygen-deficient films exhibit non- c_{\perp} -orientation. In one of these cases [38], oxygen deficient films were even deposited at high oxygen flows. This might be explained by possible oxygen re-sputtering from the films which has been observed in [40]. The deposition rate also seems to be an important parameter in structure formation [38, 93]. Mirica and coworkers [93], who sputtered films at comparatively high substrate temperatures between 450 °C and 650 °C, proposed

¹⁵An unbalanced magnetron is characterized by a typically intentional misfit between the magnetic field strengths of the center and outer magnet assemblies. This leads to an imperfect electron confinement above the target and hence to an extension of the plasma towards the substrate in typical deposition geometries.

2.6. THIN FILM GROWTH BY PHYSICAL VAPOUR DEPOSITION (PVD) PROCESSES

that the morphology of the films is governed by an interplay between deposition rate (i.e. condensation speed) and substrate temperature (i.e. thermal energy available for surface diffusion processes). The faceting behaviour of ZnO film surfaces investigated for different deposition rates and temperatures was explained by a model based on surface diffusion. It is argued that at low temperatures (up to 300 °C) the film growth is governed by negligible surface diffusivity, leading to an almost instantaneous sticking of arriving atoms to the film. Hence, atomic shadowing is expected to result in a large surface roughness and intergranular porosity. At higher temperatures, surface diffusion is stated to govern structural evolution. Different surface free energies [38], diffusion rates and growth speeds of the different crystal facets [21] are proposed to control the film texture in favour of a c_{\perp} -textured film.

It has already been mentioned that the thickness of the films can also have an influence on the average texture and that thick films may tend to exhibit c_{\parallel} -orientation. The effect of thickness was investigated by Lee, Lin, Yanagitani, Fortunato and their coworkers [37, 94–96]. Pronounced c_{\perp} -textures were observed for film thicknesses up to 600 nm [94] and 1600 nm [96], respectively. The structural quality increased with increasing thickness in favour of c_{\perp} . This was attributed to self-texturing during nucleation [94]. For thicker films, however, pronounced c_{\parallel} -textures may be observed [37, 95]. It was demonstrated that upon increasing film thickness from 500 nm to 7 μm the texture changed from (0002) to (10 $\bar{1}$ 1) and finally to (11 $\bar{2}$ 0). It is argued that a “survival of the fastest” mechanism¹⁶ that is often assumed to govern the c_{\perp} -texture formation in the early stage of film growth cannot explain the change in orientation at later growth stages. Furthermore, it is suggested that strain energy minimization might play an increasingly important role at large film thicknesses. The possible action of this mechanism of evolutionary selection has been critically discussed in section 2.4.2. However, the authors state that this mechanism would also not explain the exact chain of texture changes observed [37] and therefore propose preferential damage of the (0002) planes by energetic oxygen ion bombardment as the origin for the change in texture with increasing thickness, while initial growth is still assumed to be governed by surface energy minimization, i.e. c_{\perp} -texture formation. In [95] c_{\parallel} -orientation for thick films (5 – 15 μm) was observed under conditions promoting a strong oxygen ion bombardment (high oxygen flow, low discharge power, substrate position close to the target) at low substrate temperatures, while at other growth conditions mixed films with a stronger contribution of c_{\perp} -oriented grains were observed. This is evidence that indeed oxygen ion bombardment may play a decisive role in the change of texture with increasing film thickness. However, this explanation should be regarded with some caution since it is unclear how this explanation can be consistent with the observed self-texturing mecha-

Preferential nucleation governs texture

Preferential damage of c_{\perp} -grains might yield c_{\parallel} -texture

c_{\parallel} -texture promoted by oxygen ion bombardment?

¹⁶It is often argued that the fastest growth direction of zinc oxide is in {0002}-direction and that evolutionary selection results in the formation of a (0002)-texture.

CHAPTER 2. ZINC OXIDE - PROPERTIES, APPLICATIONS AND GROWTH

nism in the initial growth stage where most commonly a distinct c_{\perp} -texture is formed. Exactly because of that discrepancy, a preferential sputtering mechanism by oxygen ions is generally ruled out as a texture forming mechanism by other authors [97–99]. In these works, films were prepared on textured substrates¹⁷, i.e. on substrates exhibiting an explicitly non-flat surface. It was found that such films were highly oriented already in the initial growth stage at the substrate interface. Furthermore, the {0002} planes always aligned exactly parallel even to the locally tilted substrate surface. Since neighbouring grains/areas therefore exhibited strongly different orientations, a dominant effect of directed ion bombardment on the texture could be ruled out¹⁸. It has been proposed that minimization of surface free energy is the dominating force governing growth with the {0002} planes parallel to the substrate. The same argument is also put forward by many other authors (e.g. [100] or [101]). This would also explain the observation of comparatively weaker c_{\perp} -textures for deposition of ZnO films on very rough surfaces [102] since the initial spread of crystallite orientations on the non-flat substrate surface would complicate the formation of a strict c_{\perp} -texture for the thick films.

Particularly noteworthy is an investigation which shows the actual strength of the self-texturing mechanism inherent in the growth of zinc oxide films. Goto and coworkers [103] investigated the structure of films grown on MgO (100) crystal substrates. An epitaxial match typically results in the formation of ZnO films with (10 $\bar{1}$ 1) preferred orientation on these substrates. However, it was observed that under some deposition conditions films grow with c_{\perp} -orientation instead of adopting the orientation defined by the substrate.

Since the utilization of zinc oxide buffer layers will be an important topic in chapter 6 of this work, the discussion of structure formation in sputtered ZnO films will be concluded with reports on structural improvements induced by such buffers. Van de Pol and coworkers [104] reported that the film structure can be tailored by utilizing different deposition conditions for the initial and final growth stage, respectively. The morphology of thick films was strongly influenced by the structure of the buffer layer rather than by the deposition conditions during growth of the thick film. A similar experiment was demonstrated by Kim and coworkers [105] who showed that the structural quality was improved by deposition of a specifically tailored ultrathin (4 nm) ZnO buffer layer on a sapphire (0001) substrate prior to deposition of the thick film. A very interesting variation regarding the utilization of buffer layers was shown by Sato and coworkers [106] who showed that the application of thin RF sputtered buffer layers strongly improved the quality of the texture of ZnO films subsequently grown by AP-MOCVD.

¹⁷The expression *textured* should not be mistaken with preferred orientation. A textured substrate is characterized by a structured, non-flat surface morphology.

¹⁸Another explanation would be that oxygen ion bombardment was just weak in these experiments. These results therefore do not strictly rule out any role of energetic oxygen ions in texture formation.

2.6. THIN FILM GROWTH BY PHYSICAL VAPOUR DEPOSITION (PVD) PROCESSES

Ref.	Structure	Comments
[84]	c_{\perp} and c_{\parallel}	c_{\parallel} -texture formed under energetic oxygen ion bombardment
[85]	strong and weak c_{\perp}	Energetic ions damage c_{\perp} -texture; evolutionary selection based on different growth speeds proposed
[86]	mixed and c_{\perp}	Parameters suggest that strong ion bombardment changes c_{\perp} to mixed texture by selective deterioration of (002)-planes
[11]	c_{\parallel}	c_{\perp} damaged by ion bombardment
[88]	c_{\perp}	Low energy ion bombardment promotes structure formation
[89]	non- c_{\perp}	growth with unbalanced magnetron
[38, 91, 92]	non- c_{\perp}	oxygen-deficiency could inhibit c_{\perp} -texture
[93]	c_{\perp}	interplay between condensation rate and temperature determines structural quality
[94]	c_{\perp}	preferred nucleation
[37]	thin film: c_{\perp} , thick film: c_{\parallel}	preferential damage of (002)-planes by ion bombardment changes texture
[95]	thin film: c_{\perp} , thick film: c_{\parallel}	c_{\parallel} -orientation for thick films observed under conditions promoting a strong oxygen ion bombardment
[97–99]	initial c_{\perp} on non-flat substrates	preferred nucleation proposed; preferential damage generally ruled out as texture-forming mechanism
[103]	c_{\perp}	c_{\perp} -texture despite epitaxial substrate promoting c_{\parallel} ; preferred nucleation can be very strong
[104–106]	seed layers	important role of initial stage confirmed by experiments with thin seed layers

Table 2.6: Summary of the investigations for sputter-deposited ZnO films. The right column gives comments mainly about the mechanisms controlling the structure found/proposed in the reference. It is evident from this summary that preferred nucleation is often proposed. Furthermore, the important role of the initial growth stage has been observed. This is a hint that preferred nucleation should principally govern the structure of the entire film. The growth of c_{\parallel} - or not explicitly c_{\perp} -textured films is typically observed under conditions promoting a strong oxygen ion bombardment of the growing film. This may often be attributed to a possible preferential damage of (002)-oriented planes (without proof).

2.7 Summary: Texture formation in sputtered zinc oxide thin films

Since this work deals with the structure formation of sputtered zinc oxide thin films, it shall be briefly summarized which are the conditions that typically promote a specific texture in this process (see also table 2.6).

First, it can be concluded from the foregoing sections that depending on the deposition process the formation of c_{\perp} - or c_{\parallel} -textures is either triggered by chemical reactions or by energetic particles. In chemical growth processes an arbitrary tuning of the mean crystallite orientation is therefore apparently possible by adjusting precursor types and flows and by utilizing the strong influence of thermal energy in such processes. In the PVD processes this chemical component is missing such that especially c_{\parallel} -textures are observed rather seldom. It seems that zinc oxide naturally grows with the c -axis along the substrate normal (on amorphous or non-epitaxial substrates) governed by minimization of the surface free energy, which is the most commonly used mechanism to explain the dominant self-texture which mostly arises from preferred nucleation. In sputtering, there seem to be two deposition parameters which have a dominant influence on this self-texturing mechanism: stoichiometry and energetic ion bombardment. Deviations from a high quality c_{\perp} -texture seem to occur if films are grown with an oxygen-deficiency¹⁹ and if the bombardment by energetic oxygen ions becomes too intense. Interestingly, both parameters are linked with the oxygen flow in a typical reactive sputtering process. At low oxygen flows a weak c_{\perp} -texture is caused by slight deficiencies while at large oxygen flows the increased arrival ratio between oxygen ions and sputtered species at the substrate is unfavourable for the formation of the c_{\perp} -texture. Besides these important growth parameters, there is an influence of temperature, which can serve to cure defects caused by the energetic bombardment and probably to improve preferred nucleation, and of low-energy ion bombardment (e.g. 40 eV Ar⁺ in a typical RF discharge) that may support the formation of a c_{\perp} -texture. Pronounced c_{\parallel} -textures may be achieved under intense energetic oxygen ion bombardment. Therefore, it can be stated that in the sputtering process energetic particle bombardment is the key parameter governing film texture. In the absence of intense bombardment, preferred nucleation due to surface free energy minimization is the most often proposed mechanism inducing a c_{\perp} -texture.

Seed layers were found to play an important role in the growth of zinc oxide films. The influence of the structure of a seed layer often was more dominant than the growth conditions during growth of thick ZnO films onto tailored ZnO seed layers. This fact will also be explored in chapter 6 of this work. It should be emphasized that the importance of the initial growth stage for the structure

¹⁹Note the similarity with CVD processes where low oxygen precursor flows also promote films with rather random orientation.

2.7. SUMMARY: TEXTURE FORMATION IN SPUTTERED ZINC OXIDE THIN FILMS

formation of the entire film is not restricted to the sputtering process. Instead, this observation has been reported for various deposition processes and therefore appears to be a universal property of zinc oxide film growth.

Films with c_{\parallel} -texture fabricated by sputtering were only observed for large film thicknesses. Such films typically start growing with a mixed or very weak c_{\perp} -texture that changes upon increasing the film thickness. Regarding the early growth stage as a seed layer for the growth of the later stages, this finding seems to be to some extent contradictory to observations made for the utilization of buffer layers. The explanation of the change in preferred orientation as a consequence of preferential damage caused by the oxygen ion bombardment, that is typically presented in the discussion of such results, would probably contradict with the initial ordered c_{\perp} -structure formed in the early growth stage in some cases. It is proposed that changes in texture can only occur if an initial c_{\perp} -texture is already very weak. This would probably be achieved by adequately intense energetic oxygen ion bombardment during the initial growth stage, which would hinder preferred nucleation of c_{\perp} -oriented grains. Furthermore, any possible mechanism of evolutionary selection would need to have only a weak contribution to texture formation.

It should be mentioned here that a comprehensive comparison of various reports on the structure formation of sputtered zinc oxide films found in the literature is difficult. The reason for that primarily arises from the fact that the strong influence of the shape of the target surface (target age) on the oxygen ion trajectories was discovered very recently [1]. The target age therefore plays quite an essential role in structure formation since it directly governs the relative oxygen ion flux to the films grown. Unfortunately, the condition of the target surface is typically not reported in publications. As a consequence, deposition conditions which look similar at first sight might differ strongly in terms of energetic oxygen ion bombardment.

The determinant influence of ion bombardment (low-energy xenon and high energy oxygen ions) as well as the concurrently important role of the different growth stages will be discussed in chapters 5 to 7 of this work.

3

The magnetron sputtering processes

In the course of this work, two different sputter tools have been utilized, one of which is equipped with an ion source and modified for ion beam assisted sputtering (IBAS). In the following sections, the unique features of both systems will be explained. In the course of this work an elaborate software interface has been developed which enables fully computer-controlled operation of both systems¹. The basic features of this software comprise e.g. (a) full data-mining of all process parameters, (b) real-time and off-line stability analysis of all process parameters, (c) active plasma control by a feedback loop (latency ≈ 10 ms) between an oxygen probe and the plasma power supply which enables stabilization of the full transition regime in reactive sputtering of metal oxides², (d) fully programmable process characterization and deposition routines for stand-alone operation, (e) database and full session review procedures and (f) automatic generation of protocols containing information on the stability of all process parameters during deposition of each layer. The software development will be disclosed in a separate programmer's and user manual which is not part of the present work.

3.1 Coater 1: The IBAS setup

The geometry of the deposition system is shown in figure 3.1. A cylindrical body houses up to two sputter cathodes which enables sequential deposition of multi-layer films from two different material sources (targets). Prior to each deposition run, the chamber is pumped down to a base pressure of typically 2×10^{-6} mbar by a turbomolecular pump with a maximum pump speed of 520 l/s (N_2). The distance between the target surface and the substrate stage can be varied by adjusting the position of the sputter cathodes. Typical distances from the target surface to the substrates range from approximately 55 mm to 80 mm. An ion

¹Another deposition tool developed for serial co-sputtering has also been equipped with a version of this software. However, this machine was not utilized for the deposition of films investigated in this work.

²With the plasma control algorithm films can be deposited at any working point since every oxygen partial pressure of the typical s-shaped transition [107] between metallic and oxidic sputtering modes can be stabilized.

Coater 1: IBAS setup

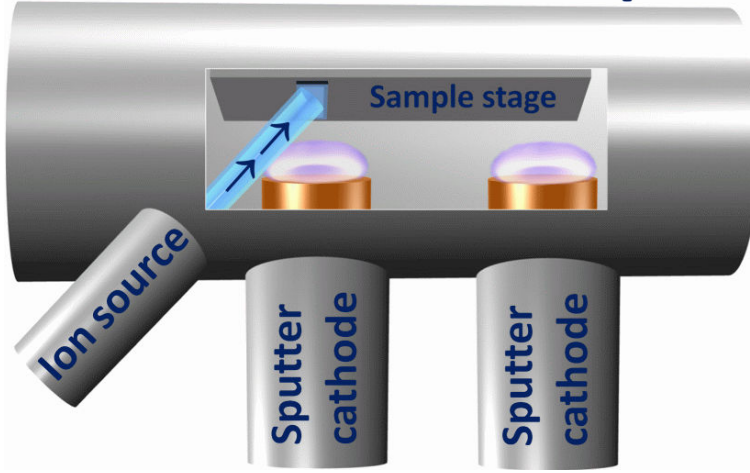


Figure 3.1: Schematic drawing of the IBAS process chamber. Two sputter cathodes that are adjustable in height are installed to a cylindrical body. A broad beam ECR plasma ion source is installed such that films deposited from one of the cathodes can be simultaneously bombarded under a fixed angle of $\approx 45^\circ$. The other cathode is used to deposit a second layer without ion assistance, e.g. for seed layer experiments. Films from the IBAS process were also transferred to **coater 2** for further deposition.

source (Tectra Gen II) with an additional differential pumping stage (cf [40] for details on the source) has been installed in this sputter deposition system. For one of the sputter cathodes simultaneous growth from the sputter target and bombardment of the films by this auxiliary ion gun is possible (see figures 3.3 and 3.2). A target-to-substrate distance of 80 mm is required for this mode of operation to clear the way for the ions. The angle of incidence of the ions at the substrate is fixed at approximately 45° . Inevitably, in a reactive sputtering process, the sputtering target constitutes a second source of ions, as discussed in section 2.6.2 already. Negatively charged oxygen ions are created at the racetrack and are accelerated towards the growing film. These ions represent a contribution to the total ion bombardment of the films that is very difficult to control. The bombardment by the oxygen ions may even result in severe structural damage [108]. However, since these ions propagate on well-defined trajectories [1], it is possible to use a mechanical shielding device (which is depicted in figures 3.2 and 3.3) to eliminate this detrimental bombardment³. With this prerequisite, the auxiliary gun enables a precise control of energetic ion bombardment. The ion source is equipped with a separate gas inlet, which feeds a gas directly into the plasma cup of the source. This ensures a high purity of the ion species even when different gases are present in the sputtering atmosphere.

In the IBAS process, the metallic Zn target (diameter: 76 mm, purity: 99.99%) is sputtered at a constant discharge current of 250 mA (≈ 400 V) in a reactive Ar/O₂ atmosphere in oxide mode. An Advanced Energy Industries *Pinnacle* DC

³See [40] for details on the development and the functionality of the shielding device.

3.1. COATER 1: THE IBAS SETUP

generator is employed to maintain the discharge. A low pressure of 0.2 Pa is utilized to minimize scattering of the auxiliary ions on their trajectories towards the growing film. These conditions result in a deposition rate of 0.1-0.15 nm/s under the geometrical conditions described. A small variation in the rate is due to target aging and placement of the shielding device. The bombarding species, xenon, is fed directly into the plasma cup of the ion source, improving the efficiency of the ionization and the purity of the ion beam. The inflow of xenon contributes with a partial pressure of approximately 0.03 Pa to the total pressure in the main chamber volume. Typical Xe^+ ion energies are around 180 eV with an ion current density at the substrate surface of $1 - 1.5 \mu\text{A}/\text{cm}^2$, which results in an ion to atom arrival ratio at the substrate of approximately 2 %. This ratio has been defined as the ratio between the Xe^+ ion flux density at the substrate position and the flux density of ZnO molecules contributing to the film growth. The ion current has been measured at the substrate position utilizing a flat probe, neglecting the small portion of secondary electrons generated by the collision of ions with the probe⁴. In good approximation, all ions are singly ionized and therefore we can express the ion flux density N_{Ion} as

$$N_{\text{Ion}} = \frac{I_{\text{Ion}}}{F \times \sqrt{2} \times e}, \quad (3.1.1)$$

where I_{Ion} is the measured ion current and e is the elementary charge. F is the area of the flat probe and the factor of $\sqrt{2}$ is a geometrical correction taking account of the 45° tilt angle of the impinging ion beam with respect to the substrate. The flux density of ZnO molecules N_{ZnO} can be derived from the deposition rate

$$N_{\text{ZnO}} = R \times \frac{\rho_{\text{ZnO}} \times N_A}{M_{\text{ZnO}}}, \quad (3.1.2)$$

where R is the deposition rate, N_A is Avogadro's constant, ρ_{ZnO} is the mass density and M_{ZnO} is the molar mass of ZnO respectively. The relative arrival ratio is then defined by $N_{\text{Ion}}/N_{\text{ZnO}}$. As a substrate, a silicon (100) wafer with a thin native amorphous oxide layer was used for the films discussed in this chapter. However, the structural improvements of the ZnO films also appear if glass substrates are utilized, which will be demonstrated in chapter 6. The substrates have not been intentionally heated. The substrate temperature has not been measured in the present study. However, Joule heating of the substrate by the ion beam is negligible since the maximum energy transfer to the $2 \times 2 \times 0.065 \text{ cm}^3$ Si substrate (specific heat capacity: $703 \text{ J}/(\text{kg} \times \text{K})$) is approximately 1 mJ/s and typical deposition times range from 100 to 1000 seconds. Consequently, the heat capacity of the substrate is approximately 0.423 J/K , which means that it would

⁴This assumption is based on reports of the secondary electron yields of xenon ions from gold [109] and MgO [110] surfaces. In both cases, secondary electron emission is clearly negligible for an ion energy of 180 eV.

CHAPTER 3. THE MAGNETRON SPUTTERING PROCESSES

heat up by approximately 2.5 K during a deposition time of 1000 s neglecting the counteracting energy loss by radiation.

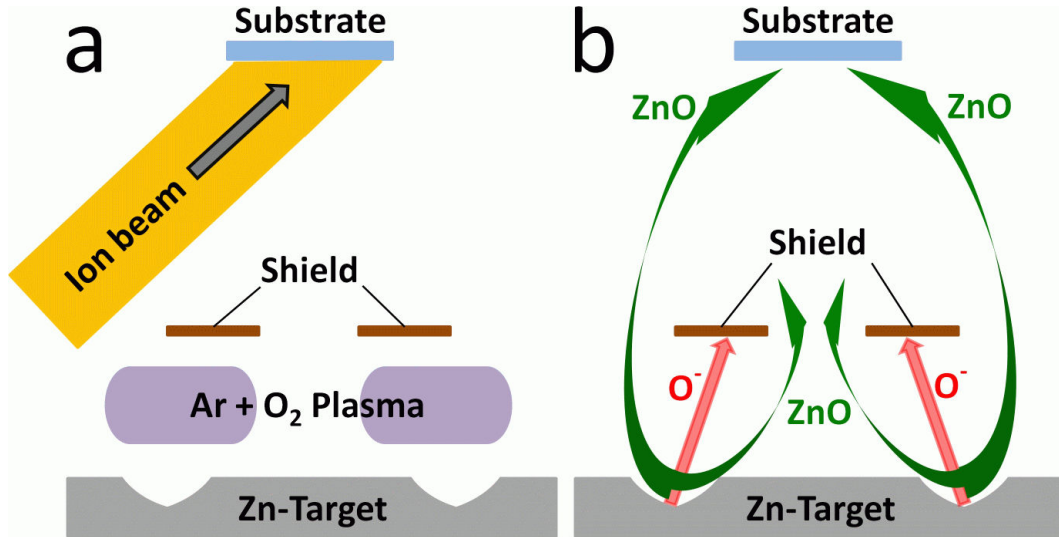


Figure 3.2: Geometry of the IBAS process: A zinc target is sputtered in a reactive Ar/O₂ atmosphere to yield stoichiometric Zinc Oxide films. (a) An auxiliary ion gun is installed to simultaneously enable a well-controlled ion bombardment at an inclination angle of approx. 45°. (b) A mechanical shield is utilized to avoid the undesirable bombardment of the growing film with oxygen ions originating from the oxidized target surface. While these ions are blocked there is still a partially diffusive ZnO particle flux to the substrate.

The deposition parameters described above, i.e. especially the discharge current, total pressure, xenon partial pressure, ion energy and ion flux, are constrained within a narrow process window for the following reasons:

- The total pressure has to be low since otherwise significant scattering of the ion beam in the gas phase would occur which would strongly decrease the ion current density at the substrate position.
- The xenon inflow and power to the ion source have been optimized for maximum ion extraction at stable operating conditions.
- The ion energy cannot be reduced to values significantly lower than 180 eV since for this type of source the extraction current scales with the ion energy and would therefore significantly drop at lower energies.
- The sputter discharge current is low compared to typical standard conditions for reactive deposition of ZnO in the coaters utilized. This is necessary to adjust the deposition rate to the limited ion current density of the ion source. This allows to realize relative arrival ratios between ions and ZnO molecules of a few percent.

3.1. COATER 1: THE IBAS SETUP

Any notable variation of any of these parameters would result either in an unstable operating condition of the ion source or in an insufficient ion current density at the substrate position. In consequence, the parameters mentioned have usually been kept fixed. Some efforts to investigate the influence of different deposition conditions will be shown in the first section of chapter 5 though.

In this work, this modified sputtering process will be referred to as **Ion Beam Assisted Sputtering (IBAS)**. Comparable processes are often referred to as Ion Beam Assisted Deposition (IBAD) which is sometimes abbreviated to the term Ion Assisted Deposition (IAD). The difference to the IBAS process is that typical IBAD processes [111–115] utilize very low pressure deposition techniques such as evaporation or ion beam sputtering. However, in recent years also sputtering discharges have been combined with ion assistance from an auxiliary gun [116].

Samples which were prepared with ion-assistance under the above-mentioned conditions are mostly referred to as **IBAS samples** in this work. Samples which were deposited without ion-assistance in any of the sputtering processes (coater 1 or coater 2) are often (but not always) referred to as **REF samples** (reference). Some of the films discussed in this work are multi-layer stacks. In this case, films are also referred to as IBAS or REF samples depending on the process utilized for the deposition of the **first layer** (at the interface to the substrate). This first layer is often named IBAS or REF **seed layer** or **buffer** where the words seed and buffer are equivalently used.

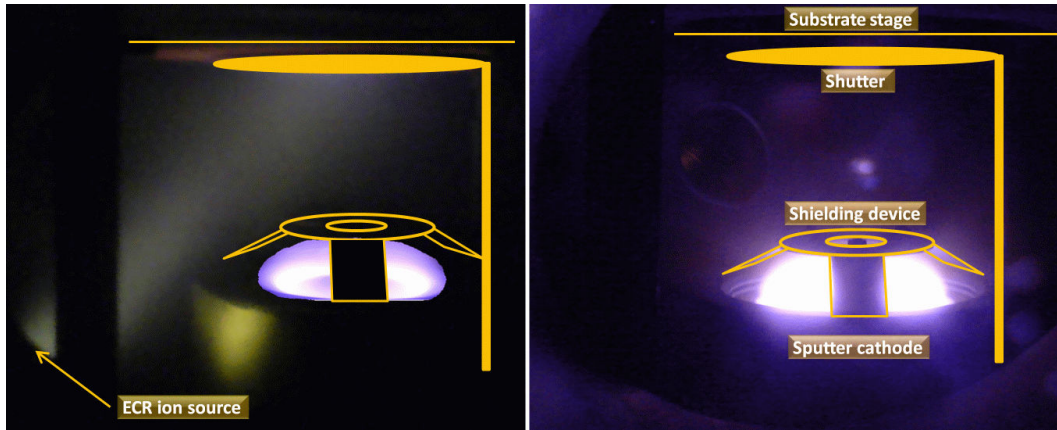


Figure 3.3: Photographs of the ion beam (left image) and a sputtering plasma with shielding device (right image) which show the geometrical conditions of the IBAS process. Ion source and sputtering plasma are simultaneously operated during an IBAS process. Some mechanical parts of the coater are highlighted in the figures for better visualization.

3.2 Coater 2: A conventional sputtering setup

For the fabrication of multi-layer films, another deposition tool was often utilized. The geometry of this coater is sketched in figures 3.4 and 3.5. The cylindrical body can be equipped with up to 6 sputtering sources. A revolving substrate stage is placed above the targets at a distance of typically 55 mm between the target surface and the substrates. Additional shields are installed which avoid both the contamination of targets that are not sputtered and the unintentional coating of substrates.

Coater 2: Standard setup

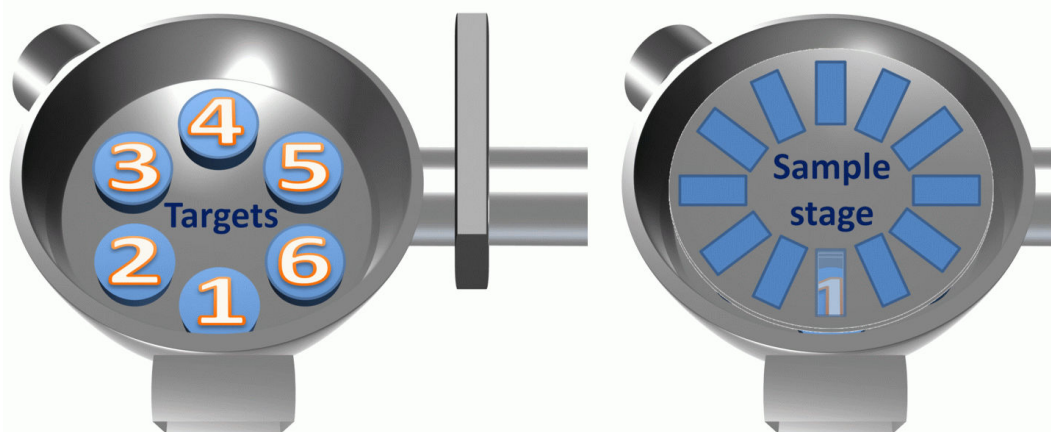


Figure 3.4: Schematic drawing of the standard coater. The cylindrical body can house up to 6 sputter cathodes for fabrication of multi-layer coatings (left image). A revolving substrate stage is placed approximately 55 mm above the target surface (right image). Additional shields cover targets/substrates that are not in use/coated.

Many layers of the films discussed in section 6.1 and 6.3 were fabricated in this sputtering system. In cases where seed layers from coater 1 (e.g. IBAS seed layers) were utilized, the specimens were transferred from coater 1 to coater 2 for further depositions. The cathodes utilized in coater 2 are structurally identical to those in coater 1. A base pressure of less than 2×10^{-6} mbar was established prior to deposition by a pumping stage equivalent to that of coater 1. Zinc oxide films in coater 2 were reactively sputtered from a metallic Zn target at standard conditions. The atmosphere was an argon/oxygen mixture with a total pressure of 0.6 Pa and the discharge current was fixed at 500 mA by the same generator as used for coater 1. Silver films were deposited from a metallic Ag target at an argon pressure of 0.8 Pa and a constant discharge power of 50 W if not stated otherwise.

3.2. COATER 2: A CONVENTIONAL SPUTTERING SETUP

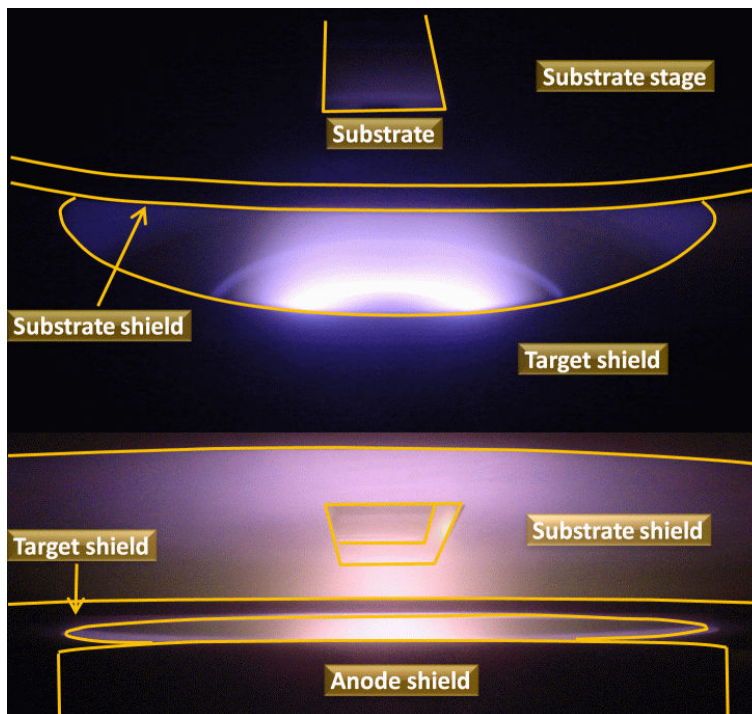


Figure 3.5: Photographs of a plasma in the standard coater during operation. Geometrical features such as anode shield, target shield and substrate shield as well as the substrate stage and the substrate position are highlighted. Note that the figure contains two photographs which show the sputtering plasma and the substrate stage from two different perspectives simply.

4

Thin film analytics

4.1 X-ray techniques

In the course of this work, films have been investigated with various x-ray techniques to conclude on crystallographic features (x-ray diffraction) as well as on film thickness, roughness and mass density (x-ray reflectometry). These techniques will be discussed in the following subsections. The diffractometer that was utilized is a *Philips X'Pert Pro MRD* which is operated with a copper tube. The characteristic wavelength of the CuK_{α} radiation is approximately 1.542 Å. The machine is typically operated with a line focus and is equipped with special optics and detectors for the different measurement geometries. The x-ray source is fixed. To allow for the different measurement geometries, both the detector and the sample stage are automatically moved. Bragg-Brentano XRD measurements were performed with an *X'Celerator* CCD line array detector in scanning mode, which allows very fast scanning along the 2θ -axis. Grazing Incidence measurements were performed with a proportional counter mounted to a parallel plate collimator with a flat crystal monochromator. For the XRR measurements a proportional counter was used in combination with a programmable anti-scatter and receiving slit optics and a curved crystal monochromator. This combination was also utilized for Rocking Curve measurements. For a very detailed description of the machine and sample alignment procedures the reader is referred e.g. to [117]. In the following, the geometry of the various scans will be discussed with special emphasis on the type of information that can be deduced from each measurement, respectively.

4.1.1 X-ray diffraction (XRD)

X-ray diffraction in Bragg-Brentano (also called $\theta - 2\theta$) geometry has typically been utilized to determine the structural quality of sputtered zinc oxide films. The basic geometrical features are shown in figure 4.1. The prominent feature is that the incident and diffracted x-ray beams have identical inclinations with respect to the substrate surface (fig. 4.1a). As a consequence, the bisecting line of the angle between these beams (the “scan normal”) is fixed and always

CHAPTER 4. THIN FILM ANALYTICS

parallel to the substrate normal. Therefore, only reflections from planes parallel to the substrate surface are detected. Statements about preferred orientation are therefore straightforward. As an example, typically sputter-deposited zinc oxide films show only a very pronounced (002) peak and higher orders in a $\theta - 2\theta$ diffraction pattern. This strongly suggests that only crystallites with the respective planes oriented parallel to the substrate surface are present in the film. Thus, there is a (002) preferred orientation. The conditions for a diffraction peak are also sketched in figure 4.1a. Incoming x-rays are scattered at the electron shells of atoms which in a crystalline structure are regularly arranged along planes with inter-planar distance d_{hkl} . The relative phase retardation δ between x-rays scattered at adjacent planes is given by $\delta = 2d_{hkl} \sin \theta$. Constructive interference and therefore an intensity maximum at the detector requires that $\delta = n\lambda$, where λ is the wavelength of the utilized radiation and n is an integer value ($n = 1, 2, 3, \dots$). This results in Bragg's law:

$$n\lambda = 2d_{hkl} \sin \theta. \quad (4.1.1)$$

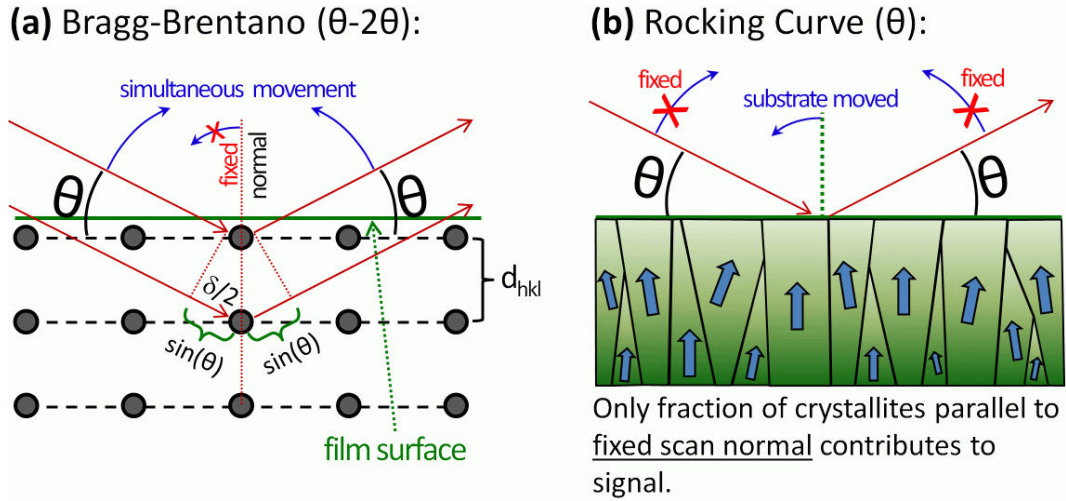


Figure 4.1: Geometries of XRD measurements in Bragg-Brentano geometry (a) and Rocking Curve measurements (b). **(a)** Sample stage and detector are simultaneously moved such that the incident and diffracted beams (as defined by the position of the detector) have identical angles with respect to the sample surface. Since in this case the intersecting line (scan normal) between the incident and diffracted beams is always perpendicular to the sample surface, only diffraction peaks from planes oriented parallel to the surface contribute to the signal intensity. **(b)** In a rocking curve scan, one of the diffraction angles at which a diffraction peak occurred in a Bragg-Brentano scan is fixed by the position of the detector. Only the sample is rotated. Since only crystallites with the selected planes perpendicular to the scan normal contribute to the intensity, the angular intensity distribution of the rocking curve contains information about the orientation distribution of these planes with respect to the sample surface.

Even though measurements in Bragg-Brentano geometry can give strong ev-

4.1. X-RAY TECHNIQUES

idence for a preferred orientation, there is typically some characteristic distribution of crystallite orientations around the preferred orientation. In zinc oxide films, crystallites are typically not perfectly aligned with their c-axis parallel to the substrate normal but there is some statistical distribution around this orientation with a characteristic FWHM. This is sketched in figure 4.1b, where blue arrows indicate the direction of the c-axis for each crystal. A simple method to measure the width of the distribution is a Rocking Curve measurement. In this geometry, the diffraction angle of a specific peak (e.g. the (002)-peak in ZnO) is fixed. Instead, only the substrate is moved (“rocked”) such that the diffracted beam intensity detected for each substrate tilt angle is proportional to the density of crystallites parallel to the scan normal. The intensity distribution typically is of Gaussian shape and the FWHM is a measure for the orientational order of the film and hence the quality of the preferred orientation.

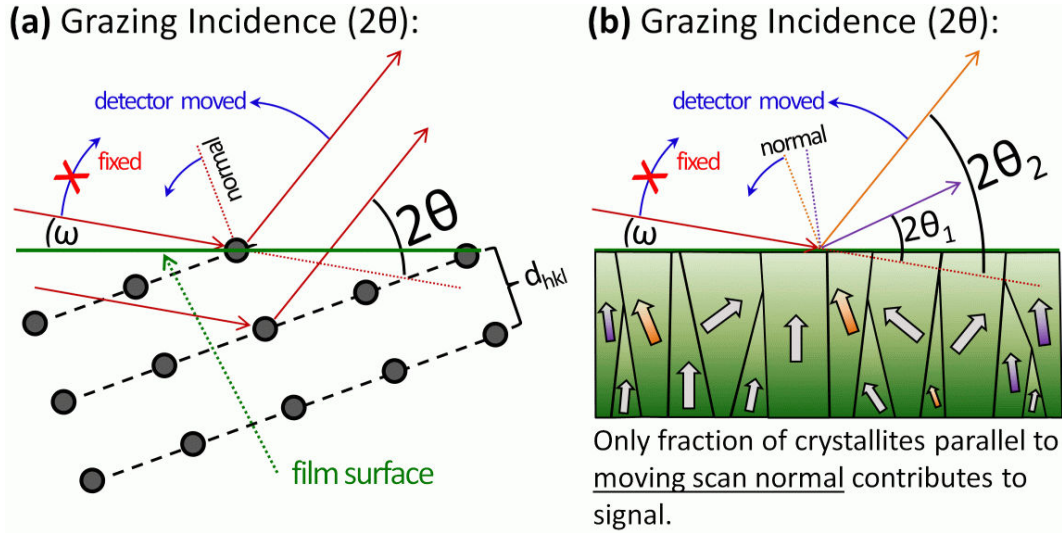


Figure 4.2: Geometry of a Grazing Incidence XRD measurement. **(a)** In contrast to a Bragg-Brentano scan the angle between the incident beam and the substrate is fixed (typically at an angle of $< 1^\circ$). This enhances the irradiated area and reduces the signal from the underlying substrate. Both facts increase the signal-to-noise ratio with respect to a Bragg-Brentano scan. Only the detector is moved, scanning the different diffraction angles. **(b)** It is evident that in grazing incidence geometry the scan normal also is a function of the total diffraction angle, i.e. the detector position. As a consequence, each peak in the diffraction pattern corresponds to differently oriented grains with respect to the sample surface. This fact has to be taken into account when discussing preferred orientations with the help of grazing incidence scans.

The discussed Bragg-Brentano geometry is typically utilized for highly crystalline samples with preferred orientation. However, for specimens that are characterized by a weak crystallinity or low orientational order (e.g. powder samples), techniques with a better signal-to-noise ratio are required. Grazing Incidence measurements are typically utilized in this case. As sketched in figure 4.2a very

2θ [°]	d_{hkl} [Å]	Intensity	hkl
31.754	2.8157	578	100
34.429	2.6028	442	002
36.243	2.4766	999	101
47.535	1.9113	229	102
56.568	1.6257	324	110
62.859	1.4772	276	103
66.343	1.4079	44	200
67.928	1.3788	243	112
69.055	1.3590	114	201
72.584	1.3014	19	004
76.934	1.2383	38	202
81.395	1.1813	19	104
89.592	1.0933	74	203

Table 4.1: Powder diffraction data of ZnO. From [118].

small fixed angles of incidence are used (typically $< 1^\circ$). The advantage of having such a small angle of incidence is that a very large area of the sample is irradiated. Also, most of the beam is diffracted in the interior of the film instead of being transmitted to the substrate. This significantly increases the signal-to-noise ratio. A special optics with a parallel plate collimator to filter the very wide diffracted beam is utilized. In a grazing incidence measurement, only the detector stage is moved during a scan. The drawback of this technique is that the scan normal varies with the diffraction angle. Since only crystallites with their respective planes perpendicular to the scan normal contribute to the diffracted beam intensity (fig. 4.2b), no conclusion can be drawn on the relative phase composition or orientational order of the film without knowledge of the full orientation distribution function of the crystallites. However, if certain assumptions on the orientation distribution are made, also information on the preferred orientation can be deduced, which will be discussed in section 4.1.2.

Table 4.1 shows powder diffraction data (from [118]) of zinc oxide. Listed are the typical diffraction angles corresponding to the different inter-planar distances in the wurtzite structure. The typical intensity of each peak in a powder sample is also given.

4.1.2 Interpretation of grazing incidence XRD patterns

To enhance the information on the structural properties, some of the specimens discussed in this work have been investigated by XRD in both Bragg-Brentano and grazing incidence geometry, respectively. However, while the interpretation of Bragg-Brentano type scans is straightforward with respect to a preferred crys-

4.1. X-RAY TECHNIQUES

tallographic orientation in the films, this is not the case for grazing incidence patterns. As discussed, in these scans a difficulty arises from the fact that the scan normal varies with the diffraction angle since the incident angle is fixed. Therefore, each diffraction peak in a grazing incidence pattern corresponds to a different orientation of the reflecting planes. This is sketched in figure 4.3 where the tilt $(\theta - \omega)$ of the scan normal is displayed with respect to the substrate surface normal for the diffraction peaks of ZnO (blue lines).

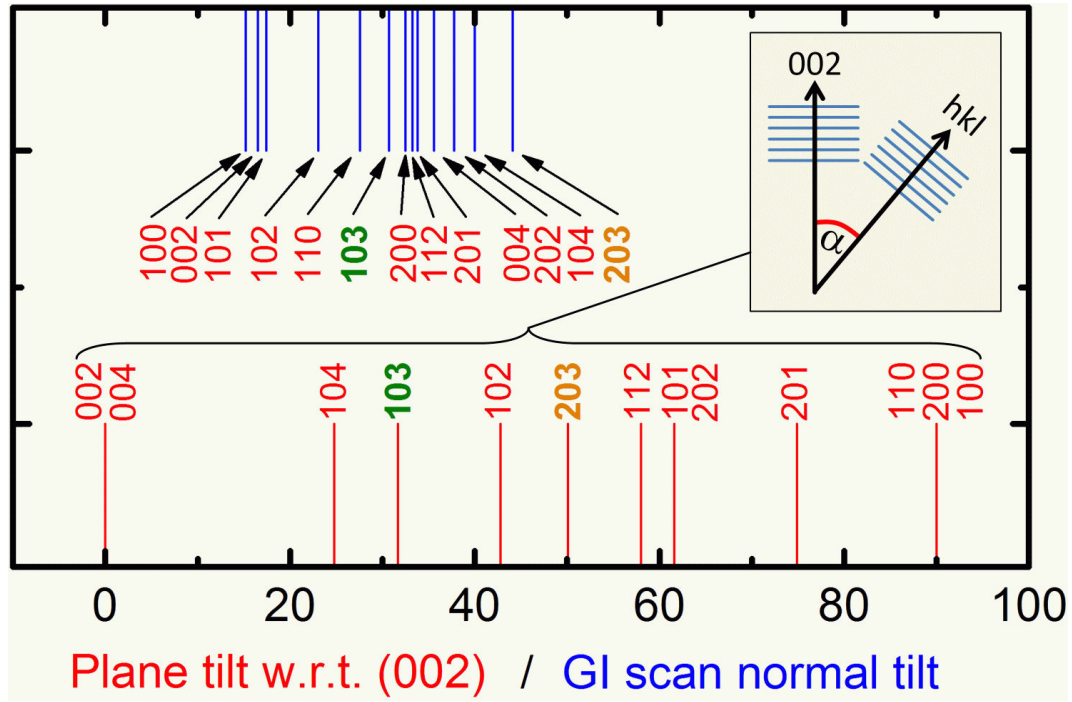


Figure 4.3: **Blue lines:** Tilt of the scan normal (cf figure 4.2) with respect to the substrate surface normal for a grazing incidence measurement ($\omega = 0.7^\circ$) for the specific 2θ angles at which the typical reflexes of a ZnO powder sample occur (Tilt = $\theta - 0.7^\circ$ with θ from table 4.1). **Red lines:** Tilt of the normal to the different planes with respect to the normal of the (002) planes (see inset). For (002)-textured films, peaks appear in the grazing incidence measurements if both tilt angles (blue and red lines) match.

To interpret grazing incidence patterns, we may assume that the ZnO film exhibits perfect c_\perp -orientational order. The tilt of the ZnO crystal planes with respect to the (0002)-direction is then identical to the tilt with respect to the substrate surface normal. The plane tilts have been calculated from the Miller indices and are also displayed in figure 4.3 (red lines). These tilt angles were deduced from the geometry of the unit cell and have been calculated according to

$$\alpha = \arctan \left(\frac{c}{a \cdot l} \sqrt{\frac{4}{3} (h^2 + k^2 + hk)} \right), \quad (4.1.2)$$

CHAPTER 4. THIN FILM ANALYTICS

where α is defined as sketched in the inset of figure 4.3, (hkl) are the Miller indices of the respective plane and a and c are the unit cell parameters.

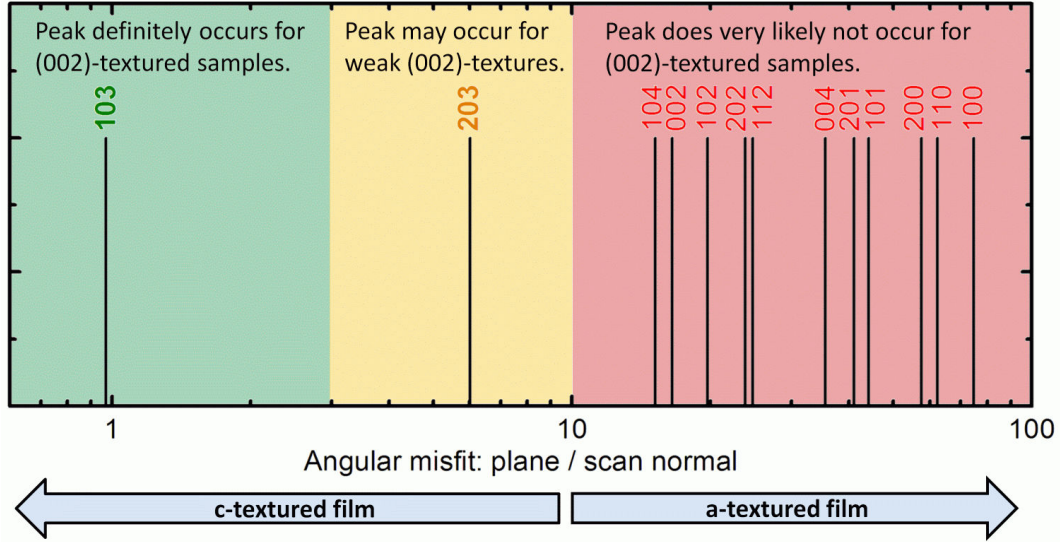


Figure 4.4: From figure 4.3 the moduli of the angular differences between the scan normal in a grazing incidence scan and the plane tilt with respect to the (002) planes have been calculated. If the film has c_{\perp} -texture, planes that exhibit a low difference (close to 0°) will show up in a grazing incidence scan. On the other hand, if peak corresponding to planes with a large difference (close to 90°) appear, this is evidence that the film has c_{\parallel} -texture.

It is now obvious that for c_{\perp} -textured films a strong peak should occur in a grazing incidence pattern for those planes where both angles (red and blue lines) in figure 4.3 are nearly identical. Therefore, in figure 4.4 the moduli of the difference between both angles is displayed for all ZnO Miller indices. Apparently there is an almost perfect match for the (103) peak. The angular deviation is less than 1° , which is small in comparison to typical orientation distributions of c_{\perp} -textured ZnO films (compare with the FWHM of rocking curves that will be shown e.g. in chapter 5). Consequently, the (103) peak should be the dominant contribution in c_{\perp} -textured films. On the other hand, if peaks appear to be dominant the angular shift of which is close to 90° , this is evidence for a film rather with a c_{\parallel} -texture instead, since this texture is perpendicular to c_{\perp} .

4.1.3 X-ray reflectometry (XRR)

X-ray reflectometry on the one hand is similar to a Bragg-Brentano measurement since the incident and diffracted beams are symmetric with respect to the substrate normal, similar to the sketch shown in figure 4.1a. On the other hand, the angle of incidence θ is very small (typically $0 - 2^{\circ}$). Instead of constructive interference of x-rays scattered at atoms in different lattice planes, the diffracted

4.1. X-RAY TECHNIQUES

beam is characterized by fractional reflection of the beam at each interface, e.g. at the film surface and the interface between the film and a substrate by the differences in the electronic density of the materials. Interference between these reflected beam fractions depends on the film thickness and the angle of incidence. Therefore, x-ray reflectometry can be regarded as an “optical” measurement. The reflection of the beam at the various interfaces can be described by the difference in the complex refractive indices $\tilde{n} = n + ik$. For x-rays the real part of the refractive index is smaller than unity and therefore $n = 1 - \delta$, where δ is positive and of the order of 10^{-5} . From Snell’s law in the form $n_1 \cos \theta_1 = n_2 \cos \theta_2$ it can be concluded that if e.g. $\delta = 10^{-5}$ the x-rays do not penetrate into the film if $\theta \lesssim 0.26^\circ$. Below this critical angle θ_c , the beam is totally reflected at the film surface, as shown in figure 4.5 which shows a typical XRR pattern of a ZnO sample produced in the course of this work. At larger angles the beam is partially diffracted into the film and reflected at the interface with the substrate. For $\theta > \theta_c$ the diffracted beam intensity continuously drops with increasing θ and is characterized by interference minima and maxima as a consequence of the superposition of the x-rays reflected at the surface and the interface, respectively. Since at x-ray-frequencies the polarizability of the film is directly correlated with the electronic density which is proportional to the mass density, the critical angle θ_c is a function of the mass density. In [117] it has been demonstrated that

$$\delta = \frac{r_0 \lambda^2}{2\pi} n_e \quad (4.1.3)$$

$$n_e = (Z + f') \cdot n_{\text{atom}} \quad (4.1.4)$$

$$n_{\text{atom}} = \frac{N_A}{M} \cdot \rho \quad (4.1.5)$$

where r_0 is the Bohr radius, λ is the x-ray wavelength, $(Z + f')$ is the charge of an atom in units of e with a correction factor, n_e and n_{atom} are electron and atom densities of the film, N_A is Avogadro’s number, M is the molar mass and ρ is the mass density of the film. It has further been shown that for compositions with molar fractions x_i

$$\delta = \frac{r_0 \lambda^2}{2\pi} N_A \sum_i x_i (Z_i + f'_i) \cdot \frac{\rho_{\text{tot}}}{A_{\text{tot}}} \quad (4.1.6)$$

with weighted total density ρ_{tot} and molar mass A_{tot} . From Snell’s law it follows that [117]

$$\theta_c \approx \sqrt{2\delta} \quad (4.1.7)$$

$$= \sqrt{\frac{r_0 \lambda^2}{\pi} N_A \sum_i \left((Z_i + f'_i) \frac{x_i}{A_{\text{tot}}} \right) \cdot \rho_{\text{tot}}}. \quad (4.1.8)$$

CHAPTER 4. THIN FILM ANALYTICS

By exactly measuring θ_c the mass density of the film can therefore be calculated. From the interference fringes at angles larger than θ_c the film thickness t can be extracted:

$$t \approx \frac{\lambda}{2} \frac{1}{\sqrt{\theta_{m+1}^2 - \theta_c^2} - \sqrt{\theta_m^2 - \theta_c^2}}, \quad (4.1.9)$$

where θ_m is the position of the m-th intensity maximum (or minimum) [117]. Furthermore, surface roughness influences the reflection pattern and can therefore also be estimated from modeling XRR patterns. The *WinGixa* software (Philips) has been utilized for modeling the patterns.

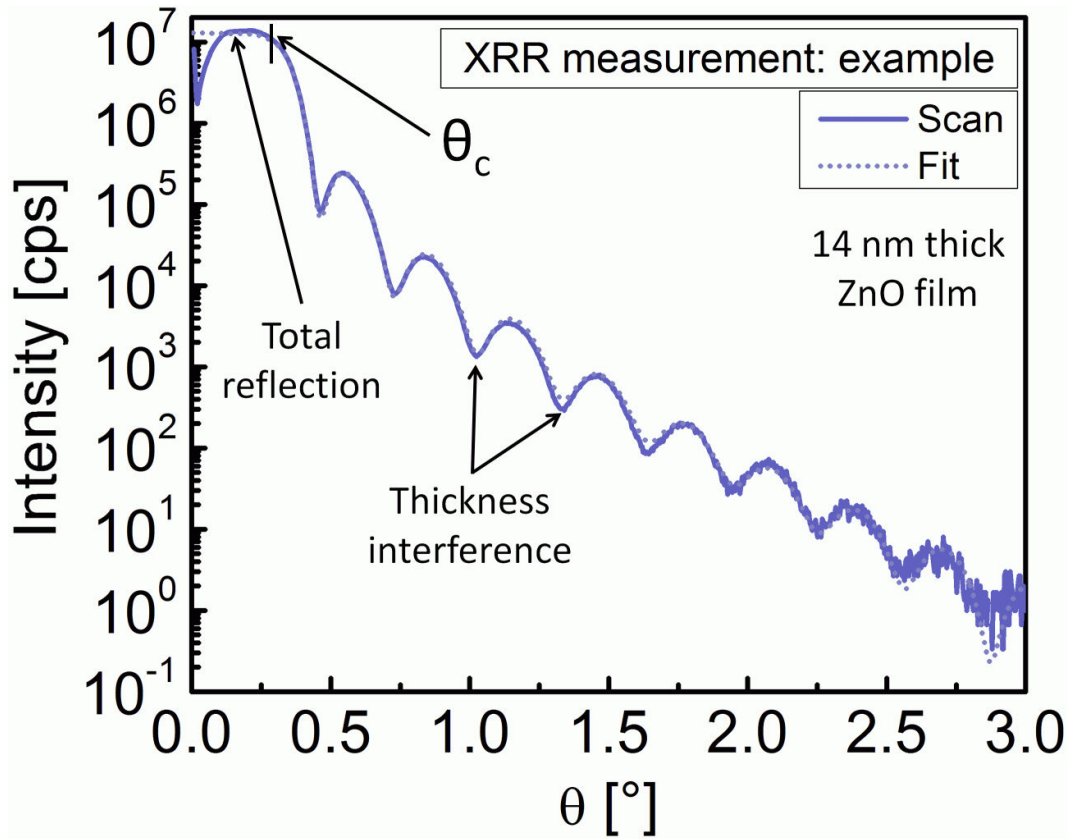


Figure 4.5: Typical x-ray reflectometry pattern. Below a critical angle of incidence θ_c the entire incident beam is specularly reflected at the film surface. Above this critical angle, a fraction of the beam is diffracted into the film and can be partially reflected at the interface to the substrate (or subsequent layers in a multi-layer stack). This reflected beam interferes with the fraction reflected at the film surface and hence an interference pattern forms which depends on the different refractive indices of the stacked materials (typically substrate/film/air) and the film thickness. From the decay of the intensity above θ_c information about the interface roughnesses can also be deduced.

4.2 Atomic force microscopy (AFM)

For investigations of the surface topography a *Digital Instruments Dimension 3100 Nanoscope* has been utilized. The instrument has been operated in *tapping mode*. The basic principle of an AFM measurement is illustrated in figure 4.6. The specimen surface is scanned by a nanoscopic tip typically with a radius of 10 nm, which is located at the front end of a cantilever (see details in figure 4.7). The scan head to which the tip is attached to is usually moved along the x-y-z-direction by piezo transducers. In tapping mode, the cantilever is stimulated to oscillations at the resonant frequency in z-direction by a piezo transducer. The amplitude of this oscillation is measured by a quadrant photodetector via a laser beam that is reflected from the cantilever. In very close approach to the sample surface, the interaction with the tip by van der Waals forces affects the oscillation by slightly altering the resonance frequency and therefore the amplitude, which is detected by the photodetector. That change is compensated by a feedback algorithm which adjusts the z-position of the tip to maintain a constant amplitude. The tip height is then a function of the drive voltage applied to the respective piezo transducer. This drive signal is used to calculate the surface topography upon utilization of a height-voltage calibration curve.

4.3 Transmission electron microscopy (TEM)

To investigate the microstructure of selected specimens TEM measurements have been performed at the Ernst Ruska Center for Electron Microscopy at the Forschungszentrum Jülich. TEM specimens were prepared by standard techniques, involving mechanical grinding, dimpling and Ar ion milling. Plan view and cross-sectional specimens have been prepared, which allow the investigation of the microstructure parallel and perpendicular to the growth direction, respectively. Bright-field images and dark-field diffraction contrast images have been recorded to investigate the crystal structure of the specimens. Additionally, SAD patterns have been recorded to gain information about the orientational distribution of preferred orientations. TEM investigations were performed with a Tecnai F20 operated at 200 kV.

4.4 In-situ stress measurements - wafer curvature method

In this work, films have been deposited where the evolution of mechanical film stresses has been monitored in-situ. A dual laser beam wafer curvature method has been utilized. Figure 4.8 shows the principle of this technique. During nucleation the deposited film forms a strong bond with the substrate surface. If

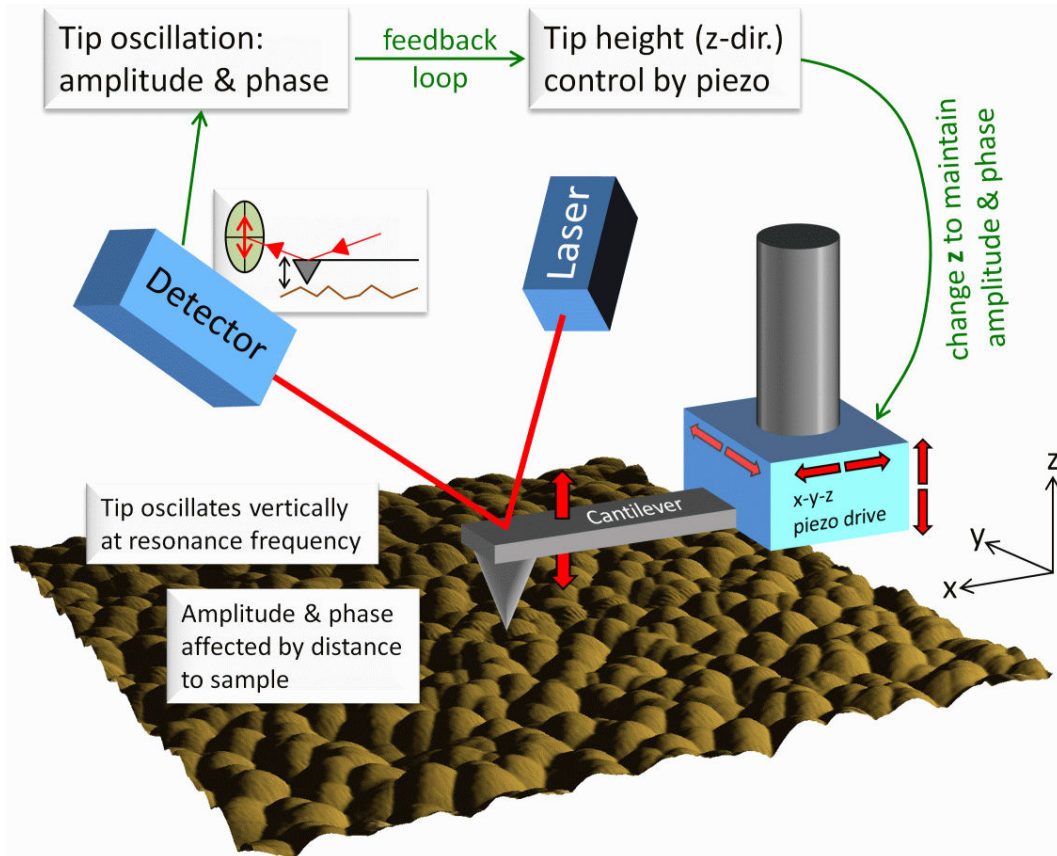


Figure 4.6: Principle of an AFM measurement in tapping mode. The tip (radius < 10 nm) oscillates at its resonance frequency and scans the surface in x-y-direction. Upon close approach to the surface, the amplitude of the oscillation is affected by van der Waals forces, which is detected by a photodetector via a laser beam which is reflected from the cantilever. A feedback algorithm to the piezo transducer adjusts the z-position to maintain a constant amplitude. The height information is derived from the piezo drive voltage.

4.4. IN-SITU STRESS MEASUREMENTS - WAFER CURVATURE METHOD

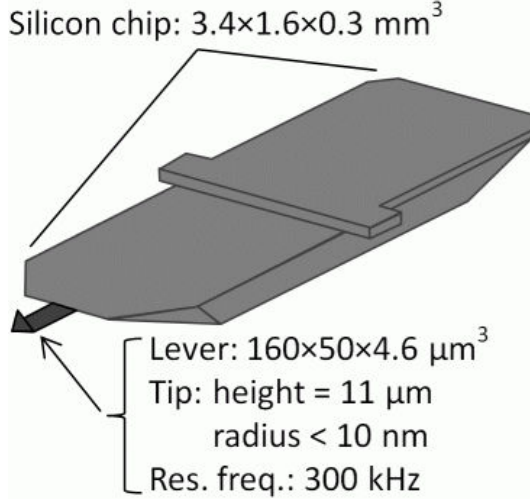


Figure 4.7: For all scans *Olympus OMCL AC 160TS* tips have been utilized. The cantilever has a resonance frequency of approximately 300 kHz and is coated with aluminium to enhance laser light reflection. The tip has a radius of $< 10 \text{ nm}$. Depending on the surface topography this allows imaging with resolutions ranging from 0.1 nm to 10 nm .

film strain changes during growth due to mechanical stresses, the substrate is therefore also forced to curve. This curvature can be monitored by the reflection of laser light at the backside of the substrate. In the utilized setup, a laser beam has been split into a parallel dual beam, which is reflected at the substrate. If the substrate is not ideally flat, the reflected beams are divergent. The divergence can be calculated from geometrical parameters upon detecting the two laser spots on a screen. The assumption is made that the curvature of the substrate is purely spherical and can therefore be described simply by the corresponding radius R , which can be expressed by

$$R = 2 \cdot \frac{b \cdot s}{d_y - s}. \quad (4.4.10)$$

The meaning of the parameters b , s and d_y is sketched in figure 4.8.

The curvature $1/R$ is correlated with the film force f , which is the force per unit width of the film which causes the stress. The film force can be expressed as

$$f = \Delta \frac{1}{R} \cdot \frac{E_s t_s^2}{6(1 - \nu_s)} \quad (4.4.11)$$

where $\Delta \frac{1}{R}$ is the relative change in substrate curvature upon deposition of the film, t_s is the thickness of the substrate and E_s and ν_s are the elastic modulus and the Poisson ratio of the substrate [119]. The film stress σ_f is then given by

$$\sigma_f = \frac{f}{t_f} = \Delta \frac{1}{R} \cdot \frac{E_s t_s^2}{6(1 - \nu_s) \cdot t_f} \quad (4.4.12)$$

where t_f is the thickness of the deposited film. The film stress as defined in equation 4.4.12 is an average value only. Although film stress can be measured

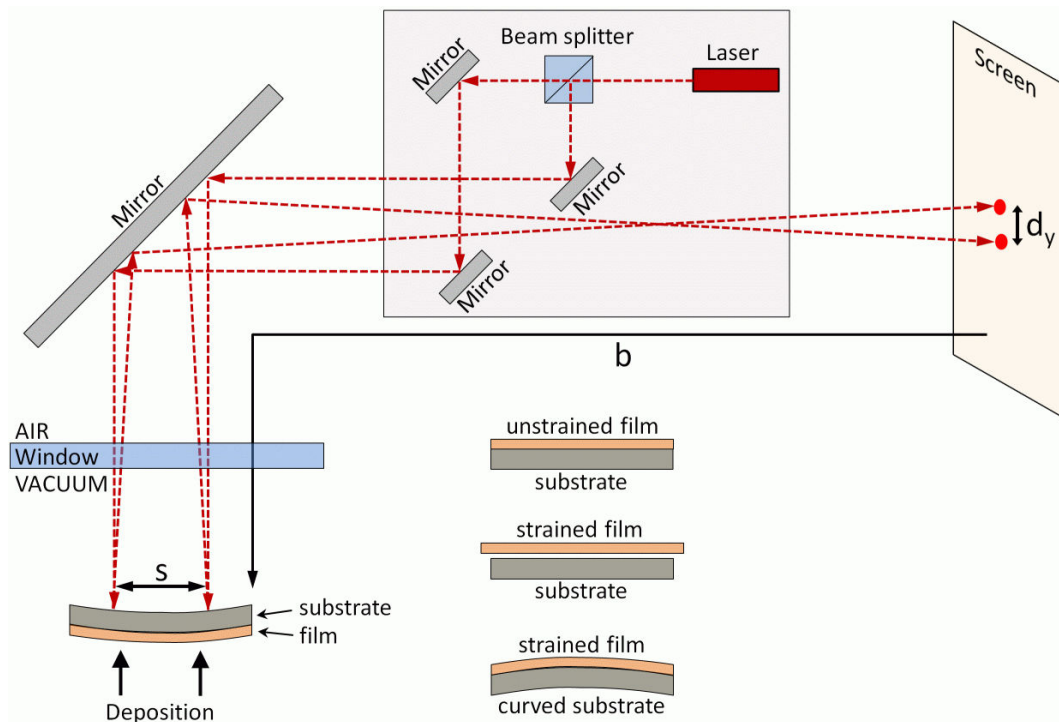


Figure 4.8: Principle of the wafer curvature measurement. A laser beam is split into a parallel dual beam and directed into the deposition chamber through a window. There the laser beams are reflected at the backside of a very thin silicon substrate during deposition of a film onto the front side. The curvature is measured as a function of time by measuring the divergence of the reflected dual laser beam. From the substrate curvature the mechanical stress can then be calculated as a function of time and also as a function of film thickness if the deposition rate is known (typically determined after the deposition).

4.5. OPTICAL TECHNIQUES

as a function of film thickness, the film force is always divided by the total film thickness corresponding to each growth stage. In chapter 5 also instantaneous changes in the film stress upon changing process conditions are investigated. For these investigations it is advantageous to define an instantaneous stress σ_i by

$$\sigma_i = \frac{\partial}{\partial t_f} f(t_f) = \frac{\partial}{\partial t_f} \left(\Delta \frac{1}{R}(t_f) \cdot \frac{E_s t_s^2}{6(1 - \nu_s)} \right) \quad (4.4.13)$$

considering that the curvature $1/R$ and therefore also the change in the curvature is a function of film thickness t_f .

In the experiment the wafer curvature is deduced from measuring the distance d_y between the laser spots on the screen. These spots are recorded by a camera at 10 fps (frames per second) during the deposition. An image calibration procedure ensures accurate determination of the real distance between the laser spots. The software code developed in [119] for the evaluation of the raw data has been significantly upgraded. The various procedures have been merged into a single code with a user-friendly interface and several slow image-processing routines have been replaced by efficient code. Also, the video file can now be directly processed without the intermediate step of converting the single frames to bitmap files. The new software allows for the calculation of the film force by analyzing the video file with 20 fps.

For the measurements typically ultrathin ($180 \mu\text{m}$) silicon wafers are utilized which are carefully cut into small substrates with a large aspect ratio. This aspect ratio avoids the formation of strong shear stresses upon bending and therefore is a prerequisite of the 2-dimensional simplification of the problem. It is assumed that the substrate curves along its longitudinal axis only. The elastic modulus and the Poisson ratio of the substrate are taken from [119] ($E/(1 - \nu) = 229 \text{ GPa}$).

4.5 Optical techniques

Optical measurements have not been in the focus of the present work. However, for the specimens that will be discussed in the experimental chapters optical spectra have often been utilized to determine the thickness of zinc oxide films. Therefore, in the following it will be briefly discussed which instruments have been utilized and how the spectra have been modeled to conclude on the thickness of the films.

4.5.1 Reflectance and transmittance

A *Perkin Elmer Lambda 25* UV/VIS spectrometer has been utilized to perform transmittance and reflectance measurements. The instrument is equipped with Deuterium and Tungsten light sources with an automatic switch-over and therefore covers the spectral range from 190 nm to 1100 nm (1.13-6.53 eV). A holo-

CHAPTER 4. THIN FILM ANALYTICS

graphic concave grating with 1053 lines per mm is used as a monochromator and the bandwidth is 1 nm. A reference beam ensures the stability of the intensity calibration over time. For reflectance measurements a reference sample consisting of a sputtered aluminium film with an oxide coating has been utilized. The recorded raw spectra have been convoluted with the reference spectrum to calculate the reflectance. The reflectance of the reference sample itself was measured with a VW optics.

4.5.2 Ellipsometry

A J.A. Woollam M-2000UI variable angle spectroscopic ellipsometer has been used to record ellipsometry spectra. The spectral range covered ranges from 240 nm to 1700 nm (0.53-5.13 eV). The quantity measured is the polarization of light reflected at the sample surface at possible angles ranging from $> 0^\circ$ to $\approx 80^\circ$. The incident light is circularly polarized by passing a linear polarizer and a rotating compensator subsequently. The light reflected at the sample surface is generally elliptically polarized. The shape of the ellipse is detected by an analyzer and fully described by the two ellipsometric angles Ψ and Δ which are the measured quantities. These angles are correlated with the Fresnel coefficients for the s- and p-polarized fractions (r_s , r_p) of the reflected light by

$$\frac{r_p}{r_s} = e^{i\Delta} \tan \Psi. \quad (4.5.14)$$

4.5.3 Modeling of the dielectric function

The experimental data for R, T, Ψ and Δ can be modeled with an appropriate dielectric function. By fitting a model DF with physically reasonable parameters and adequate accuracy, i.e. small deviation from the measured data, to the measured spectra, information on specific parameters of the DF can be concluded from the fits. For zinc oxide typically the width of the bandgap, the refractive index and the film thickness can be extracted from the model DF. For modeling zinc oxide films, two model functions to describe the fundamental gap have proven to yield reasonable results and may therefore be alternatively used. A very simple approach to modeling the fundamental absorption is realized in the *Tauc-Lorentz* model. This model is based on works of Tauc in 1966 [120] and Jellison in 1996 [121]. To model optical data of amorphous Germanium, Tauc used the fact that above the fundamental gap the density of states scales with the energy as $D \propto \sqrt{E}$ and proposed a dielectric function defined by

$$\varepsilon_2(E) = A_T \frac{(E - E_g)^2}{E^2} \cdot \Theta(E - E_g) \quad \text{Tauc joint density of states} \quad (4.5.15)$$

4.6. ELECTRICAL MEASUREMENTS

where A_T is a constant, E_g is the width of the fundamental gap and $\Theta(E - E_g)$ is the Heaviside function. The real part of the dielectric function is also already defined by this expression via the Kramers-Kronig relation. In 1996 Jellison has suggested to combine the Tauc joint density of states with a typical Lorentzian dipole oscillator describing the dispersion of the refractive index in optical materials with a single resonance frequency. A Lorentz oscillator is defined by

$$\varepsilon_2(E) = A_L \frac{E_0 C E}{(E^2 - E_0^2)^2 + C^2 E^2} \quad (4.5.16)$$

where A_L is constant, E_0 is the resonance frequency and C is the broadening parameter. Jellison et al have suggested to multiply the Tauc density of states with this expression which yields

$$\varepsilon_{2,TL} = \frac{A E_0 C (E - E_g)^2}{(E^2 - E_0^2)^2 + C^2 E^2} \cdot \frac{1}{E}, \quad E > E_g, \quad (4.5.17)$$

$$\varepsilon_{2,TL} = 0 \quad E \leq E_g, \quad (4.5.18)$$

where $A = A_T \cdot A_L$.

Another suggestion for modeling the DF of semiconductors has been made by O'Leary et al [122] (OJL model). Similar to the ansatz of Tauc et al O'Leary started with the theoretical correlation between the density of states and the energy, i.e. $D \propto \sqrt{E}$. However, it was assumed that the transition from the fully transparent to the absorbing region around the band edge is not abrupt but there is a smooth transition. This transition was empirically described by an exponential decay of the density of states into the forbidden region. The states in the bandgap region are called tail states. Details of this representation of the fundamental absorption are discussed in [122]. In the present work it has been found that the OJL representation often is better suited to describe thick (> 500 nm) zinc oxide films since apparently the presence of tail states is no longer negligible in the optical spectra of thick films. Modeling of the optical spectra with either a Tauc-Lorentz or an OJL parameterization has been performed with the *SCOUT* software¹.

4.6 Electrical measurements

The electrical resistivity of the silver films investigated in section 6.3 has been measured with an *MX 604* contactless resistivity gauge (*Eichhorn + Hausmann GmbH*). The method is based on measuring the power loss caused by eddy currents. A high frequency coil creates magnetic field lines which penetrate into the

¹SCOUT version 2.4 from W. Theiss Hard- and Software

CHAPTER 4. THIN FILM ANALYTICS

material (measured sample). The creation of eddy currents, the strength of which depends on the conductivity of the sample, causes a power loss of the oscillator. This is proportional to the conductivity of the sample which can therefore be computed with an accuracy of 3 %.

I: Growth of zinc oxide films by IBAS

The scope of this chapter is to discuss the experimental conditions under which zinc oxide thin films can be fabricated that exhibit superior structural quality. In chapter 2 it has been discussed that a variety of parameters correlated with the sputtering conditions and the ion bombardment significantly influence the structure of the films. It has been evident that highly energetic oxygen ion bombardment deteriorates film structure but it has also been proposed that low energy ions could promote structure formation. To explore this, a preliminary determination of a suitable parameter set is a prerequisite for the fabrication and investigation of films with improved structural order. This task has already been in the focus of a previous thesis [40]. Especially, the influence of different ion species, oxygen and argon, has been studied for different ion energies and current densities in the IBAS process as described. The main results can be summarized as follows:

1. No structural improvements were observed upon bombardment of growing films with oxygen ions (O^+). At low ion energies down to 80 eV and relative ion to molecule arrival ratios of $\approx 1.5\%$ no structural modifications were induced. Bombardment with medium energies ($\gtrsim 130$ eV) leads to a deterioration of the films very similar to the deterioration seen in reactive sputtering processes under conditions that promote increased O^- ion bombardment. This deterioration intensifies with increasing ion energy and relative arrival ratio. At large energies and/or current densities, the onset of amorphisation ($E_{\text{Ion}} \gtrsim 300$ eV and relative arrival ratio of approximately 8 %) and preferential re-sputtering of oxygen ($E_{\text{Ion}} \gtrsim 600$ eV) was observed. Preferential sputtering of oxygen atoms by oxygen ions might be explained by the differences in the energy transfer from the impinging ions to zinc or oxygen atoms in the film structure, respectively. It can be calculated that in a binary elastic collision the relative fraction of transferred energy is given by

$$\Delta E_{\text{rel.}} = \frac{4 \cdot m \cdot m_{\text{ion}}}{(m + m_{\text{ion}})^2}, \quad (5.0.1)$$

where m is the mass of the atom that the ion is colliding with. For oxygen ions, the ratio of the energy transfer to an oxygen or a zinc atom,

respectively, can be calculated to

$$\Delta E_{O/Zn} = \frac{\Delta E_{\text{rel.}}(O \rightarrow O)}{\Delta E_{\text{rel.}}(O \rightarrow Zn)} = \frac{m_{Zn}^2 + m_O^2 + 2m_{Zn}m_O}{4m_{Zn}m_O}. \quad (5.0.2)$$

Inserting the masses of oxygen and zinc (16 and 65 atomic mass units), this yields that the energy transferred to an oxygen atom is approximately 158 % of the energy transferred to a zinc atom. Both energies, however, are significantly larger than the binding energy of zinc oxide ($\Delta H_f = 3.61$ eV), as can be easily calculated for the typical oxygen ion energies discussed above.

2. Upon utilization of argon species (Ar^+) a narrow parameter window at low relative arrival ratios ($\approx 0.7\%$) and ion energies, ranging from approximately 150 eV to 210 eV, was found which promoted noticeable structural improvements of the bombarded ZnO films. Higher energies and/or arrival ratios caused deterioration, similar to the observations made for oxygen ions.
3. Aside crystallographic modifications, ion bombardment always manifested itself in an increased compressive film stress as deduced from x-ray diffraction patterns.

During further discussion of these results it was proposed that, as far as the influence on structure formation is concerned, the significant difference between oxygen and argon ion species originates from their different atomic masses. It was concluded that heavy ions that impinge with low kinetic energy can support sufficient transfer of momentum into the growing film without causing damage¹. Consistently, the investigation of the influence of xenon ions was the starting point of the present work. Even under conditions that had not yet been optimized for the use of xenon, first depositions already yielded zinc oxide films with significantly improved structure as compared to the un-bombarded reference films but also to the films improved by argon ion bombardment. This result was expected and therefore greatly supported the proposition regarding the importance of the ion mass. Upon parameter optimization of the ion bombardment, the excellent structural order displayed by the films that will be discussed in this chapter was achieved. Since the understanding of the underlying mechanisms that govern such a structural improvement are of foremost scientific interest, the following preliminary discussion of parameter optimization will be very concise and therefore contains only an example reflecting some of the efforts taken to

¹This assumption has been postulated without proof in [40]. However, it will be further motivated in this work in section 5.3, where ion momenta and the collisions with the film surface of light and heavy ions will be discussed.

tweak the IBAS process conditions and hence film properties.

Regarding the deposition conditions, i.e. the atmosphere and discharge properties, the same parameters as in [40] have been utilized which have also been summarized in chapter 3. It has already been explained why the available parameters for the xenon ion generation and bombardment are constricted for technical reasons. It is therefore impossible to investigate the influence of pronounced changes in the angle of incidence or the relative arrival ratio between bombarding ions and zinc oxide molecules at the substrate. To circumvent that shortcoming the substrates have been tilted by applying only minor modifications to the substrate stage for this special experiment. Besides the obvious change in the angle of incidence a substrate tilt also affects the relative arrival ratio since the ion current density per unit substrate area changes with the angle of incidence. This experiment combines several advantages in comparison e.g. to changes in the sputtering discharge power:

- Changing the deposition rate of zinc oxide would alter the relative arrival ratio if the ion source parameters were kept fixed at the same time. However, for several reasons this method would produce complications since it is typically impossible to find parameters that would yield perfectly identical film properties simply at different growth rates. Hence, changing discharge power would clearly limit the comparability of films deposited at different rates.
- Due to geometrical limitations of the IBAS deposition system, the inclination between the ion source and the substrate stage is fixed to $\approx 45^\circ$. It is therefore not possible to investigate whether this angle plays an important role in structure modification in an IBAS process. By varying the substrate tilt, this relative angle can be conveniently changed.

Figure 5.1 shows results from an experiment where the substrates have been tilted. The graph shows the dominant (0002) Bragg peak in the XRD patterns of films deposited on differently tilted substrates under simultaneous xenon ion bombardment. The inset shows a schematic sketch of the geometrical conditions and the legend contains information on the tilt of the substrate with respect to the standard position and the corresponding angle of incidence of the ion beam to the growing film with respect to the substrate plane. The pivotal axis was chosen to be the left or right edge of the substrate for negative or positive inclinations, respectively. Therefore, the set $(+\alpha, -\alpha)$ represents fully symmetric conditions except the angle of incidence of the ion beam. It should be noted that the ion current per unit area scales proportional to $\sin \beta$ which means that the modulus change in relative ion arrival ratio is an asymmetric function of the substrate tilt. In figure 5.1 two clear trends are visible. First, the intensities of

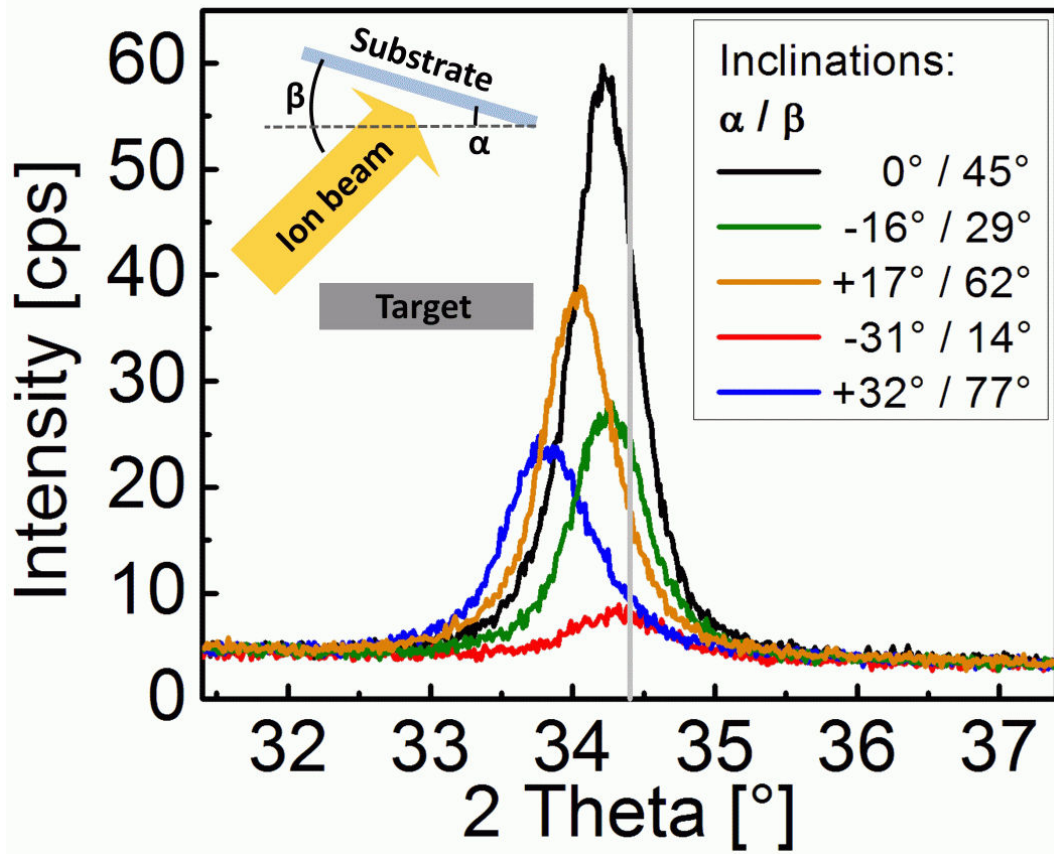


Figure 5.1: XRD-Scans showing the (0002) Bragg peak of IBAS films deposited and bombarded under different angles of incidence. By tilting the substrate, the angle of incidence and the ion current density at the substrate is changed simultaneously. The angles α and β indicate the substrate tilt and the relative ion beam direction as sketched in the inset (see text for details on pivotal axes of the substrate tilt). Shifts of the peak towards smaller diffraction angles correspond to an increasing ion current density as a function of β . Although with the substrate tilt there is a decrease in deposition rate (see text), from the peak intensity it is argued that the standard configuration ($\alpha = 0^\circ$) is close to an optimum condition.

5.1. GROWTH CONDITIONS

the (0002) Bragg peak significantly change with substrate tilt. At zero tilt the intensity is maximal. A tilt to each direction reduces the peak intensity, which means that both an increase (positive tilt angle) and a decrease (negative tilt angle) in the ion current density yields less perfect film structures. For negative tilt angles this change is more pronounced since the ion current density rapidly approaches zero at glancing angles. Second, the peak position shows a shift with tilt angle and therefore with bombardment intensity. With increasing ion current densities (from negative to positive tilt angles) there is a concomitant shift of the peak position to lower angles. This is a direct consequence of the ion bombardment and is linked with the formation of compressive stresses in the film, as will be discussed in detail in a later section. It should be mentioned here that increasing tilt angles also result in a different particle flux from the target and hence the deposition rate decreases. However, in contrast to the ion current density, the flux density from the target approximately obeys a $\cos \alpha$ rule and is therefore symmetric. Differences in the peak intensities for substrate tilts with a similar modulus can therefore directly be attributed to the difference in ion current density and angle of incidence β . According trends are clearly visible e.g. for the two sets of symmetric tilts, $(-16^\circ, +17^\circ)$ and $(-31^\circ, +32^\circ)$. Since even at small tilt angles α there is a decrease in the intensity of the 002 peak, i.e. both for decreasing and increasing relative ion arrival ratio, it is concluded that the ion bombardment parameters used are near optimum for the standard zero substrate tilt. This test has therefore backed the decision to utilize these deposition parameters (see chapter 3) for all zinc oxide films fabricated in the IBAS process and discussed in the remainder of this work.

5.1 Growth conditions

To study the impact of Xe^+ ion bombardment, films have been deposited with and without additional ion bombardment, respectively, under the conditions described in chapter 3. Bombardment was always employed at the beginning of each deposition (except for the reference films), but was terminated after different lengths of time. The duration of the ion bombardment was varied to determine the effect of ion bombardment in different growth stages. In the following, the notation “IBAS A 1/4” identifies a bombarded film from series A, where bombardment was applied only during the first quarter of growth. The notation “REF A” describes the reference sample that has been grown under identical conditions but without additional bombardment. Table 5.1 gives an overview of samples and corresponding measurements discussed in this chapter.

CHAPTER 5. I: GROWTH OF ZINC OXIDE FILMS BY IBAS

Sample	Thickness [nm]	Ion bombardment	Measurement
REF A	82	none	XRD, TEM
IBAS A 1/4	81	stopped after 20 nm	XRD, TEM
IBAS A 2/4	81	stopped after 40 nm	XRD
IBAS A 3/4	79	stopped after 60 nm	XRD
IBAS A 4/4	80	yes	XRD
REF B	119	none	AFM
IBAS B 1/2	127	stopped after 63 nm	AFM
REF C	2.2	none	AFM
IBAS C 1/1	2.5	yes	AFM
IBAS D 1/1	4.6	yes	XRD
REF E 600	15.9*	none	XRR
IBAS E 1/1 120	19*	yes	XRR
IBAS E 1/1 300	18.7*	yes	XRR
IBAS E 1/1 600	19*	yes	XRR
IBAS E 1/1 1200	18.4*	yes	XRR

Table 5.1: List of samples and corresponding measurements explicitly discussed in this chapter. (* Samples are also shown in an etched state where the thickness is smaller than the values given in the table.)

5.2 Optimization of film structure

The scope of this section is the comprehensive survey of experimental data that shows the effects of xenon ion bombardment on structure formation in the IBAS process². However, evaluation of the data will be restricted to a phenomenological level here. A full discussion including the determination of the underlying mechanism and the development of a growth model will follow in the subsequent sections (5.3 & 5.4).

5.2.1 X-ray diffraction

Figure 5.2 shows diffraction data for ZnO films from series A. On the left hand side, $\theta - 2\theta$ -scans in Bragg-Brentano geometry are shown for five samples differing in the duration of the ion bombardment at the beginning of film deposition. It is apparent that all films grown under initial bombardment have a strongly improved crystalline quality, as the intensity of the (0002) Bragg peak is significantly increased. Rocking curve scans displayed on the right hand side clearly show that this is due to an improved orientational order of the crystallite c-axis along the substrate normal. The widths of these peaks directly render the

²The experimental data and conclusions discussed in this chapter have been published in [123] and [124].

5.2. OPTIMIZATION OF FILM STRUCTURE

quality of the out-of-plane texture of the films. For the bombarded films, the corresponding FWHM is comparable with films deposited on glass at elevated substrate temperatures (cf e.g. [100]). Another striking fact displayed in figure 5.2 is that apparently bombardment only during the initial growth stage is already sufficient to produce high quality films. Starting from sample IBAS A 1/4, a further prolongation of the bombardment only leads to an angular shift of the (0002) peak ($\theta - 2\theta$), resulting in a pronounced double peak structure in the intermediate stages (2/4 & 3/4 of total film grown under bombardment). This shift in the position of the XRD peak is indicative for differences in the film stress.

5.2.2 Mechanical growth stresses

To further elucidate the origin of the shift of the XRD peaks and to relate it to the bombardment during film growth, the biaxial mechanical stress of the films has been investigated by means of the in-situ wafer curvature measurement technique [125] described in section 4.4. Figure 5.3 shows the film stress and the instantaneous stress that have both been calculated from the film force and the deposition rate, which was determined after deposition by XRR.

As discussed in section 4.4 the film stress σ is defined as

$$\sigma = \frac{\text{Film force per unit length } [Pa \times m]}{\text{Film Thickness } [m]}, \quad (5.2.3)$$

while the instantaneous stress σ_i is defined by

$$\sigma_i = \frac{d(\text{Film force per unit length}) [Pa \times m]}{d(\text{Film Thickness}) [m]}. \quad (5.2.4)$$

This means that σ represents an average at each stage of film growth whereas σ_i may be interpreted e.g. as the differential change of stress induced by each new deposited layer. Thus, sudden changes in the stress generating mechanisms should occur as a step in the latter quantity. Figure 5.3 shows a reference ZnO sample (no bombardment) in comparison with an IBAS sample that has been bombarded only during the initial half of the growth. From the upper graph it is evident that, while the ion bombardment interacts with the growing film, additional compressive forces act on the film structure as compared to the reference film. When the bombardment is terminated, a very distinct change in the stress generating mechanisms clearly manifests itself in the instantaneous stress (lower graph). The IBAS sample shows an abrupt change from compressive to tensile forces acting on the structure. It is noteworthy that the strength of the tensile contribution seems to significantly exceed the corresponding forces in the reference sample. XRD scans of samples that were deposited under exactly identical conditions in the same session are shown in figure 5.4. Similar to the films shown in figure 5.2 the partially bombarded sample exhibits a pronounced double peak

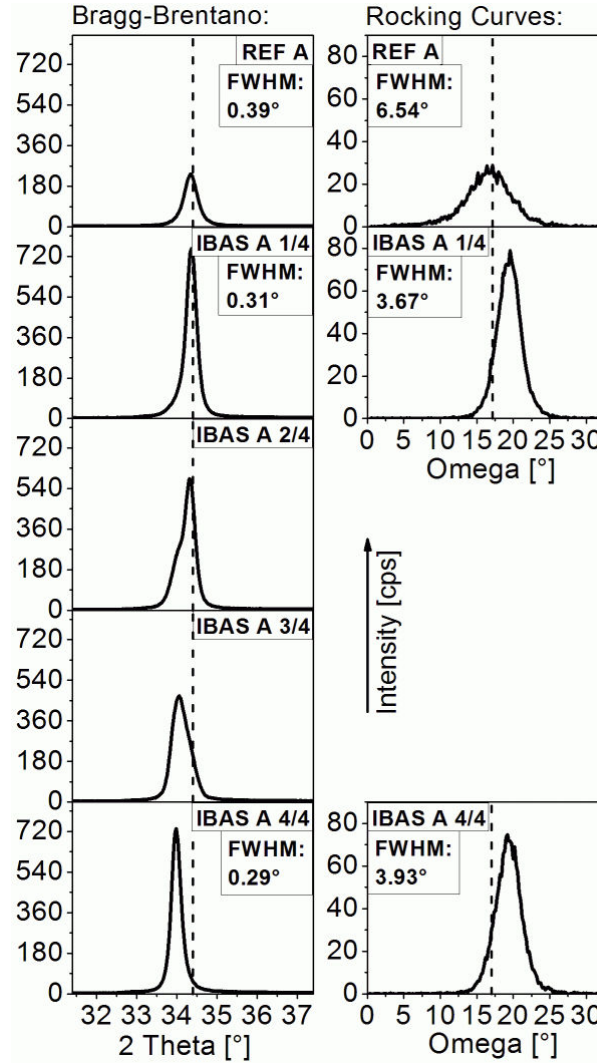


Figure 5.2: Left: XRD scans in $\theta - 2\theta$ geometry. Right: Corresponding rocking curve measurements. The two graphs at the top show an un-bombarded reference sample, which is characterized by a weak intensity of the wurtzite (0002) peak and a broad distribution of crystallite orientations as evident from the rocking curve. Despite identical film thicknesses, all films grown with initial auxiliary ion bombardment show strongly increased peak intensities. This fact is most pronounced for films grown under short (1/4) or long (4/4) duration of the bombardment. The structural enhancement is also evident from the corresponding rocking curves that give evidence for a strongly improved orientational order. The dashed line represents the 2θ literature value of 34.4° for the $\theta - 2\theta$ scans. For the Rocking Curves it represents the position of θ .

5.2. OPTIMIZATION OF FILM STRUCTURE

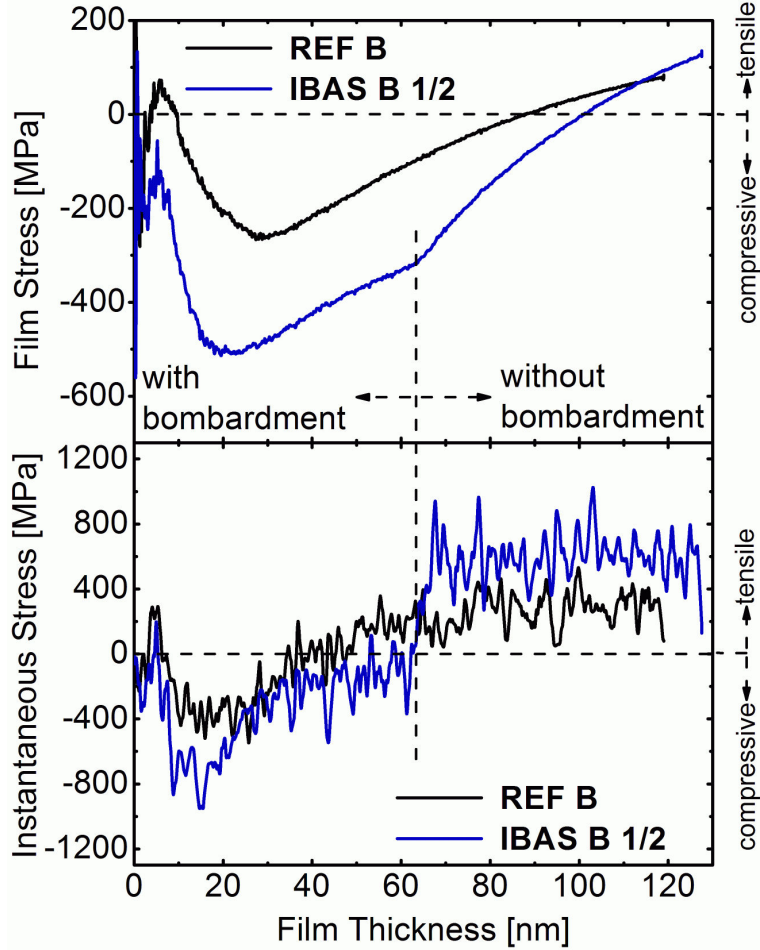


Figure 5.3: Upper graph: In-situ measurement of the biaxial mechanical stress for a reference sample (no Xe^+ -ion bombardment) and an IBAS sample that has been bombarded during the first half of the growth time. It is evident that the ion bombardment causes an additional amount of compressive stress. **Lower graph:** The instantaneous stress represents the differential change in film stress and is therefore sensitive to abrupt changes in the stress generating mechanisms. The interaction of the ion beam with the growing film is apparent in this graph, where a sudden change in the stress generating mechanisms manifests itself in a jump from compressive to tensile forces when the auxiliary ion bombardment is terminated.

feature, representing a relaxed and a strained phase. This will be explained and correlated with the biaxial film stress later in this section.

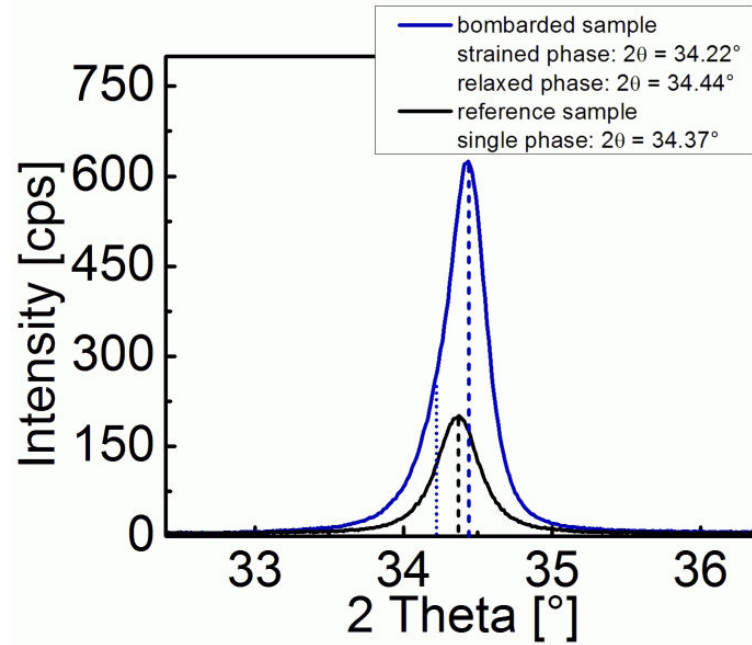


Figure 5.4: XRD-Scans of the films deposited during the in-situ stress measurements shown in figure 5.3. The reference film consists of a single phase whereas the bombed (IBAS) sample exhibits a relaxed and a strained phase as determined by a double peak fit. The corresponding positions (2θ) are marked by vertical lines.

5.2.3 Surface topography

The evolution of structural differences as a result of the ion bombardment is also evident from the surface topography. To describe the data, in this section the term “grain” will be used to refer to the surface features observed by atomic force microscopy. Admittedly, these features in the AFM images do not necessarily represent crystal grains. However, later in this section experimental evidence will be presented which suggests that the observed surface features might indeed represent crystalline grains. Since the results shown in figure 5.2 indicate that the ion bombardment has a major influence already in the early growth stage, extremely thin films have been produced for this investigation. The film thicknesses of these samples have been deduced from XRR data (figure 5.5 and 5.6), which allows determining the average film thickness with Ångstrom precision. Figure 5.7 shows the topography of the only 2.2 nm thin reference sample and the 2.5 nm thin IBAS sample.

For imaging and evaluation of the topography data obtained by AFM, the

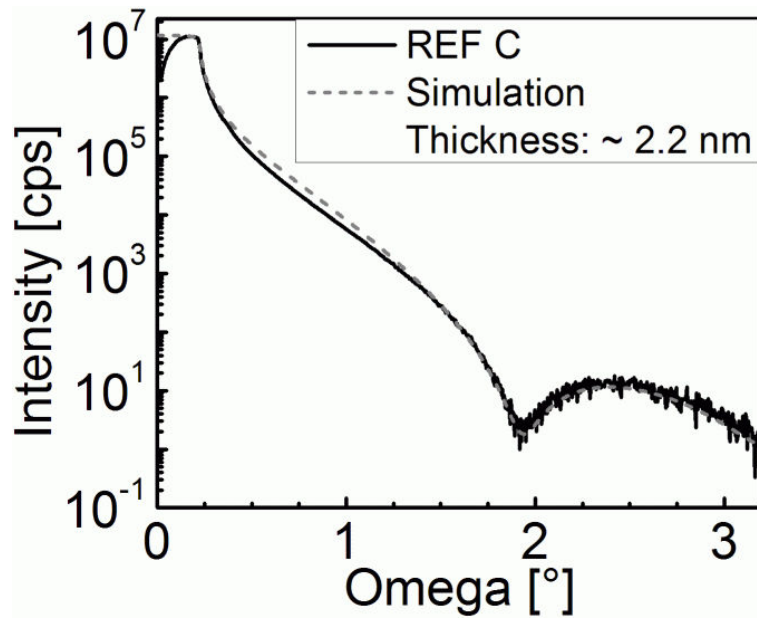


Figure 5.5: XRR-Scan of an ultra-thin reference ZnO sample (REF C).

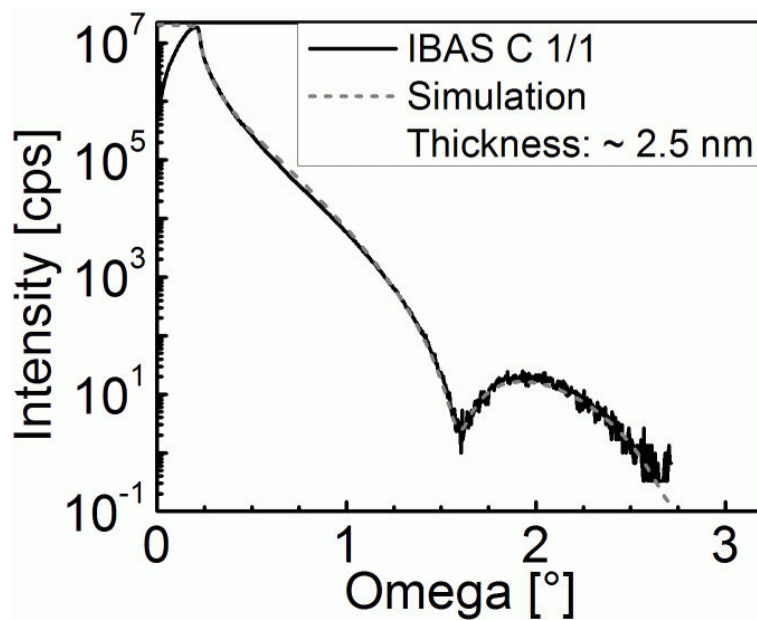


Figure 5.6: XRR-Scan of an ultra-thin IBAS ZnO sample (IBAS C 1/1).

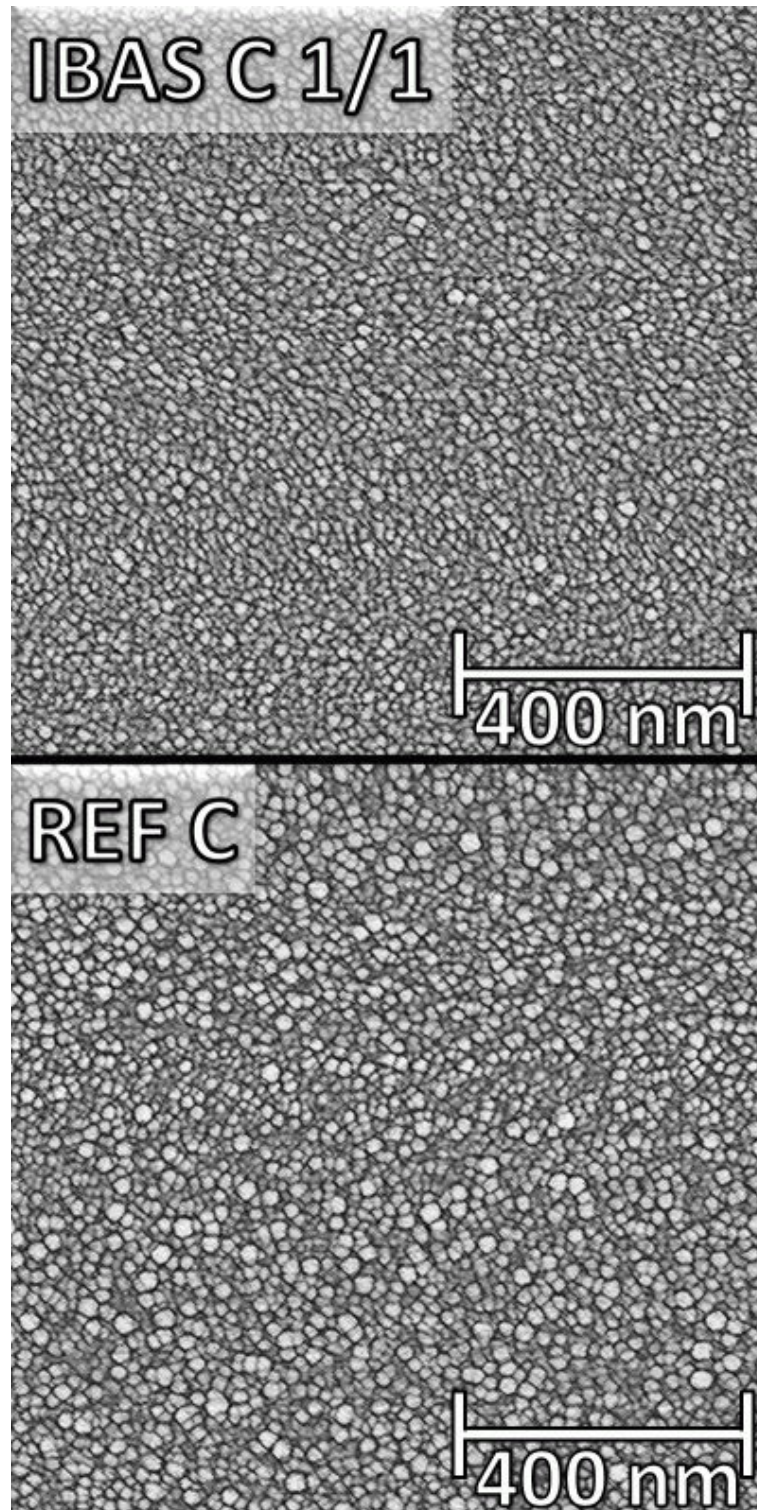


Figure 5.7: Surface structure of a 2.2 nm thick standard ZnO sample and a 2.5 nm thick IBAS sample. Images have been post-processed (for this figure only) to highlight the surface corrugation.

5.2. OPTIMIZATION OF FILM STRUCTURE

Gwyddion³ software has been utilized. The images shown in figure 5.7 have been post-processed with a convolution filter to enhance the contrast of the surface corrugation (cf [124] for the original images). The 5×5 convolution matrix utilized is defined as follows:

$$\begin{pmatrix} 0.015 & -0.01 & 0.25 & -0.01 & 0.015 \\ 0.001 & -0.25 & 0.25 & -0.25 & 0.001 \\ 0.25 & 0.25 & -1.1 & 0.25 & 0.25 \\ 0.001 & -0.25 & 0.25 & -0.25 & 0.001 \\ 0.015 & -0.01 & 0.25 & -0.01 & 0.015 \end{pmatrix} \quad (5.2.5)$$

It must be emphasized that all statistical evaluations that will be shown have been applied to the original topography data to avoid an impact of the post-processing on the analysis. From figure 5.7 it is evident that there is a striking difference in surface structure, i.e. the IBAS sample shows a more homogenous grain size distribution. This is supported by the RMS roughness that has been calculated to be 0.88 nm and 0.44 nm for the reference and the IBAS sample respectively. Differences in topography are clearly visible from image 5.8, where a line profile is shown for both films. It is apparent that the surface of the reference sample is governed by a large variation of grain heights and widths whereas the IBAS sample in contrast shows grains with rather equal dimensions. This interpretation is supported by the surface height distributions shown in figure 5.9. The graphs have been normalized to ensure that the area under each graph is unity. The centre of mass of each distribution has been adjusted to agree with the thickness determined by XRR. These distributions can be interpreted in the following way: The FWHM is a measure for the roughness R of the surface and corresponds to the average deviation from the mean height ($\text{FWHM} = 2R$). The shape directly reflects the nature of the topography. The large right hand side tail for the reference sample is due to some grains which are significantly larger and hence higher than the average (cf figure 5.8).

To investigate how the film topography changes with thickness, thicker films were studied as well. For this purpose, the approximately 120 nm thick films sputtered for the mechanical stress analysis have also been selected for AFM measurements. Analogous to figure 5.7, post-processed images are shown in figure 5.10.

The structural differences that have already been present for the thin films are even more pronounced for the thick films. There is a marked difference in the lateral structure size and distribution. The line profile shown in figure 5.11 again displays a large variation in grain heights for the reference sample in striking contrast to the IBAS film. Large differences in lateral sizes are also clearly visible only for the reference, but not for the IBAS sample. The surface height

³Freely available from: <http://gwyddion.net/>

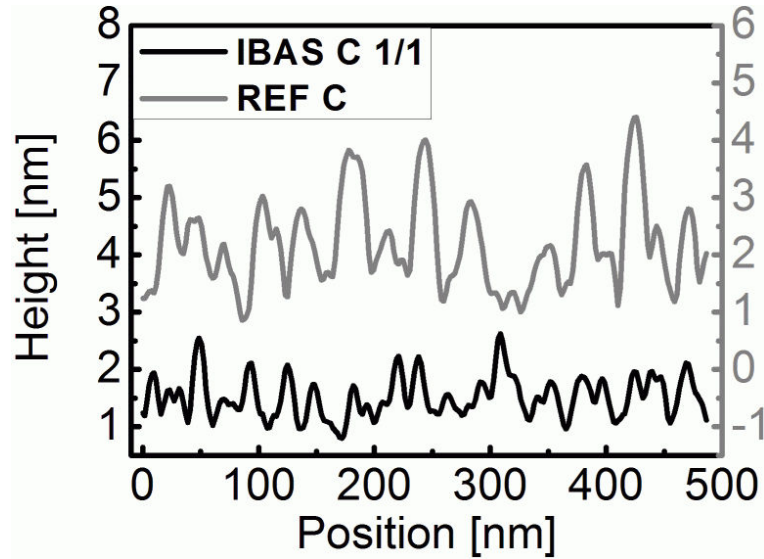


Figure 5.8: Cross-sectional height profile of the surfaces shown in figure 5.7. The IBAS sample shows a smaller distribution of grain heights than the reference.

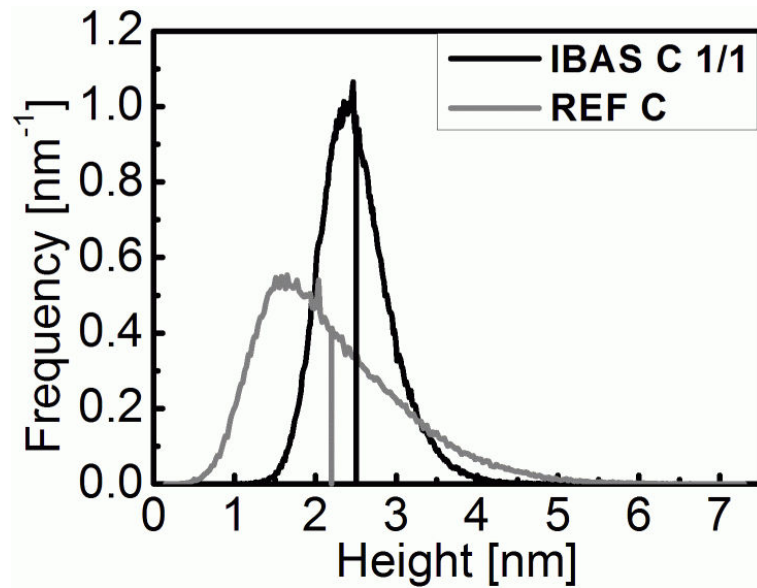


Figure 5.9: Height distribution of the thin films shown in figure 5.7. The centre of each distribution (vertical lines) is adjusted to represent the average film thickness determined by XRR.

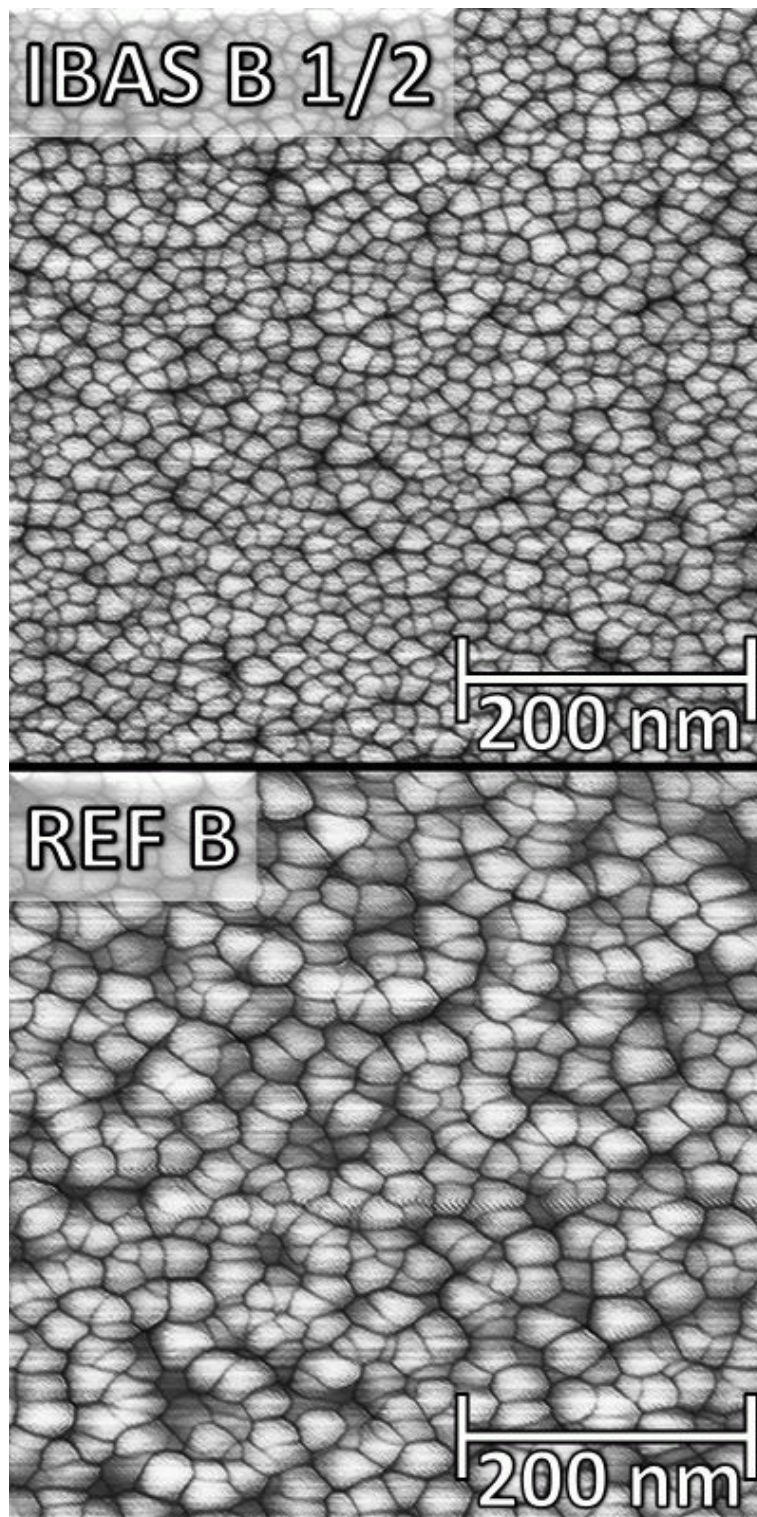


Figure 5.10: Surface structure of a 127 nm thick IBAS sample and a 119 nm thick standard ZnO sample (reference). The IBAS sample shows a smoother surface and a narrower distribution of grains sizes. The images have been post-processed (for this figure only) to highlight structural features.

CHAPTER 5. I: GROWTH OF ZINC OXIDE FILMS BY IBAS

distribution presented in figure 5.12 clearly highlights the topographical homogeneity that is found for the IBAS sample, whereas the reference film exhibits a rather broad distribution as observed already for the thin reference sample. For the thick films, the width of the distributions corresponds to an RMS roughness of 3.9 nm for the reference and only 1.37 nm for the IBAS sample.

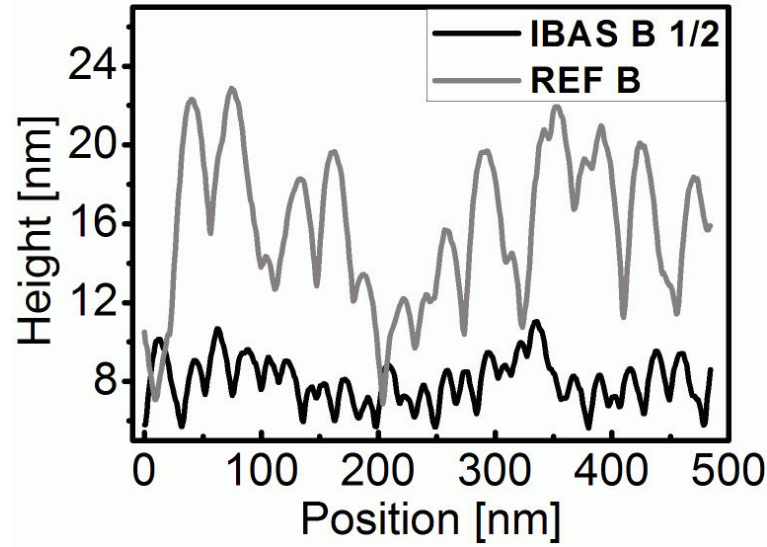


Figure 5.11: Cross-sectional height profile of the surfaces shown in figure 5.10. In contrast to the IBAS sample, the reference shows a larger lateral structure size and a stronger variation in the heights of individual grains.

As the structure size for the thick films has increased, it was also possible to successfully apply a watershed algorithm on the topography data in order to detect and analyze the grains. Hence, figure 5.13 shows a statistical analysis of the grains in terms of their equivalent lateral disc diameter. The absolute number of grains with different diameters has been plotted. The smooth lines are a guide to the eyes, while the original curves show some noise. It is evident that the IBAS sample on average exhibits much smaller grain diameters (approx. 15 nm) than the reference (approx. 24 nm) and that there is also a smaller distribution of different grain sizes for the IBAS film compared with the reference. From a comparison of the surface structure of sample series B and C it is evident that for the reference film a major change in the structure scale occurs upon increasing film thickness. On the other hand, the respective change for the IBAS film is far less pronounced. Apparently, ion bombardment establishes a growth behaviour where the lateral scale of the surface structure exhibits almost no change upon increasing film thickness.

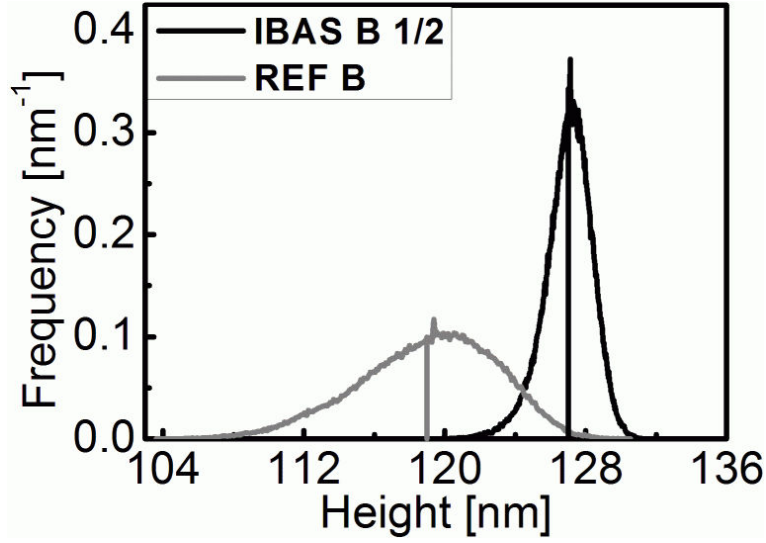


Figure 5.12: Height distribution of the surfaces shown in figure 5.10. As for the thin films (figure 5.9), the centre line of the distributions corresponds to the XRR thickness. The distribution of the IBAS sample is very narrow compared to the standard ZnO sample.

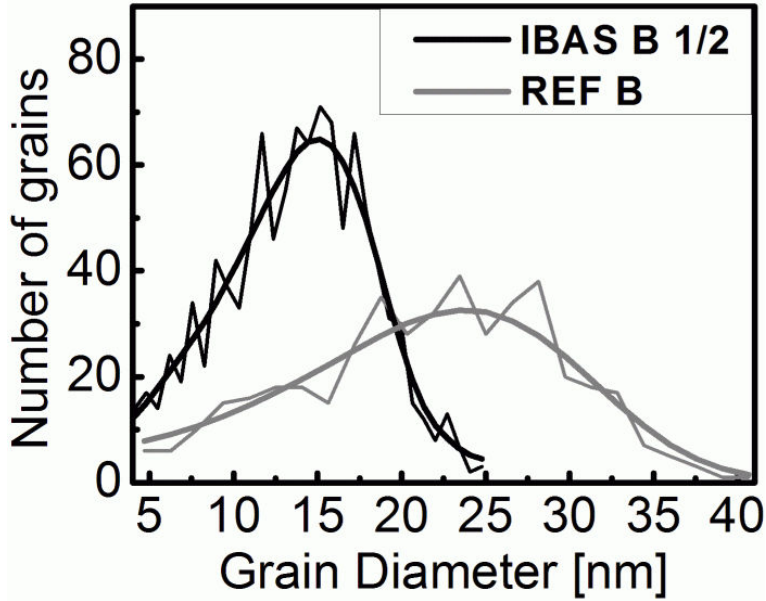


Figure 5.13: The surfaces of the films discussed in figures 5.10-5.12 have been analyzed with a watershed algorithm to detect grains and to measure their size. The graph shows the distribution of the equivalent disc diameter of the grains. The IBAS sample shows a lower mean grain diameter (lateral structure size) and a narrower distribution.

5.2.4 Microstructure

To further unravel the changes in film growth and the influence of the ion bombardment, TEM measurements have been performed on samples REF A and IBAS A 1/4. Figure 5.14 displays dark field images and SAD patterns of these two samples grown without (figs. a, b) and with Xe^+ bombardment during growth (figs. c, d). In both cases a columnar growth is observed, where columns extend throughout the whole layer. In figure 5.14a one crystalline column with a conical shape is seen, which grows from a seed of a width of about 10 nm. At the top of the layer the column reaches a width of about 20 nm. In the lower part of the column a Moiré fringe contrast appears, which is caused by the overlap of two slightly misaligned crystalline grains. In the upper part irregular lines appear which are typical for planar faults on the $\{0002\}$ planes such as stacking faults. In addition to the column, a crystalline grain shows weak contrast at the left hand side of the figure. Obviously, it does not extend in columnar fashion. The corresponding SAD pattern (figure 5.14b) reveals that the (0002) reflections of individual ZnO grains (marked by arrows) extend along an arc of about $\pm 10^\circ$ with respect to the growth direction, which is indicative of a textured growth. (Reflections arising from the Si substrate are marked by circles). For the bombarded sample a similar microstructure is observed, i.e. a columnar growth. In contrast to the non-bombarded sample, for most cases investigated, the diameters of the nuclei are observed to be constant throughout the whole layer with a width of about 15 nm, which confirms the findings from atomic force microscopy (figure 5.13). This is demonstrated in figure 5.14c, where two columns with identical in-plane orientations are shown which have a total width of 25-30 nm. Again some few contrast lines appear parallel to the substrate, which are indicative of planar faults. In addition, a fringe contrast with a spacing of $5.4 \pm 0.2 \text{ \AA}$ is observed, which agrees with the distance of the (0001) planes. The SAD pattern (figure 5.14d) reveals that the texture is well defined, i.e. the (0002) reflections show only a small deviation of $\pm 5^\circ$ with respect to the growth direction. The statement that figure 5.14 shows indeed two neighbouring columns with identical orientation is supported by supplementary TEM images shown in figure 5.15. First, images 5.15a and 5.15b show that typical grains have diameters of clearly less than 20 nm. Second, image 5.15c shows a double column feature similar to that shown in figure 5.14, but where the single columns are more clearly distinguishable.

In plan-view, the diffraction patterns corresponding to the bright field images reveal a striking difference (see figs. 5.16 a, c). The reference sample is characterized by crystallites of almost random distribution around the texture axis, i.e. (0001). This can be deduced from the ring shaped SAD pattern, which reveals closed rings of individual reflections that are perpendicular to the (0001) axis. Only few (0002) reflections are detected, which correspond to crystallites not obeying the textured growth. In contrast, the SAD pattern of the IBAS sample

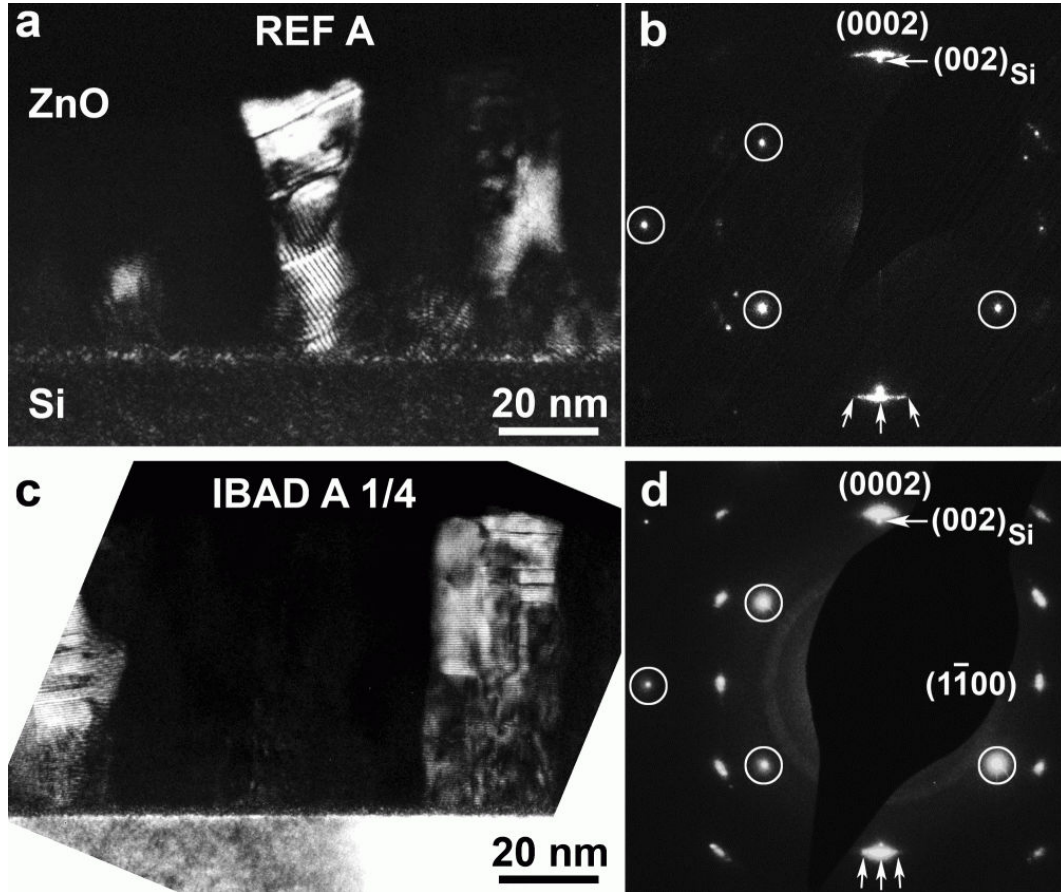


Figure 5.14: TEM images of a standard ZnO sample (a,b) and an IBAS sample (c,d) respectively. The images on the left (a,c) show dark field images where columnar grains are visible. The corresponding SAD patterns are shown on the right (b,d). Circles mark reflections from the Si substrate. Some of the Si reflections almost coincide with a (0002) ZnO reflection and are therefore marked with a single arrow at the top of the images. The arrows in the lower half of figures (b,d) point to the (0002) reflections of ZnO. The fact that these reflections appear as an arc segment allows to draw important conclusions on the orientational order of the film. Similarly to the width of an XRD (0002) rocking curve the width of an arc segment is directly correlated with the orientational distribution of the crystallographic c-axis of the crystallites around the substrate normal. The smaller arc width in case of the IBAS sample is therefore evidence for the improved orientational order.

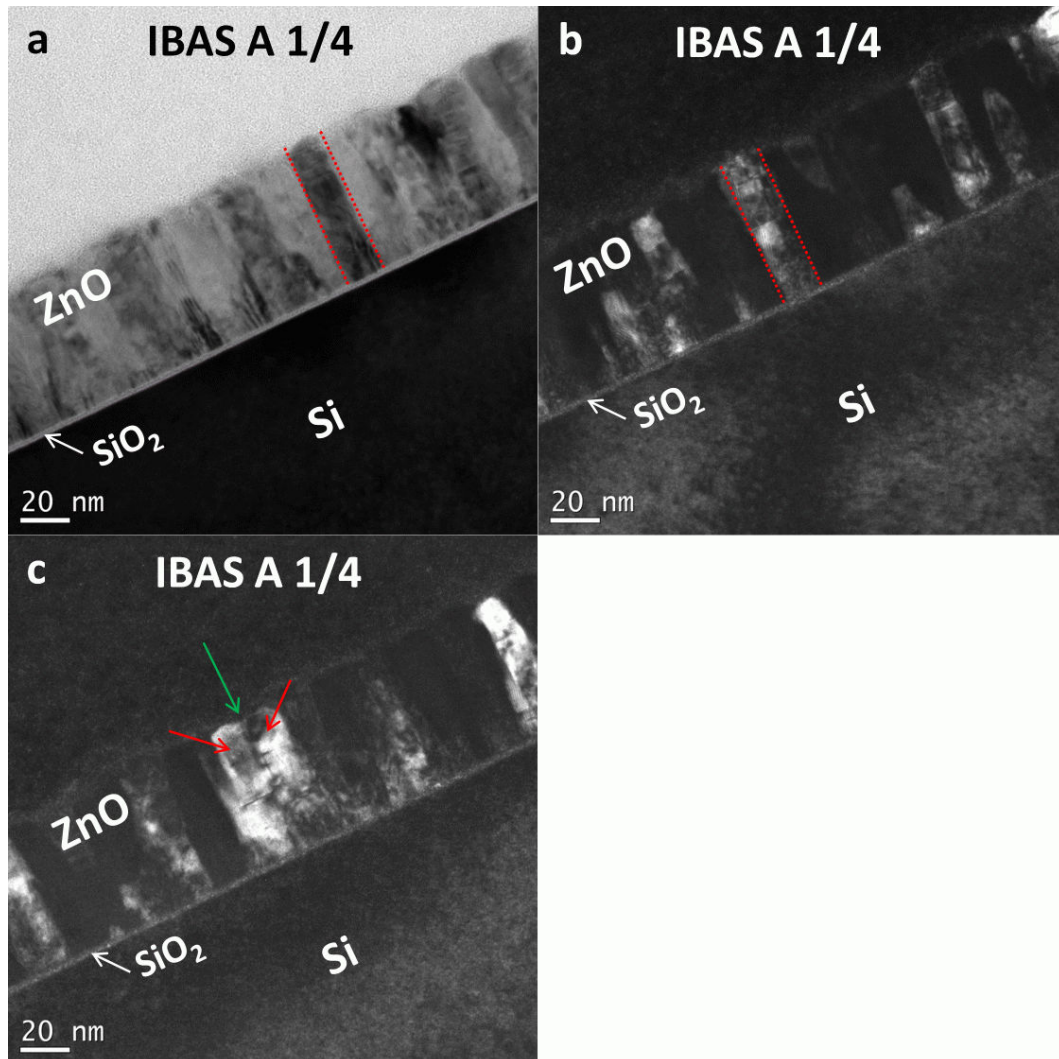


Figure 5.15: Additional bright field (a) and dark field (b,c) images of sample IBAS A 1/4. Some single grains are marked by lines (a,b). It is evident that the diameter of the grains is < 20 nm. Figure (c) shows a situation where two neighbouring grains with identical in-plane orientation appear as a single wide column.

5.2. OPTIMIZATION OF FILM STRUCTURE

is dominated by an arc-like intensity distribution along the rings. This implies an almost identical crystallographic orientation of a majority of crystalline grains seen in figure 5.16c. However, this orientation relationship between neighbouring grains does not extend throughout the whole sample, since the arc within the SAD pattern is found to “rotate”, if a different area of the sample is selected. I.a.w. adjacent crystallites show almost the same crystallographic orientation. On larger scales, i.e. >500 nm, the orientation of the grains is found to vary.

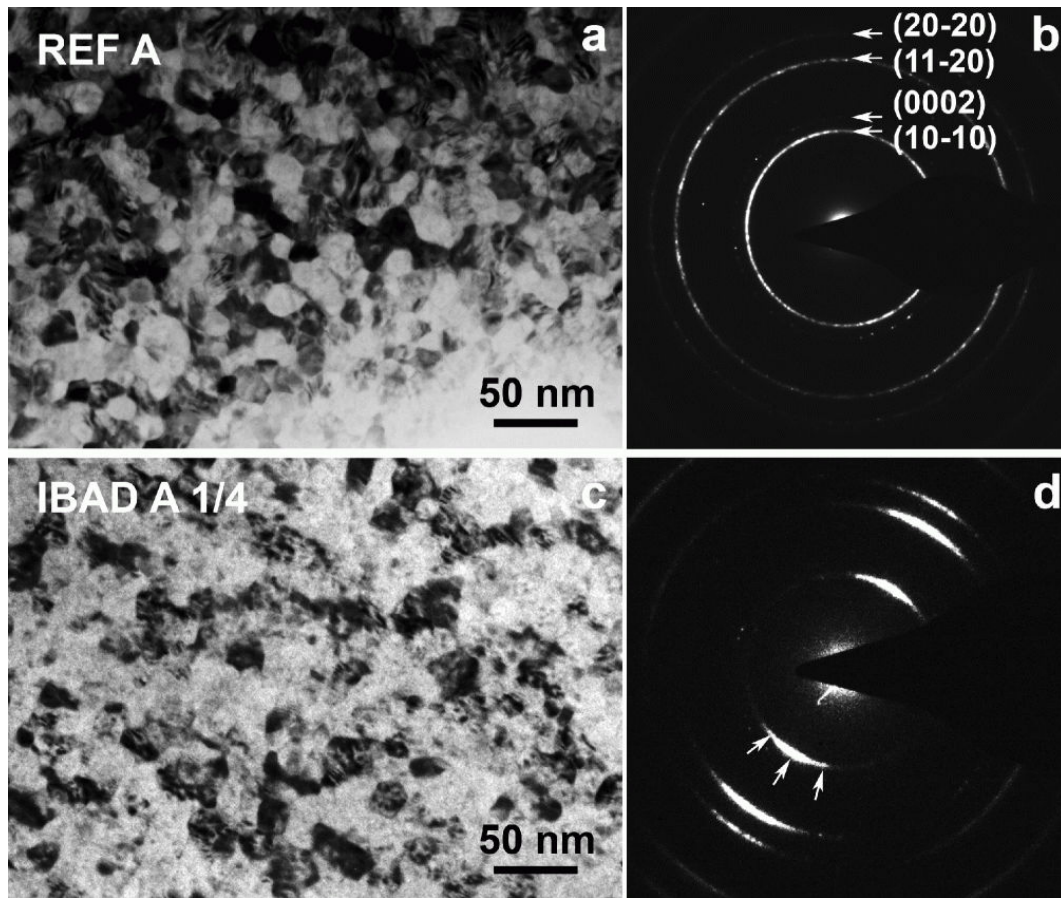


Figure 5.16: Plan-view images of samples REF A and IBAS A 1/4. The bright field images (a,c) show almost identical grain sizes at the surface. The crystallites of sample REF A are randomly distributed around the texture axis, evident from the ring pattern (b). The IBAS sample reveals some degree of in-plane texture, evident from the intensity distribution along an arc in the ring pattern (d). However, there is no long range order, as the arc segment “rotates” when a different area of the sample is scanned.

5.3 Discussion and evaluation

Summarizing the experimental results, ZnO films grown by Xe^+ ion beam assisted sputtering exhibit considerably improved structural properties compared to conventionally sputtered films under otherwise similar conditions. This advancement is evident from smaller surface corrugations, homogeneous feature sizes on the surface, in particular for thicker films, as well as in an almost identical crystallographic orientation of adjacent crystallites, and a well defined c_\perp -textured growth, where the c-axis is aligned in growth direction. It should be emphasized that an ion bombardment only during the initial stage of film growth results in the formation of a drastically improved structure and that there is no further improvement for longer durations of ion bombardment. This implies that IBAS induces important structural changes essentially in the nucleation regime. The structural evolution of the following growth stages is solely governed by the improved structure of the nucleation layer as can be seen e.g. from figure 5.2.

In order to understand, in which way IBAS affects the nucleation, the stress within the ZnO films is inspected closer. Figure 5.2 reveals that there is a noticeable shift of the (0002) peak towards lower angles as the duration of the bombardment increases. This is caused by an increased distance of the (0002) planes, which is a typical effect of compressive stress in sputtered ZnO thin films. The pronounced double peak for intermediate ion bombardment durations is indicative for the co-existence of two phases with different lattice spacing. We can immediately understand this feature from the stress behaviour shown in figure 5.3. There is a significant change in the evolution of instantaneous stress at the time when the auxiliary ion bombardment is stopped. While the ion bombardment is active, the film shows an increased compressive stress as compared to the reference. This is attributed to the implantation of atoms into e.g. interstitial places, resulting in an increased average inter-atomic spacing. Figure 5.17 displays the ion bombardment induced lattice expansion schematically. The increased lattice spacing leads to the peak shift in the XRD diffraction pattern as a consequence. Upon termination of ion bombardment there is no further implantation and hence the equilibrium inter-atomic distance is lower. However, now the subsequent layers grow on a textured film with larger inter-atomic spacing (see figure 5.17). This results in a tensile biaxial film force as detected in the stress measurement. Without implanted interstitials the planar distance in direction of the c-axis is smaller. Hence, the XRD (0002) Bragg peak occurs close to the literature value of about 34.4° [118]. We can now interpret the double peak feature as contributions from the bottom and top part of the film, where bombardment was active and inactive, respectively.

Since a pronounced structural modification takes already place in the early growth stage, a corresponding change in morphology can be expected for very thin films. This is confirmed by the AFM images (figure 5.7) of nominally 2.2 nm

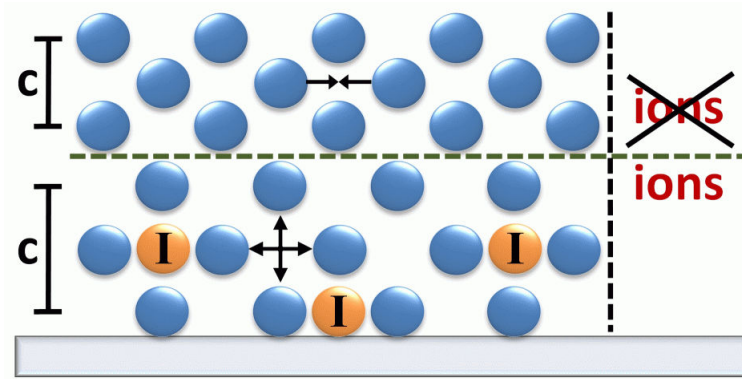


Figure 5.17: Ion bombardment leads e.g. to interstitials (atoms marked with an “I”) that expand the lattice by exerting forces in all directions in space. If bombardment is interrupted, epitaxial growth on the expanded layer leads to tensile biaxial forces because equilibrium conditions have changed. There also occurs a change in the distance between the (0002) planes.

and 2.5 nm thick reference and IBAS samples, respectively. Graphs 5.8 and 5.9 provide further confirmation of a considerable change in surface topography upon Xe^+ ion bombardment in this very early stage of growth. Hence, the structural changes have their origin in the nucleation and coalescence stage of film growth. In the later stages, grain growth proceeds in columnar fashion. The TEM images (figure 5.14) clearly show that the reference film exhibits a conical columnar grain growth. This is linked with a competitive, proliferating growth of neighbouring grains, where grains overgrow each other. For IBAS samples the grains appear to grow in a rather parallel columnar fashion. Hence, the competitive behaviour is less pronounced and the columns are therefore assumed to grow with similar speed. These findings and interpretations are supported by the AFM data. While large changes of lateral structure sizes are observed with increasing thickness for the reference sample, the thick IBAS sample shows topographical features in line with the expected parallel columnar growth in non-proliferating fashion.

The most plausible process responsible for the structural changes seen is a forward sputtering mechanism: atomic peening [126, 127] (sometimes also referred to as ion peening). This mechanism is characterized by the implantation of near surface atoms into the film by low energy ion bombardment. A number of findings for the IBAS films are consistent with this scenario. First, there is the compressive growth stress that accompanies the ion bombardment, which is evidence for an implantation mechanism. Additional support is the observed densification of the films (figure 5.18). From XRR measurements of 20 nm thick films and subsequent fitting of the data the mass density of standard ZnO was determined to $5.25 \pm 0.05 \text{ g/cm}^3$, whereas the density of IBAS samples was $5.45 \pm 0.05 \text{ g/cm}^3$ (cf bulk density: $5.61 \pm 0.05 \text{ g/cm}^3$). Second, from experiments with different bombarding species it has been found that the structure modification strongly

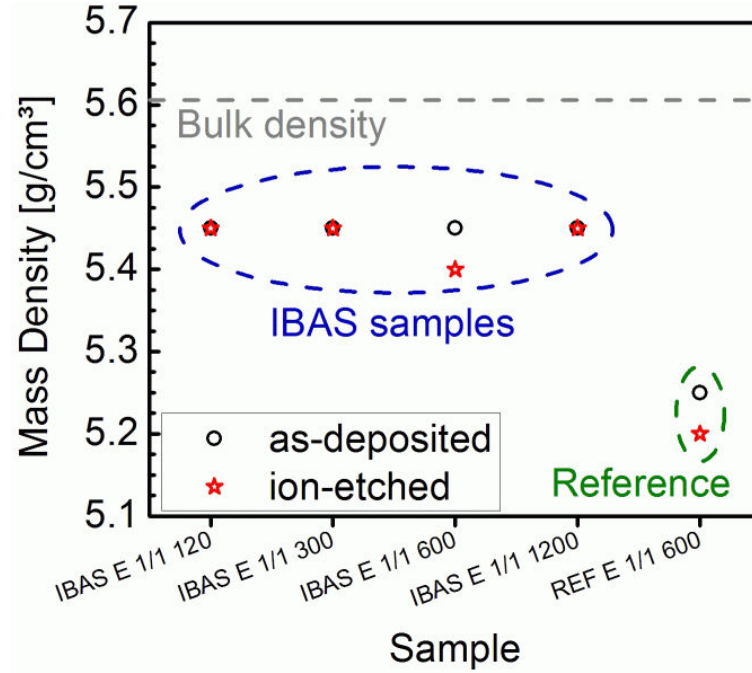


Figure 5.18: Mass density of IBAS and reference ZnO films determined from XRR patterns. The thickness of the films investigated ranged from approximately 15 nm to 20 nm. It is apparent that all IBAS samples have a mass density that is notably greater than that of the reference. Films have also been post-treated by ion-etching (see section 6.1.1).

depends on the ion species, as explained in the introduction of this chapter. If oxygen ions are utilized there is no change except for the expected detrimental effects at higher ion energies and fluxes. Argon ions cause a noticeable structural improvement at moderate energies. However, the effect is small compared to a xenon based IBAS process. This is consistent with the experimentally determined fact that the atomic peening mechanism is governed by the effective momentum (rather than energy) transfer to the film [128–130]. At a fixed ion energy, the momentum increases as the square-root of the atomic mass. As an example, for an ion energy of 180 eV the momenta of oxygen, argon and xenon ions have been calculated to approximately $1.24 \times 10^{-21} \text{ kg} \cdot \text{m/s}$, $1.96 \times 10^{-21} \text{ kg} \cdot \text{m/s}$ and $3.54 \times 10^{-21} \text{ kg} \cdot \text{m/s}$, respectively. To compensate for the lower mass, an oxygen ion would need to be accelerated to an energy of approximately 1.5 keV to have a similar momentum than a 180 eV xenon ion. The oxygen ion would be approximately eight times faster than the xenon ion in this case. Consequently, at a fixed kinetic energy, xenon ions have an approximately three times larger momentum than oxygen ions and a three times lower speed. It is therefore assumed that, in contrast to oxygen or also argon ions, xenon ions could transfer a larger fraction of momentum to the growing film at moderate fluxes and energies. Unfortunately there do not exist calculations of the momentum transfer

5.3. DISCUSSION AND EVALUATION

from the ions to the film structure. Assuming simple binary elastic collisions to estimate the momentum transfer e.g. between ions and Zn atoms would yield that oxygen, argon and xenon ions would transfer a fraction of 161 %, 124 % and 66 %, respectively. This would almost compensate for the differences in the ion momenta. In case of momentum transfer to the oxygen atoms of the film, oxygen ion bombardment would clearly deliver the largest total momentum in a binary collision as compared to argon or xenon ions of similar energy. However, an oxygen ion is very likely reflected after the first collision whereas a xenon ion still has a momentum directed towards the film and can therefore transfer additional momentum in subsequent collisions. It is therefore proposed that the total momentum transfer is largest for collisions of xenon ions with the film.

It is also important to mention that the dynamic nature of the IBAS sputtering process seems to play an important role in structure modification by ions. Experiments have also been performed where film growth and ion bombardment have been performed sequentially. Very thin layers (nominally < 1 nm) have been deposited and subsequently bombarded for different times. The procedure has been repeated 8 times before a thick layer has been deposited to yield a total film thickness of approximately 60 nm. None of the resulting films (figure 5.19) shows any structural modification due to an improved nucleation layer, which is in strong contrast to the films grown under simultaneous ion bombardment.

As discussed in chapter 2 for standard sputtered ZnO samples it was reported by many authors that in the early growth stage the films are rather weakly textured, i.e. they consist of small grains with crystallographic orientations differing from an ideal c_{\perp} -texture. From the crystal growth processes it was reported that the (0002) face may exhibit a much faster growth speed than the other faces. Although the same mechanism proposed as the origin of the anisotropic growth speed may not be valid in PVD processes, it is often argued (e.g. [85]) that anisotropic growth might also apply to sputtered films, since this assumption would phenomenologically explain the observed formation of a pronounced c_{\perp} -texture from a random initial distribution by *survival of the fastest*, i.e. by evolutionary selection. In [85], a corresponding growth model was suggested and it was also argued that the negative oxygen ions have a significant albeit detrimental influence on film growth. The orientational disorder at the early growth stage in combination with different growth speeds of the crystallographic orientations would explain why there is competitive growth that finally results in a c_{\perp} -texture for the standard samples. The connection between the atomic peening mechanism and texture control in the IBAS process presumably originates from the fact that the {0002} planes are the most densely packed planes. Densification of the structure by atomic peening therefore supports a preferred orientation with the {0002} planes parallel to the substrate. Hence, ion bombardment influences the film texture already in the nucleation stage. The fact that the ion bombardment leads to a well defined orientational order already in the early growth stage is supported by an XRD scan of a very thin film, which shows a pronounced

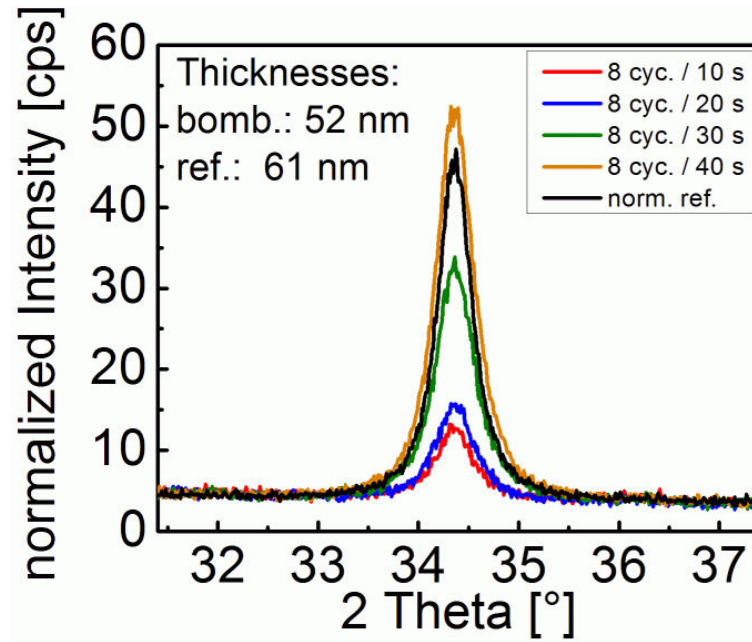


Figure 5.19: XRD-scans of films grown on seed layers which have been sequentially bombarded between sputter growth cycles. In detail, the seed layers have been deposited in steps of very thin layers (nominally < 1 nm) each of which was ion-bombarded after completion of layer deposition. This is a sequential analogue to the otherwise dynamic IBAS process. The legend shows the different bombardment periods that were applied on each layer. Evidently, the structural quality of the films increases with the bombardment time of the seed layers but is typically lower than that of the reference deposited without a seed layer. Apparently, by this method even a structural impairment is achieved. For long durations of the bombardment, the film structure becomes at least similar to that of the reference sample, but probably since most of the deposited layers was sputtered away by the ion bombardment. Although deposition times were adjusted to compensate for the expected ion sputter yield (which will be discussed in chapter 6, figure 6.5), the reference film is slightly thicker. The diffraction pattern of the reference sample has therefore been linearly renormalized.

5.4. DEVELOPMENT OF A FIRST GROWTH MODEL

(0002) peak (figure 5.20).

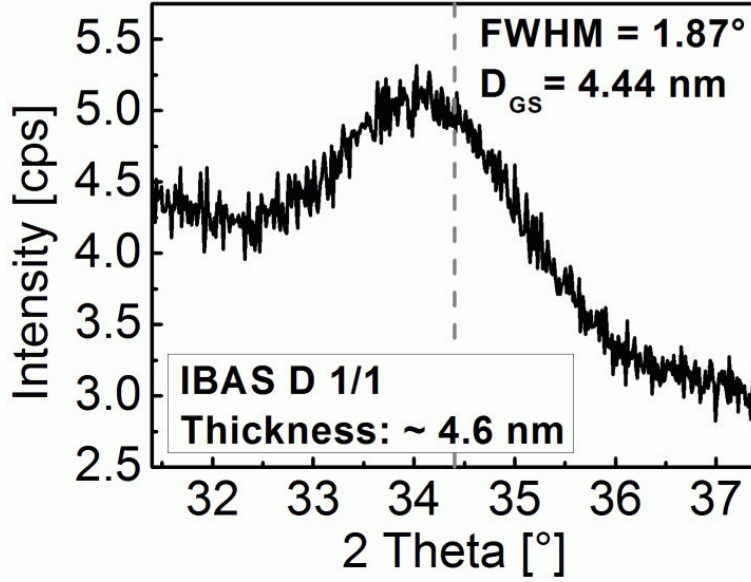


Figure 5.20: Bragg-Brentano XRD scan of a 4.6 nm thick IBAS ZnO sample. A pronounced (0002) Bragg peak with a FWHM of 1.87° is observed, which corresponds to a grain height of approximately 4.4 nm.

The grain height has been estimated with the Scherrer equation:

$$D_{GS} = \frac{K \times \lambda}{B \times \cos \theta}, \quad (5.3.6)$$

where D_{GS} is the vertical grain size, λ is the wavelength of the radiation used, B is the FWHM of the Bragg peak in radians and θ is the diffraction angle. The constant K depends on the method used to determine B and typically varies between 0.89 and 1. It has been set to 0.9 here. The fact that there is a detectable Bragg peak intensity at all and that the grain height approximately matches the thickness of this very thin film proves that there is a highly c_\perp -ordered crystalline structure already present at this early stage. The exclusive formation of highly oriented grains already in the nucleation phase eliminates a competitive growth mode from the very beginning. This also explains why no further ion bombardment is necessary after the initial growth stage and why the films extend in such a parallel columnar fashion as observed from TEM and AFM.

5.4 Development of a first growth model

From the presented data and the foregoing discussion in this chapter a first model of the growth of ZnO thin films is now proposed that summarizes the experimental

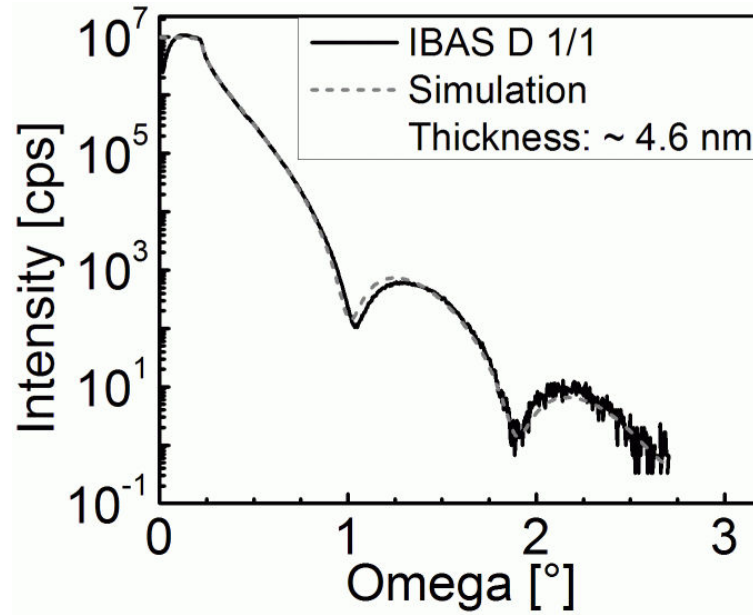


Figure 5.21: XRR-Scan of the IBAS ZnO film shown in figure 5.20.

findings and that demonstrates which role the Xe^+ ion bombardment plays in the IBAS process (figure 5.22). A distinction between IBAS samples and the standard reference films is already evident after the initial nucleation regime (1). For the reference sample there is a rather random distribution of crystallite orientations (1a). Consequently, surface roughness and lateral structure size distribution are first indications for the onset of competitive growth. Some grains already exhibit larger surfaces and start to overgrow others due to the proposed difference in growth speeds along the various orientations. This behaviour further develops as the film grows thicker (2a). At some stage (3a) the first grains are fully overgrown mainly by crystallites growing in $[0001]$ direction as a result of the proliferating growth. This leads to a broad distribution in the alignment of the $\{0002\}$ crystal planes which is responsible for the poor orientational order that is observed in the XRD measurement. For the IBAS sample atomic peening leads to a preferred orientation already during the nucleation regime (1b). Hence, there is a non-competitive growth already at this early growth stage which continues in subsequent stages (2b & 3b). Even when the ion bombardment is already interrupted when approximately 3nm of the film have been grown (which will be discussed in chapter 6), thick films with exceptionally high crystal quality are obtained. This demonstrates that stages (2) and (3) in terms of crystal quality are solely governed by the ultra-thin nucleation layer produced in stage (1). Hence, it is especially the nucleation regime that is susceptible to ion bombardment. This observation is important for applications where a perfection of film structure is

5.4. DEVELOPMENT OF A FIRST GROWTH MODEL

required.

Due to the technological importance of texture formation in thin films, a number of studies have focused on this topic as discussed in chapter 2. The present findings will therefore be related with previous studies of texture formation in ZnO films employing different deposition techniques. The beneficial role of ZnO seed layers has been discovered by several authors, e.g. [39, 104–106]. Particularly noteworthy are the works from Sato [106] and Claeysens [39] and respective co-workers who deposited ZnO films using Sputtering/CVD and ArF-PLD processes, respectively. Both works revealed that for the fabrication of highly textured films it is sufficient to grow a high quality seed layer only. These findings are in line with the experiments shown in this chapter, since both studies also provide compelling evidence that the texture of the films is solely determined by the conditions that govern the nucleation regime. Moreover, this statement even appears to hold for different thin film fabrication techniques.

There are also studies that link mechanical stresses to texture evolution (cf e.g. [131]), as discussed in section 2.4.2. Materials that exhibit a large anisotropy in their elastic properties might tend to grow in a preferred orientation under the influence of mechanical stresses. However, it has also been argued in section 2.4.2 that this effect cannot explain the formation of the initial (002)-texture in zinc oxide thin films. Therefore the growth stresses generated by the Xe^+ ion bombardment are presumably not the main reason for texture formation in thin films of zinc oxide. Also any processes based on preferential ion sputtering or damage of specific grain orientations due to channelling [132, 133] are excluded since it was discussed in chapter 2 that this mechanism would be incompatible with the typically observed structures of films grown under intense oxygen ion bombardment. Also, the inclination of the ion beam of approximately 45° would not result in the (0002)-texture since the corresponding channelling directions differ from this orientation.

The growth of zinc oxide films under the influence of ion bombardment will be further discussed in section 6.2, where an essential complement of the growth model will be proposed. This complement will be concluded from a detailed investigation of the growth of ZnO on structurally modified zinc oxide seed layers, which is the topic of the following section 6.1. In chapter 7 important investigations will be discussed for the growth of a-axis-textured films. The conclusions that will be drawn from these investigations will promote the development of a final growth model for sputtered zinc oxide films. There, the assumptions made in this chapter will be reviewed. Especially comments on the proposed growth mechanism for the un-bombarded reference films will be made. At the present stage, the proposed anisotropy in the growth speeds along different crystallographic orientations is a hypothesis without proof. Also the role of evolutionary selection in the formation of thick films will be discussed again in chapter 7.

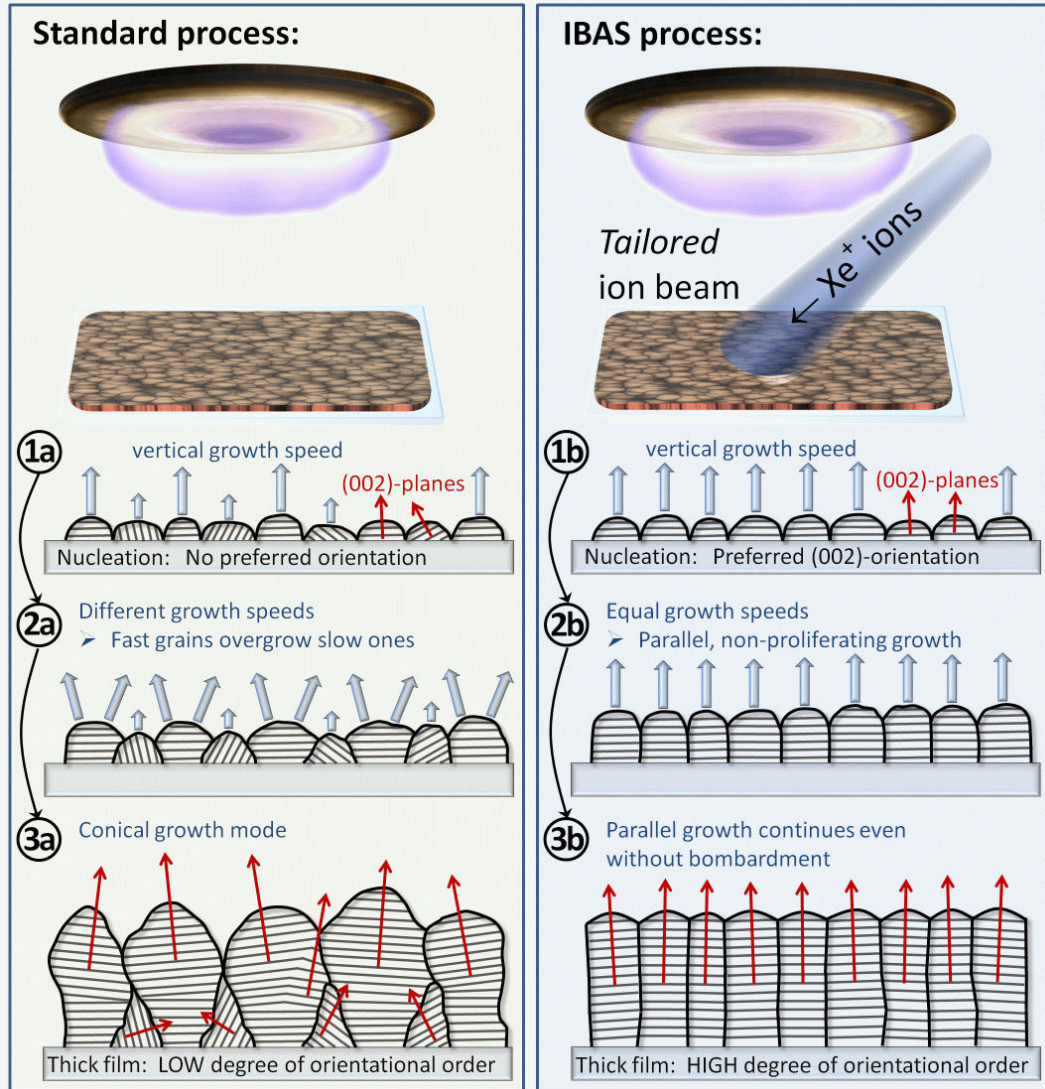


Figure 5.22: Growth model for standard ZnO (without auxiliary ion bombardment) and IBAS ZnO (with auxiliary bombardment). Sketches (1) to (3) represent different growth stages of the films, starting with the nucleation regime (1). The section lining indicates the orientation of the (0002) planes in each crystallite. There is no preferred orientation of grains during nucleation of the standard sample (1a). Different growth speeds (indicated by the vertical arrows) of the different crystal facets result in a competitive growth where the (0002) oriented grains overgrow neighbouring grains with different orientations (2a). This leads to conical grains and poor order of crystallite orientation (3a). In case of the bombarded sample, a highly (0002) oriented film is established by an atomic peening mechanism already in the nucleation regime (1b). Hence, competitive growth is avoided (2b) and the resulting structure consists of parallel columnar grains in combination with a high degree of orientational order (3b).

II: Applications of modified zinc oxide structures

6.1 Homo-epitaxial growth of ZnO and ZnO:Al thin films

In chapter 5 it has been demonstrated how ion bombardment under appropriate conditions improves the structural quality, i.e. the orientational order, of zinc oxide films in the IBAS process. A main finding has been the fact that the structure that forms during the early growth stage governs the structure of the entire film. It has been shown that a further beneficial impact of ion bombardment is obsolete after completion of this early stage. It is hence reasonable to assume that the specific deposition conditions such as atmosphere or discharge power may be changed subsequently without affecting structure formation. Therefore, this chapter focuses on the investigation of IBAS zinc oxide films that are utilized as seed layers for homoepitaxial growth of ZnO:Al films with improved structural order. The ZnO:Al films investigated for that purpose have been grown either in coater 1 or coater 2¹ under standard conditions that are used in conventional ZnO deposition runs without seed layers (see conditions for coater 2 in section 3.2). Seed layers were always deposited in coater 1 under the IBAS deposition conditions explained in section 3.1.

As a motivation, figure 6.1 shows the structure (XRD) of ZnO:Al films that were reactively deposited from a Zn:Al target. Prior to this deposition, some of the substrates were coated with a thin IBAS ZnO buffer layer in the same deposition chamber. It is evident that the use of a buffer layer yields an up to 10-fold improvement of the crystal structure as measured by the increase in the net area of the (002) peak. This is very remarkable since the total film thickness is about 750-800 nm while the buffer layer which governs the film structure is only about 5 nm thin.

The structural parameters of the IBAS ZnO buffer layers can to some extent be

¹All ZnO:Al films discussed in section 6.1.1 have been grown in coater 1 while films discussed in section 6.1.2 have been grown in coater 2.

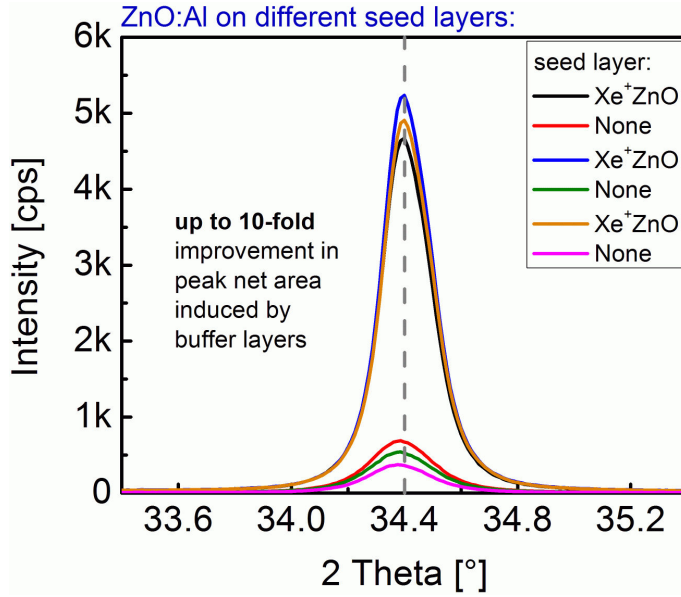


Figure 6.1: XRD-scans of thick ZnO:Al films on blank silicon substrates and on IBAS ZnO buffer layers (on silicon) respectively. The thickness of the buffer layers is approximately 5 nm. The thickness of the ZnO:Al films was derived from optical reflectance data and is approximately 750–800 nm. The structural improvement induced by the buffers is evident from an up to 10-fold increase in the net area with respect to the un-buffered specimens.

controlled. This has been evident for example from figure 5.1 where different ion current densities resulted in a different peak shift of the (002) Bragg peak, which is linked with a shift in film strain. Consequently, the focus of the forthcoming section 6.1.1 is the investigation of the influence of structural features of the buffer on the growth of a ZnO:Al film. In section 6.1.2 the growth of ZnO:Al on IBAS buffers will then be investigated in detail.

6.1.1 Tailoring buffer layers

The aim of this section is a closer investigation of the properties of the buffer layers. The following questions arise:

1. How can the structural properties of the ZnO buffer layers produced in the IBAS process be tailored to improve their efficiency, i.e. the quality of the ZnO or ZnO:Al films grown on top? In detail: What is the influence of lattice strain and surface morphology of the buffer layers on the structure formation of thick ZnO or ZnO:Al films?
2. What is the minimum thickness of the buffer layers at which the structural improvement of a film grown on top is still observed?

In this section two experiments will be discussed to find answers to these questions. The first one deals with a specific variation of the buffer layer structure by means of ion-etching. For that purpose, four initially identical IBAS ZnO films and one un-bombarded reference were deposited on silicon substrates. Their structure was investigated by XRD, XRR and AFM. Ion-etching was then

6.1. HOMO-EPITAXIAL GROWTH OF ZNO AND ZNO:AL THIN FILMS

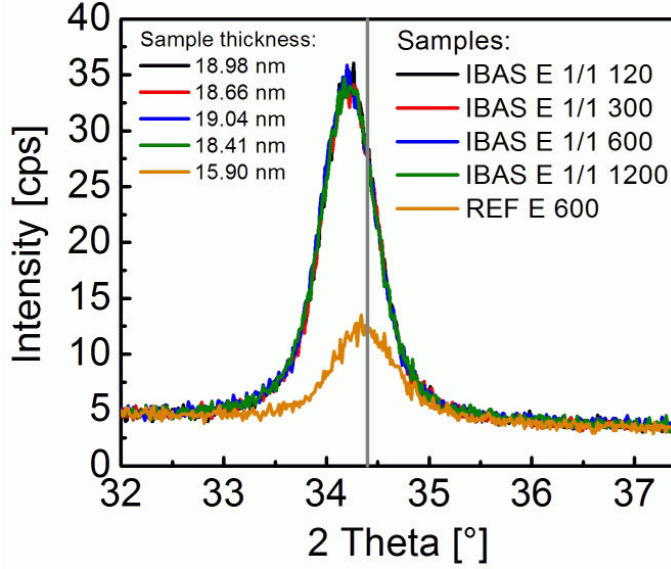


Figure 6.2: XRD scans of IBAS ZnO layers and a reference ZnO film in their as-deposited states (on silicon substrates). The thickness of the films ranges from 16 nm to 19 nm, as determined from XRR measurements. The IBAS films are slightly strained, which is evident from the shifted peak position. This is due to the ion bombardment. Their structural quality (peak net area) is greatly enhanced with respect to the reference. The films will be treated by post-deposition ion-etching in the next step (fig. 6.3). The etching times are already given in the sample names (120-1200 s).

performed to partially remove the film. Ion bombardment parameters were identical to those of the IBAS process. Structural changes induced by the etching step were investigated by XRD, XRR and AFM again before thick ZnO:Al films have been deposited onto these buffers. The second experiment aimed at determining the minimum thickness of the IBAS buffers that is necessary to promote the growth of ZnO:Al films with excellent structure.

Figure 6.2 shows four IBAS ZnO films and one un-bombarded reference ZnO film in the as-deposited state. It is evident that all IBAS films have similar structural quality as deduced from the intensity of the (002) peak. As expected, the quality of the reference film is lower. Also, the bombarded films exhibit a small peak shift towards lower angles as a consequence of the ion bombardment.

Subsequently, the specimens were ion-etched for different durations, ranging from 120 s to 1200 s for the IBAS films. The reference film was etched for 600 s. Figure 6.3 shows diffraction patterns of the etched structures.

Two dominant features characterize these diffraction patterns. First, the peak intensity of the (002) Bragg peak decreases with increasing etching time. Since films from the IBAS process typically exhibit no pronounced structural inhomogeneity in growth direction this is attributed to the decrease of film thickness. Second, there is a very pronounced shift of the peak position towards lower angles with increasing duration of the etching process, i.e. with decreasing film thickness. The centre position is close to 34° for the film that was etched for 1200 s. It is proposed that this observation is to some extent linked with the structural evolution of the films, since the etching process removes the final growth stages first. However, the observed peak shifts could also be caused by an implantation

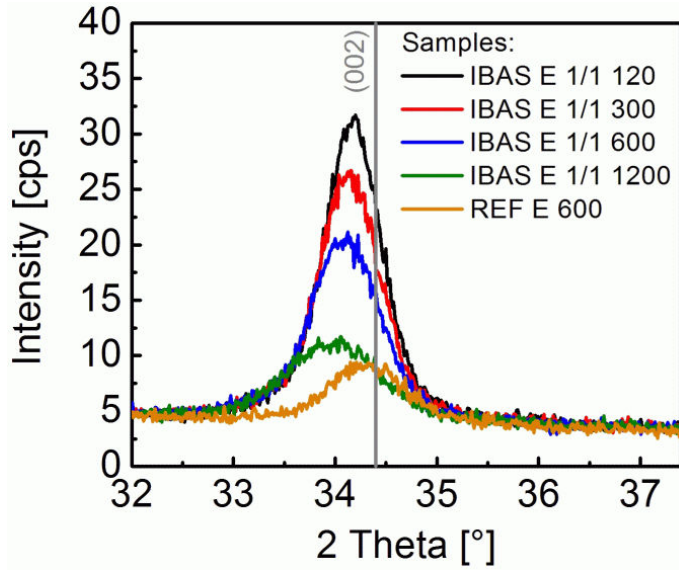


Figure 6.3: XRD scans of IBAS and reference ZnO films that have been treated by post-deposition ion-etching. The etching times range from 120 s to 1200 s as indicated in the sample names. The specimens have been shown in their as-deposited state in figure 6.2. Geometrical parameters and ion source parameters were absolutely identical to the standard conditions of the IBAS process. The etching time was varied for the IBAS films. The decrease in peak intensity is mainly due to the decreasing film thickness upon etching. A striking feature is the significant change of peak position for the IBAS films as a function of etching time. This is attributed to uncovering the early growth stage by the etching process.

mechanism due to the ion bombardment.

In chapter 5 it was shown that the vertical (i.e. in growth direction) strain in films fabricated in the IBAS process is also accompanied by a biaxial strain (cf e.g. figures 5.3 and 5.4). Assuming that this also holds for the films shown in figure 6.3 this means that by ion-etching of thin IBAS zinc oxide films the mean interatomic distance in direction parallel to the substrate plane can be adjusted. This could potentially become an important parameter for fine-tuning an epitaxial match for application of IBAS ZnO films as corresponding templates. From figure 5.1 it was evident that also a change in the intensity of the bombardment would serve to adjust the mean lattice spacing. However, structural quality might be impaired at the same time, which is not expected in the case of etching.

Figure 6.4 shows a comparison of all films in their as-deposited and ion-etched state. X-ray reflectometry was performed to determine changes in film thickness, surface roughness and mass density as a function of the extent of ion-etching. Some of the respective modeling results are shown in the legend of each graph. The mass density of these specimens has already been shown in figure 5.18, where no significant changes in mass density upon etching was observed.

From the XRR scans there is evidence that film thickness decreases upon etching, just as expected. Interesting however is the fact that the film surface seems to be noticeably smoothed upon ion bombardment. For further discussion, these results are summarized in figures 6.5 and 6.6.

Figure 6.5 depicts relative changes in film thickness and (002) peak position as a function of etching time. From a linear fit of the change in film thickness

6.1. HOMO-EPITAXIAL GROWTH OF ZNO AND ZNO:AL THIN FILMS

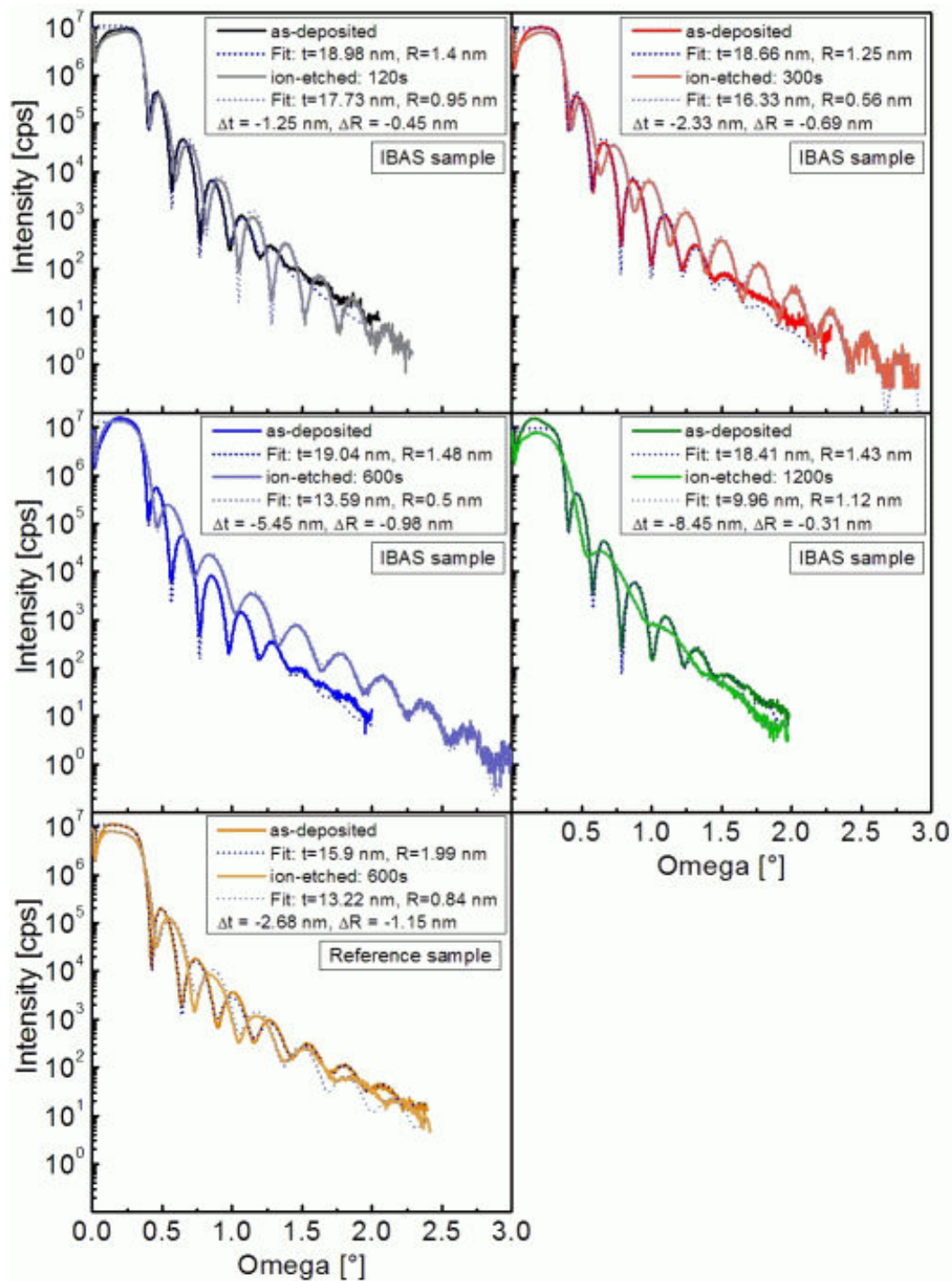


Figure 6.4: XRR scans of IBAS and reference ZnO films before and after ion-etching. The patterns have been modeled to determine the film thickness, surface roughness and mass density (fig. 5.18). Some of the modeling results (thickness and roughness) are shown in the legends. As expected, ion-etching decreases the film thickness, but also the surface roughness decreases as a consequence of the bombardment. The etching behaviour seems to be different for IBAS films and the reference, since the latter exhibits a smaller etching rate (see figure 6.5).

CHAPTER 6. II: APPLICATIONS OF MODIFIED ZINC OXIDE STRUCTURES

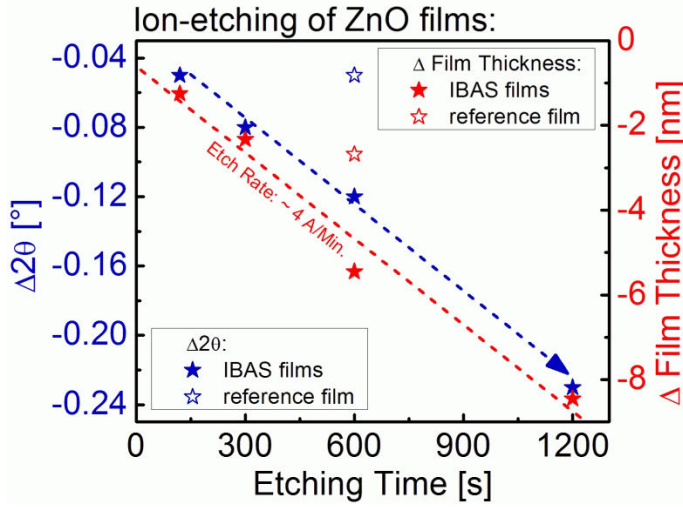


Figure 6.5: Summary of trends that occurred upon ion-etching IBAS and reference ZnO films. From the XRD patterns shown in figures 6.2 and 6.3 the differences $\Delta 2\theta$ in peak positions have been calculated. This is a measure for the change of average strain in growth direction. From the XRR measurements (figure 6.4) the change of film thickness has been determined for the different etching times. From a corresponding linear fit (red line) the etch rate was calculated to be $\approx 4 \text{ \AA/min}$.

an etch rate of $\approx 4 \text{ \AA/min}$ has been determined. The change in peak position with etching time is also a linear function. However, this might be a coincidence. Striking is the pronounced difference in the etch rate of the reference film which is smaller by a factor of 2 approximately. Even less pronounced is the shift of the (002) Bragg peak of the reference film which compares to that of an IBAS film that was etched for only 1/5 of the time. This supports the above-mentioned assumption that the peak shift observed for the IBAS samples is linked with the evolution of film structure during growth rather than with an implantation mechanism during etching.

Figure 6.6 clearly shows that ion-etching decreases surface roughness. Regarding the IBAS films, surface roughness is almost similar for all films in the as-deposited state. Upon ion-etching the decrease in roughness is most pronounced for an etching time of 600 s. The less pronounced decrease for 1200 s might potentially result from inaccuracies in modeling the XRR pattern. As can be seen in figure 6.4 the intensity contrast and the number of thickness oscillations is largely decreased by the long-term bombardment. This will be further elucidated in the discussion of topography data later in this section.

After ion-etching, films have been utilized as buffers for the growth of ZnO:Al films. Except one film, all ZnO:Al films have been deposited at identical conditions and with identical film thicknesses to investigate the influence of the different buffer layer features on their growth. A completely un-coated substrate has also been covered with ZnO:Al. Therefore, one of the ion-etched samples (IBAS E 1/1 1200) was coated in a second deposition run due to limited availability of carrier slots². XRD patterns of the coated specimens are displayed in figure 6.7 showing the prominent (002) Bragg peak of ZnO:Al.

²Deposition parameters in that run were nominally identical to that of the first run.

6.1. HOMO-EPITAXIAL GROWTH OF ZNO AND ZNO:AL THIN FILMS

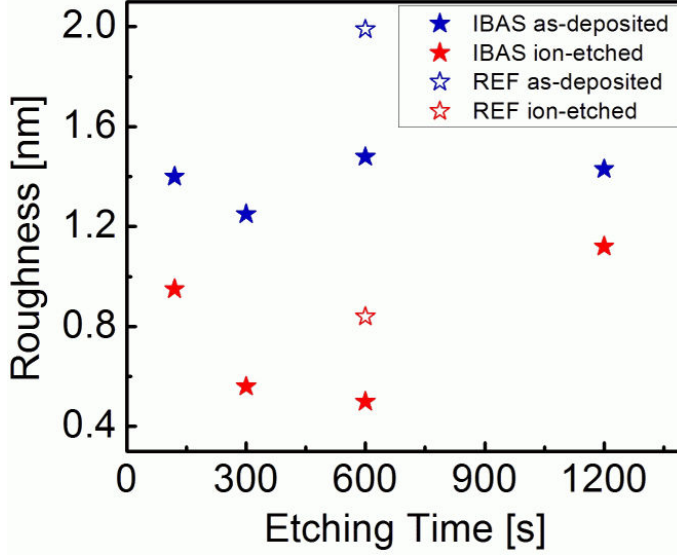


Figure 6.6: Surface roughness of films discussed e.g. in figure 6.4. The values were deduced from modeling of the XRR patterns. A clear decrease of surface roughness upon ion-etching is evident. The lowest roughness is found for the IBAS sample that was etched for 600 s.

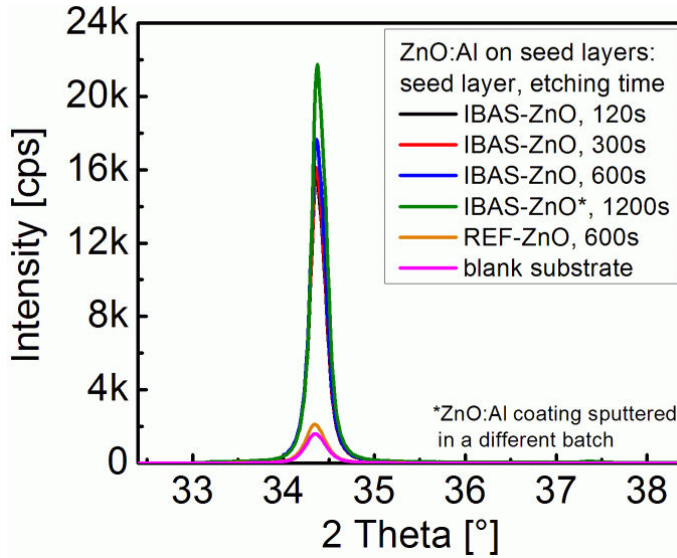


Figure 6.7: XRD patterns of ZnO:Al films that have been deposited onto ion-etched buffer layers. A blank substrate was also utilized for one film as another reference. It is evident that all IBAS buffer layers promote the growth of ZnO:Al films with excellent structural quality with respect to the reference films. One of the ZnO:Al films (on the massively etched buffer) has been deposited in a different deposition run due to limited availability of free carrier positions. Some care should therefore be taken when comparing with the other films. The thickness of the ZnO:Al films has not been measured but is estimated to approximately 800 nm from the deposition time.

CHAPTER 6. II: APPLICATIONS OF MODIFIED ZINC OXIDE STRUCTURES

Apparently, all IBAS buffer layers applied promote the growth of ZnO:Al films with an approximately 10-fold increase in the intensity of the (002) peak with respect to the reference samples. One of these was grown on an un-coated substrate (REF E) while the other one was grown on the ion-etched reference ZnO film (REF E 600). Figure 6.8 provides evidence that this improvement originates from an enhanced orientational order of grains along the growth direction, which is consistent with the findings discussed in chapter 5. The textural quality achieved (measured by the FWHM of the (002) rocking curve) upon utilization of an IBAS buffer compares well with the improved structures shown in figure 5.2.

Discussing the IBAS films only, there seems to be an improvement of the ZnO:Al quality with increasing ion-etching time of the buffer layers. While the buffers that were etched for 120 s and 300 s yield similar ZnO:Al structures, the buffers etched for 600 s and 1200 s to some extent promote more excellent film structures (fig. 6.7). However, there is limited comparability for the latter film (IBAS E 1/1 1200) since the ZnO:Al coating was not fabricated in the same run, albeit at nominally identical conditions. To summarize, except for the buffer that was ion-etched for 1200 s the influence of etching on the structure of the ZnO:Al films is small with respect to the general influence of an IBAS buffer layer. However, a possible influence of etching, especially in the case of this specific film (IBAS E 1/1 1200), will be discussed with the help of the surface topography now.

In figures 6.9 to 6.11 the evolution of surface topography is displayed, including all three stages of fabrication: the as-deposited and the ion-etched state of the buffer layers and the ZnO:Al films grown on top of the etched structures. Starting with the as-deposited buffers, figure 6.9 shows the topography of the four IBAS ZnO buffers and the un-bombarded ZnO reference film. Although not all of the images nicely resolve the tops of single grains it is evident that the films produced in the IBAS process exhibit a fine-grained nature with respect to the reference film. This finding is consistent with the results shown in chapter 5. Noteworthy is also the difference in height scales between the IBAS samples and the reference. This is further evidence for the proliferating growth of the un-bombarded reference film.

Upon ion-etching the surface topography noticeably alters. This is shown in figure 6.10. For the short etching times (120 s and 300 s) there is almost no noticeable change in the appearance of the surface features. However, continued ion-etching results in rather smooth surfaces that are characterized by the absence of any distinct features (600 s and 1200 s), yet at least for sample IBAS E 1/1 600 the original grainy nature is still weakly noticeable. The reference film is still rough in comparison with the IBAS films, although the decreased height scale shows that ion-etching smoothed the surface. It should be noted here that the AFM image of sample IBAS E 1/1 1200 after ion-etching provides clear evidence that surface roughness has significantly decreased by ion-etching, whereas modeling of the XRR patterns suggested a less pronounced decrease. In the dis-

6.1. HOMO-EPITAXIAL GROWTH OF ZNO AND ZNO:AL THIN FILMS

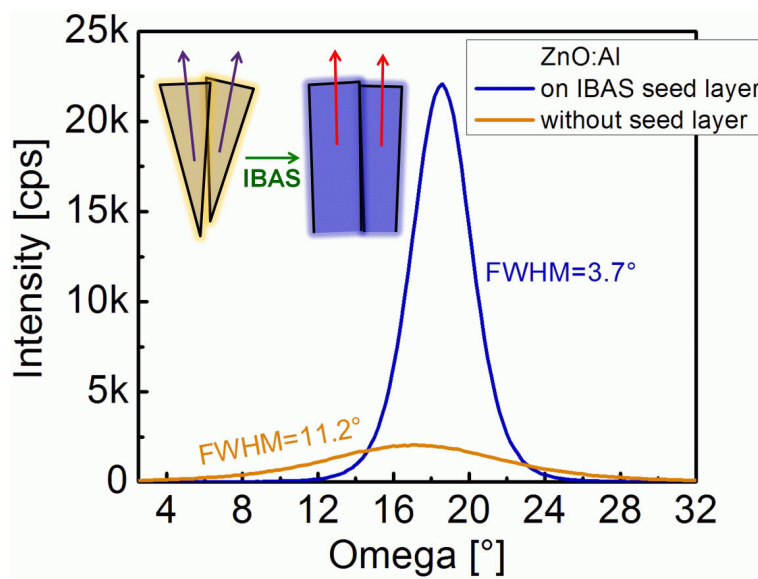


Figure 6.8: XRD rocking curves of the (002) peak recorded for samples deposited onto ion-etched IBAS buffers. As a reference, the ZnO:Al film deposited onto the blank silicon substrate (cf figure 6.7) has been investigated while the IBAS film is represented by the ZnO:Al layer sputtered onto the IBAS buffer that was ion-etched for 600 s. The widths of the rocking curves correspond to the extent of deviation from a perfect fibre texture with the {002} planes aligned parallel to the substrate surface. Hence, parallel alignment of grains in the direction of the substrate surface normal is greatly enhanced by the IBAS buffer as evident from the narrow width of the corresponding rocking curve.

CHAPTER 6. II: APPLICATIONS OF MODIFIED ZINC OXIDE STRUCTURES

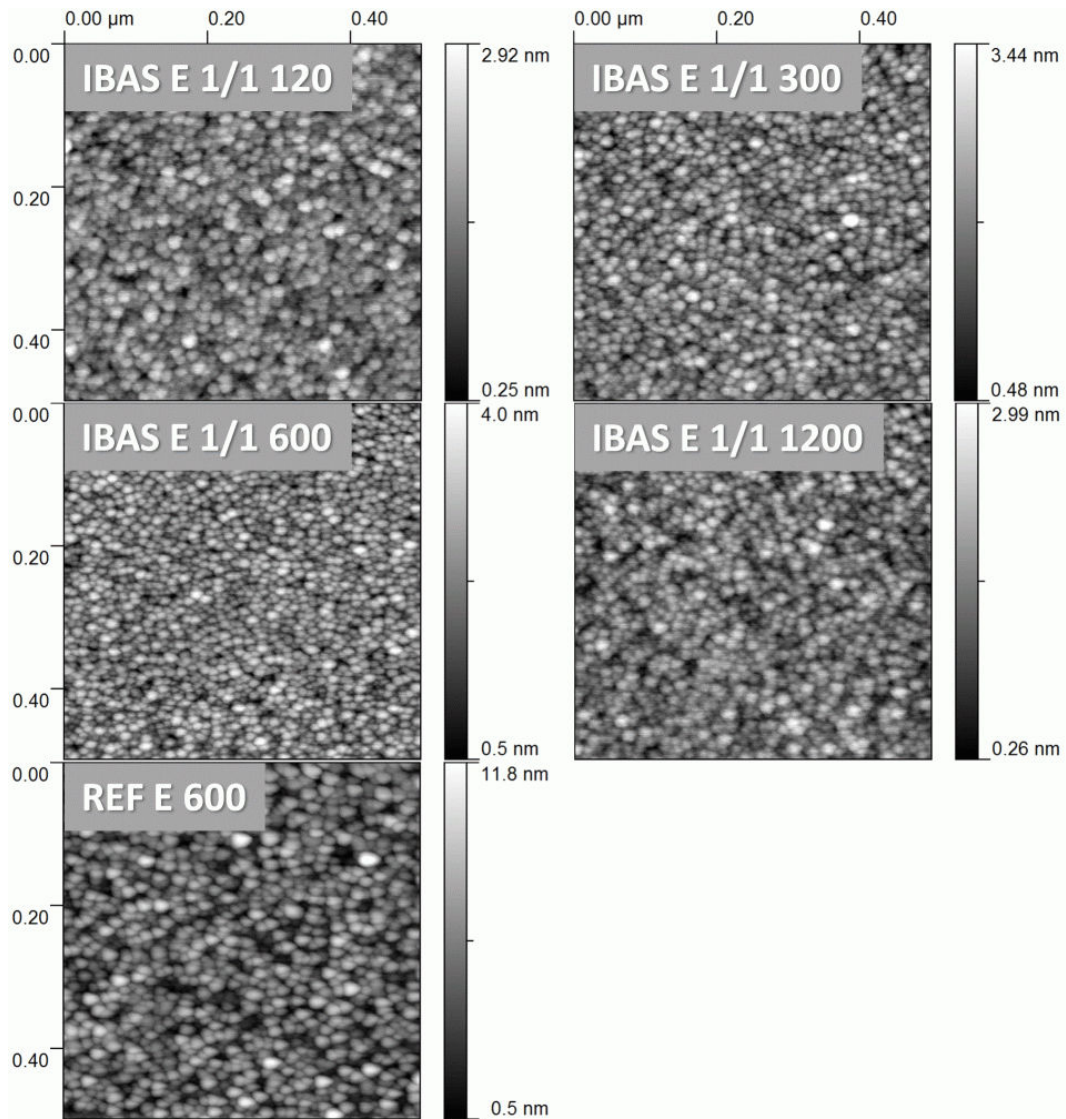


Figure 6.9: Surface topography of as-deposited IBAS and reference ZnO films (series E). IBAS films generally show a smaller roughness than the reference, which is evident from the height scales. Also, IBAS films exhibit a comparatively ordered structure with a narrow distribution of feature sizes as discussed in chapter 5, which is especially pronounced for sample IBAS E 1/1 600 here. Film thicknesses range from 16 nm to 19 nm.

6.1. HOMO-EPITAXIAL GROWTH OF ZNO AND ZNO:AL THIN FILMS

cussion of the XRR patterns this was attributed to the rather flat intensity curve (cf figure 6.4) and some difficulty in modeling therefore.

Since the surface topography has been proven to be quite different for each ion-etched IBAS film, the question about the resulting film structure of ZnO:Al films grown on top is especially interesting. And so is the answer, which is given by figure 6.11. The specimen named REF E is a ZnO:Al film that was deposited directly onto a blank substrate, without any kind of buffer layer. It is very clear that the resulting surface topography is almost identical to that of the film grown onto the ion-etched reference ZnO buffer (REF E 600). The IBAS buffers however promote the growth of ZnO:Al with distinctly different surface features. The striking consequence from this is that even the surface topography of approximately 800 nm thick ZnO:Al films is strongly affected by the influence of an only about 10-15 nm thin buffer layer. Quite surprisingly, as a function of etching time there is no significant change in the topography of the ZnO:Al top layer up to an etching time of 600 s. However, for the buffer that exhibited a very flat featureless surface upon etching for 1200 s the topography looks very different. It appears that grains grow larger on average and also that some of the grains are closely connected, forming larger areas where none of the typical trenches are visible that would separate single grains.

To summarize the investigation of surface topography, the following statements can be made:

- The fine-grained ordered topography of buffers from the IBAS process is to some extent imposed on the structure of the ZnO:Al films. Even at comparatively large thicknesses, the ZnO:Al films show an improved order and smoothness if grown on IBAS buffers. However, the lateral width of the grains seems to be larger than for the thin buffer layers. This is in contrast to the observations made in chapter 5, where no pronounced increase of the grain diameter has been observed for films up to about 120 nm (cf figures 5.7 and 5.10). This difference is very likely a consequence of the large film thickness of the ZnO:Al films.
- A change of the surface roughness of IBAS buffers by ion-etching does not affect the structure of a ZnO:Al film if etching is stopped at a stage where surface features are still visible. However, if etching is continued until the surface is absolutely featureless (on the scale of the resolution of the measurements performed) and flat (compared to the as-deposited films), then the topography of the ZnO:Al film changes and shows large connected regions. It is proposed that in this case only the orientational order of the buffer but not its grainy nature is imposed on the ZnO:Al film.

The IBAS buffer that was ion-etched for 1200 s had a thickness of only about 10 nm after etching. Nonetheless, a ZnO:Al film with superior structural quality

CHAPTER 6. II: APPLICATIONS OF MODIFIED ZINC OXIDE STRUCTURES

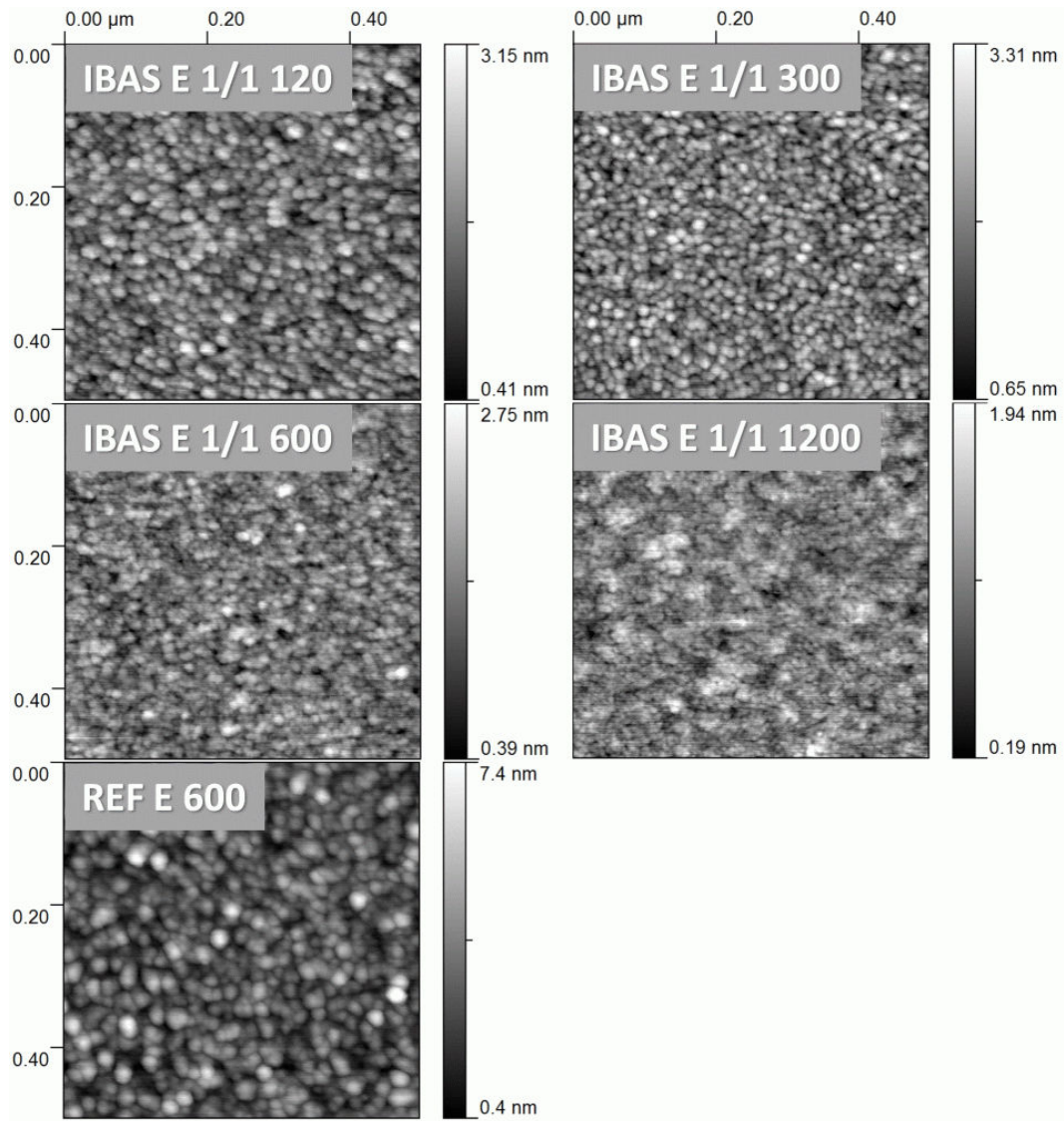


Figure 6.10: Surface topography of ion-etched IBAS and reference ZnO films. Etching times ranged from 120 s to 1200 s and can be extracted from the sample descriptions. The etch rate was $\approx 4 \text{ \AA}/\text{min}$ and $\approx 2 \text{ \AA}/\text{min}$ for the IBAS and the reference samples, respectively. Etching decreases surface roughness for all samples. Surface features become less distinct for long etching times for the IBAS samples.

6.1. HOMO-EPITAXIAL GROWTH OF ZNO AND ZNO:AL THIN FILMS

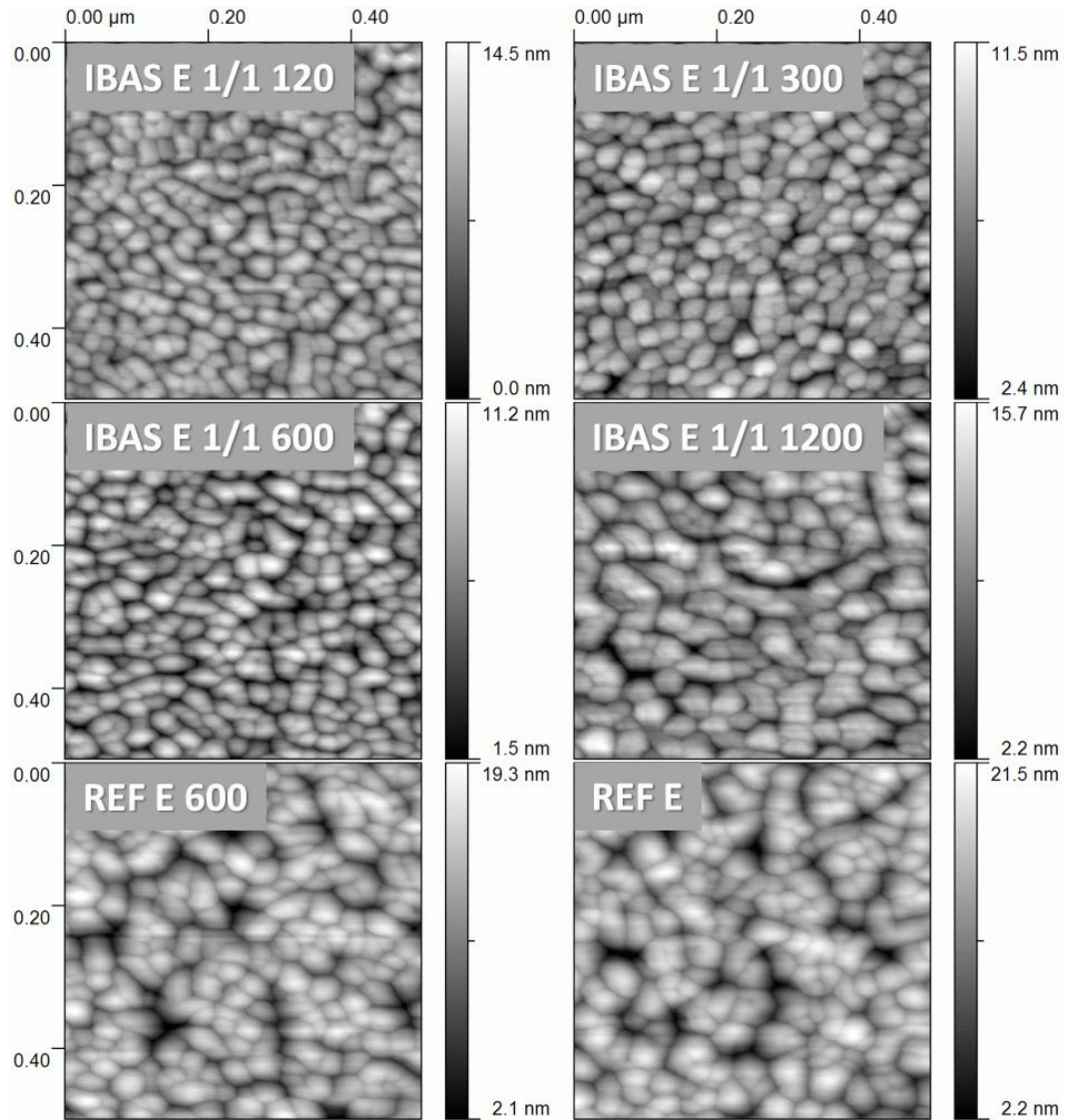


Figure 6.11: Surface topography of ≈ 800 nm thick ZnO:Al films deposited onto the samples shown in figure 6.10. An additional reference sample, REF E, has been deposited onto a blank substrate, while REF E 600 is a ZnO:Al film on a reference ZnO film that has been ion-etched for 600 s. The IBAS samples utilize ion-etched IBAS ZnO buffers. A detailed discussion of the topographies is given in the text.

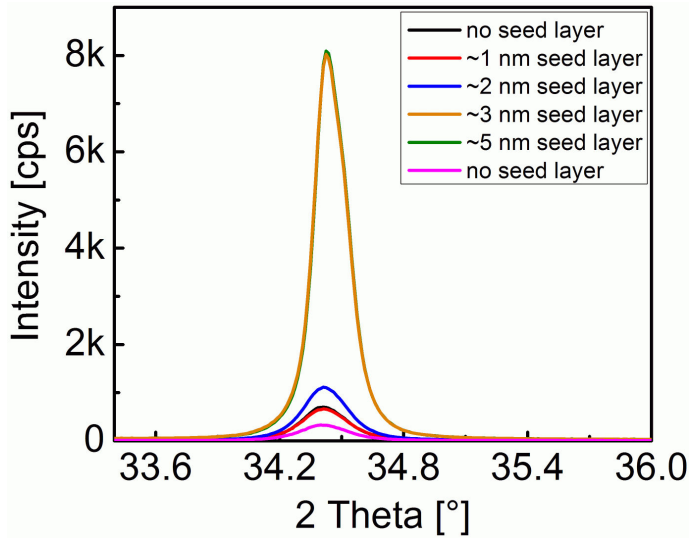


Figure 6.12: XRD scans of ZnO:Al films of approximately 800 nm (estimated from the deposition time) deposited onto IBAS ZnO buffer layers with different thicknesses. Although there is some scattering in the peak intensities of the reference films grown without buffer layers, it can be stated that an only 1 nm thick buffer is insufficient to improve the structural quality of the ZnO:Al. There seems to be some improvement for a 2 nm thick buffer. However, if the buffer layer thickness is similar or greater than 3 nm the quality of the ZnO:Al film is constantly high. The thickness of the buffer layers has been calculated from the known deposition rate and time. A small deviation is therefore possible. Silicon substrates have been utilized.

could be grown on this buffer. Therefore, the question arises about the minimum buffer layer thickness that is needed to grow high quality films. In chapter 5, a 4.6 nm thin IBAS ZnO film has been shown (figure 5.20) that already exhibited excellent structural order. It is therefore expected that buffer layers can be even thinner. An experiment was performed on silicon substrates where the thickness of the IBAS ZnO buffers was varied from extremely thin films (1 nm) to films with a thickness of 5 nm. A thick ZnO:Al film has then been deposited onto each of these buffer layers to investigate their structural perfection. Figure 6.12 shows corresponding X-ray diffraction patterns.

It is evident that the very thin buffer (1 nm) has no influence on the growth of the ZnO:Al. However, a 2 nm thin buffer seems to already have some influence since the corresponding (002) peak intensity is larger than that of the two reference samples. If the thickness of the buffer is increased to 3 nm, a ZnO:Al film with excellent structural order is grown already. This is consistent with topography data shown in chapter 5 where it has been demonstrated that films with thicknesses of 2-3 nm already exhibit a clearly ordered grainy structure (cf figure 5.7). There is no further improvement for thicker buffer layers (see data for the 5 nm thick buffer).

6.1. HOMO-EPITAXIAL GROWTH OF ZNO AND ZNO:AL THIN FILMS

6.1.2 Influence of modified buffer layers

In the preceding section the growth of ZnO:Al on ZnO buffers was investigated with respect to different buffer layer properties. The aim of the present section will be a detailed inspection of the implication of the ZnO:Al growth conditions on structure formation on blank substrates and IBAS buffers, respectively. For that purpose, IBAS ZnO buffer layers are always fabricated at the same conditions, i.e. without any post-deposition treatment and at a standard thickness of 10 nm. The oxygen flow during ZnO:Al deposition is the parameter that was varied during the experiments since especially the oxygen content in the sputtering atmosphere has a distinct impact on the structural quality of films in a reactive sputtering process. This is directly linked with the unintended bombardment of the growing films with negatively charged oxygen ions created at the target surface and accelerated towards the film by the full cathode potential (several hundred volts), as discussed in chapter 2. Unless otherwise stated, a new (i.e. with only a shallow erosion trace) Zn:Al target was utilized for deposition of the ZnO:Al films discussed in the following. Nonetheless, clear evidence for a deterioration of film structure at high oxygen flows will be given that is attributed to the action of energetic oxygen ions. The conclusions that will be drawn will motivate an extension of the growth model developed in chapter 5.

Figures 6.13 and 6.14 display XRD patterns of ZnO:Al films characterized by a prominent (002) Bragg peak. Silicon wafers with a thin native oxide layer have been used as a substrate for this experiment. The silicon dioxide prevents any influence of the crystal structure of the silicon on the growth of the sputtered films. However, the small roughness of only a few Ångströms promotes somewhat improved structural properties in comparison to films deposited on standard microscope glass slides. The films shown in figure 6.13 have been sputtered directly onto the silicon wafers while the films presented in figure 6.14 are buffered by a thin ZnO film with improved structural order fabricated in the IBAS process. Deposition conditions for the ZnO:Al films were otherwise identical. This means that the films deposited at each oxygen flow may be regarded as *twin* samples the structure of which differs only as a consequence of the utilized buffer for one of the samples.

The deposition time of the ZnO:Al films was identical for all oxygen flows. Since the deposition rate is a monotonically decreasing function of the oxygen flow under the deposition conditions selected, the thickness of the films decreases from approximately 830 nm to 580 nm with increasing oxygen flow. It has been demonstrated in [40] that for zinc oxide films that are not too thin (but thinner than the extinction length of the used x-ray radiation) the net area of the (002) peak is proportional to the film thickness in very good approximation. However, evidently the un-buffered films (fig. 6.13) deteriorate much faster with increasing

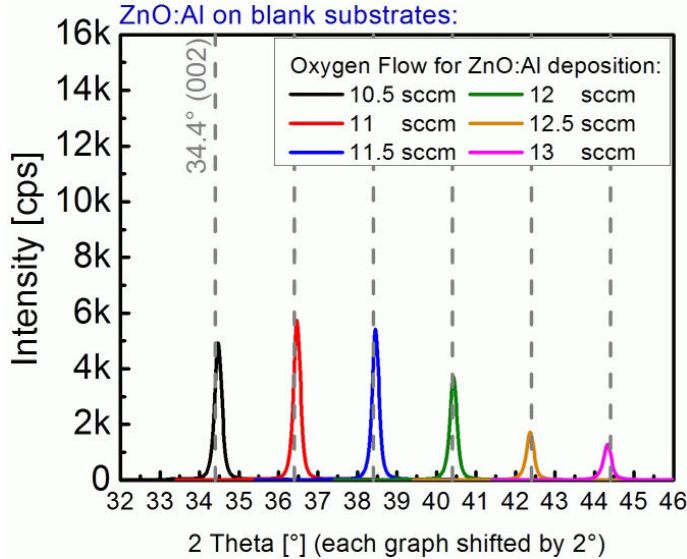


Figure 6.13: XRD-Scans of thick ZnO:Al films deposited on silicon wafers at different oxygen flows. Graphs have been shifted along the 2 Theta axis for better visualization. The vertical lines represent the position $2\theta = 34.4^\circ$ for each sample and oxygen flow, respectively. Due to a constant deposition time, the thickness of the films decreases with increasing oxygen flow. From 10.5 sccm to 13 sccm the thickness decreases from approximately 830 nm to 580 nm as deduced from optical data. At high oxygen flows there is a pronounced decrease in peak intensity that cannot be explained by the decreased film thickness solely.

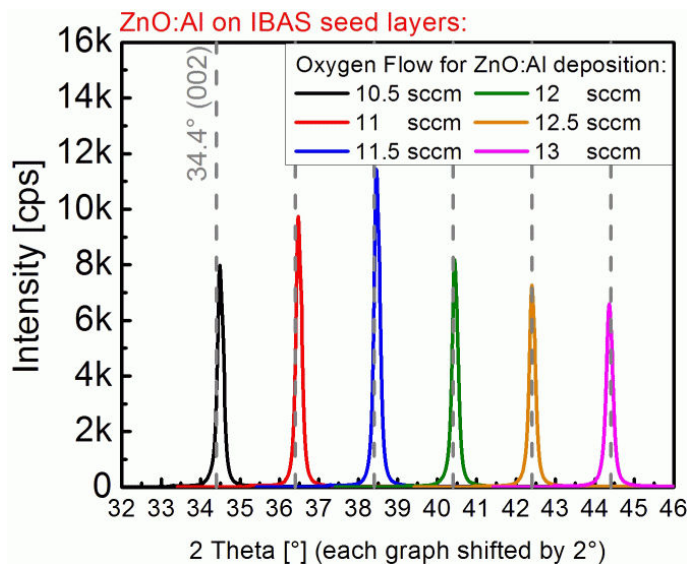


Figure 6.14: XRD-Scans of thick ZnO:Al films deposited onto silicon wafers at different oxygen flows. Films have been simultaneously deposited with the samples shown in figure 6.13 but IBAS ZnO buffer layers were applied to improve the structural quality. Film thicknesses also range from approximately 830 nm to 580 nm with increasing oxygen flow. Peak intensities are generally higher than without buffers and there is no pronounced deterioration at high oxygen flows (cf figure 6.13).

6.1. HOMO-EPITAXIAL GROWTH OF ZNO AND ZNO:AL THIN FILMS

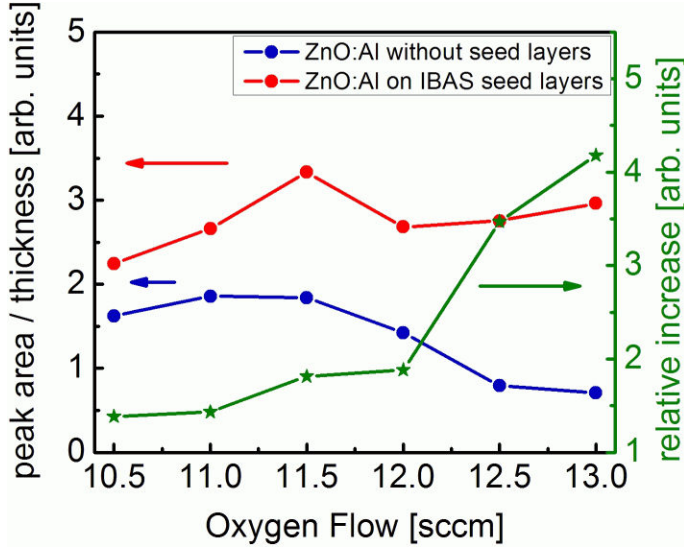


Figure 6.15: Comparison of ZnO:Al film grown on blank silicon wafers and IBAS ZnO buffers (on silicon) respectively. As a measure of crystalline quality the peak net areas deduced from the XRD scans shown in figures 6.13 and 6.14 are divided by the film thickness. The relative ratio of these numbers is also displayed and measures the structural improvement imposed by the IBAS buffer layer.

oxygen flow than could be explained by the decreasing film thickness solely. Since there is also a noticeable shift of the (002) peak position to lower angles at high oxygen flows, which is indicative for increased compressive stresses, it is proposed that the structural deterioration is a consequence of the increased oxygen ion bombardment from the target. The picture is quite different for the films grown on the thin IBAS buffers (figure 6.14). First of all, the intensity of the (002) peak and hence the structural quality of these films is notably larger than for the reference films. Second, there is no strong decrease of the intensity at high oxygen flows although the action of negative oxygen ion bombardment is again evident from the peak shift. Considering the decrease of film thickness it is reasonable to assume that there is no structural degradation of the films at all upon increasing the oxygen flow. This assumption is confirmed in figure 6.15. From the XRD patterns discussed (figs. 6.13 and 6.14), the net areas of the (002) peaks were extracted and normalized with the film thickness (cf [40]). These numbers represent a reasonable measure for the structural quality of the films. In figure 6.15 this quantity is plotted for all films. Additionally, the relative change in this quantity (ratio) upon utilization of IBAS buffers is given, which directly shows the extent of structural enhancement induced by these IBAS buffers. Although there is a clear improvement for all oxygen flows, the effect of the IBAS buffers apparently is distinctly increased at high oxygen flows.

From figure 6.8 for example we know that the improvement evident from the increase in the intensity of the (002) peak is directly correlated with an increase of the orientational order. To investigate the orientational order of the films shown in figures 6.13 and 6.14 the area around the (100) Bragg peak at $2\theta = 31.75^\circ$ is magnified and displayed in figures 6.16 and 6.17 for the reference and the IBAS buffered films respectively. The extent of deviation from a perfect c_\perp fibre texture

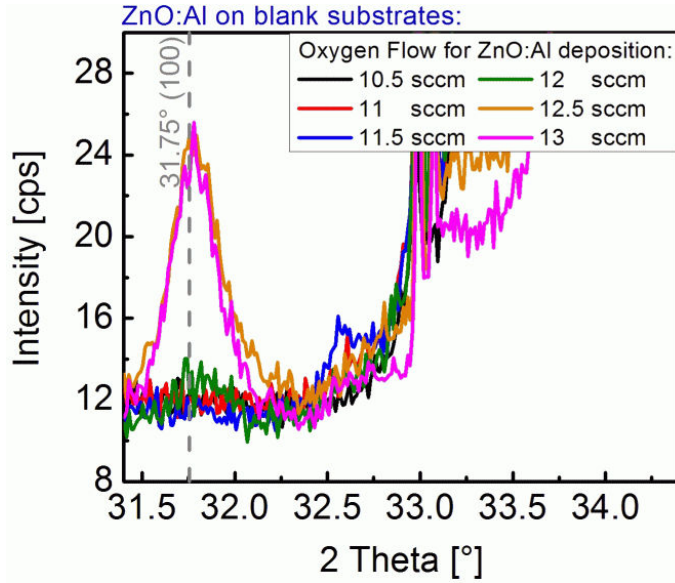


Figure 6.16: XRD scans of films that have been shown in figure 6.13. The region around the (100) Bragg peak of ZnO has been magnified. It is evident that with increasing oxygen flow during deposition of the ZnO:Al there is an increase in the intensity of the (100) peak. This is evidence for a non-perfect texture, i.e. a degradation of structural order with increasing oxygen flow. Films that exhibit a perfect (002) fibre texture must not show any other peaks than (002) and higher orders.

cannot only be deduced e.g. from the width of a rocking curve but also from the appearance and the intensity of diffraction peaks with indices other than (002) in the XRD patterns. In the presence of a perfect (002) fibre texture, no other peaks than (002) and higher orders are detectable in scans performed in Bragg Brentano geometry. Hence, from figure 6.16 it is obvious that upon increasing the oxygen flow the orientational order of the ZnO:Al films is noticeably disturbed as concluded from the clear presence of a (100) peak. This is unambiguous evidence for the damaging influence of the negative oxygen ion bombardment. From figure 6.17 it is concluded that there is no similarly harmful effect of this bombardment if IBAS buffers are utilized. This fact is extremely interesting since the buffer layer constitutes only a negligible fraction of the total film and the negative oxygen ions otherwise bombard the ZnO:Al films to the same extent as without a buffer. This fact will be further evaluated in section 6.2. Rocking curves of the (002) peak have been recorded for the ZnO:Al films deposited at oxygen flows of 11.5 sccm and 13 sccm and support the trend observed in figures 6.16 and 6.17: For the reference films the FWHM increases by 45% upon increasing the flow from 11.5 sccm to 13 sccm while for the films on IBAS buffers there is only an increase by 18%. This provides further evidence for the enhanced quality of the c_{\perp} -texture of the ZnO:Al films grown on IBAS seed layers. But it is also striking evidence that the influence of negative oxygen ion bombardment during ZnO:Al deposition is different if an IBAS seed layer is utilized.

To further investigate the influence of the negative oxygen ion bombardment, sample profiles were created from a laterally resolved XRD study. Several XRD scans were performed at different sample positions along the longitudinal axis of

6.1. HOMO-EPITAXIAL GROWTH OF ZNO AND ZNO:AL THIN FILMS

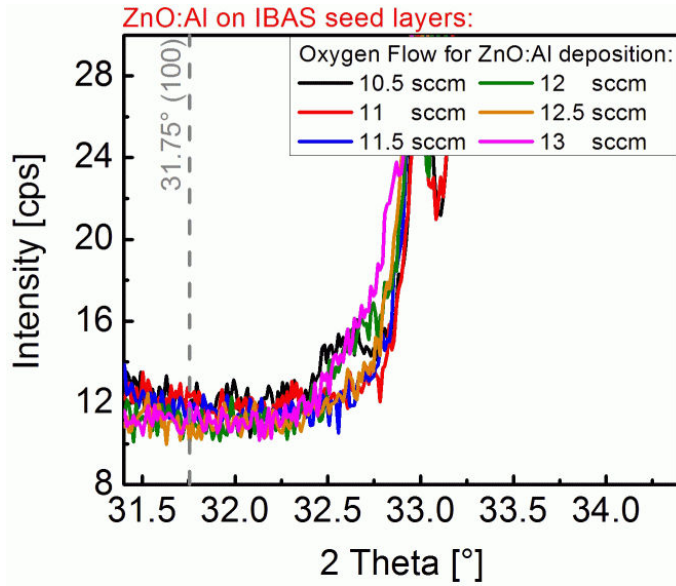


Figure 6.17: XRD scans of films that have been shown in figure 6.14. The region around the position of the (100) Bragg peak of ZnO has been magnified. Apparently, even at high oxygen flows there is no indication for a (100) peak in the diffraction patterns. Upon utilization of the IBAS ZnO buffers, the highly ordered (002) fibre texture is not only improved but also maintained under conditions that typically result in a deterioration of structural quality (cf figure 6.16).

$26 \times 76 \text{ mm}^2$ large glass substrates at distances of 5 mm each³. For the evaluation, the fact has been exploited that the high structural quality of the IBAS ZnO buffers is ensured only in the centre of the substrate as a consequence of both the diameter of the ion beam and the deposition profile of the ZnO in the IBAS process. Hence, the IBAS buffers are in-effective at positions outside of the sample centre by approximately more than 10 mm. This is demonstrated in figure 6.18, where profiles of the (002) peak net area are shown for ZnO films deposited from two different Zn targets: an almost new one without any pronounced erosion trace and a used one that exhibited a deep trace already. It is evident that the pronounced structural improvement induced by the IBAS buffers is restricted to a limited area at the sample centre. The use of differently aged targets was motivated by the respective profile in the intensity of the bombardment of the substrate by negatively charged oxygen ions from the target. In section 2.6.2 it has been explained that this intensity profile depends on the geometry of the target surface. A new target creates massive oxygen ion bombardment above the racetrack, whereas an aged target often promotes strong bombardment of the substrate centre in typical deposition geometries. Figure 6.19 depicts profiles created from the peak positions of the same diffraction patterns analyzed in figure 6.18. The typical film strain pattern inherent in depositions from old and new targets are markedly pronounced (compare with fig. 2.9). However, special attention should be paid to the relative change of the peak position resulting from the utilization of IBAS buffers. There is a distinct increase in the position around the sample centre for both the old and the new target. This may be interpreted as a decrease in film strain induced by the buffers, which is especially

³The method is discussed in detail in [40] (section 7.2).

CHAPTER 6. II: APPLICATIONS OF MODIFIED ZINC OXIDE STRUCTURES

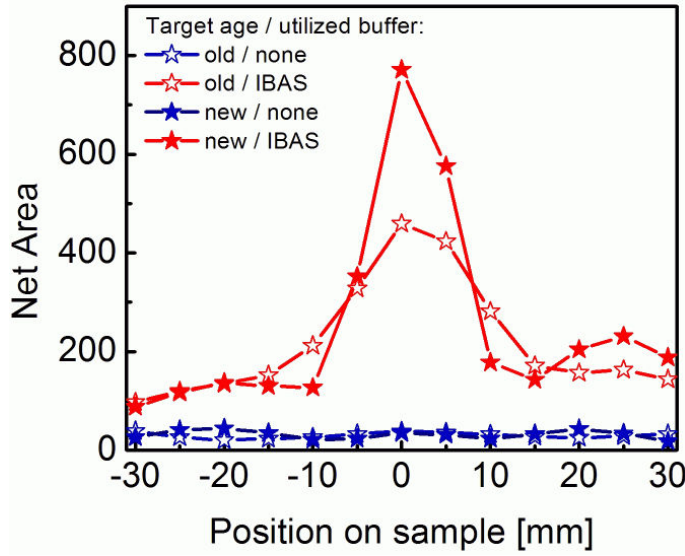


Figure 6.18: Net areas of the (002) peak extracted from XRD profiles of ZnO films along the full length of the substrate. Two pairs of films were investigated for the deposition of which an old and a new target was utilized, respectively. It is evident that both films on IBAS buffers exhibit a significantly increased structural quality at the substrate centre. This is linked with the deposition and ion bombardment profile of the IBAS seed layers.

astonishing since film strain is not only reduced for a new target, where the sample centre is not subjected to intense oxygen ion bombardment at all, but also for an old target, where oxygen ion bombardment is specifically pronounced at the sample centre. Hence, this data provides additional proof that the deteriorating influence of energetic oxygen ion bombardment is substantially diluted when films are grown on IBAS ZnO buffers.

So far, all ZnO or ZnO:Al films discussed in this work were deposited onto silicon wafers⁴. Although the thin native amorphous oxide layers do not permit any epitaxial interference in the growth of the zinc oxide films, structure formation is promoted by the very smooth surface of the substrate. It will now be demonstrated that this is not a prerequisite neither for the growth nor for the effectiveness of the IBAS ZnO buffers. Figures 6.20 to 6.24 show experimental data for ZnO:Al films grown on standard microscope glass slides. Figures 6.20 and 6.21 show XRD patterns for films grown at different oxygen flows and on approximately 10 nm thin IBAS buffers and blank glass substrates respectively. It is evident that on the bare substrate the ZnO:Al structure deteriorates especially for elevated oxygen flows, which is attributed to the pronounced oxygen ion bombardment. For the films sputtered on IBAS buffers there is a general increase of the peak intensity as a consequence of the buffers which also prevent structural deterioration at high oxygen flows. Similar to the results shown for films on silicon (cf figure 6.14) the structure even seems to improve at high flows if the decrease in film thickness is considered when evaluating the (002) peak intensities or net areas.

Figure 6.22 displays the relative ratio of the peak net areas that have been

⁴Except specimens discussed in figures 6.18 and 6.19 of course.

6.1. HOMO-EPITAXIAL GROWTH OF ZNO AND ZNO:AL THIN FILMS

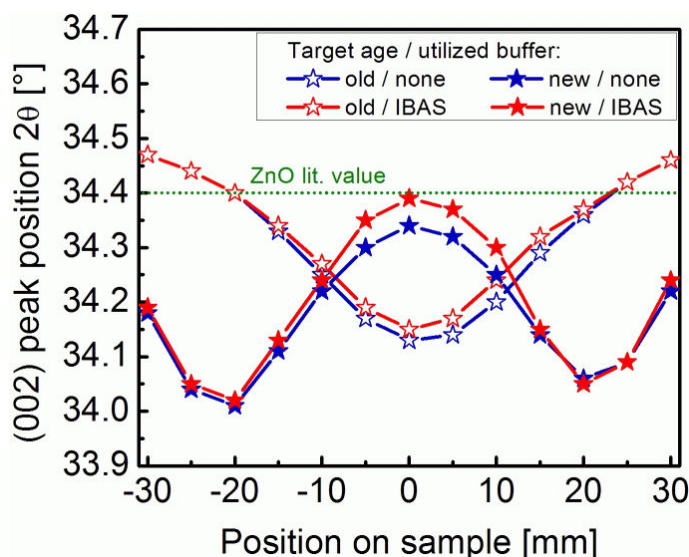


Figure 6.19: 2θ -positions of the (002) peak extracted from XRD profiles of ZnO films along the full length of the substrate. Two pairs of films were investigated for the deposition of which an old and a new target was utilized, respectively. The profiles of the curves shown are typical for old and new targets, respectively, and are governed by the distribution of the negative oxygen ion bombardment originating from the target surface. It is evident that for both targets the peak positions are increased at the sample centre where the IBAS buffers evolve their influence on film structure (cf figure 6.18). Lattice strain is therefore decreased by the use of IBAS buffers.

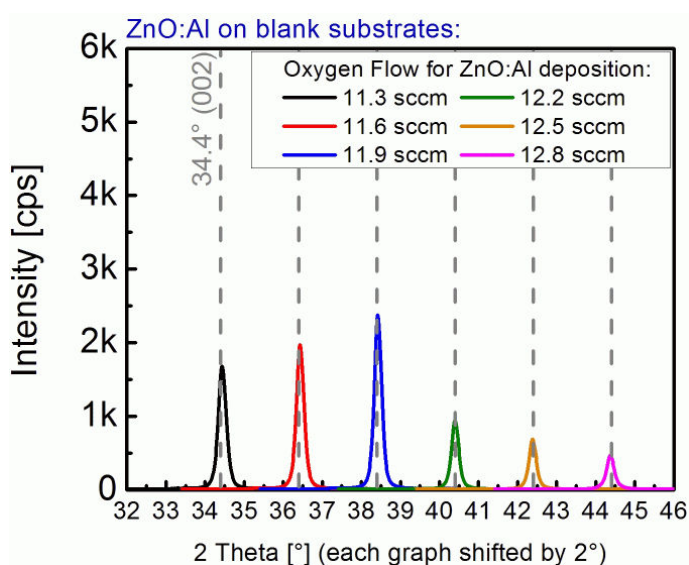


Figure 6.20: XRD-Scans of thick ZnO:Al films deposited on glass substrates at different oxygen flows. Graphs have been shifted along the 2θ -axis for better visualization. The vertical lines represent the position $2\theta = 34.4^\circ$ for each sample and oxygen flow, respectively. Due to a constant deposition time, the thickness of the films decreases with increasing oxygen flow (cf figure 6.13). At high oxygen flows there is a pronounced decrease in peak intensity that cannot be explained by the decreased film thickness solely.

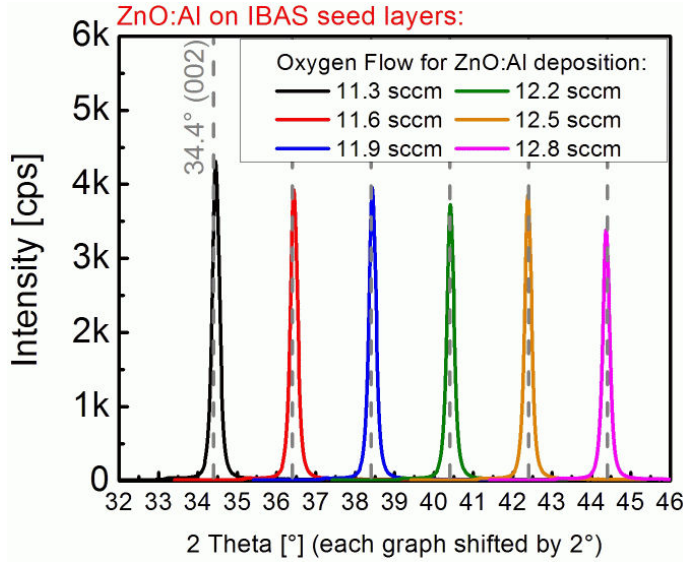


Figure 6.21: XRD-Scans of thick ZnO:Al films deposited onto glass substrates at different oxygen flows. Films have been simultaneously deposited with the samples shown in figure 6.20 but IBAS ZnO buffer layers were applied to improve the structural quality. Peak intensities are generally higher than without buffers and there is no notable decrease in the intensity at high oxygen flows even though film thickness decreases (cf figure 6.20) which provides evidence that the overall crystallinity or the structural order must even improve at high flows.

deduced from the XRD patterns. It is obvious that in any case the film structure profits from the presence of an IBAS buffer. But it is especially the regime of high oxygen flows where this improvement is boosted. Once again this is evidence that ZnO:Al films buffered by an IBAS layer are not affected in the same way as unbuffered films by the energetic oxygen ions during their growth. Moreover, since the damaging influence of bombardment is eliminated by the IBAS buffers, high oxygen flows appear to even improve the overall crystallinity and/or structural order.

Like shown for the films on silicon wafers in figures 6.16 and 6.17, figures 6.23 and 6.24 demonstrate that the formation of a (100) Bragg peak at high oxygen flows is also effectively suppressed by the IBAS buffers on glass, whereas the presence of this peak in the patterns of unbuffered films once more shows the impaired orientational order that typically occurs at high oxygen flows for standard films.

The far-reaching consequences of the findings presented in this section will be thoroughly discussed in the consecutive section. The insight gained about the influence of the highly energetic oxygen ions will facilitate an important extension of the growth model developed in chapter 5. This enhanced version of the model will disclose new strategies for the efficient fabrication of zinc oxide films with excellent structural order.

6.2 Generalization of the growth model

In chapter 5 a growth model has been developed that describes the specific improvement of zinc oxide films that grow under tailored ion assistance. One of

6.2. GENERALIZATION OF THE GROWTH MODEL

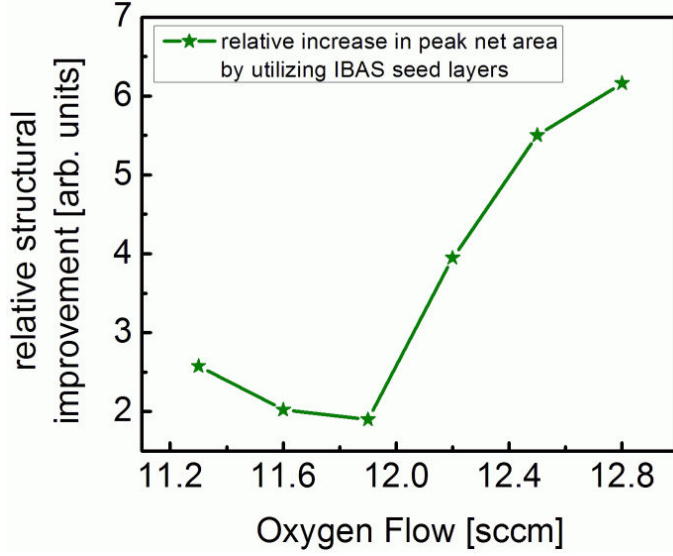


Figure 6.22: Comparison of ZnO:Al films grown on blank glass substrates and IBAS ZnO buffers (on glass) respectively. The relative ratio of the peak net areas deduced from the XRD scans shown in figures 6.20 and 6.21 are displayed. Note the strong improvement of structural quality especially at high oxygen flows.

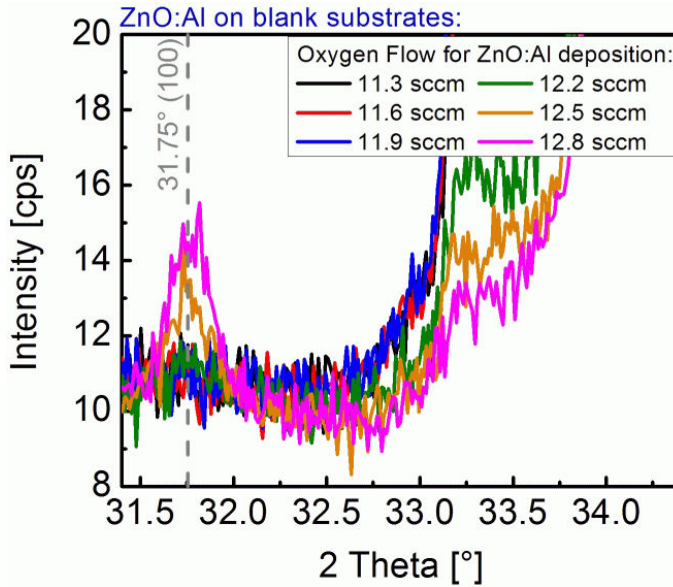


Figure 6.23: XRD scans of films that have been shown in figure 6.20. The region around the (100) Bragg peak of ZnO has been magnified. Similar to the patterns discussed in figure 6.16 the increase in the intensity of the (100) peak with increasing oxygen flow is evidence for a non-perfect texture, i.e. a degradation of structural order with increasing oxygen flow.

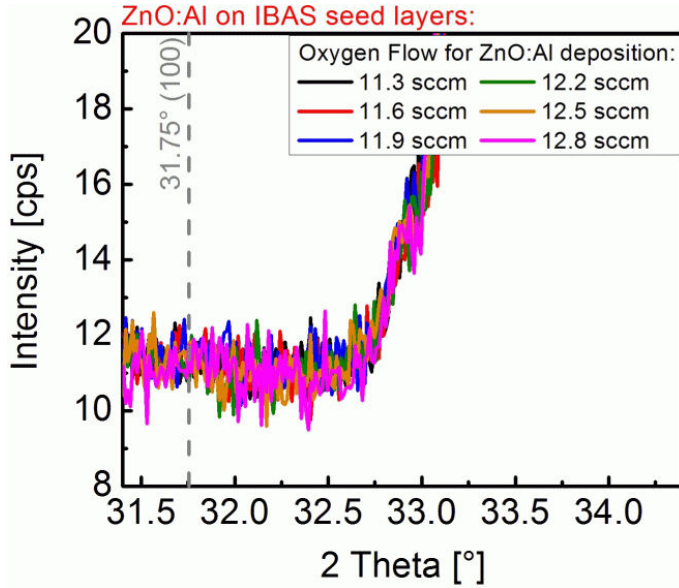


Figure 6.24: XRD scans of films that have been shown in figure 6.21. The region around the position of the (100) Bragg peak of ZnO has been magnified. As for the films shown in figure 6.17 there is no indication for a (100) peak in the diffraction patterns even at high oxygen flows. Consequently, the high orientational order ((002) fibre texture) is maintained upon utilization of the IBAS ZnO buffers. This is in contrast to the un-buffered reference films (cf figure 6.23).

the key findings has been that bombardment only during the early growth stage suffices for the fabrication of films with excellent structural order. In other words, it is essentially the nucleation stage that is sensitive to the tailored bombardment as far as the evolution of structural order is concerned. Prolonged bombardment mainly causes strain only but is otherwise ineffective. The investigations shown in section 6.1 however are clear evidence that these statements can even be extended and applied to the influence of the typically harmful negative oxygen ion bombardment inherent in reactive sputtering. This extension of the model is motivated by the following summary and interpretation of the results discussed in section 6.1:

1. X-ray diffraction patterns of ZnO:Al films sputtered at different oxygen flows without a buffer layer provide clear evidence that the standard films structurally deteriorate at elevated oxygen flows. This deterioration is characterized by a decreased net area of the prominent (002) peak of the ZnO fibre texture, by the accompanying emergence of a noticeable (100) Bragg peak and by a marked shift of the (002) peak position towards smaller diffraction angles which is typical for the formation of compressive stresses. Data from rocking curve measurements has also supported this finding since a clear broadening of the corresponding intensity distribution shows a declining order of the fibre texture. These facts clearly indicate a deterioration of structural order induced by negative oxygen ion bombardment.
2. Evolution of crystal structure for ZnO:Al films grown on modified IBAS ZnO buffer layers is distinctly different. First, orientational order is noticeably improved by such a buffer layer as evidenced by XRD scans. This

6.2. GENERALIZATION OF THE GROWTH MODEL

fact is very similar to the situation where tailored ion bombardment is interrupted after the nucleation stage. However, it has been demonstrated that the extent of structural improvement (in comparison to un-buffered films) markedly increases with increasing oxygen flow during ZnO:Al deposition. More astonishing though is the finding that the structural quality of the IBAS buffered ZnO:Al films even improves at elevated oxygen flows; A fact that clearly explains the large span that emerges between the films deposited with or without IBAS ZnO buffer layers at high oxygen flows.

3. The observations presented have a simple but far-reaching explanation: Not only the well-tailored xenon ion bombardment in the IBAS process but also the harmful bombardment of the films by negatively charged oxygen ions originating from the target surface has its primal impact during the nucleation stage of growth.

The 2nd statement reveals quite some interesting parallels to films grown by CVD or PLD processes. In chapter 2 it was discussed that in such processes high oxygen flows typically favour the formation of a sound c_{\perp} -texture. In a sputtering discharge, however, an increasing amount of oxygen also promotes the formation of negative oxygen ions and therefore the detrimental bombardment of the growing films. A striking conclusion drawn from the results discussed above is the fact that also in a sputtering process a high oxygen flow promotes the growth of c_{\perp} -textured films if the detrimental influence of the oxygen ions is suppressed by the utilization of IBAS seed layers. The 3rd statement explains how this is possible: Apparently, films develop excellent structural order in spite of significant oxygen ion bombardment if there is only a thin structurally sound buffer layer. Reversely this means that the oxygen ion bombardment harms structural order predominantly during the nucleation phase, comparable with the action of xenon ion bombardment, which also affects film growth mostly in the nucleation stage. This conclusion is particularly significant, since it discloses strategies for fabricating films with improved properties with minimum efforts and expenses. Only for the nucleation stage of growth, deposition parameters need to be optimized for structural quality, while for the major part of the coating, parameters may be utilized that are tuned for high output and effectiveness. Furthermore, these results are first evidence that a mechanism of preferred nucleation primarily governs the structural quality of sputtered zinc oxide films. Otherwise a mechanism of evolutionary selection should compensate for the ion damage that is apparently caused primarily in the initial growth stage of the un-buffered films.

The afore-mentioned conclusions are visualized in figure 6.25. On the left-hand side a standard reactive sputtering process is shown that is characterized by a significant bombardment of the growing film by negative oxygen ions. Formation of structural order during the nucleation regime is strongly inhibited. In consequence, the resulting structure of thick films shows an imperfect (002) fibre

CHAPTER 6. II: APPLICATIONS OF MODIFIED ZINC OXIDE STRUCTURES

texture only. The importance of structural order in the nucleation stage and its consequences on film growth has been explained in the growth model on page 104 and it also applies here. In a case where the nucleation stage is governed by a highly textured structure, as achieved in the IBAS process under tailored xenon ion bombardment for example, process conditions may be changed after completion of this stage, as depicted on the right-hand side of figure 6.25. On this modified buffer, the otherwise harmful oxygen ion bombardment in a standard sputtering process is entirely ineffective and thus a highly ordered (002) fibre texture regardlessly develops. Furthermore, high oxygen flows during this second growth stage even improve the structural quality of the films, despite the simultaneous promotion of energetic oxygen ion bombardment.

In chapter 7 the interesting topic about the mechanisms that govern texture formation in sputtered zinc oxide films will be further elucidated. Especially the relative contribution of mechanisms that typically act during different growth stages will be unravelled. In the course of the corresponding investigations it will also be shown how films with explicitly non- c_{\perp} -texture can be deposited upon utilizing tailored ion bombardment in the IBAS process. Finally, a significantly enhanced growth model for sputtered zinc oxide films will be developed. In the following section, however, the utilization of ZnO with improved c_{\perp} -texture as seed layers will be further investigated first. It will be demonstrated how the structural quality of epitaxially grown silver films can be improved by the modified seed layers.

6.2. GENERALIZATION OF THE GROWTH MODEL

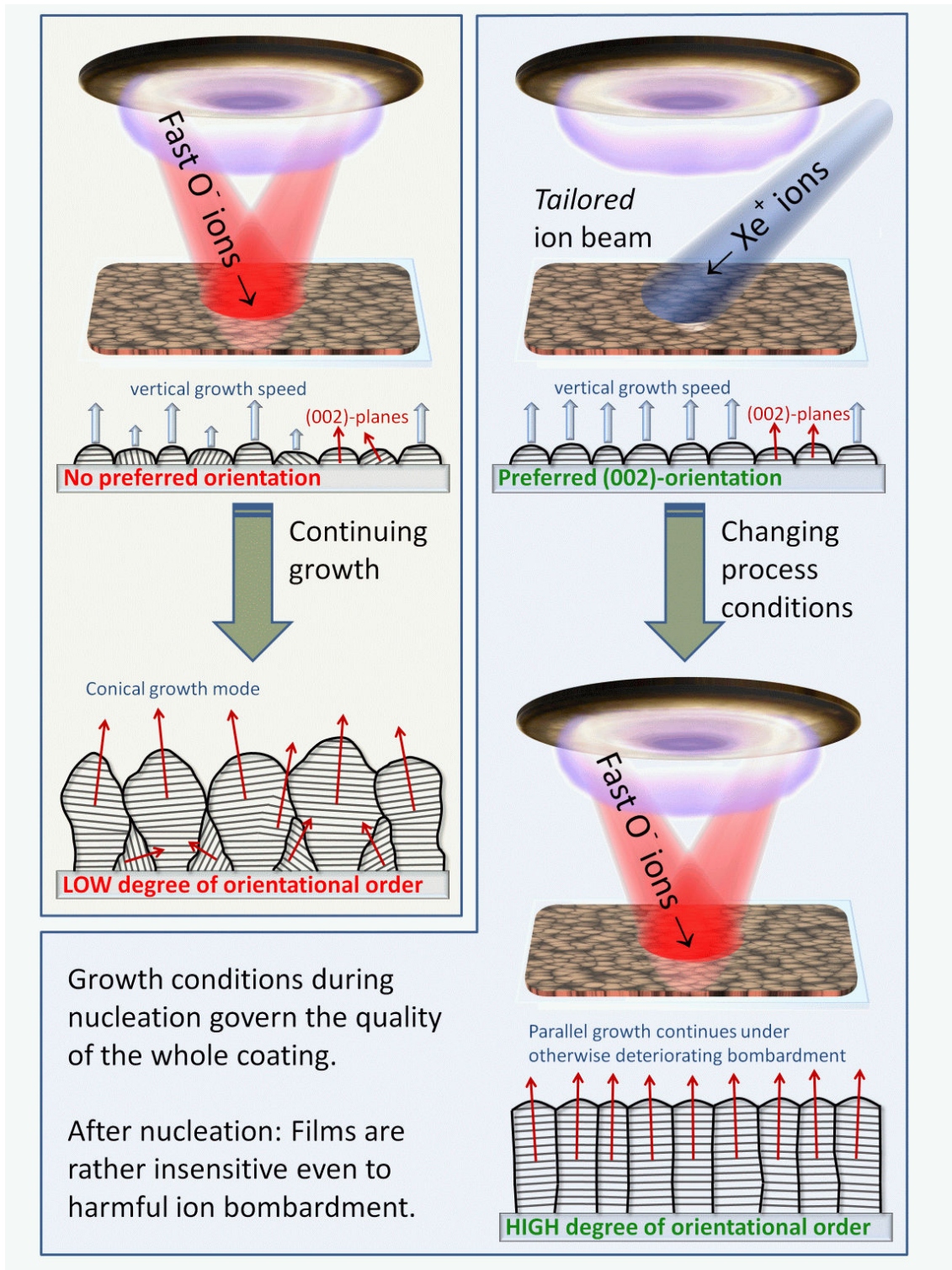


Figure 6.25: Generalized growth model: The influence of ion bombardment on the growth of zinc oxide films in different growth stages. See text for discussion.

6.3 Hetero-epitaxial growth of Ag thin films

6.3.1 Introduction

Zinc oxide thin films can be utilized to grow silver films with improved structural order. This is a consequence of a good epitaxial match between the ZnO (0001) and the Ag (111) crystal facets. This is shown in figure 6.26. It is evident that the {111}-planes of the fcc Ag structure exhibit hexagonal character which is why the epitaxial relationship is ZnO(0001)/Ag(111). It is evident from figure 6.26a that a coherent (1×1) boundary would result in a large strain of approximately +11 % of the silver structure along the (111)-plane. In [134] it is stated that for sputtered ZnO/Ag films an incoherent $(2 \times \sqrt{3})R30$ boundary is observed which is characterized by a strain of only -2.6 % for the silver film⁵. Since zinc oxide predominantly forms a (002) fibre texture, respective buffers promote the formation of highly oriented Ag films with the (111)-axis parallel to the substrate normal, i.e. to the (002)-axis of ZnO. Consequently, the orientational order of the ZnO film governs the structural quality of the Ag film. For this reason, it is obvious to investigate the influence of structurally improved ZnO films produced in the IBAS process on the structure formation of thin silver films.

The main motivation for fabricating silver films with improved structural quality arises from the strong correlation between the structure and the electrical conductivity of these films. One of the most prominent applications of silver films in the large area coating industry is in the fabrication of low-emissivity architectural glazing. The emissivity is directly proportional to the electrical resistance of metal films [135]. Upon definition of the emissivity ϵ by $R + T + \epsilon = 1$ and with $T = 0$ in the infrared spectral region, the emissivity can be expressed by the sheet resistance R_{\square} as follows:

$$\epsilon = 1 - R = \frac{4R_{\square}}{z_0} \approx 0.0106R_{\square}/\Omega, \quad (6.3.1)$$

where $z_0 = 377\Omega$ is the vacuum impedance. It is evident that a high electrical conductivity of the silver films is prerequisite to complying with the requirements of the application (i.e. low emissivity). A second basic requirement however is a maximum optical transmittance in the visible range of the solar spectrum. This imposes specific restrictions on the thickness of such silver layers, which typically ranges between 10 nm and 12 nm for that reason. The fabrication of thinnest possible silver films also directly improves the cost-effectiveness of the production line and thus the competitive capacity. While bulk silver exhibits an unrivalled resistivity of $1.586 \mu\Omega\text{cm}$, especially for very thin films the conductivity is limited by the structure for several reasons:

⁵See [134] for a detailed discussion of the ZnO(0001)/Ag(111) interface.

6.3. HETERO-EPITAXIAL GROWTH OF AG THIN FILMS

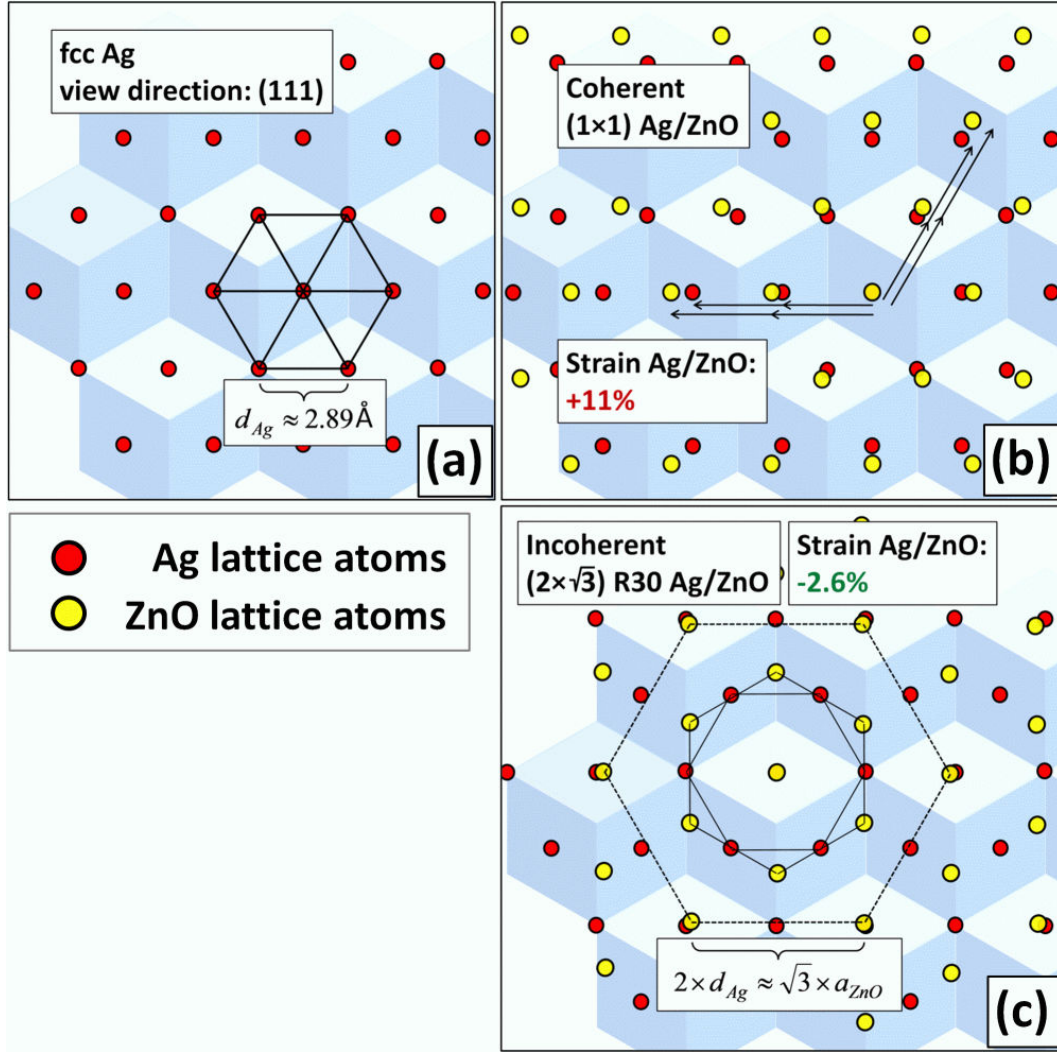


Figure 6.26: The Ag(111)/ZnO(0001) interface: (a) Ag (111)-planes have hexagonal character, (b) Upon formation of a coherent (1 × 1) Ag/ZnO boundary the lattice mismatch between Ag and ZnO is +11%, as calculated from $a = 3.25 \text{ \AA}$ for ZnO and $a = 4.086 \text{ \AA}$ for Ag. (c) An incoherent $(2 \times \sqrt{3})R30$ Ag/ZnO boundary yields a mismatch of only −2.6% and has been observed for sputtered films [134]. This boundary is characterized by a 30° rotational difference between the Ag and ZnO lattices.

CHAPTER 6. II: APPLICATIONS OF MODIFIED ZINC OXIDE STRUCTURES

- Film thickness and grain size become smaller than typical electron mean free paths. Scattering at boundaries and interfaces constitutes a dominant scattering channel.
- The surface roughness adds to diffuse scattering (cf e.g. [136,137]). Bottlenecks in lateral charge transport are formed by e.g. craters or trenches that locally lower the effective film thickness.
- The percolation limit sets a lower threshold to the thickness. As will be shown in this section, silver films slowly percolate. Films grown with thicknesses smaller than typically 10 nm still exhibit holes which of course significantly deteriorate charge transport.

It is fairly evident that a high structural order and, closely correlated, also the smoothness of the surface are key properties that need to be mastered for the fabrication of very thin silver films with outstanding electrical conductivity and hence low emissivity. In the following example the important role of structural quality will be demonstrated by means of an experiment that actually failed. In figure 6.27 x-ray diffraction patterns are displayed for layer stacks comprising a zinc oxide buffer layer (fabricated in a standard reactive sputtering process) and a top layer of silver with a targeted thickness of 24 nm.

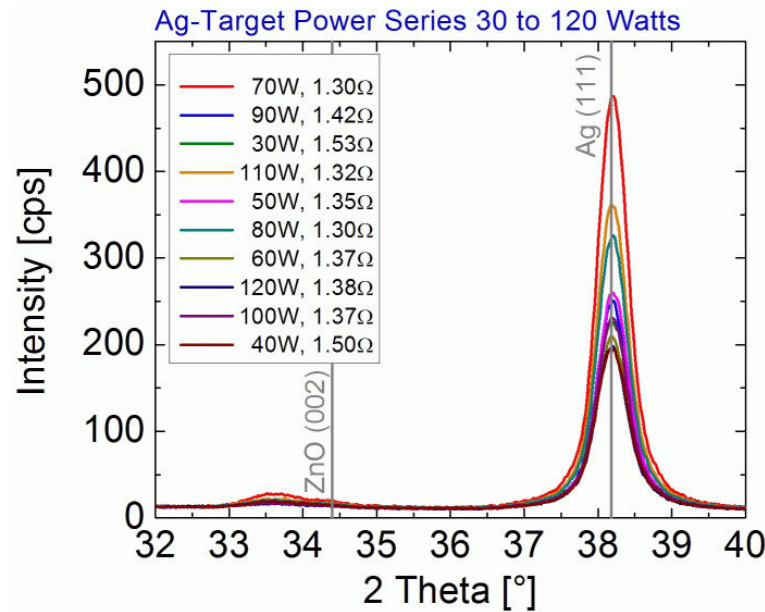


Figure 6.27: XRD patterns of Ag films deposited at different discharge powers. Silver films with targeted thicknesses of 24 nm have been deposited at discharge powers ranging from 30 to 120 W with the aim to determine an optimum growth condition. Standard zinc oxide layers were utilized as seed layers. ZnO (002) peaks are shifted towards lower angles due to lattice strain. The intensities of the Ag (111) peaks do not show any trend with the discharge power.

6.3. HETERO-EPITAXIAL GROWTH OF AG THIN FILMS

The original aim of this study was to determine optimum growth conditions for the silver layers upon variation of the discharge power of the metallic sputtering process utilized for silver film deposition. For this reason the silver film thickness was increased to 24 nm to reduce any influence of unintended thickness fluctuations. To guide the reader in apprehending the various patterns shown in figure 6.27 it is herewith declared that there is virtually no trend in the intensity of the silver (111) peak with discharge power. A detailed analysis of property correlations is depicted in figure 6.28. Plots (b) and (e) underscore the statement made above since there is no correlation of both the silver peak net area and the electrical resistivity with discharge power. However, plot (g) shows that film thicknesses differ for different discharge powers. But as expected, film thickness alone does not play a major role for these comparatively thick films, which is demonstrated in plots (a) and (d). It was finally found that there was a drift in the quality of the underlying zinc oxide buffer layers and a corresponding clear trend in the silver peak net area, as displayed in plot (c). Accordingly, the structural quality of the silver films is proven to govern the respective resistivity (f). In summary this means that even though the deposition conditions for the silver films and also the thickness of these films differs for all investigated films, their electrical resistivity is dominated by the structural quality imposed by the utilized buffer layers solely. This fact is obvious motivation for the application and investigation of structurally tailored zinc oxide films grown by the IBAS process as seed layers for the growth of thin silver films.

6.3.2 Silver structure improvement by modified ZnO seed layers

In the following it will be investigated and discussed which influence the properties of structurally modified zinc oxide seed layers have on the growth of thin silver films. Starting with a proof of principle, figure 6.29 clearly demonstrates that the structural improvement of ZnO films produced in the IBAS process transfers to the formation of highly ordered Ag films in comparison to the application of a standard ZnO seed layer. Seed layers of different thicknesses have been utilized and it appears that the thinnest layer (≈ 10 nm) yields the best silver structure. Furthermore, the electrical resistance could be decreased to $3.9\ \Omega$ (reference film: $5.2\ \Omega$). However, the relationship between the structural modification and the improvement of electrical conductivity does not seem to be entirely clear. Compare for example the silver films on the 30.9 nm thick IBAS and REF seed layers. Even though the structural difference of the silver films is evident, there is no similar trend in the resistance. Possible reasons for that will be discussed in a later section.

In a second experiment ultra-thin IBAS ZnO seed layers have been tested (figure 6.30). The thickness of the IBAS ZnO seed layers ranges from 2.45 nm

CHAPTER 6. II: APPLICATIONS OF MODIFIED ZINC OXIDE STRUCTURES

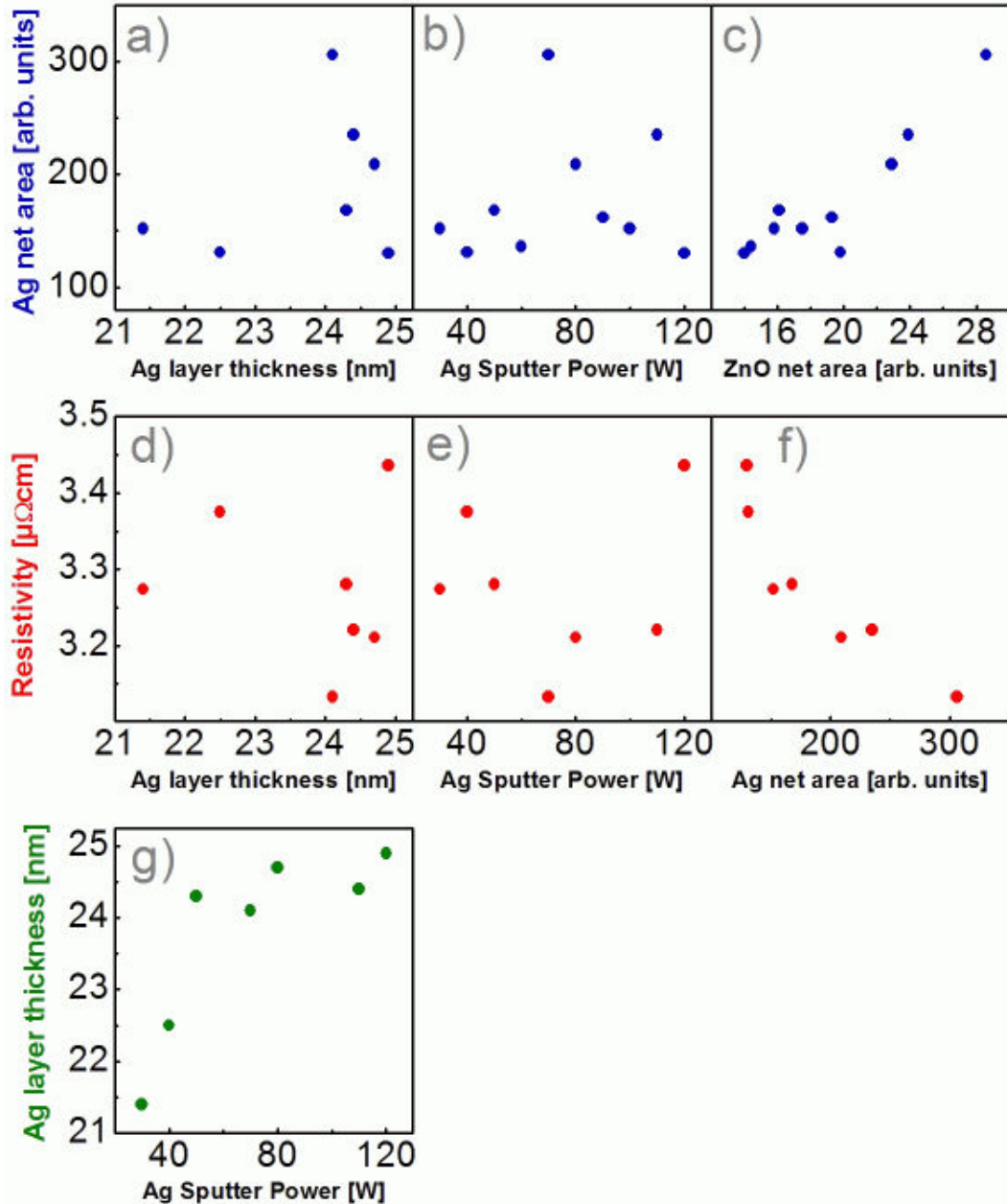


Figure 6.28: Analysis of Ag films sputtered at different discharge powers onto ZnO seed layers. Evident from graph (g) is a variation in Ag layer thickness for different discharge powers. Graphs (a) and (d) show that this variation does not dictate structural and electrical properties. Neither does the discharge power, as demonstrated in graphs (b) and (e). Surprisingly, the structural quality of the Ag films strongly follows a variation in the ZnO seed layer quality instead, which is similarly true for the resistivity (graphs (c) and (f)).

6.3. HETERO-EPITAXIAL GROWTH OF AG THIN FILMS

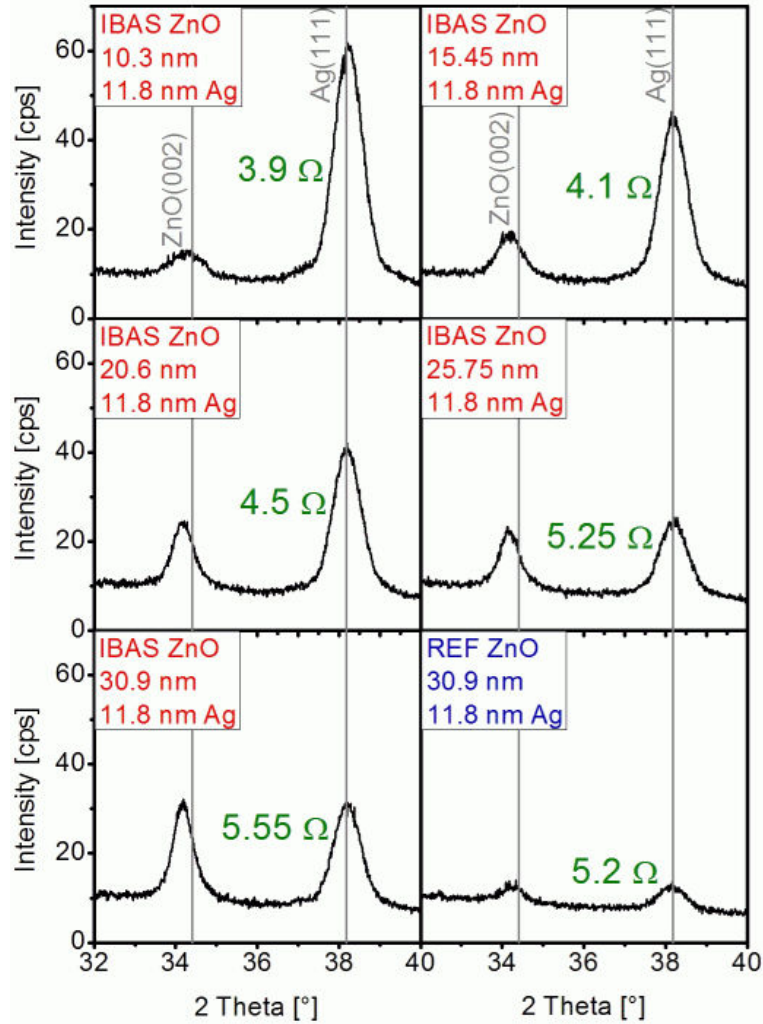


Figure 6.29: XRD scans of ZnO seed layers deposited in an IBAS process and subsequently coated with Ag. A reference film, the ZnO seed layer of which was not grown under ion assistance, was similarly deposited. The thickness of the seed layers has been varied from 10.3 nm to 30.9 nm. The Ag film structure is generally improved by the IBAS seed layers in comparison with the reference sample. An improvement of the conductivity with the Ag structure is not as strict. Film thicknesses were determined from an XRR scan for one of the layer stacks and an additional silver reference. Thicknesses for all films were then calculated under the assumption of constant deposition rates.

CHAPTER 6. II: APPLICATIONS OF MODIFIED ZINC OXIDE STRUCTURES

to 12.25 nm as calculated from the deposition rates which was determined from an XRR investigation for one of the samples. It is obvious from the figure that seed layers with a thickness of only 2.45 nm are insufficient for the growth of an ordered silver film structure. Upon increasing the seed layer thickness to 4.9 nm there is an instant increase in silver film structure and there is no significant change upon further increase of thickness. This finding is well consistent with the results shown in section 6.1 (figure 6.12). A clear improvement in comparison with the silver structure formed on a standard ZnO reference seed layer is also quite evident. However, the electrical resistance does not show any trend, which means that other parameters influence these results, as will be discussed later.

This inconsistency as well as some of the unclear correlations in figure 6.29 might also be linked with non-ideal deposition conditions for the silver sputtering process. The silver films shown in figures 6.29 and 6.30 have been deposited in the same coating tool where the IBAS process is performed (coater 1). Parameters for silver film deposition have however been optimized for coater 2 in earlier works. Consequently, all silver films discussed in the following have been deposited in this tool after deposition of the seed layers in the IBAS coater. While standard microscope slides were used as a substrate for some of the specimens discussed above, float glass was utilized for the fabrication of the samples that will be discussed in the remainder of this section.

Figure 6.31 shows XRD patterns of films where the IBAS and reference ZnO seed layers have been fabricated in the IBAS tool (coater 1) while the silver films have been deposited in coater 2 after an airbreak. It is evident that the airbreak does not diminish the seed layer effect and that the IBAS seed layers significantly improve the order of the silver film structure.

It is also evident that the improvement of the silver structure nicely correlates with an improvement (decrease) of the electrical resistivity which is displayed in figure 6.32 as a function of the silver (111) peak net area deduced from the XRD scans. The thickness of the seed layers is approximately 8 nm while the silver films have a nominal thickness of 12 nm as calculated from the deposition rate.

Since especially lattice strain might have a marked influence on the hetero-epitaxial growth of silver on zinc oxide, possible correlations of this kind are now investigated in detail. In section 6.1.1 it has been demonstrated how the mean lattice strain and the surface roughness of IBAS ZnO films can be tailored by means of an additional ion-etching treatment. Figure 6.33 shows XRD patterns for silver films that have been deposited onto differently treated seed layers. The thickness of all seed layers has been approximately 20 nm after deposition. Some of these layers however have been ion-etched for different times prior to silver layer deposition. From the etch rate determined in section 6.1.1 it is expected that the seed layer etched for 600 s has a thickness of approximately 15 nm. The silver films have a thickness of 12 nm.

It is obvious from figure 6.34 that ion-etching does actually not improve the silver film structure any further. Instead, there is a decrease in structural quality

6.3. HETERO-EPITAXIAL GROWTH OF AG THIN FILMS

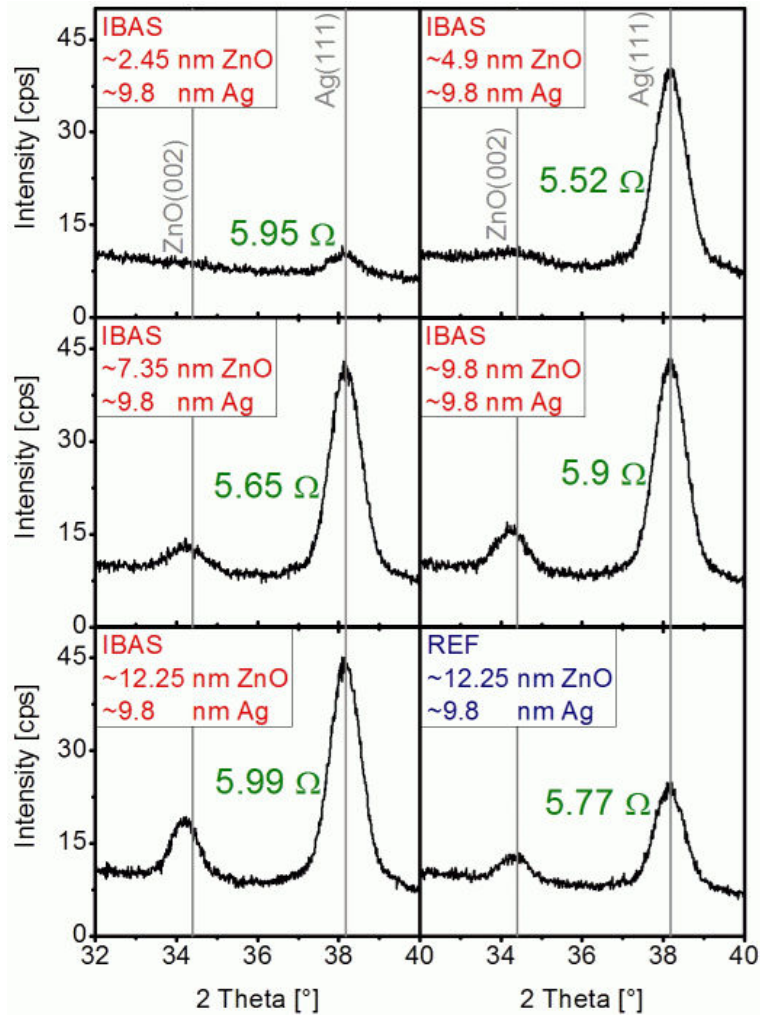


Figure 6.30: XRD scans of ZnO seed layers deposited in an IBAS process and subsequently coated with Ag. The thickness of the seed layers was varied to determine the minimum thickness that is needed to improve the Ag structure. Consistent with results shown in section 6.1 the minimum thickness is between 2.45 nm and 4.9 nm. The reference film with a standard ZnO seed layer exhibits a weaker Ag structure. See the caption of figure 6.29 for the determination of film thicknesses.

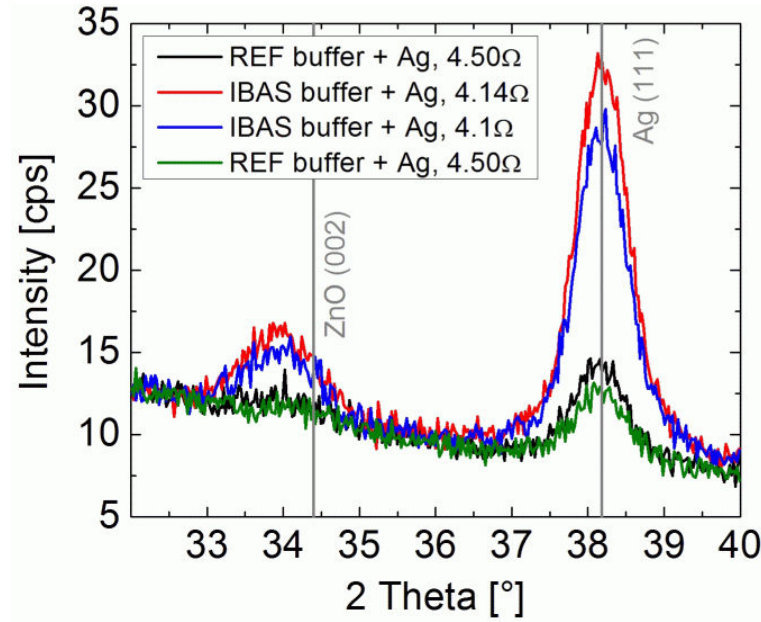


Figure 6.31: XRD scans of 12 nm thin Ag films sputtered onto 8 nm thin IBAS and standard ZnO seed layers, respectively. The structural quality of the IBAS ZnO films and the corresponding improvements of the Ag films are evident from the intensities of the (002) and (111) peaks of ZnO and Ag, respectively.

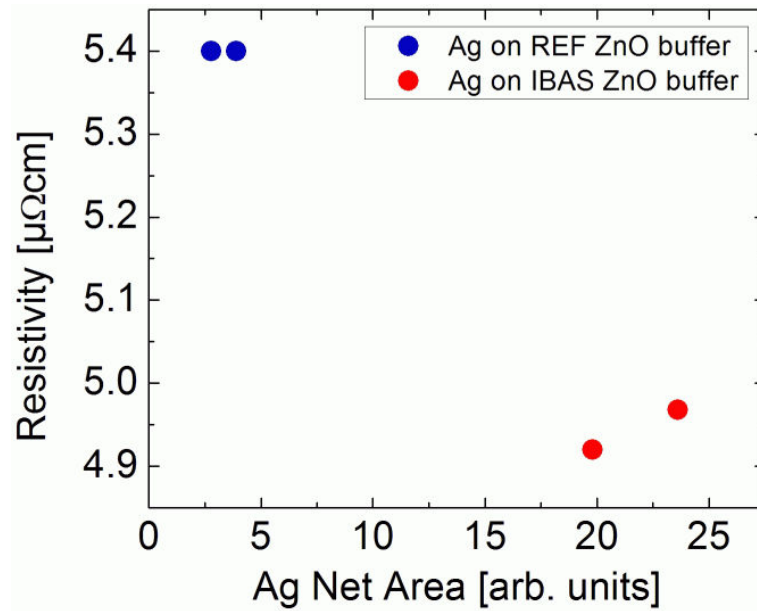


Figure 6.32: Electrical resistivities of the films shown in figure 6.31 as a function of the Ag (111) peak net area. The decrease of the resistivity clearly correlates with the structural improvement induced by the application of modified IBAS ZnO films.

6.3. HETERO-EPITAXIAL GROWTH OF AG THIN FILMS

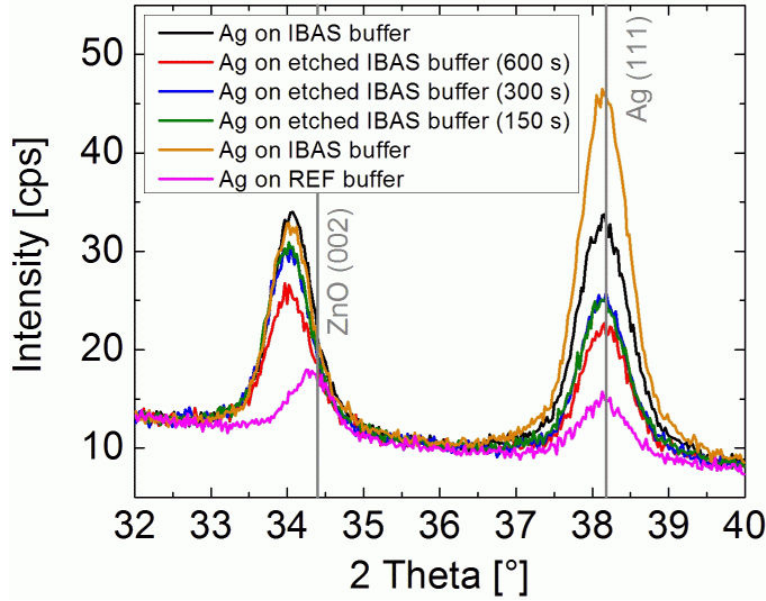


Figure 6.33: XRD scans of 12 nm thin Ag films on IBAS ZnO seed layers and one reference ZnO film, respectively. Some of the IBAS ZnO films were ion-etched prior to Ag deposition to affect strain and surface roughness (cf section 6.1.1 for a detailed discussion of ion-etching). The etching times are given in the legend and range from 0 to 600 s. See figure 6.34 for a discussion of the diffraction patterns.

that correlates to some extent with the decrease in the net area of the (002) ZnO peak. It should however be taken into account that this decrease is mostly due to the decrease in ZnO film thickness as a consequence of the etching step. For example, the thickness of the film that has been etched for 600 s should have decreased by approximately 25 %. Since the net area of the as-deposited seed layers in arbitrary units is approximately 18 this would coincide with a decrease of the net area of the (002) peak by 4.5 to 13.5 for the etched film, which agrees well with the measured value shown in figure 6.34. Hence, it must be considered that probably the changes in surface structure upon ion-etching instead of a reduction in the structural quality of the ZnO films diminishes the effectiveness of the seed layer.

Except a scattered value for one of the non-etched seed layers, this trend is also evident for the resistivity of the silver films grown on this series of seed layers. The decrease in the Ag (111) net area appears to coincide with an increase in the electrical resistivity (figure 6.35). Since the effect of the altered surface structure of the seed layers upon ion-etching is unclear and since the shift in the ZnO (002) peak position to lower angles of 2θ by approximately 0.05° is not

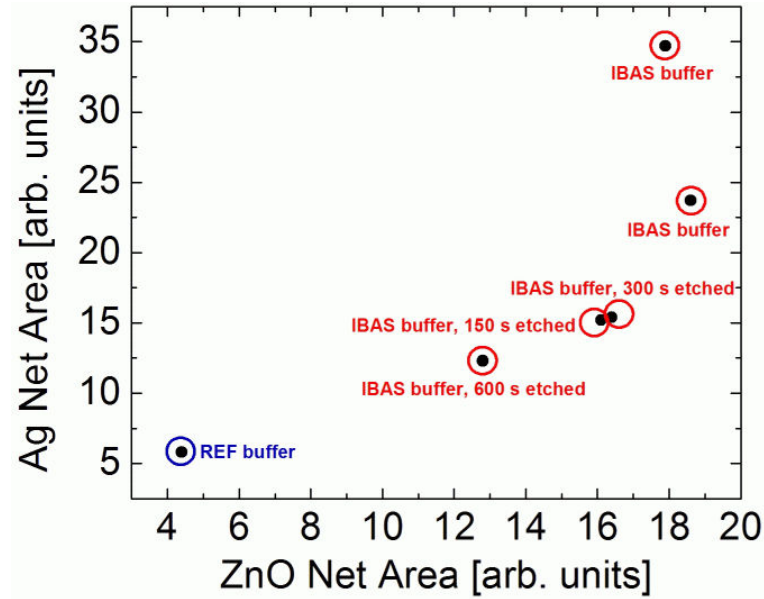


Figure 6.34: Analysis of the diffraction patterns of Ag films on ion-etched IBAS ZnO buffers. The Ag (111) peak net areas are plotted against the ZnO (002) peak net areas. Both quantities have been extracted from the diffraction data shown in figure 6.33. Except some scattering the Ag film quality (net area) correlates with the net area of the ZnO buffers. Assuming a linear correlation between ZnO film thickness and (002) peak net area for the high quality IBAS ZnO structures, the decreased net area for the buffer etched for 600 s can be explained by a reduction in film thickness solely. However, the silver film quality degrades with decreasing ZnO (002) net area.

strongly pronounced for these etched films⁶, the influence of film strain will now be investigated with a more effective strategy.

Dual zinc oxide seed layers were prepared consisting of an ion-bombarded IBAS ZnO layer at the substrate interface and a non-bombarded ZnO layer grown on top. The method of preparation of these dual buffers is principally identical to that utilized for films discussed in chapter 5 (cf e.g. figure 5.2). There it has been shown that by interrupting the ion bombardment after different durations the mean lattice strain can be significantly influenced. Figure 6.36 displays such dual ZnO seed layers with a total thickness of 17 nm that were applied to the growth of silver layers with a nominal thickness of 12 nm. The deposition times for the bombarded (IBAS) and the un-bombarded (REF) fractions of the seed layers are given in the legend. These times can be regarded as relative layer thicknesses. It is evident that the change in the ZnO (002) peak position can be changed very efficiently with this preparation method. The maximum shift in peak position achieved is approximately 0.32° in 2θ which is larger by a factor of

⁶Compare with figure 6.5, where a similar shift of 0.07° in 2θ has been found for an etching time of 600 s.

6.3. HETERO-EPITAXIAL GROWTH OF AG THIN FILMS

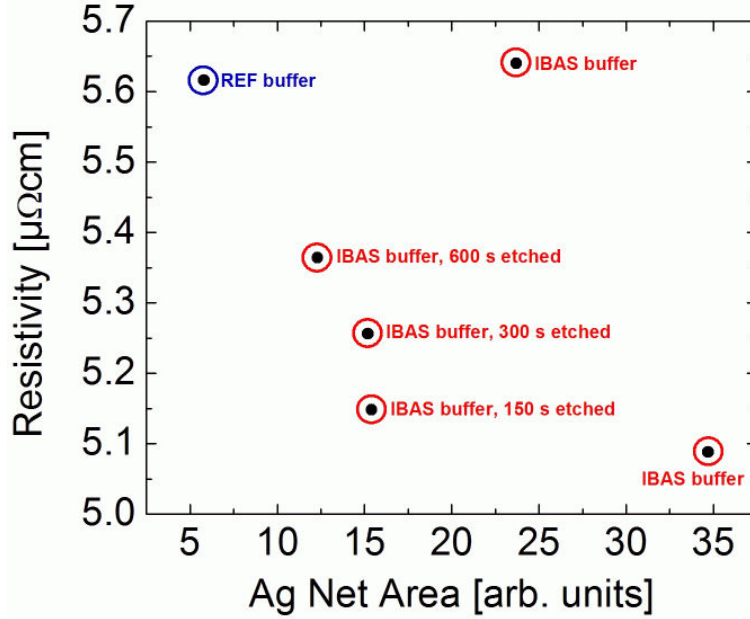


Figure 6.35: The resistivity of Ag films deposited on ion-etched IBAS ZnO films and corresponding reference films is clearly governed by the Ag (111) peak net area (except one scattered value). The films denoted with “IBAS buffer” have not been etched. The film denoted with “REF buffer” is a Ag film on a ZnO seed layer that was grown without ion assistance.

6 in comparison to the ion-etching method. Thus, if there is an influence of ZnO lattice strain on the structure formation of the silver films, then it might become evident in this experiment. There is one restriction to this assumption however, which will be discussed with the following results.

In figure 6.37 the properties of the seed layers and the silver films are summarized. The trend in the Ag (111) peak net area as a function of the ZnO (002) peak position is not entirely clear since there seems to be some scattering of values. However, the correlation between the resistivity and the Ag peak net area is very clear since resistivity monotonically decreases with increasing net area, i.e. structural quality. In contrast, the resistivity is not a monotonically decreasing function of the ZnO (002) peak position. In summary, the influence of the ZnO lattice strain on the electrical properties does not seem to be very strong.

The question also arises to which extent the strain observed in the XRD measurements can be expected to have an influence on the growth of silver films. In chapter 5 it has been demonstrated that a clear distinction must be made between the vertical strain as measured by XRD (in Bragg Brentano geometry) and the biaxial strain in direction of the substrate plane. Hence, the observed strong shifts in the ZnO (002) peak position do probably not coincide with a large change in interatomic distance perpendicular to the growth direction. Therefore, a strong influence of the observed peak shifts cannot without limitations be as-

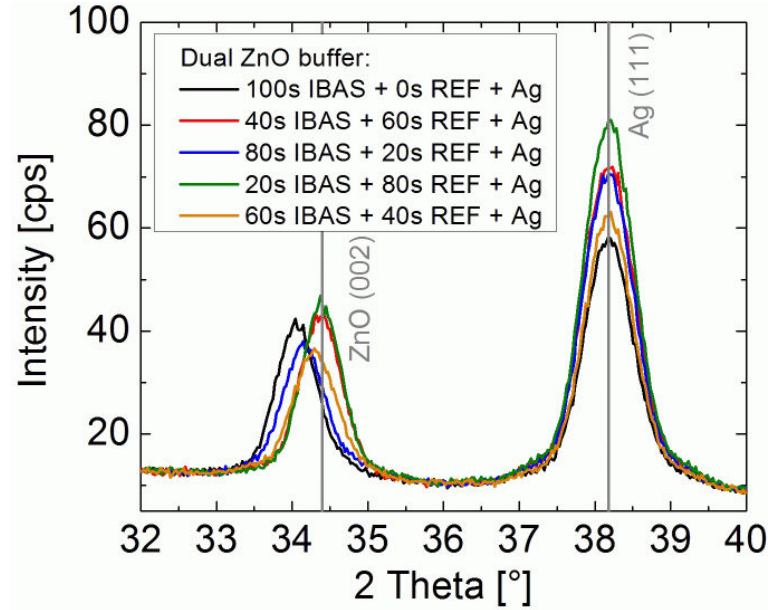


Figure 6.36: XRD scans of 12 nm thin Ag films on IBAS ZnO seed layers. The ZnO seed layers are called “dual buffers” since bombardment in the IBAS process was interrupted after different durations during ZnO film growth. This method allows for a significant change of film strain. A detailed discussion about the origin and the nature of this strain is given in the text. A possible influence of the ZnO seed layer strain is depicted in figure 6.37.

sumed to strongly affect hetero-epitaxial nucleation of the Ag films. A different approach to significantly influence film strain almost isotropically is the strong oxygen ion bombardment that typically causes significant strain in standard deposition processes (see e.g. figure 6.19). In some situations this strain can cause shifts of the (002) peak by up to -0.9° from experience before relaxation occurs upon reaching the maximum yield stress. Interestingly, from figure 6.26 it is evident that for the formation of an incoherent $(2 \times \sqrt{3})R30$ boundary a negative strain of -2.6 % for the silver film would be advantageous for epitaxial growth. On the other hand a positive strain of +2.67 % of the ZnO lattice would similarly yield perfect epitaxial match. Under the assumption that lattice strain caused by ion implantation might be approximately isotropic, we may calculate the respective change in the c-axis lattice parameter and hence the corresponding shift of the (002) peak in an XRD pattern. From table 4.1 we deduce that the mentioned strain of +2.67 % would correspond to an inter-planar distance d_{002} of 2.6723 Å. From Bragg’s law it follows that the diffraction angle 2θ is then 33.51° ⁷. An experiment where significant strain has been induced by the growth conditions is shown in figure 6.38. Even though the structural quality

⁷Note: The lattice strain that corresponds to typical 2θ -angles ($\geq 34^\circ$) achieved by buffer layer variations as shown in figure 6.36 is in the range 0-1 % only.

6.3. HETERO-EPITAXIAL GROWTH OF AG THIN FILMS

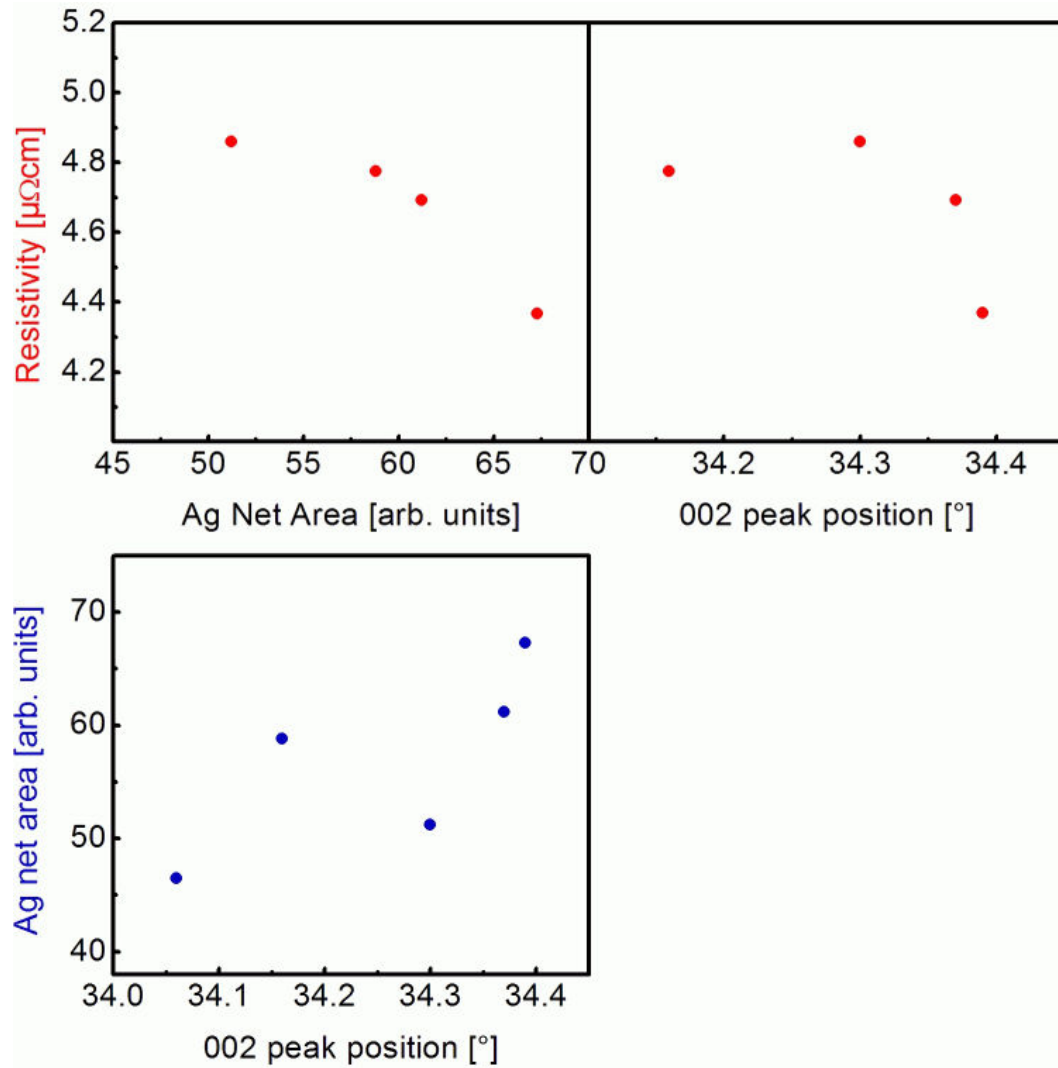


Figure 6.37: Analysis of Ag films deposited on differently strained IBAS ZnO seed layers (cf figure 6.36). While the correlation of the Ag (111) peak net area and the resistivity with the ZnO (002) peak position is not unique, there is a clear correlation of the resistivity with the net area of the (111) Ag peak, i.e. with the structural quality of the Ag film.

CHAPTER 6. II: APPLICATIONS OF MODIFIED ZINC OXIDE STRUCTURES

of the modified IBAS ZnO seed layers is strongly improved, the silver film quality is largest on the massively strained buffer deposited in a non-optimized standard process. The (002) peak position of this ZnO buffer is close to 33.5° . Note that also the electrical resistance of that silver film is improved with respect to the films on IBAS seed layers, as indicated in the legend. This result suggests that strain might play a decisive role in determining the silver layer quality. Adequate strain might even compensate for an otherwise imperfect structural quality.

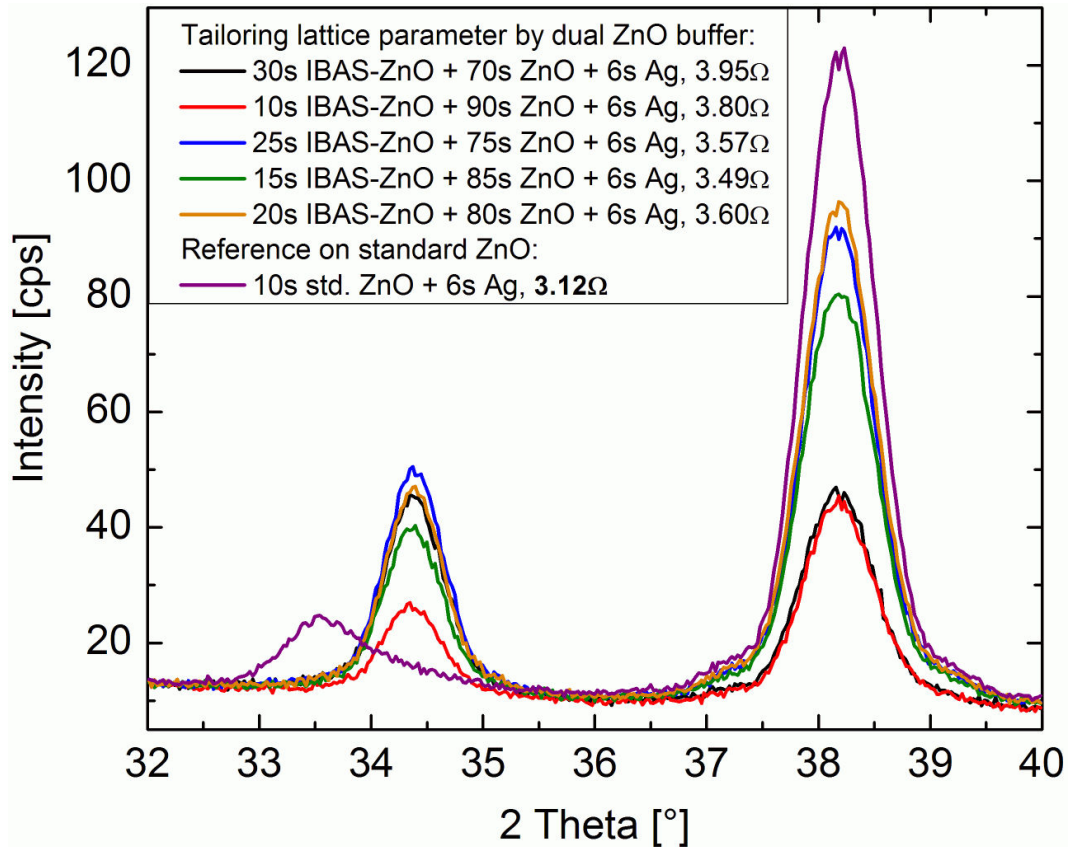


Figure 6.38: XRD patterns of Ag films grown on massively strained seed layers. One of the seed layers which was deposited in a non-optimized standard ZnO deposition process in coater 2 is largely strained by oxygen ion bombardment. Ag films have been deposited on this buffer and on modified seed layers from an IBAS process. Interestingly, even though the IBAS seed layers exhibit superior structural quality, the silver film grown on the strained reference film exhibits topmost quality of the (111)-texture. This coincides with the lowest electrical resistance, as indicated in the legend.

The data discussed in this section can be summarized as follows:

1. There is unambiguous evidence that the improved structural quality of IBAS zinc oxide seed layers promotes the growth of silver films with markedly

6.3. HETERO-EPITAXIAL GROWTH OF AG THIN FILMS

increased structural quality. This correlation has been observed for all investigated specimens. A minimum thickness of the IBAS seed layers is required which consistently appears to be identical to the minimum buffer layer thickness determined in section 6 for the growth of ZnO:Al films.

2. Generally there seems to be a correlation between the structural quality, as measured by the net area of the Ag (111) Bragg peak, and the electrical conductivity of the silver films. However, albeit this correlation has often been observed (also in data which is not shown in this work) there seem to be exceptions to that rule. The data presented in figures 6.29 and 6.30 are examples for this.
3. In experiments where quantities other than either ZnO or Ag texture have been intentionally varied, the structural quality of the Ag film always seems to dominate electrical conductivity but with the exceptions mentioned in statement 2.
4. There is evidence that the strain of the zinc oxide seed layers plays a very dominant role. Significantly strained ZnO films might promote epitaxial growth and the electrical conductivity of the silver layer. The influence of strain might even compensate for an imperfect structural order of the ZnO seed layer. Further confirmation of this statement is however needed but will not be given in the present work.

In the following the investigation of the influence of zinc oxide seed layers on the growth of silver films will be extended by investigations on a microscopic scale. The results of a corresponding growth study will be presented and evaluated.

6.3.3 Microscopical growth study of Ag films on ZnO seed layers

In the introduction to section 6.3 it has already been mentioned that, aside orientational order of the crystal structure, surface topography and percolation control the electrical performance of thin silver films. In the following, the growth evolution of thin silver films on ZnO seed layers will therefore be investigated. It will also be demonstrated how silver films evolve on structurally insufficient ZnO seed layers to illustrate the importance of having buffers that are of high quality. Finally, the influence of highly ordered IBAS ZnO seed layers on silver film growth will be elucidated.

In figure 6.39 the surface topography of thin silver films is shown which were grown on ZnO seed layers that had been deposited in a standard sputtering process prior to silver deposition. The deposition times for the silver coatings were varied to yield nominal layer thicknesses ranging from 2 nm to 12 nm. It is

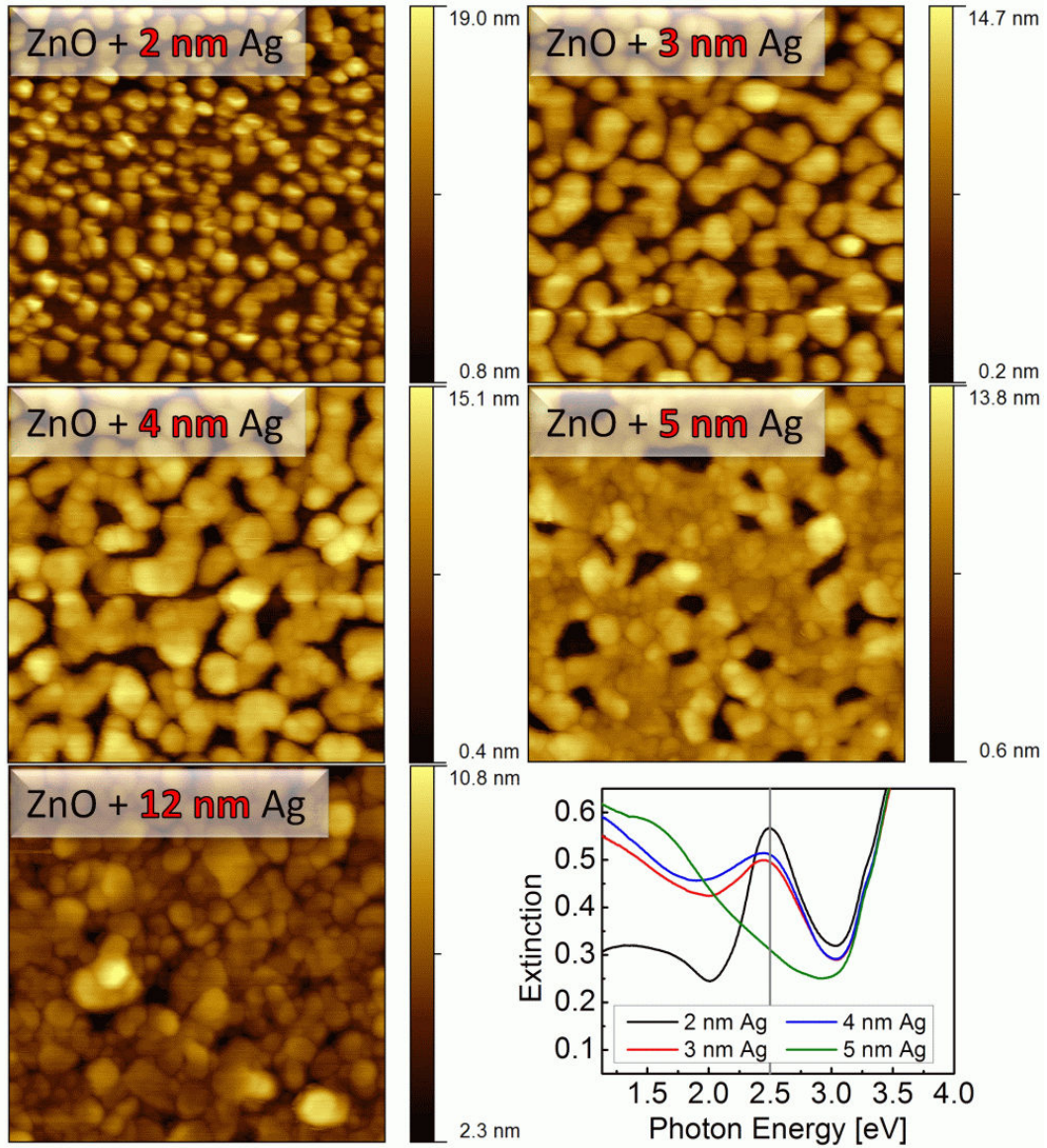


Figure 6.39: AFM study of nucleation and growth of Ag films on standard ZnO seed layers (no ion assistance). Shown is the evolution of Ag surface topography with increasing nominal thickness as controlled by the deposition time and based on a known and constant deposition rate. It is evident that the roughness which is apparent in the height scale of the scans is larger than the nominal film thickness. There is of course some influence also from the roughness of the ZnO seed layer. Ag film formation is governed by island formation and subsequent island growth accompanied by sintering or island migration to form Ag clusters. The film with a nominal thickness of 5 nm is not yet fully percolated. This has been observed for films up to 8 nm (not shown here). Films of 12 nm are closed but still rough. Incompletely percolated Ag films show a broad particle plasmon resonance as apparent from the optical extinction spectra.

6.3. HETERO-EPITAXIAL GROWTH OF AG THIN FILMS

evident that the nucleation and coalescence regime of silver film growth is strongly governed by island formation (*Volmer-Weber* growth) followed by sintering or island migration (cf [40]). It is apparent that due to the non-wetting behaviour of Ag on the ZnO film surface the silver film is not closed even at a thickness of 5 nm. It was found (not shown here) that silver films exhibit holes up to thicknesses of approximately 8 nm. In other words, the typical silver film thicknesses of 10-12 nm resemble films just slightly beyond the percolation limit defined by the thickness that corresponds to the first fully closed silver surface. Figure 6.39 also displays a film with a thickness of 12 nm. This film exhibits a closed silver surface, but with clearly visible (shallow) holes and hillocks which likely are remnants of the late percolation. Incomplete percolation of thin silver films is also visible with the bare eye since the isolated silver islands and clusters exhibit a strong particle plasmon resonance around a photon energy of approximately 2.5 eV which results in a pronounced pink colour. Corresponding extinction spectra are shown in figure 6.39 for the thin films.

An interesting observation is made when investigating silver film formation at a different substrate position. As has been discussed e.g. in section 6.1 (cf figure 6.19) film properties of ZnO films, and therefore also of the ZnO seed layers applied for silver film growth, may significantly depend on the position above the target. Furthermore, also silver film growth is inhomogeneous along the substrate at least in terms of deposition rate which is largest at the substrate centre and drops to approximately 70-80 % at the position above the racetrack. Therefore, the films discussed in figure 6.39 have also been investigated at a substrate position directly above the target racetrack⁸. Corresponding results are depicted in figure 6.40. It is quite obvious that coalescence of the silver films greatly differs at this substrate position. In contrast to the substrate center, the tendency to form flat clusters appears to be much weaker above the racetrack resulting in comparatively rough surfaces also at elevated thicknesses. By comparing figures 6.39 and 6.40 it is clear that this difference is not simply resulting from the shift in film thickness. At present it is unclear whether the different growth behaviour at different substrate positions is an effect only of the different ZnO seed layer structure or also of the geometry of the silver sputter discharge and corresponding Ag particle flux.

The important role of the structural quality of the ZnO seed layer in silver structure formation is demonstrated in figure 6.41. As has been proven e.g. in figure 6.30 a seed layer thickness of only 2 nm is insufficient to grow high quality silver films even if an IBAS seed layer is applied. Consequently, a silver film grown on such a thin buffer exhibits a very weak structural order which is also resembled in the surface topography. Figure 6.41 clearly shows that large silver grains with random orientation are embedded in a probably also randomly oriented small-

⁸Investigations shown in figure 6.39 have been performed exactly at the sample centre.

CHAPTER 6. II: APPLICATIONS OF MODIFIED ZINC OXIDE STRUCTURES

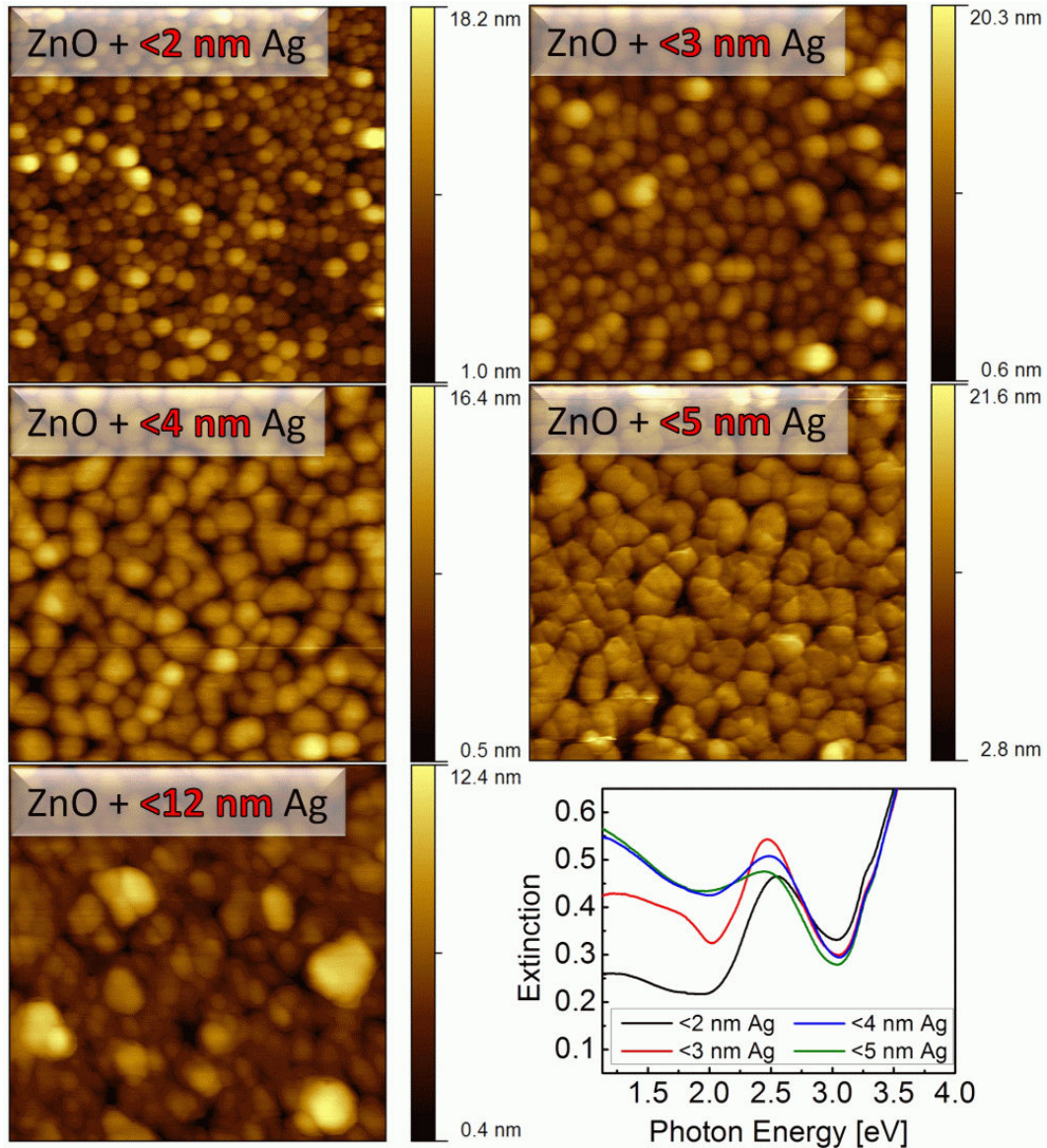


Figure 6.40: AFM study of nucleation and growth of Ag films on standard ZnO seed layers (no ion assistance). The specimens are identical to those discussed in figure 6.39 but were investigated at a substrate position that was directly above the target racetrack during deposition of the ZnO and Ag films. Percolation of the surface appears to be different from the sample centre (fig. 6.39), resulting in films that seem to exhibit rougher surfaces. A particle plasmon resonance is also seen at this substrate position. Film thickness is smaller than at the substrate centre by about 20-30 %, i.e. the notation “< 12 nm” means that the silver layer is approximately 9-10 nm thin.

6.3. HETERO-EPITAXIAL GROWTH OF AG THIN FILMS

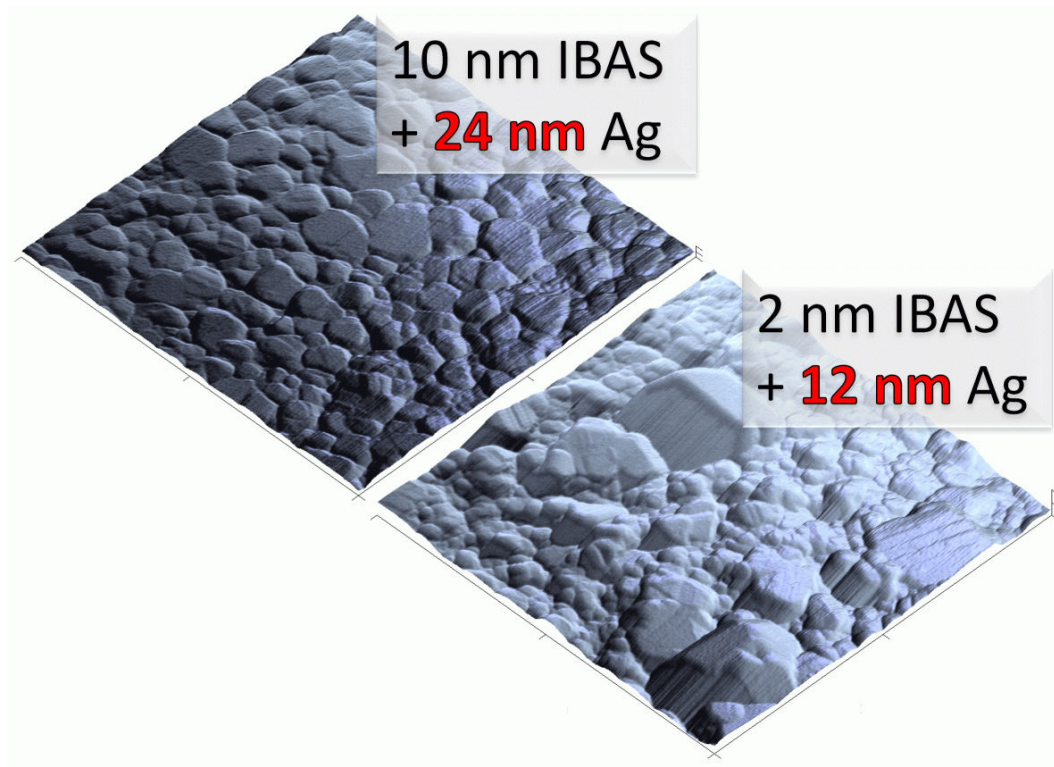


Figure 6.41: Ag surface topography: Example of high and low quality seed layers. In the lower right a 12 nm thin Ag film is shown which was grown on a too thin IBAS ZnO buffer. The topography is governed by large but randomly oriented grains surrounded by small and probably also randomly oriented grains. The top left shows a 24 nm thick Ag film grown on a high quality 10 nm thick IBAS ZnO seed layer. The flat grain/cluster tops represent a near-optimum surface topography.

CHAPTER 6. II: APPLICATIONS OF MODIFIED ZINC OXIDE STRUCTURES

grained background. A comparatively perfect surface structure is depicted in the same figure, where a thicker silver film has been deposited onto a well-structured 10 nm thick IBAS ZnO seed layer. This example clearly underlines the necessity for applying high quality ZnO seed layers for the hetero-epitaxial growth of silver films.

In a final attempt to unravel the influence of IBAS zinc oxide seed layers on the structure formation and the conductivity of thin silver films, a double layer buffer has been applied. The reason for this was to establish a situation where optimum comparability is given for standard and modified seed layers. The silver films were always grown on ZnO:Al films (≈ 20 nm) that were deposited just prior to Ag deposition in the same sputter tool (coater 2). The only difference was in the utilized substrates which were either blank float glass substrates or such that had been coated with an additional IBAS ZnO buffer layer (≈ 10 nm) first (coater 1). The latter substrates promoted a pronounced improvement in the orientational order of the ZnO:Al films grown. One of the substrates was also coated with ZnO from the IBAS tool but without any ion bombardment. To investigate the growth of silver films on the different seed layers, films with thicknesses of approximately 2, 3 and 10 nm were grown. Results from x-ray diffraction measurements are displayed in figure 6.42. The upper graphs show the diffraction patterns for the thick (10 nm) and thin silver films (2-3 nm) respectively. Note the logarithmic intensity scale. First, it is evident that the structure of the ZnO:Al film was greatly improved in cases where an IBAS ZnO buffer layer was applied. This can be concluded from the relative intensities of the respective ZnO (002) Bragg peaks. Second, it is quite obvious that also the silver film quality is essentially promoted by these modified seed layers. The pronounced increase in the Ag (111) peak intensity for cases where an IBAS ZnO buffer was applied is apparent from the graphs. Especially noteworthy is the structure of the 2 nm thin silver films, one of which was also deposited directly onto a blank float glass substrate. While this film does not show any diffraction peak, a clear silver (111) peak is visible for a standard ZnO:Al seed layer. Astonishingly, the intensity of this peak is clearly doubled if an IBAS buffer layer was utilized in addition. The lower two graphs in figure 6.42 show the pronounced structural improvements (for the 10 nm thick silver films) induced by the IBAS buffer layers underneath the ZnO:Al seed layers. On the left-hand side the expected increase of the Ag (111) peak net area as a function of the corresponding ZnO (002) peak net area is displayed. On the right-hand side rocking curves are shown that were performed for two samples, differing in the presence of an additional IBAS buffer. Both, the ZnO (002) peak and the Ag (111) peak were investigated with this method. The width of the rocking curves displayed can be interpreted as the extent of deviation from a perfect ZnO (002) and Ag (111) out-of-plane texture, respectively. The improvement of the ZnO:Al texture by the IBAS ZnO buffer layer is quite evident. But it is also clear that this structural difference nicely transfers into a

6.3. HETERO-EPITAXIAL GROWTH OF AG THIN FILMS

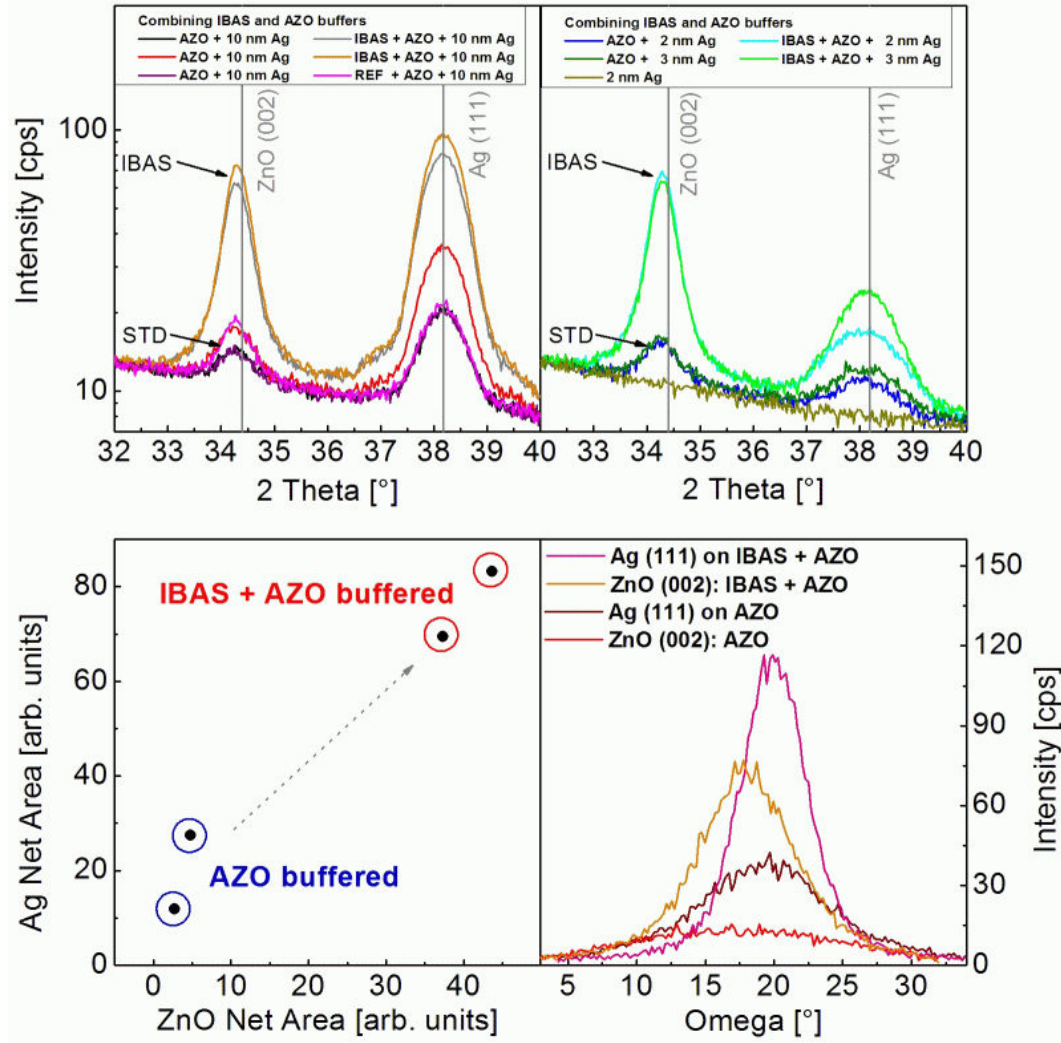


Figure 6.42: XRD growth study of Ag films on dual IBAS-ZnO + ZnO:Al (AZO) seed layers. Films consist of either a double or a triple layer stack, where the two top layers always consist of a ZnO:Al film sputtered at standard conditions in a standard process and a silver film. For some of the films an additional ZnO film deposited in the IBAS process forms a buffer layer for the growth of the ZnO:Al layer. Industrial float glass was utilized as a substrate. **Top left:** XRD scans of Ag films with a thickness of 10 nm grown on standard seed layers on such that are improved by an additional IBAS buffer layer. For one film, an additional ZnO seed layer (REF) has been deposited without ion assistance in the IBAS tool. **Top right:** XRD scans of thin Ag films grown on the different seed layers. One Ag film was also deposited on a blank substrate without any seed layer. **Bottom left:** Ag (111) peak net area as a function of the corresponding (002) peak net area of the ZnO seed layer. Data has been extracted from the XRD scans for the 10 nm thick Ag films. Only two pairs of films are shown. **Bottom right:** Rocking curves performed for two of the 10 nm thick Ag films on a standard ZnO:Al and on a ZnO:Al film supported by an additional IBAS ZnO buffer, respectively. A detailed discussion of the data is given in the text.

CHAPTER 6. II: APPLICATIONS OF MODIFIED ZINC OXIDE STRUCTURES

corresponding difference in the texture of the silver films. Therefore, all graphs shown in figure 6.42 constitute unambiguous evidence that the structural quality of the silver films is greatly enhanced by the application of modified seed layers.

In figure 6.43 some results from AFM and resistivity measurements are summarized. The top four images show the surface topography of nominally 2 and 3 nm thin silver films grown on ZnO:Al single and IBAS + ZnO:Al dual seed layers, respectively. These early stages of film growth are dominated by separated Ag islands and clustering. From visual inspection and the height scale it is evident that upon utilization of an additional IBAS buffer layer there is a weak improvement in terms of a faster percolation. Evidence for this observation is also seen in the topography of the 10 nm thick silver films which appear to exhibit flatter grain tops to some extent if an IBAS buffer is applied. However, first it should be stated that these improvements are really weak and that they also cannot be measured by any kind of statistical analysis of the AFM images. The latter fact although is rather due to the specific nature of the silver surface. As a consequence of the tilt of these flat grain tops with respect to the substrate surface but also with respect to each other, no statistical function has been found that would have been capable of characterizing the *flatness* of such surfaces even in cases where a pronounced difference was clearly visible in the images. Nonetheless, the resistivities displayed in figure 6.43 for the 10 nm thick silver films reveal that in spite of all the obvious and the less obvious improvements the electrical properties of the film which utilizes an additional IBAS ZnO buffer underneath the ZnO:Al seed layer are even worse. There is no obvious physical explanation for this surprising anomalous finding in any of the data discussed for these samples.

The results discussed in section 6.3 can be summarized as follows:

1. The orientational order of the (111) out-of-plane texture of thin silver films grown on zinc oxide films with a (002) fibre texture can be noticeably increased by improving the texture of the zinc oxide seed layer. This is especially true if the IBAS process is utilized to tweak the structural quality of such ZnO layers. It has been concluded that the enhanced orientational order of the zinc oxide films, which typically projects into an enlarged (002) peak net area in a Bragg Brentano XRD scan, is a vital quantity that determines the corresponding structural enhancement of the silver films.
2. It has also been discovered that possibly the lattice strain of the zinc oxide seed layer may have a significant influence on the structural quality of the silver film. This results from an improved epitaxial match in cases where the ZnO film is positively strained (enlarged).
3. It has been found that the electrical conductivity of the silver films strongly correlates with the structural order in terms of the Ag (111) peak net area if conductivity is not otherwise limited by a different parameter. However,

6.3. HETERO-EPITAXIAL GROWTH OF AG THIN FILMS

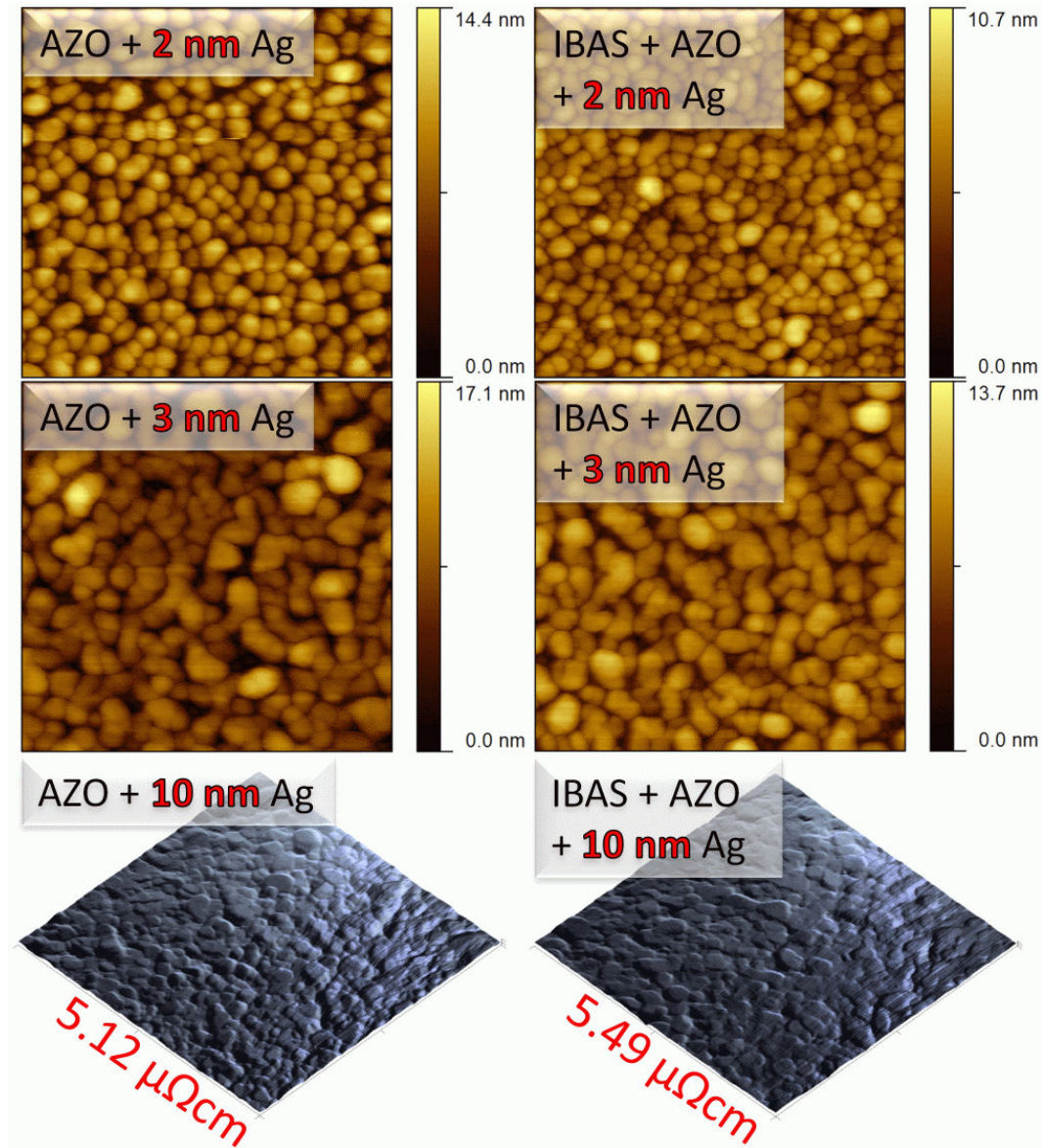


Figure 6.43: AFM growth study of Ag films on dual IBAS-ZnO + ZnO:Al seed layers. For the evolution of the thin Ag films, island formation and subsequent clustering is found (cf figure 6.39). The Ag films that were structurally improved by an additional IBAS ZnO seed layer underneath the ZnO:Al buffer appear to form a closed surface slightly faster than films without the IBAS buffer. This also results in a *flatter* appearance of the 10 nm thick Ag film upon utilization of the IBAS buffer. However, this effect is not strongly pronounced. A discussion is given in the text. In spite of the obvious structural improvements (that are especially evident in figure 6.42) the resistivity of the Ag film on the dual buffer (i.e. with an additional IBAS layer) is even higher compared to the film on the single (i.e. non-optimized) ZnO:Al buffer.

CHAPTER 6. II: APPLICATIONS OF MODIFIED ZINC OXIDE STRUCTURES

it has also been found that a large number of silver films, the structure of which is improved by applying seed layers modified by the IBAS process, show an exception to that rule. Even in cases where a structural improvement is explicitly developed, corresponding tweaks in the electrical properties are often absent.

The statement made in point 2 implicitly provides evidence that there is an additional quantity that affects the electrical properties of silver films which very likely is different from the obvious factors listed in the introduction to section 6.3. It also appears that in some cases this additional parameter even dominates the resistivity. However, it is strongly expected that if this influence can be isolated it should be possible to exploit the apparent potential of modified seed layers for the fabrication of thin silver films with greatly enhanced electrical conductivity.

III: Finally unravelling the origin of preferred orientation in zinc oxide thin films

In the previous chapters, emphasis was put on optimizing ZnO film growth by tailored utilization of ion bombardment in the early growth stage. Unambiguous evidence has been given that the initial growth stage (nucleation and coalescence regime) plays the dominant role in structure formation since it strongly governs the quality of the orientational order in the later growth stages. All experiments shown have in common that the overall preferred c_{\perp} -orientation was improved by supporting the process of **preferred nucleation**. Even though the respective results are remarkable, they do, however, not shed much light on the possible action of **evolutionary selection** mechanisms. It therefore remains unclear to what extent evolutionary selection would contribute to texture formation if the initial growth stage is characterized by a very weak orientational order. Thus, a different type of experiments has been performed where ion bombardment was utilized to intentionally *damage* structural order in the initial growth stage. It was shown in [40] that e.g. oxygen ion bombardment with sufficiently high ion energies and current densities massively deteriorates the formation of c_{\perp} -textured films. Consequently, buffer layers have now been bombarded by an 800 eV oxygen ion beam with an ion flux density which was approximately by two orders of magnitude larger than typical ion currents utilized in the standard IBAS process as described in chapter 3. The mechanical shielding device above the target was not used for these experiments. The discharge power was somewhat reduced to keep the relative arrival ratio of ions to ZnO molecules as large as possible. By such massive ion bombardment, it was possible to entirely suppress the formation of crystallites with c_{\perp} -orientation in the films. Details will be discussed in the following sections.

7.1 Blocking (002) preferred orientation by IBAS: a-axis textured ZnO

As described in the introduction of this chapter, zinc oxide films have been deposited in an altered IBAS process under intense high energy oxygen ion bombardment. The corresponding deposition conditions therefore differ from the IBAS parameters given in chapter 3. Instead of xenon, oxygen has been directly fed into the ion source at a flow rate of 10 sccm. The total pressure was kept constant at ≈ 0.2 Pa and the plasma power supply was operated at a constant discharge power of typically 50 W for the deposition of bombarded films. Where bombarded specimens were utilized as seed layers for subsequent ZnO layers, also larger discharge powers or pressures have been utilized for the deposition of these subsequent layers. The ion current density has not been measured for each deposition run. Instead, the excitation current of the microwave source of the ECR ion gun is often given, which is proportional to the ion current at a fixed ion energy. As already mentioned, typical ion current densities were by two orders of magnitude larger than the ion currents utilized in the standard IBAS process discussed in the previous chapters.

A corresponding Bragg-Brentano diffraction pattern of a film produced in this altered IBAS process is shown in figure 7.1. It is evident that, in contrast to the typical (002) preferred orientation in ZnO thin films, there are clear indications that this film exhibits both a (100) and a (110) preferred orientation. Both of these orientations have in common that the c-axis is parallel to the substrate surface. The corresponding $(10\bar{1}0)$ and $(11\bar{2}0)$ crystal orientations are sketched in the inset. The low intensity of the diffraction peaks arises from the low film thickness of 50 nm and probably also from the fact that there might be crystallites with the c-axis parallel to the substrate but with rotations around this axis corresponding to neither a perfect (100) nor a perfect (110) texture.

To further confirm the finding that an a-axis textured ZnO film has been deposited, XRD scans have also been performed in grazing incidence geometry with an angle of incidence of 0.7° . Figure 7.2 shows the diffraction pattern. Based on the discussion in section 4.1.2, it can be concluded that all peaks indicate that the film is a-axis textured (c_{\parallel}) since (i) there is no (103) peak and (ii) the most intense peaks correspond to angles expected for c_{\parallel} -oriented films (see inset).

In summary it has been shown that intense high energy oxygen ion bombardment effectively suppresses the growth of crystallites with c_{\perp} -orientation and instead (or therefore) promotes the growth of c_{\parallel} -textured specimens. This result is remarkable for many reasons, one of which is that the IBAS process apparently facilitates the fabrication of films with arbitrarily tailored texture (c_{\perp} or c_{\parallel}). Another reason is that such films can now be utilized to study a very specific aspect of ZnO film growth: the strength of contributions from **preferred nucleation**

7.1. BLOCKING (002) PREFERRED ORIENTATION BY IBAS: A-AXIS TEXTURED ZNO

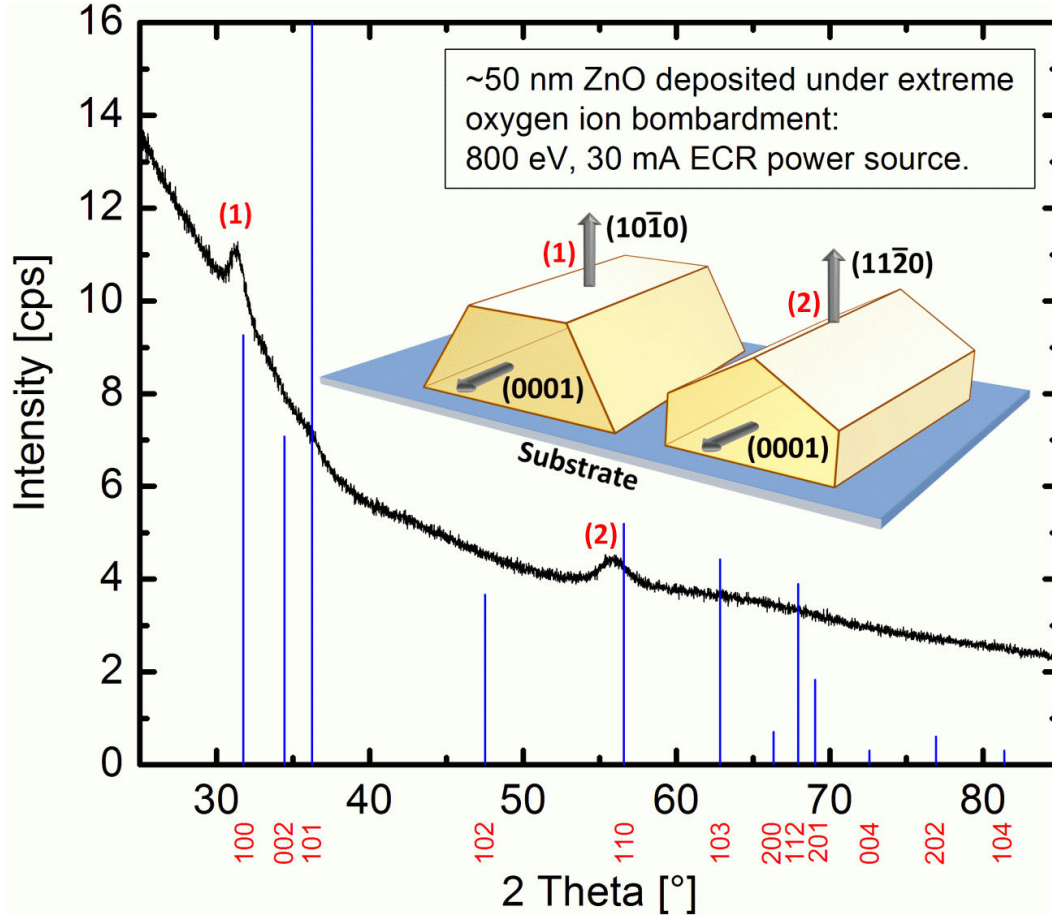


Figure 7.1: The figure displays a Bragg-Brentano XRD scan of a ZnO film which has been deposited in the IBAS process under intense energetic (800 eV) oxygen ion bombardment. According to the diffraction pattern, this film exhibits a mixed (100) and (110) c_{\parallel} -texture, as sketched in the inset. There is no peak from the {002} planes, confirming that the fraction of crystallites with c_{\perp} -orientation is very small.

and **evolutionary selection** to the structure formation in zinc oxide films. To tackle this question, thin films (≈ 10 nm) prepared under identical conditions as the specimen just discussed have been utilized as seed layers for the growth of ZnO films under standard conditions, i.e. without additional ion bombardment. The results of one of these experiments are presented in figure 7.3. The figure again shows the sample already displayed in figure 7.1 as a reference (black curve). The blue curve represents a film deposited on a respective seed layer whereas the red curve shows a sample that was deposited directly onto the glass substrate (no seed layer). It is evident that under the latter condition a typical c_{\perp} -textured film is grown, which is evident from the dominant (002) peak in the Bragg-Brentano diffraction pattern. The film grown on the bombarded seed layer, however, shows a comparatively weak (002) peak as well as (100) and (110) peaks, the latter of

CHAPTER 7. III: FINALLY UNRAVELLING THE ORIGIN OF PREFERRED ORIENTATION IN ZINC OXIDE THIN FILMS

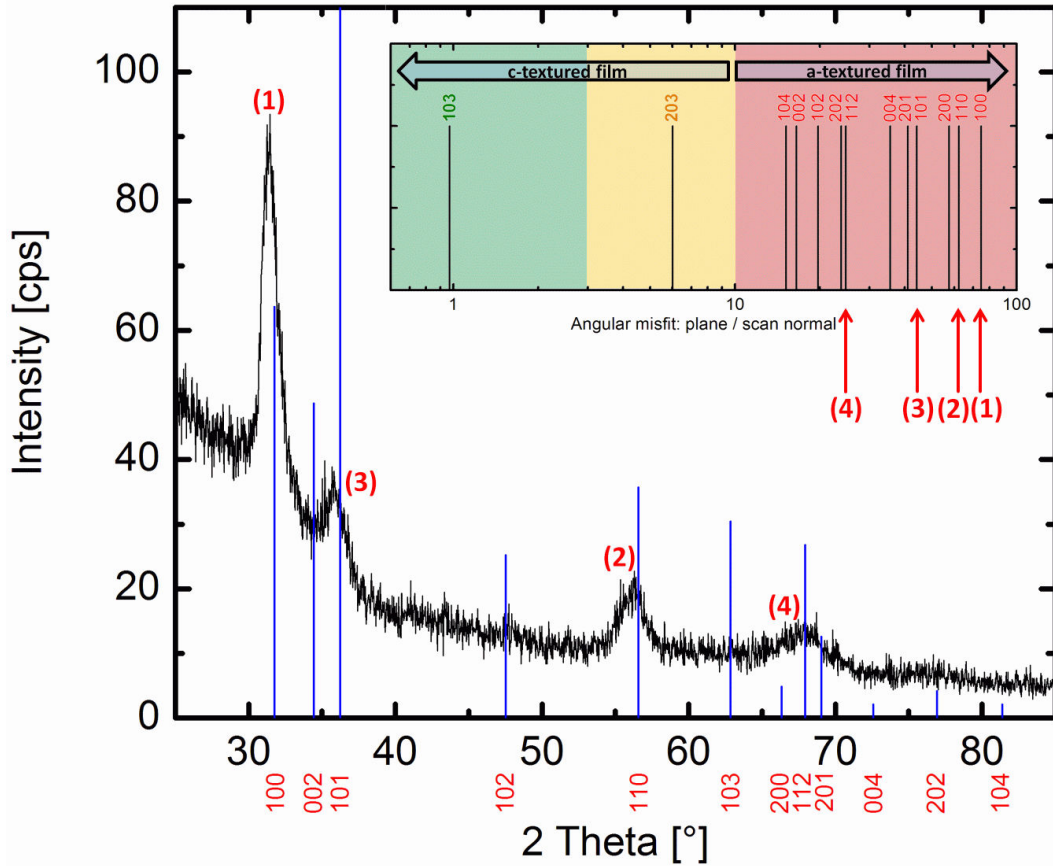


Figure 7.2: The figure shows a grazing incidence XRD pattern of the specimen shown already in figure 7.1. The pattern confirms the assumption that this film is $c_{||}$ -textured, which is evident from the comparison of the peaks with the chart presented in figure 4.4. This is shown in the inset.

which are clear evidence that some fraction of the film is $c_{||}$ -textured.

There are three consequences of these results that should be emphasized:

1. An a-axis textured thin seed layer promotes the growth of a thick film a significant fraction of which is also a-axis textured. This means that the transfer of the texture from the seed layer to the subsequent film also works in the case of a-axis textured films.
2. There is some fraction of crystallites that exhibit c_{\perp} -orientation. Since this orientation appears to be absent in the seed layer, this implies that some evolutionary selection mechanism favours the growth of these grains.
3. The film is clearly not c_{\perp} -textured on average. The intensity of the (002) peak is quite weak in comparison with the specimen deposited onto a blank

7.1. BLOCKING (002) PREFERRED ORIENTATION BY IBAS: A-AXIS TEXTURED ZNO

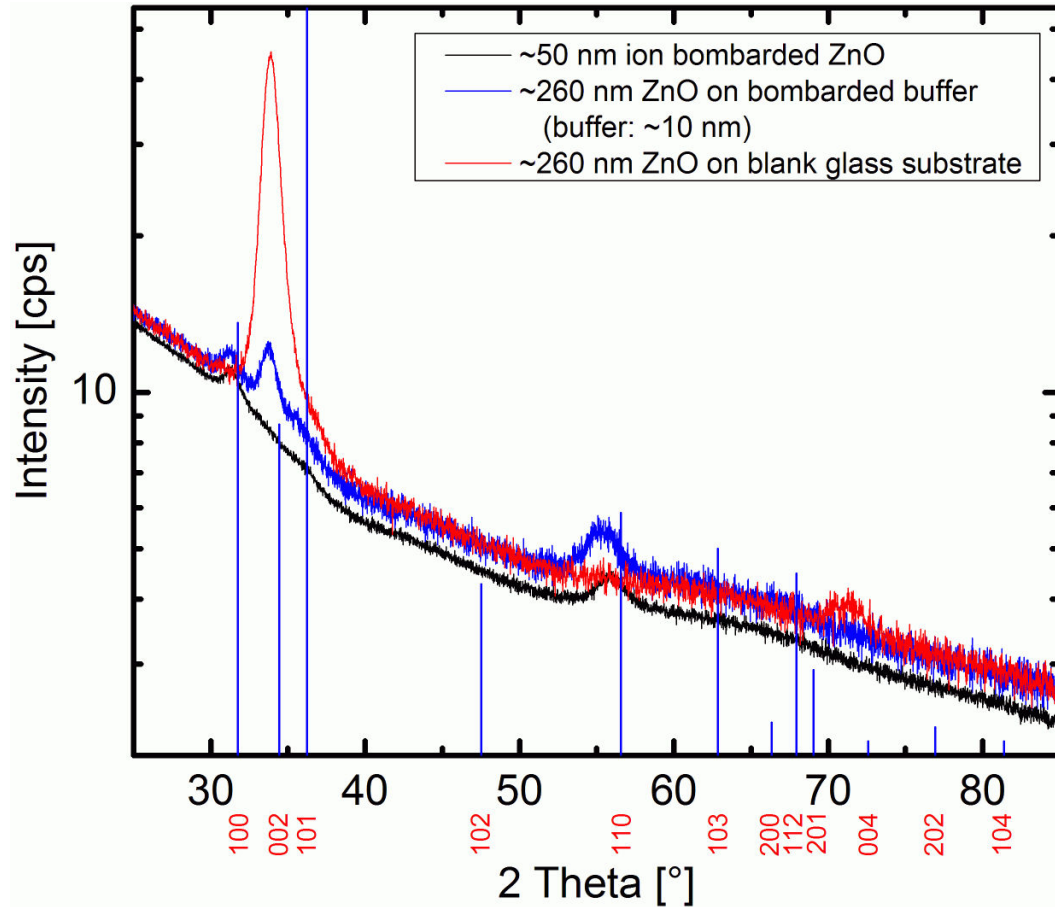


Figure 7.3: Intensively ion bombarded ZnO films with c_{\parallel} -texture have been utilized as seed layers for the growth of ZnO films. The red curve displays the Bragg-Brentano XRD pattern of a reference film which was deposited without a seed layer. This film exhibits clear c_{\perp} -texture. If grown on a ≈ 10 nm thin c_{\parallel} -oriented seed layer, films do not develop a c_{\perp} -texture (blue curve). Instead, there is only a minor contribution of (002)-oriented crystallites in an otherwise c_{\parallel} -textured matrix. The black curve shows a thick version (≈ 50 nm) of the seed layers again.

CHAPTER 7. III: FINALLY UNRAVELLING THE ORIGIN OF PREFERRED ORIENTATION IN ZINC OXIDE THIN FILMS

substrate and it is comparable with the intensities of the (100) and (110) peaks.

The second point proves that a principle of evolutionary selection does contribute to structure formation in reactive sputtering of zinc oxide films. This was expected and has been argued in the growth models discussed in the previous chapters (cf e.g. section 5.4). However, the third point clearly proves that evolutionary selection has a weak impact only. In turn, this is unambiguous evidence that **the initial growth stage, i.e. preferred nucleation, is by far the dominant part governing the texture of the film**¹.

The experiments discussed above have been repeated under slightly different conditions. The intensity of the ion bombardment has been increased towards the technical limit and films grown on respective seed layers have been grown significantly thicker. Corresponding results are shown in figure 7.4, displaying Bragg-Brentano XRD scans of the films. The red curve shows a reference ZnO film which has been grown on the blank glass substrate. The pattern clearly shows a highly c_{\perp} -textured film that is significantly strained which is due to the target age and the deposition conditions. Aside the dominant (002) and (004) peaks there is a weak contribution from the CuK_{β} representation of the (002) peak at around 30° . As expected, the films grown on the bombarded seed layers only show a weak (002) peak. Instead, peaks indicating a c_{\parallel} -texture dominate the diffraction pattern. The turquoise curve shows a scan at the edge of the sample represented by the blue curve. This edge was geometrically screened from the ion bombardment during the buffer layer fabrication. This proves that without the ion bombardment the seed layers also promote c_{\perp} -textured growth. Figure 7.5 shows the diffraction patterns of the films grown on bombarded seed layers in more detail. These two films differ in the intensity of the ion bombardment during seed layer deposition. It is evident that with increasing intensity (blue curve) the final film exhibits an even weaker contribution of the (002) peak. However, it can be stated that both films are c_{\parallel} -textured with only small fractions of c_{\perp} -oriented grains. This conclusion is further confirmed by grazing incidence XRD patterns recorded for the reference film (ZnO on glass) and the film on the massively bombarded seed layer (blue curve in figure 7.5). Figure 7.6 clearly shows diffraction patterns resembling c_{\perp} - and c_{\parallel} -textured films, respectively (compare with fig. 4.4 and the interpretation thereof). In summary, the results shown in figures 7.4 to 7.6 prove that under intense ion bombardment only of the initial growth stage, zinc oxide films can be grown that show a negligible contribution of c_{\perp} -oriented grains in an otherwise c_{\parallel} -textured matrix. Also, even in a 600 nm thick film, the principle of evolutionary selection does not seem to be strong enough to promote a notable c_{\perp} -texture.

¹This statement is based on the assumption that evolutionary selection promotes the formation of a c_{\perp} -texture solely.

7.1. BLOCKING (002) PREFERRED ORIENTATION BY IBAS: A-AXIS TEXTURED ZNO

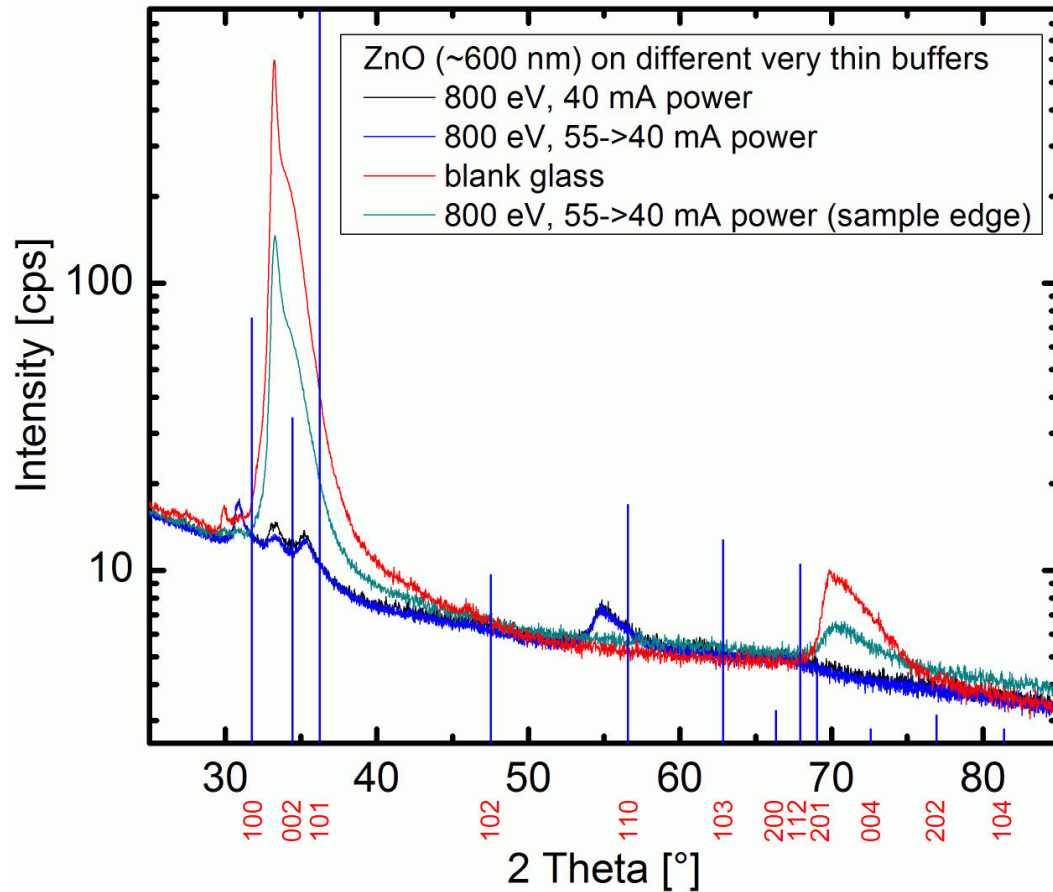


Figure 7.4: The figure shows thick ($\approx 600\text{nm}$) ZnO films grown on a-axis textured seed layers that have been deposited under very intense energetic oxygen ion bombardment. From the reference film (red curve) it is evident that without seed layer the films grow into a c_{\perp} -textured structure. On the seed layers, the formation of c_{\perp} -oriented crystallites is strongly suppressed. Instead, a significant fraction of the film grows into a c_{\parallel} -textured structure (black and blue curves). At the edges where ion bombardment was screened during the deposition of the bombarded seed layers, the films grow with c_{\perp} -texture (turquoise curve). Scans have been performed in Bragg-Brentano geometry.

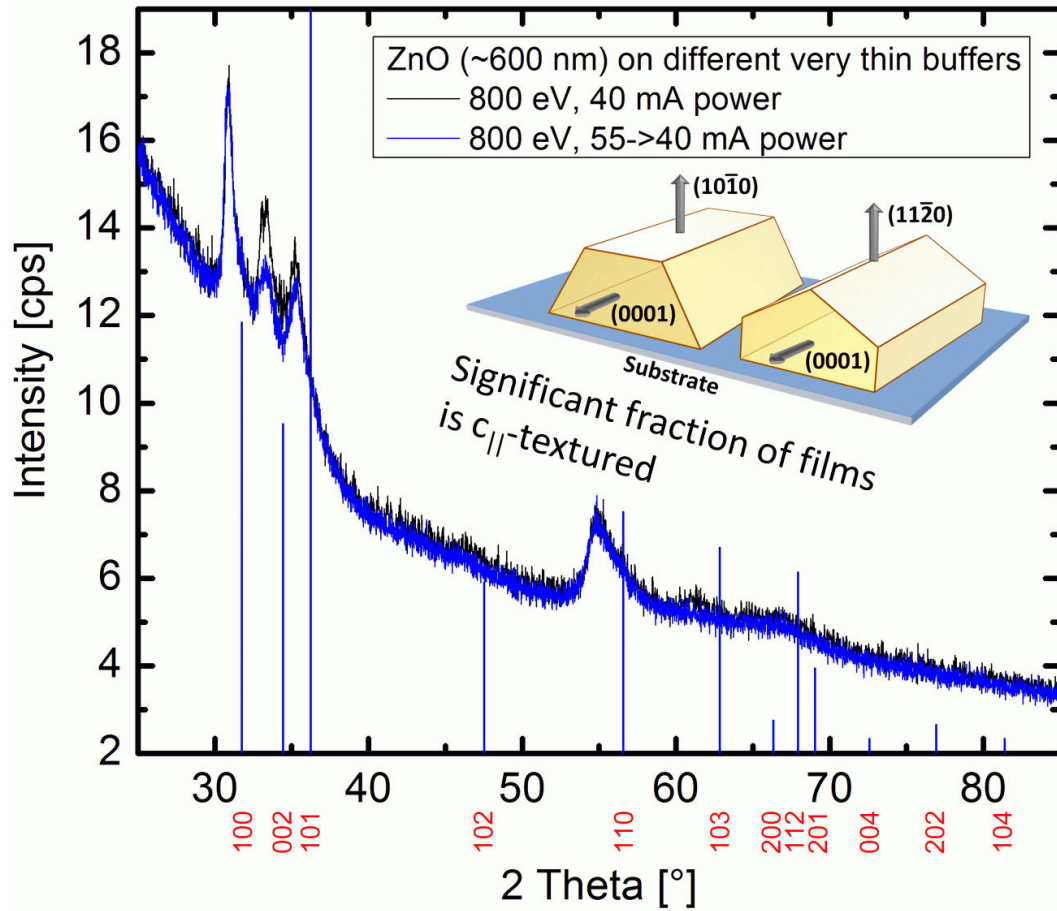


Figure 7.5: Upon a closer look at the specimens grown on $c_{||}$ -textured seed layers (cf figure 7.4) it is evident that the film grown on the seed layer bombarded with higher intensity shows an even less pronounced (002) peak. However, both films are clearly $c_{||}$ -textured since the (002) peak intensity is very small.

7.1. BLOCKING (002) PREFERRED ORIENTATION BY IBAS: A-AXIS TEXTURED ZNO

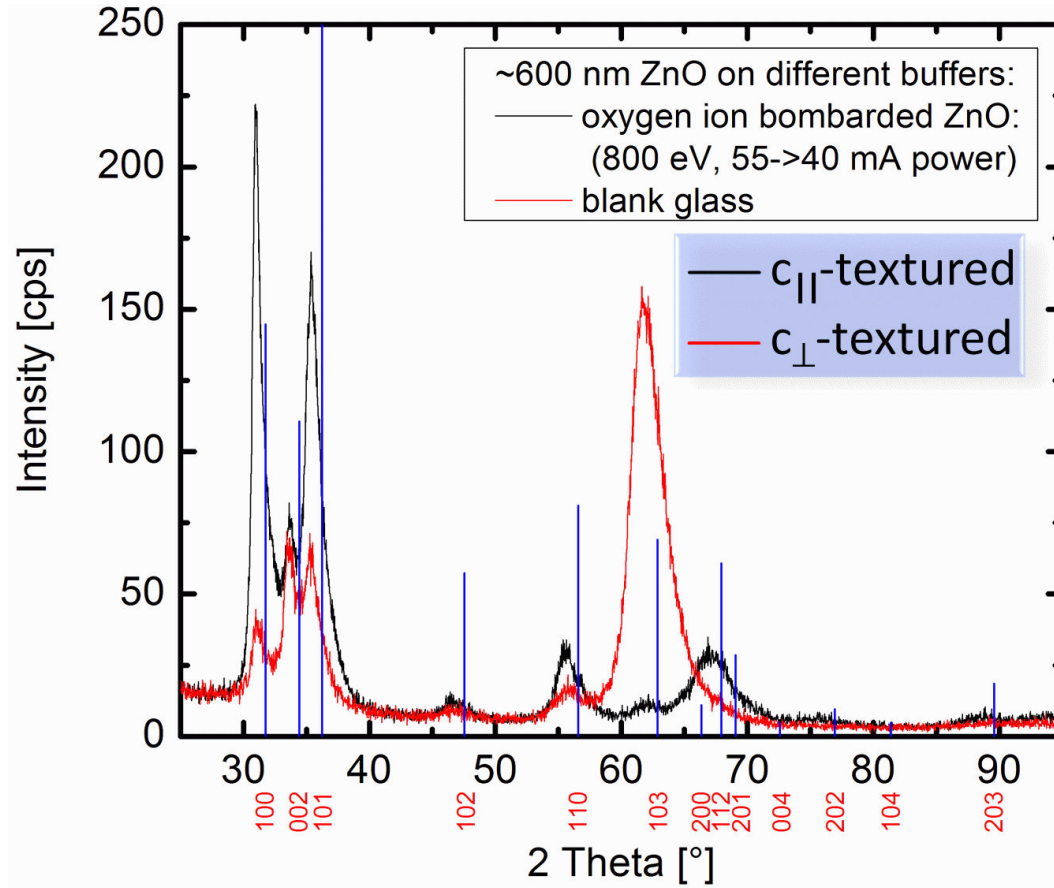


Figure 7.6: This figure shows GI XRD scans of two specimens already shown in figure 7.4. The diffraction patterns of the reference and the film grown on the intensively bombarded seed layer clearly support the assumption that the seed layer promotes the growth of a $c_{||}$ -textured structure. Compare visible peaks with figure 4.4.

CHAPTER 7. III: FINALLY UNRAVELLING THE ORIGIN OF PREFERRED ORIENTATION IN ZINC OXIDE THIN FILMS

In the c_{\parallel} -textured films shown in this section, both the (100) and (110) preferred orientations are simultaneously present. In another set of experiments there has been evidence that the ratio between these very similar orientations could also be influenced by deposition or bombardment conditions. This is shown in figures 7.7 and 7.8, where two films have been deposited under different discharge conditions. The ion bombardment was employed for the entire deposition time. It is evident from figure 7.7 that the ratio between the (100) and (110) peaks strongly differs for the two films. The origin for that is presently unknown but the result clearly shows that upon further investigation it should also be possible to tailor the fractions of (100)- and (110)-oriented crystals in c_{\parallel} -textured films. Figure 7.8 shows a profile along the longitudinal axis of the sample with the strong (110) preferred orientation shown in figure 7.7. It is evident that the large $I(110)/I(100)$ ratio is only found in the centre of the film where the ion bombardment is most intense². Towards the substrate edge, where the beam intensity is lower, a significant change in the ratio of the peak intensity $I(110)/I(100)$ occurs. However, since also the deposition rate and any influence from the sputtering plasma differs towards the substrate edge, the exact origin of the change in texture cannot be determined. Further investigation would be necessary before a clear statement could be made.

7.2 Discussion: Preferred nucleation vs evolutionary selection and the influence of energetic oxygen ions

In the foregoing section, unambiguous evidence has been given that the principle of preferred nucleation is the dominant mechanism governing texture evolution in zinc oxide thin films. Even though some c_{\perp} -oriented crystallites have evolved also on preferentially c_{\parallel} -textured seed layers, their relative contribution to the full volume of the film seems to be negligible. Hence, if there does not form a significant number of c_{\perp} -oriented nuclei in the initial growth stage already, the final thick film very likely will at most be weakly c_{\perp} -textured only³. In conclusion, structure formation mechanisms promoting the principle of evolutionary selection are only weakly active in ZnO film growth. However, so far only films have been investigated that were grown on unheated substrates. The influence of thermal energy on the texture formation should allow for an additional detailed insight to the

²See e.g. [40] for a discussion of the radial intensity distribution of the ion beam. Also compare with figure 6.18. Note however that in the altered IBAS process the effect of the ion bombardment is not as strictly limited to the sample centre. Otherwise there would be a clear c_{\perp} -texture at the edge of the sample discussed in figure 7.8.

³This statement is valid for the investigated parameter range, which particularly includes deposition at room temperature only.

7.2. DISCUSSION: PREFERRED NUCLEATION VS EVOLUTIONARY SELECTION AND THE INFLUENCE OF ENERGETIC OXYGEN IONS

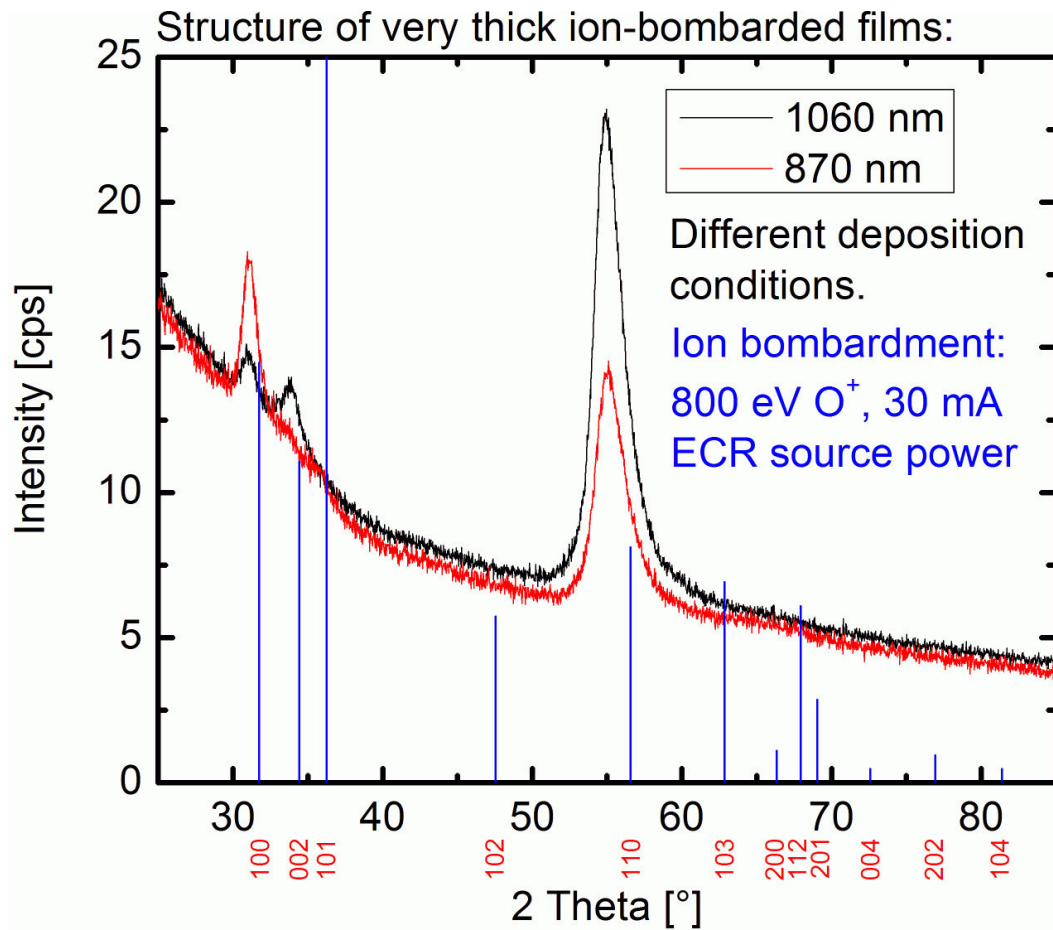


Figure 7.7: Thick films have been deposited under different sputtering conditions but under identical oxygen ion bombardment. Apparently a strong difference occurs in the intensity ratios of the (100) and (110) peaks in these Bragg-Brentano XRD patterns. These are different representations of the $c_{||}$ -texture. The exact origin of the difference is presently unknown.

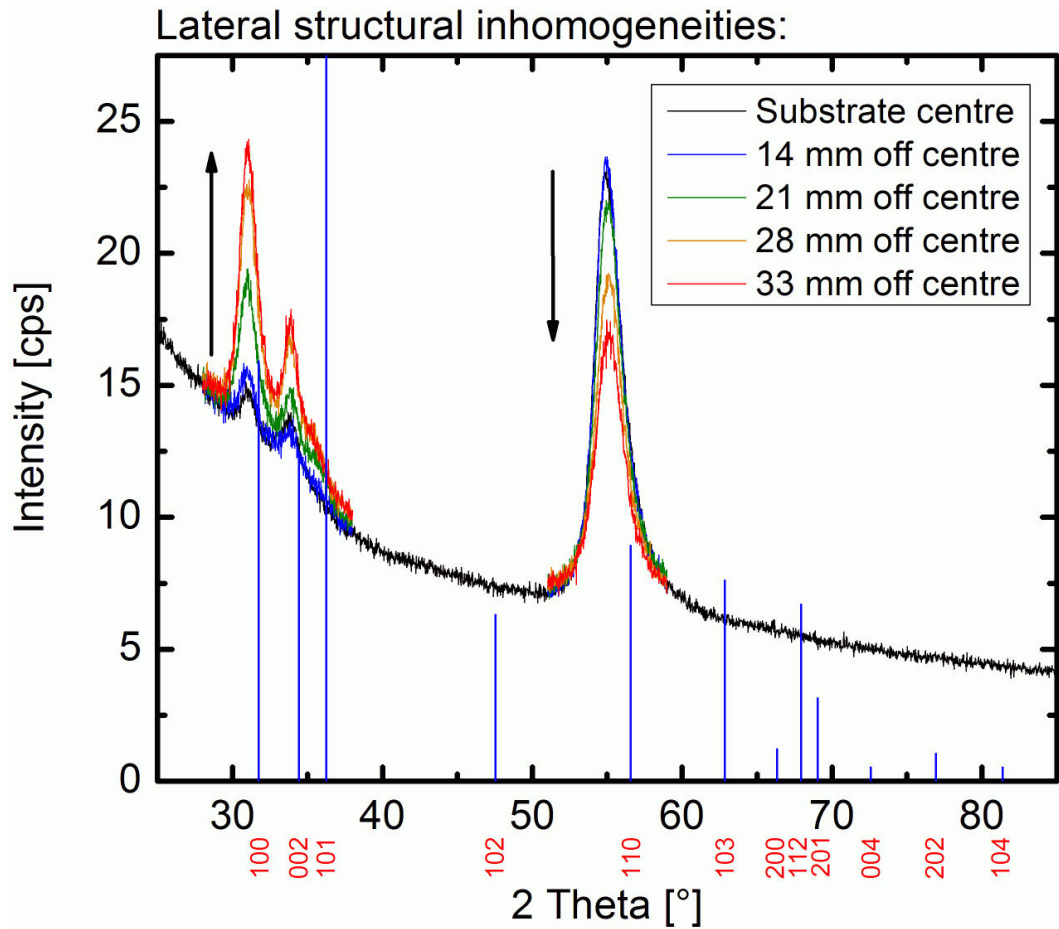


Figure 7.8: One of the films already shown in figure 7.7 has been scanned at different substrate positions along the longitudinal axis of the $76 \times 26 \text{ mm}^2$ large glass substrate. Due to differences both in the ion bombardment intensity (profile of the ion beam) and the deposition conditions (rate and influence of the plasma) a significant change in the relative $I(100)/I(110)$ ratio occurs, as indicated by the arrows. A direct comparison of patterns recorded at different positions is not possible due to the difference in film thickness.

7.2. DISCUSSION: PREFERRED NUCLEATION VS EVOLUTIONARY SELECTION AND THE INFLUENCE OF ENERGETIC OXYGEN IONS

nature e.g. of the evolutionary selection mechanism. As discussed in section 2.4 thermally activated surface diffusion towards preferentially oriented grains might be a possible mechanism for texture formation by evolutionary selection. In this case, an increase of the substrate temperature should have a significant effect on the resulting film texture. Therefore, ZnO films have also been deposited onto heated substrates where heating was applied either during the entire deposition time of bombarded films or only for the deposition of a thick film onto a bombarded seed layer. A temperature of 300 °C was utilized⁴, which corresponds to an increase of the homologous temperature $T_H = T/T_M$ ⁵ from $T_H(293K) = 0.13$ to $T_H(573K) = 0.25$. Experimental results are presented in figures 7.9 and 7.10, showing Bragg-Brentano XRD patterns of the specimens. On both figures, one film has been deposited entirely under simultaneous oxygen ion bombardment (800 eV and high intensity) while of the other films only a thin seed layer has been bombarded and the second layer is grown without ion bombardment on this buffer. In figure 7.9 the completely bombarded film has been deposited onto a heated substrate while deposition at room temperature was utilized for the respective film in figure 7.10. The seed layers have all been deposited without heating while of the films deposited onto the seed layers, only one of two films has been heated during deposition, as indicated in the figures. Except these discussed differences between the films shown in figures 7.9 and 7.10, all other deposition conditions were nearly identical. Several conclusions can be drawn from the figures. First, heating seems to increase the deposition rate. There is typically a difference of at least 50 nm between heated and unheated films. The increase of the deposition rate for films grown under simultaneous bombardment seems to be even larger, as evident from the completely bombarded films in both figures. The increase in the rate is approximately 100 % for these films. Apparently, desorption and re-sputtering of adsorbed species is reduced by heating. The films have been sputtered far in the oxidic regime such that desorption of metallic zinc, which is often reported to decrease the deposition rate on heated substrates, apparently does not play a significant role. Second, the films deposited completely under simultaneous oxygen ion bombardment do not show notable differences in their texture upon heating. However, there is a very weak contribution of c_{\perp} -oriented grains if the substrate is heated. Third, films deposited on bombarded seed layers also do not show any significant differences in texture upon heating the substrate. There is rather an increase of the overall crystalline quality instead. This latter observation is of significant importance since this is evidence that a change in texture during film growth, i.e. evolutionary selection, is not a thermally activated

⁴This is the temperature of the radiative heater placed at very small distance directly above the substrate. The actual substrate temperature is expected to be slightly lower.

⁵The melting temperature T_M of ZnO is 2248 K (cf table 2.1).

CHAPTER 7. III: FINALLY UNRAVELLING THE ORIGIN OF PREFERRED ORIENTATION IN ZINC OXIDE THIN FILMS

process⁶. Otherwise there would be clear differences in the textures of the films discussed here. Nonetheless, since the overall structural quality is improved by the substrate heating, it is assumed that surface diffusion is enhanced. However, it is also proposed that the net diffusion towards grains with preferred orientations (e.g. towards c_{\perp} -oriented grains) as discussed in section 2.4 is (close to) zero. This also follows from the fact that no pronounced evolutionary selection towards e.g. a c_{\perp} -texture is notable in figures 7.9 and 7.10.

A question that remains is how the intense energetic oxygen ion bombardment does affect structure formation. First of all, for the beneficial low energy xenon bombardment it was evident that it was the initial growth stage that was susceptible to that bombardment only. This was explained in terms of structure densification promoting the preferred nucleation with the $\{002\}$ planes parallel to the substrate surface. If the oxygen ion bombardment would also significantly act only during the initial growth stage, there should be no effect if the bombardment was delayed to a later growth stage. This has been tested in an experiment where the energetic intense bombardment has been started only after a significant fraction of the film had already formed under standard growth conditions. The result is displayed in figure 7.11. The figure shows zinc oxide films with a thickness of approximately 300 nm. For one of the films, intense bombardment was applied after about 60 nm had already grown. The duration of the bombardment nominally⁷ corresponded to the growth of 20 nm.

It is apparent that the film with the bombarded layer shows a significantly lower amount of c_{\perp} -oriented crystallites, evident from the smaller (002) peak intensity. Since the area under the (002) peak is roughly proportional to the film thickness (cf [40]), the relative ratio of net areas of 4:1 is evidence that c_{\perp} -textured growth was almost entirely interrupted by the bombardment, which for the case of complete interruption would yield a net area ratio of 5:1⁸. In conclusion, the energetic intense oxygen ion bombardment is effective at any stage of film growth. This is in contrast to the mechanism by which xenon ion bombardment affects film growth specifically during the nucleation regime (cf chapter 5).

It is therefore proposed that the influence of energetic intense oxygen ion bombardment is based on a mechanism of preferential damage or sputtering rather than on preferred nucleation. A preferential sputtering mechanism would also be in line with the large observed ion-etching rate, which can be concluded from figure 7.3. There, all films have been deposited for the same time but one of

⁶This statement is restricted to $T_H \leq 0.25$, which was the largest homologous temperature utilized in these studies. Further experiments with $T_H \gtrsim 0.5$, where significant surface diffusion is expected, are necessary to fortify this statement.

⁷The real thickness of the film deposited during the bombardment was lower due to ion-etching.

⁸That ratio corresponds to the ratio of the fractions of the films that were grown without interference. This is the complete film (300 nm) in case of the reference sample and 60 nm in case of the film with the bombarded layer.

7.2. DISCUSSION: PREFERRED NUCLEATION VS EVOLUTIONARY SELECTION AND THE INFLUENCE OF ENERGETIC OXYGEN IONS

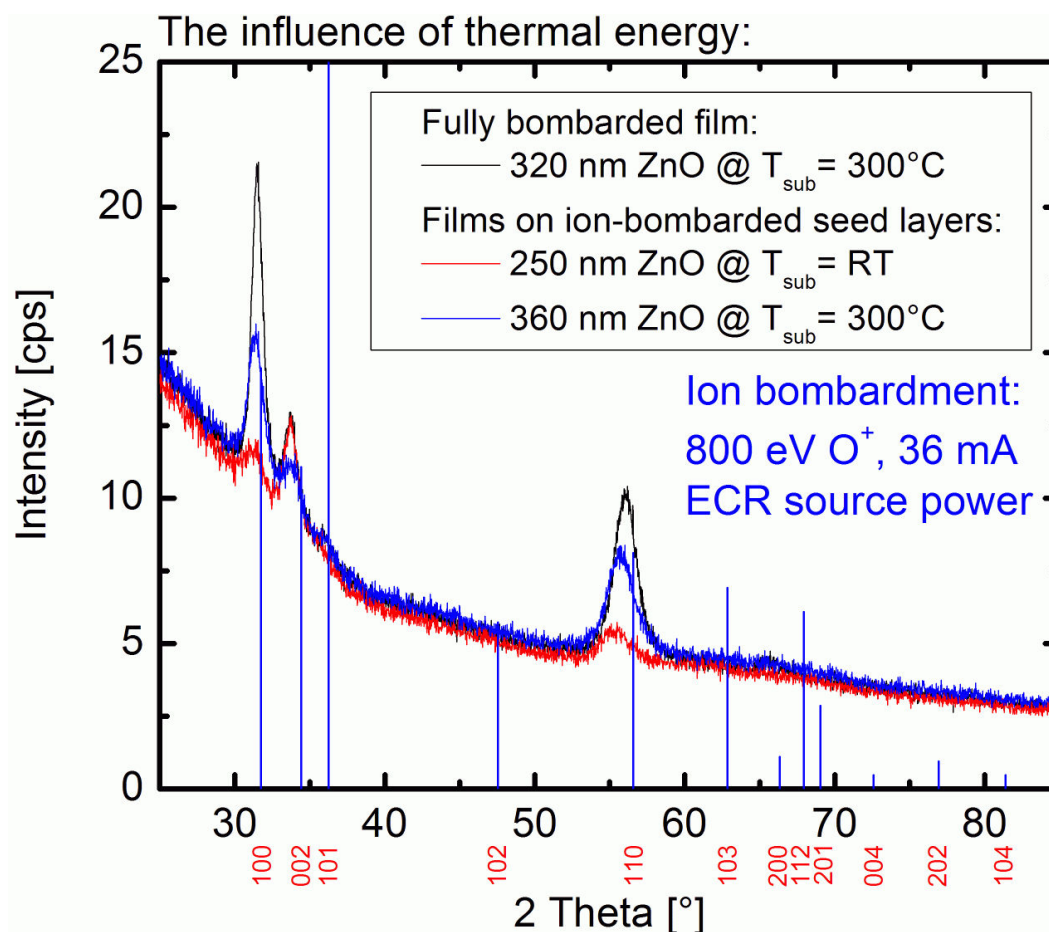


Figure 7.9: Bragg-Brentano XRD patterns of ZnO films. One specimen has been deposited entirely under simultaneous oxygen ion bombardment onto a heated substrate. The deposition time has been 5400 s. Two films have been deposited for 1800 s without ion bombardment onto seed layers. One of these films was heated during deposition. The seed layers have been deposited for 600 s under simultaneous ion bombardment without substrate heating. Sputtering conditions were otherwise identical for all films. It is apparent that heating does not change the texture of the films. There is merely an overall increase in the crystalline quality. See text for a detailed discussion.

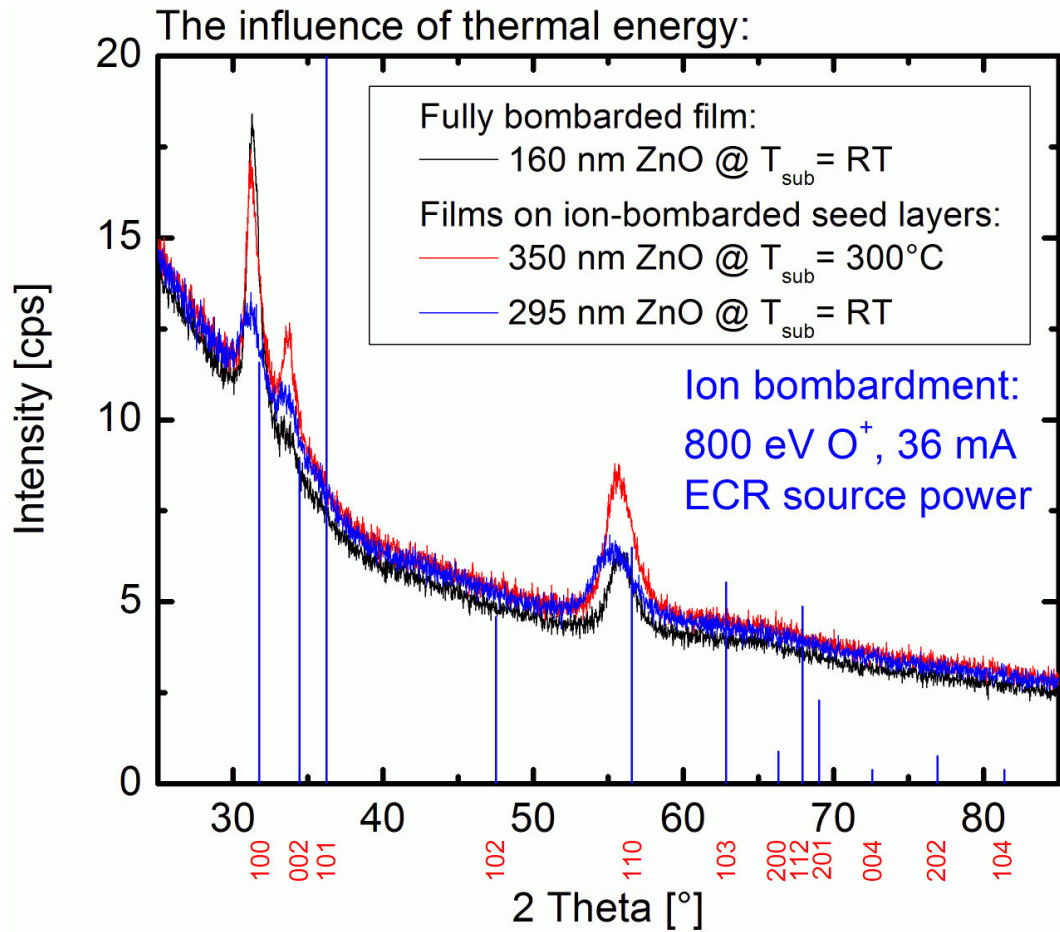


Figure 7.10: Bragg-Brentano XRD patterns of ZnO films. One specimen has been deposited entirely under simultaneous oxygen ion bombardment without substrate heating. The deposition time has been 5400 s. Similar to figure 7.9 two films have been deposited for 1800 s without ion bombardment onto seed layers. One of these films was heated during deposition. The seed layers have been deposited for 600 s under simultaneous ion bombardment without substrate heating. Sputtering conditions were otherwise identical to the films shown in figure 7.9. See text for a detailed discussion.

7.2. DISCUSSION: PREFERRED NUCLEATION VS EVOLUTIONARY SELECTION AND THE INFLUENCE OF ENERGETIC OXYGEN IONS

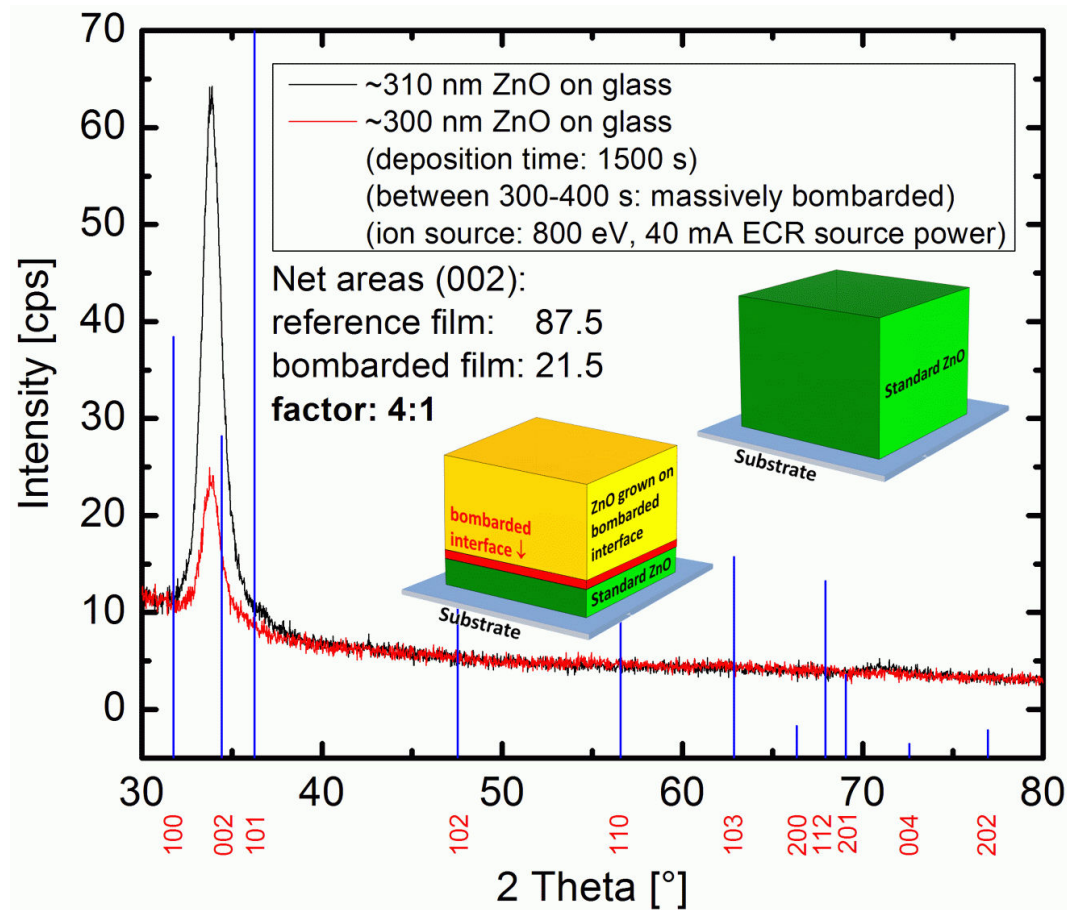


Figure 7.11: Bragg-Brentano XRD scans of films with identical thicknesses that have been deposited at identical discharge parameters. However, one of the films (red curve) has been intensively ion bombarded (800 eV oxygen ions at very strong intensity) after 20 % of the deposition was completed. The duration of the bombardment has been very short (approximately 6 % of the total deposition time). Even though only a very thin layer has been intensively bombarded, textured growth of this specimen has apparently been stopped. The relative ratio of the (002) peak net areas of the two specimens is 4:1. This is evidence that almost no textured growth took place in the bombarded sample even after the interruption of the bombardment. See text for further details.

CHAPTER 7. III: FINALLY UNRAVELLING THE ORIGIN OF PREFERRED ORIENTATION IN ZINC OXIDE THIN FILMS

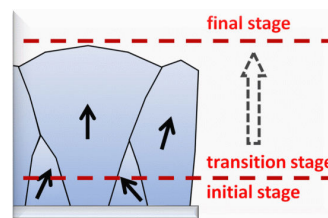
the samples was bombarded for the full growth time. The difference in the film thickness must therefore result from ion-re-sputtering. Hence, the ion-etching rate is approximately 80 % of the deposition rate.

It is also proposed that re-sputtering affects various crystallite orientations differently since otherwise there would be no preferred c_{\parallel} -texture upon the bombardment. If a channelling effect as described e.g. in [40] would be responsible for the selective damage of c_{\perp} -oriented crystallites this would not yield a mixed (100) and (110) texture. A possible explanation might arise from the fact that the {002} planes exhibit the highest packing density. Therefore, crystallites oriented with these planes parallel to the film surface provide the largest target and are therefore preferentially sputtered by the ion beam. Consequently, any orientation where the (002) planes grow perpendicular to the film surface would be preferred. This would result in a mixed (100) and (110) texture, which is observed, and is therefore a plausible explanation.

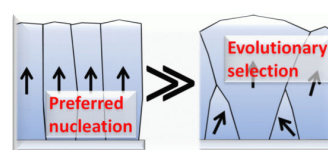
7.3 The final growth model

With the data discussed in chapters 5 to 7 a comprehensive growth model for sputtered zinc oxide films can now be developed. This model will not only comprise information about the influence of different kinds of ion bombardment. It will also clearly specify the growth stages that are susceptible for bombardment and explain respective effects on structure formation. Furthermore, apart from ion bombardment of the growing films the model will make a general statement of the role that different growth stages and texture formation mechanisms play during structure formation. The proposed model comprises the following statements which have been derived for room temperature deposition if not otherwise stated:

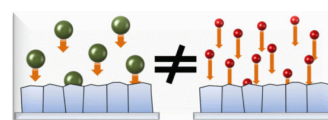
1. Zinc oxide film growth can be separated into three growth stages: the initial, transition and final growth stage. The initial stage comprises nucleation and coalescence while the final stage is characterized by a structure that does not change anymore upon further increasing the film thickness. In case that there is a difference in the basic structural properties between the initial and the final growth stage the corresponding structural transition takes place in the transition stage. **Of these growth stages it is the initial growth stage that almost solely governs the structure of the final film.** Preferred nucleation is proposed to govern structure formation in the initial growth stage.



2. A direct consequence of the first statement is that **any kind of evolutionary selection has a negligible influence on structure formation as compared to preferred nucleation.** However, in some cases evolutionary selection leads to at least noticeable changes in texture, as observed. It is however proposed that evolutionary selection can have a more clearly noticeable influence on structure evolution if there is a significant fraction of c_{\perp} -oriented crystallites formed by preferred nucleation. This directly follows from the observations made in chapter 5, where proliferating growth, i.e. evolutionary selection, was evident for un-bombarded ZnO films.

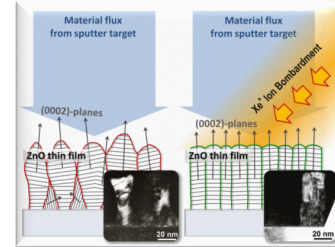


3. The influence of ion bombardment depends on the ion mass, energy and current density.

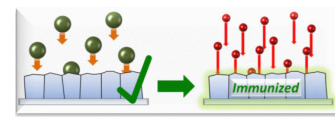


CHAPTER 7. III: FINALLY UNRAVELLING THE ORIGIN OF PREFERRED ORIENTATION IN ZINC OXIDE THIN FILMS

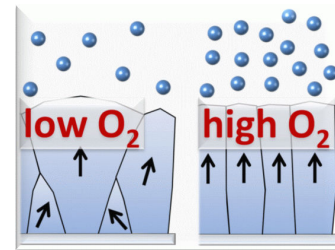
4. **Preferred nucleation can be strongly promoted by ion bombardment.** Upon utilization of heavy ions at moderate ion energies and current densities it is possible to significantly improve the structural order in favour of a c_{\perp} -oriented film during the initial growth stage. Such ion bombardment, however, has no effect anymore during later growth stages.



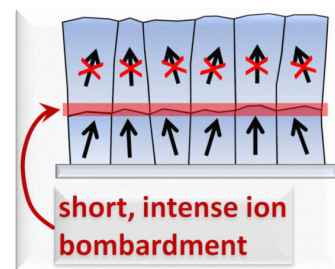
5. **Zinc oxide films can to some extent be immunized against oxygen ion bombardment.** If c_{\perp} -texture formation is improved during the initial growth stage, immunity of the films against energetic oxygen ion bombardment of moderate intensity, such as inherent in a reactive sputter process, is improved (at least regarding XRD structure).



6. **A high oxygen partial pressure strongly promotes the growth of c_{\perp} -oriented zinc oxide films in a sputter process.** However, this effect is typically not observed in standard processes since the concurrent energetic oxygen ion bombardment, which also increases with the oxygen partial pressure, typically annihilates that improvement by ion damage.



7. **Highly energetic intense oxygen ion bombardment interrupts the growth of c_{\perp} -oriented crystallites at any growth stage.**

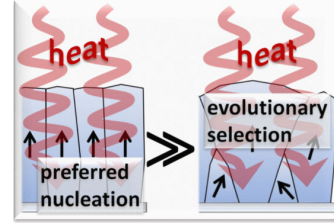


8. **Under intense energetic oxygen ion bombardment ZnO films can be grown with a preferred c_{\parallel} -texture.** Such films can also be utilized as seed layers for the growth of films with a very low contribution of c_{\perp} -oriented crystallites.



7.3. THE FINAL GROWTH MODEL

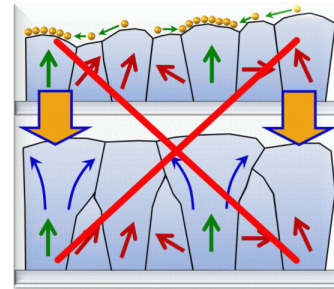
9. Thermal energy (induced by substrate heating) does promote structure formation in terms of improving the overall crystalline quality. **However, heat has no influence on the principal texture formation mechanism. Thermal energy does not govern film texture, which means that whether a film is c_{\perp} - or c_{\parallel} -textured is not affected by heat.**



Statement 9 is restricted to the temperature range from room temperature to 300 °C, which is also the typical range of substrate temperatures typically utilized for the fabrication of zinc oxide coatings. Putting statements 1-9 in other words means that

i. The substrate interface (and the nucleation on that) plays an important role in the structure formation of zinc oxide films. Attempts to tailor the structural properties of zinc oxide films must focus on tailoring the interfacial layers (substrate surface and zinc oxide nucleation layer).

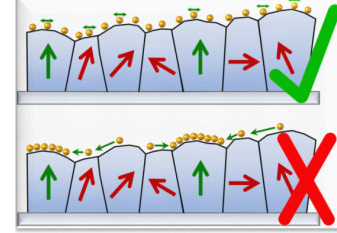
ii. The principle of evolutionary selection which seems to very weakly promote the growth of a c_{\perp} -oriented fraction of the film is not based on a diffusion mechanism in the temperature range $T_H \leq 0.25$. This is evident since the delivery of additional thermal energy (substrate heating) does not increase this fraction.



iii. As a consequence of the previous statement it is proposed that the increase of the orientational order that is often observed as a function of film thickness especially for zinc oxide films deposited onto unheated substrates might be a result of gradual (in terms of a gradually increasing temperature during the coating process when the substrate is exposed to the plasma) unintended heating by the deposition source (e.g. by the sputtering discharge). Substrate temperature is expected to increase quickly upon exposure to the source. It might therefore be a consequence of the increasing temperature in terms of statement 9, but not of an evolutionary selection mechanism which would specifically promote c_{\perp} -texture, that the structural quality improves during the transition growth stage.

CHAPTER 7. III: FINALLY UNRAVELLING THE ORIGIN OF PREFERRED ORIENTATION IN ZINC OXIDE THIN FILMS

iv. Regarding the role of thermal energy during film growth, it is proposed that substrate heating increases structural order (e.g. by minimizing stacking faults) potentially by enhancing the mean surface diffusion length of adsorbed species. However, it is also proposed that, if there is inter-granular diffusion, this diffusion is not biased by grain orientations. In other words, there is no net flow towards grains with specific orientations.



v. It is apparent why upon deposition by chemical routes (e.g. by ALD) it is easily possible to grow zinc oxide films with different textures (e.g. $c_{||}$ -textured films). The reason is very likely that adsorption and nucleation mechanisms in a chemical process can be quite different from PVD processes. Since the structural evolution at the substrate interface governs the texture of the complete film this would directly result in an entirely different film structure. This statement is based on the hypothesis that the initial growth stage governs film texture not only for sputter-deposited films.

Some of these statements on texture formation in zinc oxide films are summarized in figure 7.12. It should be noted here that the statements made in the previous models (sections 5.4 and 6.2) are still valid. Especially some specific statements made in the previous models are not repeated in figure 7.12 where we focus on more general principles. The reader is therefore encouraged to consider all three growth models presented in this work.

7.3. THE FINAL GROWTH MODEL

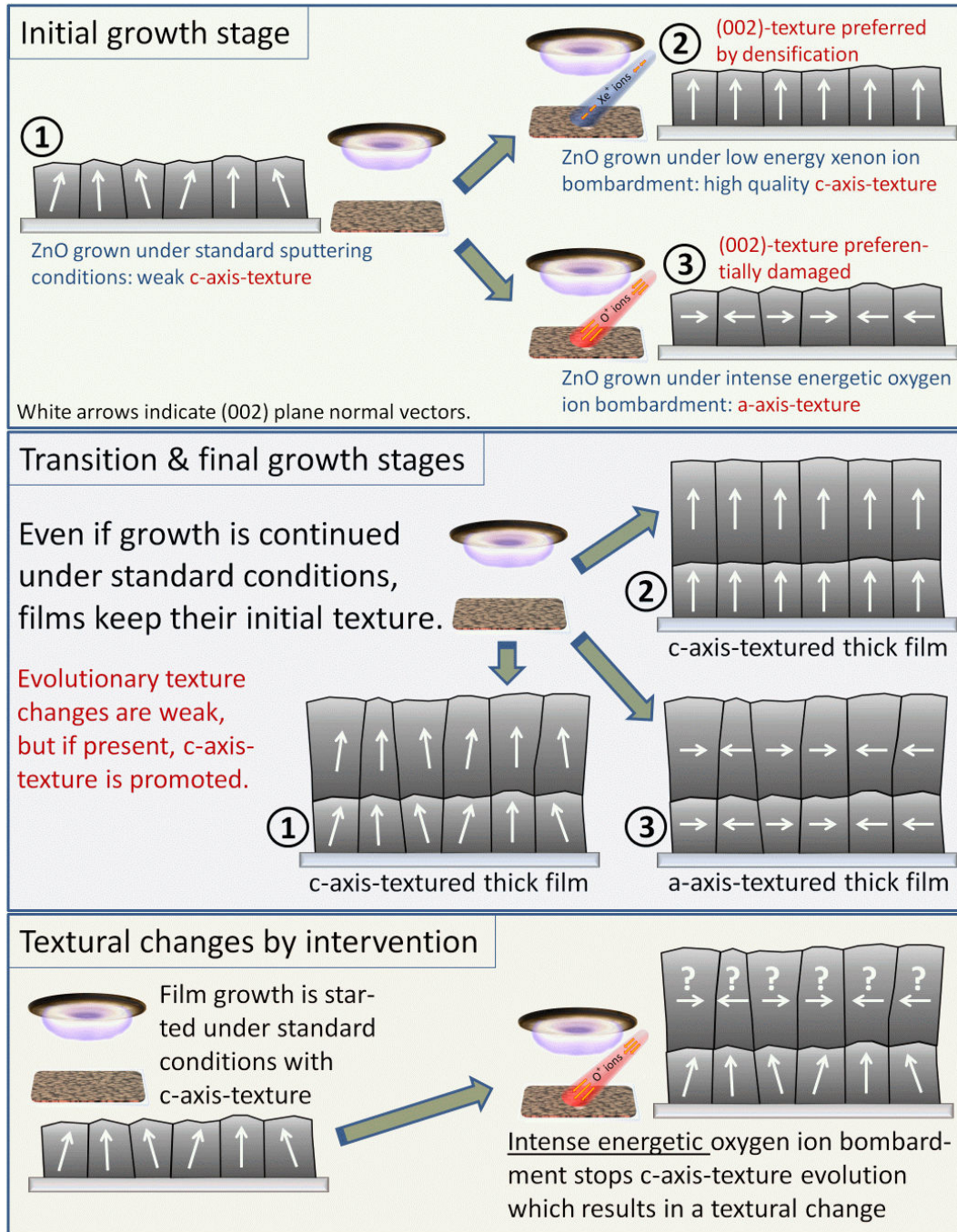


Figure 7.12: Final growth model for zinc oxide films. Models presented in sections 5.4 and 6.2 are still valid and contain complementary information. See text for a detailed discussion.

8

Summary and outlook

By exploiting the advantages of an ion beam assisted sputtering process with variable ion energy, flux density and species, a comprehensive investigation of zinc oxide film growth has been performed. This work has demonstrated that under the influence of tailored ion bombardment in a modified sputtering process (Ion Beam Assisted Sputtering —IBAS) zinc oxide films can be deposited with a variety of tailored textures. Especially **(i)** films with c_{\perp} -texture that exhibit outstanding structural quality have been grown in a room temperature process¹ under xenon ion assistance and **(ii)** the possibility to grow films with preferred c_{\parallel} -texture has been demonstrated in an oxygen ion assisted process. Furthermore, it has been shown that the nature of the c_{\parallel} -texture, i.e. the relative fractions of (100)- and (110)-oriented grains can also be controlled in principle.

In the course of this work a comprehensive knowledge has been developed about some of the underlying principles that govern structure formation in zinc oxide thin films. This knowledge has facilitated the development of three subsequent growth models and a final formulation of several statements that explain the mechanisms that promote the growth of films with different textures and the role of the different growth stages. Thereby also fundamental questions about the origin of preferred orientations in zinc oxide films have been discussed. Especially the quantitative contribution of preferred nucleation and evolutionary selection mechanisms in the temperature range $0.13 < T_H < 0.25$ has been revealed. Furthermore, the majority of reported film structures that have been discussed in chapter 2, especially in section 2.6, can be explained from the respective deposition conditions and the models developed in chapters 5 to 7.

In the following a detailed summary of some of the important experimental findings of this work is given:

It has been shown that xenon ion bombardment affects film growth in the nucleation regime where it promotes a densification of the crystal structure, which enforces growth with the most densely packed planes parallel to the surface of the amorphous substrate. Experimental evidence has been given that this leads to the formation of a distinctly ordered ZnO (0002) fibre texture already at a

¹A comparison of the achieved structural order with film qualities reported in literature is given in table 8.1.

CHAPTER 8. SUMMARY AND OUTLOOK

film thickness of approximately 2.5 - 3 nm. This seed layer has turned out to play the essential role in the structure formation of the whole thick film, almost irrespective of the growth conditions governing subsequent film growth. This has been summarized in a growth model emphasizing the importance of the structural changes engendered by the ion bombardment during the nucleation stage of growth. When this knowledge was applied to the growth of ZnO:Al films on respective IBAS ZnO seed layers, it was further discovered that even distinctly detrimental influences on film growth are markedly attenuated by these seed layers. In particular, the typical effect of strong negative oxygen ion bombardment, that increasingly deteriorates film structure at high oxygen partial pressures, was found to be strongly attenuated. Moreover, in strong contrast to films deposited without seed layer, high oxygen flows were even demonstrated to improve the overall quality of the films growing in a highly ordered c_{\perp} -texture. This finding is remarkable since it clearly decouples the effect of a high oxygen partial pressure from the impact of negative oxygen ions. It provides evidence that, apart from the necessity to suppress energetic oxygen ion bombardment, also in a sputter discharge high oxygen flows are beneficial for the formation of an ordered c_{\perp} -texture. The advantageous influence of high oxygen flows in this respect was also shown in the literature for coating processes where energetic oxygen ions are not an issue. However, so far this was never shown for a sputtering process.

The growth model was generalized by the experience from the seed layer experiments. It is demonstrated that structurally improved zinc oxide films can even be grown by sputtering under conceivably unfavourable conditions if only a seed layer is utilized which possesses pronounced structural order. When the fabrication of films with strikingly improved c_{\perp} -texture was accomplished, insight became available about the very distinct contribution of the different growth stages to texture formation. This motivated to investigate highly energetic oxygen ion bombardment again, since this was known to deteriorate the growth of c_{\perp} -oriented films from a preliminary work. Information about the possible action of a texturing mechanism based on evolutionary selection during post-coalescence growth stages was expected from experiments where a non- c_{\perp} -textured seed layer was grown under intense energetic bombardment. Interestingly energetic oxygen ion bombardment turned out to selectively inhibit the formation of a c_{\perp} -texture and consequently lead to the growth of c_{\parallel} -textured films, where the c -axis is parallel to the substrate surface. With this development, zinc oxide film structures can now be precisely tailored in a wide range by the ion beam assisted sputtering process.

From experiments with c_{\parallel} -textured seed layers it could be demonstrated that any action of a texturing mechanism based on evolutionary selection has at most a weak influence on the structure formation. It could also be shown, that for zinc oxide such a mechanism is very likely not thermally stimulated at least in the range of typical substrate temperatures between room temperature and 300 °C. From these results the striking statement could be concluded that any texture of

Process	Substrate	Temperature [°C]	FWHM
ArF-PLD, ceram.	Si	100	10.4°
	Si	300	1.7°
	Si	1 Min. 300 44 Min. 100	3.7°
	Si	2 Min. 300 43 Min. 100	3.1°
KrF-PLD, ceram.	GaAs	300	3.965°
	GaAs	350	2.854°
	GaAs+SiO ₂	350	2.187°
RFMS, react.	Pt(111)	650	1.37°
RFMS, ceram.	Sapphire(0001)	550	0.65-0.95°
RFMS, ceram.	Glas	250	3.9°
	Au	250	5.4°
	Al	250	7.1-8.8°
	Ni	250	14.2°
	Cu	250	14.2°
IBAS	Si+SiO ₂	80-100	3.67°

Table 8.1: Comparison of structural perfection of c_{\perp} -textured IBAS ZnO films with results from literature. The structural perfection of the films is comparable with films otherwise deposited at elevated substrate temperatures. This is evident from comparing the FWHM of the (0002) rocking curves.

zinc oxide films is almost solely governed by the very initial growth stage, i.e. by preferred nucleation.

The results of this work may be of relevance for the industrial application of c_{\perp} -textured zinc oxide films in market segments where specifically a high structural order is mandatory for device performance. The obvious reason is that with the developed knowledge possible strategies are presented to fabricate ZnO coatings exhibiting outstanding quality without the drawback of investing similarly outstanding technological efforts and costs. Similarly interesting might be the fabrication of c_{\parallel} -textured films, if required. Since any texture is solely governed by the initial growth stage, upon investment in a thin and ideally pristine seed layer, almost the entire ZnO coating may be deposited at parameters solely optimized for productivity. A similar potential may arise in the industrial fabrication of silver-based low-emissivity coatings. The explicit structural improvements of silver coatings grown on modified zinc oxide seed layers are highly promising. However, an indisputable improvement also in the electrical properties of these silver coatings has not yet been demonstrated. This clearly has to be the aim of further efforts in research on this topic.

CHAPTER 8. SUMMARY AND OUTLOOK

For application of ZnO:Al films as TCOs it is also mandatory to explore possible improvements in the electrical properties of such coatings upon improving the structural quality by utilizing seed layers. Since correlations between structural and electrical properties are reported in the literature, respective improvements are expected. Therefore, forthcoming experiments on zinc oxide will clearly focus on the electrical properties of ZnO:Al films. Especially the influence of film texture can now be comprehensively investigated. By utilizing seed layers fabricated by ion beam assisted sputtering, doped films can be deposited under conditions optimized for the doping efficiency while the texture of these films can be tailored in a wide range by the precisely controlled texture of the seed layer. Similarly, the growth of silver films on ZnO seed layers with tailored texture, surface topography and strain will be further investigated in future works. Especially the utilization of c_{\parallel} -textured ZnO seed layers should give some important insight in the strength of epitaxial growth of silver on zinc oxide and the influence of the structural perfection of the silver film on its conductivity.

Bibliography

- [1] Severin D, Kappertz O, Nyberg T, Berg S and Wuttig M 2007 *Thin Solid Films* **515**(7-8) 3554–3558
The effect of target aging on the structure formation of zinc oxide during reactive sputtering
- [2] Pauling L 1960 *The nature of the chemical bond 3rd edition* (New York: Cornell University Press)
- [3] Lide D R 2006 *CRC handbook of chemistry and physics: A ready-reference book of chemical and physical data. 87. edn.* (Boca Raton Fla.: CRC Taylor & Francis)
- [4] Özgür Ü, Alivov Y I, Liu C, Teke A, Reshchikov M A, Doğan S, Avrutin V, Cho S J and Morkoç H 2005 *J. Appl. Phys.* **98** 041301
A comprehensive review of ZnO materials and devices
- [5] Ellmer K, Klein A and Rech B 2008 *Transparent Conductive Zinc Oxide (Springer Series in Materials Science vol 104)* ed Hull R, Jr R M O, Parisi J and Warlimont H (Heidelberg: Springer)
- [6] Szyszka B 2001 *Vakuum in Forschung und Praxis* **1** 38–45
Transparente und leitfähige Oxidschichten
- [7] Look D C, Claflin B, Alivov Y I and Park S J 2004 *Phys. Stat. Sol. (a)* **201**(10) 2203–2212
The future of ZnO light emitters
- [8] Look D C, Coşkun C, Claflin B and Farlow G C 2003 *Physica B* **340-342** 32–38
Electrical and optical properties of defects and impurities in ZnO
- [9] Norton D P, Heo Y W, Ivill M P, Ip K, Pearton S J, Chisholm M F and Steiner T 2004 *Materials Today* **June 2004** 34
ZnO: growth, doping & processing
- [10] Birkholz M, Selle B, Fenske F and Fuhs W 2003 *Phys. Rev. B* **68** 205414
Structure-function relationship between preferred orientation of crystallites and electrical resistivity in thin polycrystalline ZnO:Al films
- [11] Sundaram K B and Khan A 1997 *Thin Solid Films* **295** 87–91
Characterization and optimization of zinc oxide films by r.f. magnetron sputtering
- [12] Muthukumar S, Emanetoglu N W, Patounakis G, Gorla C R, Liang S and Lu Y 2001 *J. Vac. Sci. Technol. A* **19**(4) 1850
Two-step metalorganic chemical vapor deposition growth of piezoelectric ZnO thin film on SiO₂/Si substrate
- [13] Muthukumar S, Gorla C R, Emanetoglu N W, Liang S and Lu Y 2001 *Journal of Crystal Growth* **225** 197–201
Control of morphology and orientation of ZnO thin films grown on SiO₂/Si substrates
- [14] Kluth O, Rech B, Houben L, Wieder S, Schöpe G, Beneking C, Wagner H, Löffl A and Schock H W 1999 *Thin Solid Films* **351** 247–253
Texture etched ZnO:Al coated glass substrates for silicon based thin film solar cells
- [15] Müller J, Rech B, Springer J and Vanecek M 2004 *Solar Energy* **77** 917–930
TCO and light trapping in silicon thin film solar cells

BIBLIOGRAPHY

- [16] Berginski M, Hüpkes J, Schulte M, Schöpe G, Stiebig H and Rech B 2007 *J. Appl. Phys.* **101** 074903
The effect of front ZnO:Al surface texture and optical transparency on efficient light trapping in silicon thin-film solar cells
- [17] Scharowsky E 1953 *Zeitschrift für Physik* **135** 318–330
Optische und elektrische Eigenschaften von ZnO-Einkristallen mit Zn-Überschuß
- [18] Nielsen J W and Dearborn E F 1960 *J. Phys. Chem.* **64**(11) 1762–1763
The growth of large single crystals of zinc oxide
- [19] Laudise R A, Kolb E D and Caporaso A J 1964 *J. Amer. Ceram. Soc.* **47**(1) 9–12
Hydrothermal Growth of Large Single Crystals of Zinc Oxide
- [20] Wang B G, Shi E W and Zhong W Z 1997 *Cryst. Res. Technol.* **32** 659–667
Understanding and Controlling the Morphology of ZnO Crystallites under Hydrothermal Conditions
- [21] Li W J, Shi E W, Zhong W Z and Yin Z W 1999 *Journal of Crystal Growth* **203** 186–196
Growth mechanism and growth habit of oxide crystals
- [22] Sekiguchi T, Miyashita S, Obara K, Shishido T and Sakagami N 2000 *Journal of Crystal Growth* **214/215** 72–76
Hydrothermal growth of ZnO single crystals and their optical characterization
- [23] Ohshima E, Ogino H, Niikura I, Maeda K, Sato M, Ito M and Fukuda T 2004 *Journal of Crystal Growth* **260** 166–170
Growth of the 2-in-size bulk ZnO single crystals by the hydrothermal method
- [24] Zhang C L, Zhou W N, Hang Y, Lü Z, Hou H D, Zuo Y B, Qin S J, Lu F H and Gu S L 2008 *Journal of Crystal Growth* **310** 1819–1822
Hydrothermal growth and characterization of ZnO crystals
- [25] Baruah S and Dutta J 2009 *Sci. Technol. Adv. Mater.* **10** 013001
Hydrothermal growth of ZnO nanostructures
- [26] Vayssieres L, Keis K, Hagfeldt A and Lindquist S E 2001 *Chem. Mater.* **13**(12) 4395
Three-Dimensional Array of Highly Oriented Crystalline ZnO Microtubes
- [27] Wu J J and Liu S C 2002 *J. Phys. Chem. B* **106** 9546–9551
Catalyst-free Growth and Characterization of ZnO Nanorods
- [28] Yamabi S and Imai H 2002 *J. Mater. Chem.* **12** 3773–3778
Growth conditions for wurtzite zinc oxide films in aqueous solutions
- [29] Kajikawa Y 2006 *Journal of Crystal Growth* **289** 387–394
Texture development of non-epitaxial polycrystalline ZnO films
- [30] Bauer E 1956 *Zeitschrift für Kristallographie* **107** 72–98
Struktur und Wachstum dünner Aufdampfschichten
- [31] Bauer E 1956 *Zeitschrift für Kristallographie* **107** 290–317
Über Orientierungserscheinungen beim Kristallwachstum fern vom Phasengleichgewicht
- [32] van der Drift A 1967 *Philips Res. Repts* **22** 267–288
Evolutionary selection, A principle governing growth orientation in vapour-deposited layers
- [33] Knuyt G, Quaeysaegens C, D’Haen J and Stals L M 1995 *Thin Solid Films* **258** 159–169
A quantitative model for the evolution from random orientation to a unique texture in PVD thin film growth

BIBLIOGRAPHY

-
- [34] Knuyt G, Quaeyhaegens C, D'Haen J and Stals L M 1995 *Surface and Coatings Technology* **76-77** 311–315
A model for texture evolution in a growing film
 - [35] Knuyt G, Quaeyhaegens C, D'Haen J and Stals L M 1996 *Phys. Stat. Sol. (b)* **195** 179
A Model for Thin Film Texture Evolution Driven by Surface Energy Effects
 - [36] Smith R W 1996 *J. Appl. Phys.* **81(3)** 1196
A kinetic Monte Carlo simulation of fiber texture formation during thin-film deposition
 - [37] Lee Y E, Kim Y J and Kim H J 1997 *J. Mater. Res.* **13(5)** 1260
Thickness dependence of microstructural evolution of ZnO films deposited by rf magnetron sputtering
 - [38] Fujimura N, Nishihara T, Goto S, Xu J and Ito T 1992 *Journal of Crystal Growth* **130** 269–279
Control of preferred orientation for ZnO_x films: control of self-texture
 - [39] Claeysens F, Freeman C L, Allan N L, Sun Y, Ashfold M N R and Harding J H 2005 *J. Mater. Chem.* **15** 139–148
Growth of ZnO thin films - experiment and theory
 - [40] Köhl D 2006 *Der Einfluß von Ionenbeschuß auf Filmeigenschaften beim reaktiven DC-Magnetron-Sputtern* Diploma thesis RWTH Aachen
 - [41] Fujihara S, Sasaki C and Kimura T 2001 *Appl. Surf. Sci.* **180** 341–350
Crystallization behavior and origin of c-axis orientation in sol-gel-derived ZnO:Li thin films on glass substrates
 - [42] McKenzie D R and Bilek M M M 2001 *Thin Solid Films* **382** 280–287
Thermodynamic theory for preferred orientation in materials prepared by energetic condensation
 - [43] Drese R J and Wuttig M 2005 *J. Appl. Phys.* **98** 073514
Stress evolution during growth in direct-current-sputtered zinc oxide films at various oxygen flows
 - [44] Pelleg J, Zevin L Z, Lungo S and Croitoru N 1991 *Thin Solid Films* **197** 117–128
Reactive-sputter-deposited TiN films on glass substrates
 - [45] Bao D, Gu H and Kuang A 1998 *Thin Solid Films* **312** 37–39
Sol-gel-derived c-axis oriented ZnO thin films
 - [46] Znaidi L, Soler Illia G J A A, Benyahia S, Sanchez C and Kanaev A V 2003 *Thin Solid Films* **428** 257–262
Oriented ZnO thin films synthesis by sol-gel process for laser application
 - [47] Aslan M H, Oral A Y, Menşur E, Gül A and Başaran E 2004 *Solar Energy Materials & Solar Cells* **82** 543–552
Preparation of c-axis-oriented zinc-oxide thin films and the study of their microstructure and optical properties
 - [48] Zhang R and Kerr L L 2007 *Journal of Solid State Chemistry* **180** 988–994
A simple method for systematically controlling ZnO crystal size and growth orientation
 - [49] Shinde V R, Gujar T P and Lokhande C D 2007 *Solar Energy Materials & Solar Cells* **91** 1055–1061
Studies on growth of ZnO thin films by a novel chemical method
-

BIBLIOGRAPHY

- [50] Li C, Li Y, Wu Y, Ong B S and Loutfy R O 2007 *J. Appl. Phys.* **102** 076101
ZnO field-effect transistors prepared by aqueous solution-growth ZnO crystal thin film
- [51] Huang S M, Bian Z Q, Chu J B, Wang Z A, Zhang D W, Li X D, Zhu H B and Sun Z 2009 *J. Phys. D: Appl. Phys.* **42** 055412
One-step growth of structured ZnO thin films by chemical bath deposition in aqueous ammonia solution
- [52] Li B S, Liu Y C, Zhi Z Z, Shen D Z, Lu Y M, Zhang J Y, Kong X G and Fan X W 2002 *Thin Solid Films* **414** 170–174
Effect of the growth temperature on ZnO thin films grown by plasma enhanced chemical vapor deposition
- [53] Kim K S, Kim H W and Lee C M 2003 *Materials Science and Engineering* **B98** 135–139
Effect of growth temperature on ZnO thin film deposited on SiO₂ substrate
- [54] Chen X L, Geng X H, Xue J M and Li L N 2007 *Journal of Crystal Growth* **299** 77–81
Two-step growth of ZnO films with high conductivity and high roughness
- [55] Hahn B, Heindel G, Pschorr-Schoberer E and Gebhardt W 1998 *Semicond. Sci. Technol.* **13** 788–791
MOCVD layer growth of ZnO using DMZn and tertiary butanol
- [56] Chen Y J, Shih Y Y, Ho C H, Du J H and Fu Y P 2010 *Ceramics International* **36** 69–73
Effect of temperature on lateral growth of ZnO grains grown by MOCVD
- [57] Kobayashi K, Matsubara T, Matsushima S and Okada G 1993 *Thin Solid Films* **235** 20–21
Growth of ZnO films by low-pressure organometallic chemical vapor deposition
- [58] Volintiru I, Creatore M, Kniknie B J, Spee C I M A and van de Sanden M C M 2007 *J. Appl. Phys.* **102** 043709
Evolution of the electrical and structural properties during the growth of Al doped ZnO films by remote plasma-enhanced metalorganic chemical vapor deposition
- [59] Volintiru I, Creatore M and van de Sanden M C M 2008 *J. Appl. Phys.* **103** 033704
In situ spectroscopic ellipsometry growth studies on the Al-doped ZnO films deposited by remote plasma-enhanced metalorganic chemical vapor deposition
- [60] Chen X L, Geng X H, Xue J M, Zhang D K, Hou G F and Zhao Y 2006 *Journal of Crystal Growth* **296** 43–50
Temperature-dependent growth of zinc oxide thin films grown by metal organic chemical vapour deposition
- [61] Steinhäuser J, Fay S, Oliveira N, Vallat-Sauvain E and Ballif C 2007 *Appl. Phys. Lett.* **90** 142107
Transition between grain boundary and intragrain scattering transport mechanisms in boron-doped zinc oxide thin films
- [62] Fay S, Steinhäuser J, Oliveira N, Vallat-Sauvain E and Ballif C 2007 *Thin Solid Films* **515** 8558–8561
Opto-electronic properties of rough LP-CVD ZnO:B for use as TCO in thin-film solar cells
- [63] Nicolay S, Fay S and Ballif C 2009 *Crystal Growth & Design* **9(11)** 4957–4962
Growth Model of MOCVD Polycrystalline ZnO

BIBLIOGRAPHY

-
- [64] Mar G L, Timbrell P Y and Lamb R N 1995 *Chem. Mater.* **7** 1890–1896
Factors Influencing the Chemical Vapor Deposition of Oriented ZnO Films Using Zinc Acetate
 - [65] Koch M H, Hartmann A J, Lamb R N, Neuber M and Grunze M 1997 *J. Phys. Chem. B* **101** 8231–8236
Self-Texture in the Initial Stages of ZnO Film Growth
 - [66] Wu J J and Liu S C 2002 *Adv. Mater.* **14**(3) 215
Low-Temperature Growth of Well-Aligned ZnO Nanorods by Chemical Vapor Deposition
 - [67] Deng H, Russell J J, Lamb R N, Jiang B, Li Y and Zhou X Y 2004 *Thin Solid Films* **458** 43–46
Microstructure control of ZnO thin films prepared by single source chemical vapor deposition
 - [68] Dai L P, Deng H, Chen G, Tang C F, Wei M and Li Y 2007 *Vacuum* **81** 969–973
Growth of a-b-axis orientation ZnO films with zinc vacancies by SSCVD
 - [69] Guzewicz E, Kowalik I A, Godlewski M, Kopalko K, Osinniy V, Wójcik A, Yatsunenkov S, Lusakowska E, Paszkowicz W and Guzewicz M 2008 *J. Appl. Phys.* **103** 033515
Extremely low temperature growth of ZnO by atomic layer deposition
 - [70] Sang B and Konagai M 1996 *Jpn. J. Appl. Phys.* **35** L602–L605
Growth of Transparent Conductive Oxide ZnO Films by Atomic Layer Deposition
 - [71] Pung S Y, Choy K L, Hou X and Shan C 2008 *Nanotechnology* **19** 435609
Preferential growth of ZnO thin films by the atomic layer deposition technique
 - [72] Hayamizu S, Tabata H, Tanaka H and Kawai T 1996 *J. Appl. Phys.* **80**(2) 787
Preparation of crystallized zinc oxide films on amorphous glass substrates by pulsed laser deposition
 - [73] Liu C, Chang S H, Noh T W, Abouzaid M, Ruterana P, Lee H H, Kim D W and Chung J S 2007 *Appl. Phys. Lett.* **90** 011906
Initial growth behavior and resulting microstructural properties of heteroepitaxial ZnO thin films on sapphire (0001) substrates
 - [74] Lee J H, Chou C Y, Bi Z, Tsai C F and Wang H 2009 *Nanotechnology* **20** 395704
Growth-controlled surface roughness in Al-doped ZnO as transparent conducting oxide
 - [75] Bruncko J, Vincze A and Netrvalova M 2010 *Vacuum* **84** 162–165
Study of ZnO layers growth by pulsed laser deposition from Zn and ZnO targets
 - [76] Choi J H, Tabata H and Kawai T 2001 *Journal of Crystal Growth* **226** 493–500
Initial preferred growth in zinc oxide thin films on Si and amorphous substrates by a pulsed laser deposition
 - [77] Prasad S V, Walck S D and Zabinski J S 2000 *Thin Solid Films* **360** 107–117
Microstructural evolution in lubricious ZnO films grown by pulsed laser deposition
 - [78] Shao J, Shen Y Q, Sun J, Xu N, Yu D, Lu Y F and Wu J D 2008 *J. Vac. Sci. Technol. B* **26**(1) 214
Low-temperature c-axis oriented growth of nanocrystalline ZnO thin films on Si substrates by plasma assisted pulsed laser deposition
 - [79] Nistor L C, Ghica C, Matei D, Dinescu G, Dinescu M and van Tendeloo G 2005 *Journal of Crystal Growth* **277** 26–31
Growth and characterization of a-axis textured ZnO thin films

BIBLIOGRAPHY

- [80] Ohring M 1992 *The Materials Science of Thin Films* (San Diego: Academic Press)
- [81] Tominaga K, Iwamura S, Fujita I, Shintani Y and Tada O 1982 *Jpn. J. Appl. Phys.* **21**(7) 999–1002
Influence of Bombardment by Energetic Atoms on c-Axis Orientation of ZnO Films
- [82] Tominaga K, Yuasa T, Kume M and Tada O 1985 *Jpn. J. Appl. Phys.* **24**(8) 944–949
Influence of Energetic Oxygen Bombardment on Conductive ZnO Films
- [83] Ngaruiya J M, Kappertz O, Mohamed S H and Wuttig M 2004 *Appl. Phys. Lett.* **85**(5) 748–750
Structure formation upon reactive direct current magnetron sputtering of transition metal oxide films
- [84] Hada T, Wasa K and Hayakawa S 1970 *Thin Solid Films* **7** 135–145
Structures and electrical properties of zinc oxide films prepared by low pressure sputtering system
- [85] Petrov I, Orlinov V and Misiuk A 1984 *Thin Solid Films* **124** 55–67
Highly oriented ZnO films obtained by d.c. reactive sputtering of a zinc target
- [86] Lee Y E, Lee J B, Kim Y J, Yang H K, Park J C and Kim H J 1996 *J. Vac. Sci. Technol. A* **14**(3) 1943
Microstructural evolution and preferred orientation change of radio-frequency-magnetron sputtered ZnO thin films
- [87] Doh S J, Park S I, Cho T S and Je J H 1999 *J. Vac. Sci. Technol. A* **17**(5) 3003
Effects of grid bias on ZnO/ α -Al₂O₃(0001) heteroepitaxy
- [88] Ma H L, Hao X T, Yang Y G, Huang S L, Chen F, Wang Q P and Zhang D H 2002 *Surface and Coatings Technology* **161** 58–61
Bias voltage dependence of properties for ZnO:Al films deposited on flexible substrate
- [89] Sharma P, Sreenivas K and Rao K V 2003 *J. Appl. Phys.* **93**(7) 3963
Analysis of ultraviolet photoconductivity in ZnO films prepared by unbalanced magnetron sputtering
- [90] Nagata T, Ashida A, Fujimura N and Ito T 2004 *J. Appl. Phys.* **95**(8) 3923
The effects of Xe on an rf plasma and growth of ZnO films by rf sputtering
- [91] Aita C R, Purdes A J, Lad R J and Funkenbusch P D 1980 *J. Appl. Phys.* **51**(10) 5533
The effect of O₂ on reactively sputtered zinc oxide
- [92] Matsuoka M and Ono K 1988 *Appl. Phys. Lett.* **53**(15) 1393
Photochromism and anomalous crystallite orientation of ZnO films prepared by a sputtering-type electron cyclotron resonance microwave plasma
- [93] Mirica E, Kowach G, Evans P and Du H 2004 *Crystal Growth & Design* **4**(1) 147–156
Morphological Evolution of ZnO Thin Films Deposited by Reactive Sputtering
- [94] Lin S S and Huang J L 2004 *Surface & Coatings Technology* **185** 222–227
Effect of thickness on the structural and optical properties of ZnO films by r.f. magnetron sputtering
- [95] Yanagitani T, Tomohiro S, Nohara T, Matsukawa M, Watanabe Y and Otani T 2004 *Jpn. J. Appl. Phys.* **43**(5B) 3004–3007
Characterization of (11 $\bar{2}$ 0) Textured ZnO Films Fabricated by RF Magnetron Sputtering

BIBLIOGRAPHY

-
- [96] Fortunato E, Assunção V, Gonçalves A, Marques A, Águas H, Pereira L, Ferreira I, Vilarinho P and Martins R 2004 *Thin Solid Films* **451-452** 443–447
High quality conductive gallium-doped zinc oxide films deposited at room temperature
 - [97] Jiang X, Jia C L and Szyszka B 2002 *Appl. Phys. Lett.* **80(17)** 3090
Manufacture of specific structure of aluminum-doped zinc oxide films by patterning the substrate surface
 - [98] Jiang X, Jia C L and Hong R J 2005 *Journal of Crystal Growth* **289** 464–471
Microstructure dependence of ZnO:Al films on the deposition conditions and the surface morphology of silicon substrate
 - [99] Hong R J and Jiang X 2006 *Appl. Phys. A* **84** 161–164
Microstructure evolution of Al-doped zinc oxide films prepared by in-line reactive mid-frequency magnetron sputtering
 - [100] Yoshino Y, Inoue K, Takeuchi M and Ohwada K 1998 *Vacuum* **51(4)** 601–607
Effects of interface micro structure in crystallization of ZnO thin films prepared by radio frequency sputtering
 - [101] Lee H S, Lee J Y, Kim T W, Kim D W and Cho W J 2004 *Journal of Materials Science* **39** 3525–3528
Formation mechanism of preferential c-axis oriented ZnO thin films grown on p-Si substrates
 - [102] Yoshino Y, Inoue K, Takeuchi M, Makino T, Katayama Y and Hata T 2000 *Vacuum* **59** 403–410
Effect of substrate surface morphology and interface microstructure in ZnO thin films formed on various substrates
 - [103] Goto S, Fujimura N, Nishihara T and Ito T 1991 *Journal of Crystal Growth* **115** 816–820
Heteroepitaxy of zinc oxide thin films, considering non-epitaxial preferential orientation
 - [104] Van de Pol F C M, Blom F R and Popma T J A 1991 *Thin Solid Films* **204** 349–364
R.F. planar magnetron sputtered ZnO films I: Structural properties
 - [105] Kim I W, Kim H S, Kwon Y B, Doh S J, Kim C C, Je J H, Ruterana P and Nouet G 2004 *Appl. Surf. Sci.* **241** 261–265
Effect of ultra-thin buffer on the structure of highly mismatched epitaxial ZnO during sputter growth
 - [106] Sato D, Kashiwaba Y, Haga K, Watanabe H, Zhang B P and Segawa Y 2004 *Vacuum* **74** 601–605
Effect of ZnO buffer layer prepared by rf sputtering on heteroepitaxial growth of high-quality ZnO films
 - [107] Berg S and Nyberg T 2005 *Thin Solid Films* **476** 215–230
Fundamental understanding and modeling of reactive sputtering processes
 - [108] Kappertz O, Drese R J, Ngaruiya J M and Wuttig M 2005 *Thin Solid Films* **484** 64–67
Reactive sputter deposition of zinc oxide: Employing resputtering effects to tailor film properties
 - [109] Winter H, Aumayr F and Lakits G 1991 *Physics Research B* **58** 301–308
Recent advantages in understanding particle-induced electron emission from metal surfaces
 - [110] Uhm H S, Choi E H and Lim J Y 2002 *Appl. Phys. Lett.* **80(5)** 737–739
Secondary electron emission in a mixed gas for application to the plasma display panel
-

BIBLIOGRAPHY

- [111] Colligon J S 2004 *Phil. Trans. R. Soc. Lond. A* **362** 103–116
Ion-assisted sputter deposition
- [112] Ebert J 1990 *Surface and Coatings Technology* **43/44** 950–962
Ion-assisted reactive deposition processes for optical coatings
- [113] Mattox D M 1989 *J. Vac. Sci. Technol. A* **7(3)** 1105–1114
Particle bombardment effects on thin-film deposition: A review
- [114] Colligon J S 1995 *J. Vac. Sci. Technol. A* **13(3)** 1649–1657
Energetic condensation: Processes, properties, and products
- [115] Martin P J 1986 *Journal of Materials Science* **21** 1–25
Review: Ion-based methods for optical thin film deposition
- [116] Deniz D and Harper J M E 2008 *J. Appl. Phys.* **104** 063519
Fiber textures of titanium nitride and hafnium nitride thin films deposited by off-normal incidence magnetron sputtering
- [117] Weis H J *Untersuchung gasochrom schaltender Wolframoxide* Ph.D. thesis RWTH Aachen
- [118] Powder Diffraction Files, Joint Committee on Powder Diffraction Standards, JCPDS, Card 80-0075
- [119] Drese R J 2005 *In-Situ-Messungen der mechanischen Spannungen in gesputterten Metall- und Oxidschichten* Ph.D. thesis RWTH Aachen
- [120] Tauc J, Grigorovici R and Vancu A 1966 *Phys. Stat. Sol.* **15** 627
Optical Properties and Electronic Structure of Amorphous Germanium
- [121] Jellison G E and Modine F A 1996 *Appl. Phys. Lett.* **69(3)** 371
Parameterization of the optical functions of amorphous materials in the interband region
- [122] O’Leary S K, Johnson S R and Lim P K 1997 *J. Appl. Phys.* **82(7)** 3334–3340
The relationship between the distribution of electronic states and the optical absorption spectrum of an amorphous semiconductor: An empirical analysis
- [123] Köhl D, Luysberg M and Wuttig M 2010 *J. Phys. D: Appl. Phys.* **43** 205301
Structural improvement of zinc oxide films produced by ion beam assisted reactive sputtering
- [124] Köhl D, Luysberg M and Wuttig M 2009 *Phys. Status Solidi RRL* **3(7-8)** 236–238
Highly textured zinc oxide films by room temperature ion beam assisted deposition
- [125] Drese R J and Wuttig M 2005 *J. Appl. Phys.* **98** 073514
Stress evolution during growth in direct-current-sputtered zinc oxide films at various oxygen flows
- [126] d’Heurle F M and Harper J M E 1989 *Thin Solid Films* **171** 81–92
Note on the origin of intrinsic stresses in films deposited via evaporation and sputtering
- [127] Davis C A 1993 *Thin Solid Films* **226** 30–34
A simple model for the formation of compressive stress in thin films by ion bombardment
- [128] Windischmann H 1992 *Crit. Rev. in Solid State and Mat. Sci.* **17(6)** 547–596, pp. 583
Intrinsic Stress in Sputter-Deposited Thin Films
- [129] Hoffman D W and Gaerttner M R 1980 *J. Vac. Sci. Technol.* **17(1)** 425–428
Modification of evaporated chromium by concurrent ion bombardment
- [130] Kester D J and Messier R 1992 *J. Appl. Phys.* **72(2)** 504–513
Phase control of cubic boron nitride thin films

BIBLIOGRAPHY

- [131] McKenzie D R 1993 *J. Vac. Sci. Technol. B* **11**(5) 1928–1935
Generation and applications of compressive stress induced by low energy ion beam bombardment
- [132] Dobrev D 1982 *Thin Solid Films* **92** 41–53
Ion-beam-induced texture formation in vacuum-condensed thin metal films
- [133] Dong L and Srolovitz D J 1999 *Appl. Phys. Lett.* **75**(4) 584–586
Mechanism of texture development in ion-beam-assisted deposition
- [134] Lin Z and Bristow P D 2007 *Phys. Rev. B* **75** 205423
Microscopic characteristics of the Ag(111)/ZnO(0001) interface present in optical coatings
- [135] Müggenburg T 1998 *Veredelung von Flachglas durch Beschichten: Stabilisierung von Low-E Systemen durch Aluminium-Zwischenschichten* Ph.D. thesis RWTH Aachen
- [136] Fuchs K 1938 *Math. Proc. Camb. Phil. Soc.* **34** 100
The conductivity of thin metallic films according to the electron theory of metals
- [137] Sondheimer E H 1952 *Advances in Physics* **1** 1–42
The mean free path of electrons in metals

BIBLIOGRAPHY

List of Figures

2.1	The wurtzite structure	10
2.2	Hexagonal basic vectors	13
2.3	Types of crystallographic texture	14
2.4	Typical crystal shapes of hydrothermally grown ZnO	17
2.5	Structure formation in hydrothermal growth of ZnO	19
2.6	Principles of preferred nucleation and evolutionary selection	22
2.7	Nucleation by minimization of Gibb's free energy	25
2.8	Strain energy as a function of crystallite orientation in an external biaxial stress field	28
2.9	Energetic oxygen ion trajectories as a function of target age	42
3.1	The IBAS coater	52
3.2	Geometry of the IBAS process	54
3.3	The IBAS process	55
3.4	The standard coater	56
3.5	Plasma image of the standard coater	57
4.1	XRD: Bragg-Brentano and Rocking Curve geometry	60
4.2	XRD: Grazing Incidence geometry	61
4.3	Tilts of ZnO crystal planes and the scan normal in a grazing incidence scan	63
4.4	Angular deviations between the scan normal and planes of c-textured ZnO in a grazing incidence XRD scan	64
4.5	Example of an XRR pattern	66
4.6	Principle of Tapping Mode AFM	68
4.7	AFM tip	69
4.8	Principle of wafer curvature measurement	70
5.1	XRD-Scans of IBAS films deposited and bombarded under different angles of incidence	78
5.2	XRD-Scans of IBAS films deposited under different durations of the ion bombardment	82
5.3	In-situ film stress measurements of IBAS and reference films	83
5.4	XRD-Scans of films deposited for in-situ stress measurements	84
5.5	XRR-Scan of an ultra-thin reference ZnO sample	85
5.6	XRR-Scan of an ultra-thin IBAS ZnO sample	85
5.7	AFM surface topography of ultra-thin IBAS and reference films	86
5.8	AFM cross-sectional surface profile of ultra-thin IBAS and reference films	88
5.9	AFM height distribution of ultra-thin IBAS and reference films	88
5.10	AFM surface topography of 120 nm thick IBAS and reference films	89
5.11	AFM cross-sectional surface profile of 120 nm thick IBAS and reference films	90
5.12	AFM height distribution of 120 nm thick IBAS and reference films	91
5.13	AFM grain size distribution of 120 nm thick IBAS and reference films	91
5.14	TEM cross-sectional dark field images of IBAS and reference films	93
5.15	TEM cross-sectional images of an IBAS film	94
5.16	TEM plan-view images of IBAS and reference films	95
5.17	Schematic depiction of the origin of biaxial and out-of-plane strains in IBAS ZnO films	97
5.18	Mass density of IBAS and reference ZnO films determined from XRR patterns	98

LIST OF FIGURES

5.19	XRD-scans of films sequentially bombarded between growth cycles	100
5.20	XRD-Scan of an extremely thin textured IBAS ZnO film	101
5.21	XRR-Scan of an extremely thin textured IBAS ZnO film	102
5.22	Atomistic growth model for sputtered ZnO films: Comparison of IBAS and standard processes	104
6.1	XRD-scans of thick ZnO:Al films on IBAS ZnO buffer layers	106
6.2	XRD-Scans of 20 nm thin IBAS ZnO buffers before ion-etching	107
6.3	XRD-Scans of IBAS ZnO films after ion-etching	108
6.4	XRR-Scans of IBAS and reference ZnO films: Before and after ion-etching . . .	109
6.5	Etching rate and lattice strain of ion-etched IBAS buffer layers	110
6.6	Surface roughness of IBAS films prior and after ion-etching	111
6.7	XRD-Scans of thick ZnO:Al films deposited onto ion-etched IBAS buffer layers	111
6.8	Rocking curves of ZnO:Al films: Improvement of texture by an IBAS buffer . .	113
6.9	Topography of 20 nm thick IBAS and reference buffers: as-deposited	114
6.10	Topography of 20 nm thick IBAS and reference buffers: ion-etched	116
6.11	Topography of 800 nm thick ZnO:Al films deposited on ion-etched buffers . . .	117
6.12	XRD-Scans of ZnO:Al films on buffers with different thicknesses	118
6.13	XRD-Scans of thick ZnO:Al films deposited at different oxygen flows	120
6.14	XRD-Scans of thick ZnO:Al films deposited onto IBAS buffers at different oxygen flows	120
6.15	Structural improvement of ZnO:Al films by IBAS buffers as a function of the oxygen flow during ZnO:Al deposition	121
6.16	XRD-Scans: Evolution of the (100) peak of ZnO:Al as a function of oxygen flow	122
6.17	XRD-Scans: Absence of the (100) peak of ZnO:Al deposited onto IBAS buffers	123
6.18	XRD sample profile: Structural improvements of ZnO:Al by IBAS buffers as a function of substrate position for differently aged targets	124
6.19	XRD sample profile: Lattice strain of ZnO:Al on IBAS buffers as a function of substrate position for differently aged targets	125
6.20	XRD-Scans of thick ZnO:Al films deposited at different oxygen flows	125
6.21	XRD-Scans of thick ZnO:Al films deposited onto IBAS buffers at different oxygen flows	126
6.22	Structural improvement of ZnO:Al films by IBAS buffers as a function of the oxygen flow during ZnO:Al deposition	127
6.23	XRD-Scans: Evolution of the (100) peak of ZnO:Al as a function of oxygen flow	127
6.24	XRD-Scans: Absence of the (100) peak of ZnO:Al deposited onto IBAS buffers	128
6.25	Generalized growth model for sputtered ZnO films	131
6.26	Ag(111)/ZnO(0001) interface	133
6.27	XRD patterns of Ag films deposited at different discharge powers	134
6.28	Physical properties of Ag films deposited at different discharge powers	136
6.29	XRD: First Ag films on IBAS seed layers	137
6.30	XRD: Ag films on very thin IBAS seed layers	139
6.31	XRD: Ag films on IBAS seed layers	140
6.32	Improved conductivity of Ag films on IBAS seed layers	140
6.33	XRD: Ag films on ion-etched IBAS seed layers	141
6.34	Silver film quality on ion-etched seed layers: Comparison of XRD peak net areas	142
6.35	Resistivity of Ag films on ion-etched seed layers	143
6.36	XRD: Ag films on IBAS buffers with different structural strain	144
6.37	Analysis of Ag films on IBAS buffers with different structural strain	145
6.38	XRD patterns of Ag films grown on massively strained seed layers	146

LIST OF FIGURES

6.39 AFM study of nucleation and growth of Ag films on standard ZnO seed layers at the sample centre	148
6.40 AFM study of nucleation and growth of Ag films on standard ZnO seed layers at the sample position above the target racetrack	150
6.41 Ag surface topography: Example of high and low quality seed layers	151
6.42 XRD growth study of Ag films on dual IBAS-ZnO + ZnO:Al seed layers	153
6.43 AFM growth study of Ag films on dual IBAS-ZnO + ZnO:Al seed layers	155
7.1 Bragg-Brentano XRD scan of ZnO deposited under intense oxygen ion bombardment	159
7.2 GI-XRD scan of ZnO deposited under intense oxygen ion bombardment	160
7.3 ZnO films grown on a-axis textured seed layers	161
7.4 Bragg-Brentano XRD patterns of thick ZnO films grown on a-axis textured seed layers	163
7.5 Bragg-Brentano XRD patterns of thick ZnO films grown on a-axis textured seed layers	164
7.6 GI XRD patterns of thick ZnO films grown on a-axis textured seed layers . . .	165
7.7 Thick oxygen ion bombarded films with different (100)/(110) fractions	167
7.8 Lateral inhomogeneity in the (100)/(110) fraction	168
7.9 XRD patterns of heated ZnO films	171
7.10 XRD patterns of heated ZnO films	172
7.11 Interruption of textured growth by ion bombardment: XRD patterns.	173
7.12 Final growth model	179

Lebenslauf

Name	Köhl
Vorname	Dominik
Geburtstag	22.11.1978
Geburtsort	Gießen
Staatsangehörigkeit	Deutsch
1999	Abitur
2000-2006	Studium der Physik an der RWTH Aachen University mit Abschluß Diplom
2007-2010	Promotion am I. Physikalischen Institut (IA) der RWTH Aachen University unter Betreuung durch Prof. Dr. M. Wuttig
2011	mündliche Prüfung: 17.02.2011